



## City Research Online

### City, University of London Institutional Repository

---

**Citation:** Razavi, A. K. (1998). Measurement and computation of vortex shedding and its control. (Unpublished Doctoral thesis, City, University of London)

This is the accepted version of the paper.

This version of the publication may differ from the final published version.

---

**Permanent repository link:** <https://openaccess.city.ac.uk/id/eprint/31067/>

**Link to published version:**

**Copyright:** City Research Online aims to make research outputs of City, University of London available to a wider audience. Copyright and Moral Rights remain with the author(s) and/or copyright holders. URLs from City Research Online may be freely distributed and linked to.

**Reuse:** Copies of full items can be used for personal research or study, educational, or not-for-profit purposes without prior permission or charge. Provided that the authors, title and full bibliographic details are credited, a hyperlink and/or URL is given for the original metadata page and the content is not changed in any way.

MEASUREMENT AND COMPUTATION OF  
VORTEX SHEDDING  
AND ITS CONTROL

Armin K. Razavi, MEng

Thesis submitted for the degree of  
Doctor of Philosophy  
in the School of Engineering  
City University  
London

Hydraulics Division  
Department of Civil Engineering  
City University  
Northampton Square  
London EC1V 0HB

May 1998

# TABLE OF CONTENTS

	Page
<b>TITLE PAGE</b> .....	<b>1</b>
<b>TABLE OF CONTENTS</b> .....	<b>2</b>
<b>LIST OF TABLES</b> .....	<b>6</b>
<b>LIST OF FIGURES</b> .....	<b>8</b>
<b>ACKNOWLEDGEMENTS</b> .....	<b>15</b>
<b>ABSTRACT</b> .....	<b>16</b>
<b>NOMENCLATURE</b> .....	<b>17</b>

---

<b>CHAPTER ONE: INTRODUCTION</b> .....	<b>20</b>
1.1 Introductory Remarks .....	20
1.2 Basic Definitions .....	21
1.3 Suppression Techniques .....	27
1.4 Computational Fluid Dynamics .....	31
1.5 Motivation and Objectives of Present Study .....	32
<b>CHAPTER TWO: MATHEMATICAL FORMULATION</b> .....	<b>34</b>
2.1 Introductory Remarks .....	34
2.2 Governing Equations .....	34
2.3 Averaged Equations .....	35
2.4 Boussinesq's Eddy Viscosity Concept .....	37
2.5 The $k - \epsilon$ Turbulence Model .....	38
2.6 Finite Volume Discretisation .....	40
2.6.1 Rate of Change - temporal discretisation .....	41
2.6.2 Convection and diffusion fluxes .....	42
2.6.3 Sources .....	42
2.7 Algebraic Form Of The Discretised Transport Equations .....	43
2.8 Choice of Interpolation Scheme .....	43
2.8.1 Central Differencing Scheme .....	44
2.8.2 Upwind-Differencing Scheme .....	44
2.8.3 Linear-Upwind Differencing Scheme .....	45
2.8.4 The SMART Scheme .....	46

2.9 Pressure - Velocity Coupling .....	47
2.10 Treatment Of Boundary Conditions .....	47
2.10.1 Inlet Boundaries:.....	48
2.10.2 Outlet Boundaries .....	48
2.10.3 Planes or Axes of Symmetry .....	48
2.10.4 Solid Walls .....	49
2.11 Time-Step Size .....	50
2.12 Flow-Solver Outline .....	51
2.13 Overall Flow Chart .....	52
<b>CHAPTER THREE: APPLICATION TO SINGLE CYLINDERS.....</b>	<b>54</b>
3.1 Introductory Remarks.....	54
3.2 Review of Experimental Findings.....	54
3.2.1 Circular Cylinders .....	55
3.2.2 Square Cylinders.....	57
3.3 Review Of Previous Predictions.....	60
3.4 Grid Generation.....	62
3.5 Grid and Time-step Dependence .....	66
3.5.1 Circular Cylinder.....	66
3.5.2 Square Cylinder .....	69
3.6 Laminar Flow Results .....	73
3.6.1 Circular Cylinder.....	73
3.6.2 Square Cylinder .....	77
3.7 Turbulent Flow.....	80
3.7.1 Square Cylinder .....	81
3.7.2 Circular Cylinder.....	82
3.8 Reynolds Number Dependence .....	88
3.9 Conclusions.....	92
<b>CHAPTER FOUR: APPLICATION TO TWO CIRCULAR CYLINDERS IN TANDEM .....</b>	<b>94</b>
4.1 Introductory Remarks.....	94
4.2 Review of Experimental Results.....	94
4.3 Review of Previous Predictions.....	98
4.4 Computational Details .....	99
4.5 Laminar Flow Simulations .....	102
4.6 Turbulent Flow Simulations.....	109
4.7 Conclusions.....	117

<b>CHAPTER FIVE: PREDICTION OF SUPPRESSION BY CONTROL</b>	
<b>CYLINDER.....</b>	<b>119</b>
5.1 Introductory Remarks.....	119
5.2 Experimental Results.....	120
5.3 Previous Predictions.....	121
5.4 Computational Details.....	121
5.5 Laminar Flow Simulations.....	122
5.5.1 Circular Cylinder.....	122
5.5.2 Square Cylinder.....	131
5.6 Turbulent Flow Simulations.....	141
5.6.1 Circular Cylinder.....	141
5.6.2 Square Cylinder.....	154
5.7 Conclusions.....	162
<b>CHAPTER SIX: EXPERIMENTATIONS ON SUPPRESSION BY FORWARD</b>	
<b>INJECTION.....</b>	<b>164</b>
6.1 Introductory Remarks.....	164
6.2 Experimental Set-up.....	164
6.3 Data Reduction.....	167
6.4 Results.....	168
6.4.1 Parametric Study.....	168
6.4.2 Detailed Re analysis.....	175
6.4.3 Strouhal Number Analysis.....	178
6.4.4 Penetration Length.....	180
6.4.5 Sensitivity To Yaw.....	181
6.5 Conclusions.....	183
<b>CHAPTER SEVEN: PREDICTION OF SUPPRESSION BY FORWARD</b>	
<b>INJECTION.....</b>	<b>184</b>
7.1 Introductory Remarks.....	184
7.2 Computational Details.....	185
7.2.1 Boundary Conditions.....	185
7.2.2 Re-defining the Drag Term.....	187
7.2.3 SIPSOL.....	188
7.3 Grid Generation.....	190
7.4 Laminar Flow.....	191
7.5 Turbulent Flow.....	207

7.6 Conclusions .....215

**CHAPTER EIGHT: PREDICTION OF SUPPRESSION BY A REAR**

**STAGNATION JET .....216**

8.1 Introductory Remarks.....216

8.2 Laminar Flow .....216

8.3 Turbulent Flow .....224

8.3.1 Square Cylinder .....224

8.3.2 Circular Cylinder.....231

8.4 Conclusions .....239

**CONCLUSIONS AND FURTHER WORK .....240**

**REFERENCES.....244**

# LIST OF TABLES

Table	Page
1.1: Visualisation of vortex trails and Karman Vortex Streets .....	26
3.1: Terminology according to Roshko (1961) for flow regimes .....	55
3.2: Geometric data used in the grid code to generate a grid for a circular cylinder (all measurements are in metres).....	64
3.3: Geometric data used in the grid code to generate a grid for a square cylinder (all measurements are in metres).....	65
3.4: Grid and time step dependence for a circular cylinder in laminar flow (Re=100). .....	68
3.5: Number of time-steps and CPU time required per cycle for RUNs 1 to 5. ....	68
3.6: Grid and time step dependence for a circular cylinder in turbulent flow .....	69
3.7: Grid and time-step dependence for a square cylinder in laminar flow.....	71
3.8: Number of time-steps and CPU time required per cycle for RUNs 1 to 5. ....	71
3.9: Grid and time step dependence for a square cylinder in turbulent flow.....	72
3.10: Results for a circular cylinder at Re=100.....	76
3.11: Results for a square cylinder at Re=100.....	79
3.12: Predicted and measured parameters for a square cylinder at Re=20,000. ....	84
3.13: Grid and time-step arrangements for predictions of square cylinder.....	84
3.14: Predicted and measured parameters for a circular cylinder at Re=65,000.....	86
3.15: Predicted and measured parameters for a circular cylinder at Re=5x10 <sup>6</sup> . ....	86
3.16: Results a circular cylinder in the transcritical regime. ....	89
4.1: Grid arrangements for two cylinders in tandem in turbulent flow.....	110
5.1: Results of the behaviour of the drag and lift coefficients with a control cylinder collected by present method at Re=100 and Lin and Wu (1994) at Re=80.	127
5.2: FFT analysis of the drag and lift coefficients with a control cylinder.....	127
5.3: Behaviour of the drag and lift coefficients with a control cylinder. ....	133
5.4: FFT analysis of the drag and lift coefficients with a control cylinder for a square cylinder in laminar flow. ....	133
5.5: Results for the circular cylinder with control cylinder at Re=6.5x10 <sup>4</sup> .....	146
5.6: Predictions and experimental values of the main parameters for a square cylinder at Re=4.2x10 <sup>4</sup> . ....	156
5.7: Behaviour of drag, lift and Strouhal number with a control cylinder. ....	157

6.1: Experiments performed. ....	169
6.2: Optimum geometry for vortex suppression by forward injection.....	169
7.1: Results for forward injection, for a circular cylinder at $Re=100$ .....	193
7.2: Turbulence sensitivity results for forward injection. ....	209
7.3: Results for forward injection, for a circular cylinder at $Re=6.5 \times 10^4$ .....	210
8.1: Results for rear stagnation jet behind a circular cylinder at $Re=200$ .....	219
8.2: Experimental and numerical results for $Re=14285 \sim 22000$ .....	227
8.3: Results for rear stagnation jet behind a square cylinder at $Re=14285$ .....	227
8.4: Results for rear stagnation jet behind a circular cylinder at $Re=6.5 \times 10^4$ .....	232

# LIST OF FIGURES

<b>Figure</b>	<b>Page</b>
1.1: Flow past a circular cylinder. ....	22
1.2: Typical time history for drag and lift coefficients over time t. ....	23
1.3: Drag coefficient for a sphere and a cylinder. ....	25
1.4: Reynolds number versus Strouhal number for circular cylinders (Shin and Wambsganss, 1977) and (Jendrzeczyk and Chen, 1985). ....	25
2.1: Two-dimensional control volume. ....	41
2.2: Normalised Variable Diagram for different interpolation schemes ....	46
2.3: Flow chart of programmes and data flow in the project with FORTRAN names. ....	53
3.1: Experimental data for a smooth circular cylinder for a) Mean Drag Coefficient; b) Strouhal number; c) RMS Lift Coefficient. ....	58
3.2: Experimental and numerical data for a square cylinder for a) Mean Drag Coefficient; b) Strouhal number. ....	59
3.3: Typical grid arrangements used to model single a) Circular (148x102) and b) Square cylinder (121x110). ....	63
3.4: Close up of circular cylinder with important parameters highlighted. ....	64
3.5: Close up of square cylinder with important parameters highlighted. ....	65
3.6: Flow visualisation of vortex shedding from a circular cylinder at Reynolds number of 140. ....	74
3.7: Streaklines behind a circular cylinder at Re=100 as obtained with the SMART scheme. ....	75
3.8: Time histories of drag and lift for a circular cylinder at Re=100; showing also the power spectra. ....	76
3.9: Streaklines behind a square cylinder at Re=100 as obtained with alternative interpolation schemes. ....	78
3.10: Time histories of drag and lift for a square cylinder at Re=100; showing also the power spectra. ....	79
3.11: Predicted drag and lift coefficients with and without the k-ε model modification for a square cylinder at Re=20,000. ....	85
3.12: Predicted drag and lift coefficients with and without the k-ε model modification for a circular cylinder at Re=65,000. ....	85
3.13: Parametric study of Ct coefficient for Re=65,000. ....	87
3.14: Parametric study of Ct coefficient for Re=5x10 <sup>6</sup> . ....	87

3.15: Variation of mean drag Strouhal number, and fluctuating lift with Reynolds number for a single circular cylinder. ....	90
3.16: Variation of mean drag and Strouhal number with Reynolds number for a single square cylinder. ....	91
4.1: Interference Drag Coefficient for two cylinders in tandem (data from Bierman and Hernstein (1933)). ....	96
4.2: Classification of regimes for two circular cylinders in tandem.....	98
4.3: Definitions of quantities involved in generating grids. ....	100
4.4: The area around the two cylinders, with a separation of three diameters.....	100
4.5: A grid of 115x78 used for two cylinders in tandem at three diameter spacing..	101
4.6: A grid of 111x66 used for two cylinders in tandem at seven diameter spacing.	101
4.7: Time histories for drag and lift coefficient of two circular cylinders in tandem at P/D=3 at Re=100 and 300. ....	104
4.8: Streaklines for two cylinders in tandem at P/D=3 with Re=300. ....	104
4.9: Time histories for drag and lift coefficient of two circular cylinders in tandem at P/D=7 at Re 100 and 300. ....	105
4.10: Streaklines for two cylinders in tandem at P/D=7 with Re=300. ....	105
4.11: Mean drag coefficient for different cylinder spacing (P/D).....	106
4.12: RMS lift coefficient for different cylinder spacing (P/D) at a) Re=100 and b) Re=300. ....	107
4.13: Strouhal number ratio for different cylinder spacing (P/D) for the .....	108
4.14: Grid used for turbulent flow simulations of two cylinder in at P/D=3. ....	109
4.15: a) Upstream and b) downstream cylinder time histories of the drag and lift coefficients for two cylinder in tandem with a separation of P/D=5 at $Re=6.5 \times 10^4$ with and without the k- $\epsilon$ modification.....	113
4.16: Two cylinders in tandem, showing a) interference drag, and b) mean drag in turbulent flow.....	114
4.17: Strouhal number analysis for two cylinders in tandem at $Re=6.5 \times 10^4$ . ....	115
4.18: Velocity vectors for two cylinders in flow of $Re=65,000$ at different separation: a) P/D=1.35, b) P/D=2.5, c) P/D=5. ....	116
5.1: Schematics of arrangement for control of vortex shedding. ....	125
5.2: Grid arrangement (2) for a circular cylinder with control cylinder. ....	125
5.3: Grid arrangement (3) for a circular cylinder with control cylinder. ....	126
5.4: Grid arrangement (4) for a circular cylinder with control cylinder. ....	126
5.5: Time histories and power spectra for a circular cylinder at Re=100 with no control cylinder (RUN 1).....	128
5.6: Time histories and power spectra for a circular cylinder at Re=100 with control cylinder (RUN 2: D/d=4.12, x/D=1, y/D=0.92).....	128

5.7: Time histories and power spectra for a circular cylinder at $Re=100$ with control cylinder (RUN 3: $D/d=5.38$ , $x/D=0.5$ , $y/D=1$ ).	129
5.8: Time histories and power spectra for a circular cylinder at $Re=100$ with control cylinder (RUN 4: $D/d=7.78$ , $x/D=0$ , $y/D=0.64$ ).	129
5.9: Streaklines for the four runs before and after inserting a control cylinder.	130
5.10: Schematics of arrangement for control cylinder.	134
5.11: Grid arrangement (2) for a square cylinder with control cylinder.	134
5.12: Grid arrangement (3) for a square cylinder with control cylinder.	135
5.13: Grid arrangement (4) for a square cylinder with control cylinder.	135
5.14: Time histories for the drag and lift coefficients for a square cylinder at $Re=100$ with no control cylinder (RUN 1); showing also the power spectra.	136
5.15: Time histories for the drag and lift coefficients for a square cylinder at $Re=100$ with a control cylinder (RUN 2: $D/d=7.14$ , $x/D=1.02$ , $y/D=0.95$ ); showing also the power spectra.	136
5.16: Time histories for the drag and lift coefficients for a square cylinder at $Re=100$ with a control cylinder (RUN 3: $D/d=5.5$ , $x/D=0.59$ , $y/D=1.21$ ); showing also the power spectra.	137
5.17: Time histories for the drag and lift coefficients for a square cylinder at $Re=100$ with a control cylinder (RUN 4: $D/d=7.3$ , $x/D=0.22$ , $y/D=0.76$ ); showing also the power spectra.	137
5.18: Streaklines for the four runs before and after inserting a control cylinder.	138
5.19: Velocity vectors around a square cylinder at $Re=100$ , with no control.	139
5.20: Velocity vectors around a square cylinder at $Re=100$ , with control as in grid arrangement (2).	139
5.21: Velocity vectors around a square cylinder at $Re=100$ , with control as in grid arrangement (3).	140
5.22: Velocity vectors around a square cylinder at $Re=100$ , with control as in grid arrangement (4).	140
5.23: Definition sketch and coordinate system.	141
5.24: Grid without control cylinder and close up of the main cylinder.	142
5.25: Grid arrangements for the runs with control cylinder.	143
5.26: Drag and lift time histories and power spectra for RUN 1	146
5.27: Drag and lift time histories and power spectra for RUN 2	147
5.28: Drag and lift time histories and power spectra for RUN 3	147
5.29: Drag and lift time histories and power spectra for RUN 4	148
5.30: Drag and lift time histories and power spectra for RUN 5	148
5.31: Drag and lift time histories and power spectra for RUN 6	149
5.32: Drag and lift time histories and power spectra for RUN 7	149
5.33: Predicted distribution of the time averaged pressure coefficient ( $C_p$ ) for a) $G/D=0.082$ and b) $G/D=0.122$ .	150

5.34: Distribution of mean CD for different positions of the control cylinder, showing comparisons between the results of Sakamoto and Haniu (1994) and the present predictions. ....	151
5.35: Streaklines with no control cylinder (RUN 1). ....	151
5.36: Streaklines with control cylinder for a) RUN 2; b) RUN 3 and c) RUN 4.....	152
5.37: Streaklines with control cylinder for a) RUN 5; b) RUN 6 and c) RUN 7.....	153
5.38: Definition sketch and coordinate system. ....	154
5.39: Position of maximum velocity along the cylinder, and positions of control cylinder modelled, highlighting the optimum positions. ....	157
5.40: a) Predicted and b) Experimental values of minimum mean drag along S/W at the point of maximum velocity.....	158
5.41: a) Predicted and b) Experimental values of minimum fluctuating drag along S/W at the point of maximum velocity.....	158
5.42: a) Predicted and b) Experimental values of fluctuating lift along S/W at the point of maximum velocity.....	158
5.43: Time histories for the drag and lift coefficients for a square cylinder at $Re=4.2 \times 10^4$ with no control cylinder; showing also the power spectra.....	159
5.44: Time histories for the drag and lift coefficients for a square cylinder at $Re=4.2 \times 10^4$ with control cylinder at $S/W=0.282$ , $T/W=0.280$ (RUN 6); showing also the power spectra.....	159
5.45: Streaklines around a square cylinder at $Re=4.2 \times 10^4$ . ....	160
5.46: Streaklines around a square cylinder at $Re=4.2 \times 10^4$ a) without control cylinder, and with control cylinder at b) $S/W=0.5$ $T/W=0.177$ (RUN 10); c) $S/W=0.282$ , $T/W=0.280$ (RUN 6); and d) $S/W=1.0$ , $T/W=0.535$ (RUN 22). ....	161
6.1: The experimental set-up. ....	166
6.2: Picture of the laboratory and experimental set-up. ....	166
6.3: Stage 1 results for the variation of $V_r$ with Reynolds number in the a) in-line and b) transverse directions.....	170
6.4: Stage 2 results for the variation of $V_r$ with Reynolds number in the a) in-line and b) transverse directions.....	171
6.5: Stage 3 results for the variation of $V_r$ with Reynolds number in the a) in-line and b) transverse directions.....	172
6.6: Stage 4 results for the variation of $V_r$ with Reynolds number in the a) in-line and b) transverse directions.....	173
6.7: a) In-line b) transverse direction analysis of sensitivity of vortex shedding suppression to geometry.....	174
6.8: Detailed analysis of Reynolds number range for the geometry 13holes, 3mm diameter, 10mm apart ( $G1=0.250$ , $G2=0.384$ ). ....	175
6.9: Trace of accelerometer output for a) In-line and b) transverse directions	

for geometry: 13 holes, 3mm diameter, 10mm apart at $Re=7517$ . .....	176
6.10: Power spectra for in-line and transverse direction signals, before and after injection for geometry: 13 holes, 3mm diameter, 10mm apart at $Re=7517$ . ....	177
6.11: Vortex shedding frequency for the in-line and the transverse directions. ....	179
6.12: Relationship between Reynolds number and Strouhal number with no injection. ....	179
6.13: Penetration length.....	180
6.14: Cylinder orientations in tests for sensitivity to yaw.....	181
6.15: Results for sensitivity to yaw. ....	182
7.1: Injection cells on the a) west side of the cylinder for modelling forward injection and the b) east side of the cylinder modelling rear stagnation jet.....	188
7.2: Solution to the asymmetry caused by SIPSOL. ....	189
7.3: Close-up of the region around the cylinder, showing the splitting lines. ....	190
7.4: Schematics for forward injection.....	193
7.5: Behaviour of main parameters with $U_r$ for laminar flow with forward injection. ....	194
7.6: Streamlining of bluff body by forward injection.....	197
7.7: Drag and lift time histories with their power spectra for $Re=100$ , with no forward injection. ....	198
7.8: Drag and lift time histories with their power spectra for $Re=100$ , with forward injection of $U_r=1.498$ . ....	198
7.9: Drag and lift time histories with their power spectra for $Re=100$ , with forward injection of $U_r=1.552$ . ....	199
7.10: Drag and lift time histories with their power spectra for $Re=100$ , with forward injection of $U_r=2.0$ . ....	199
7.11: Velocity vectors around a circular cylinder at $Re=100$ , with no forward injection. ....	200
7.12: Velocity vectors around a circular cylinder at $Re=100$ , with forward injection ratio of $U_r=1.498$ . ....	200
7.13: Velocity vectors around a circular cylinder at $Re=100$ , with forward injection ratio of $U_r=1.552$ . ....	201
7.14: Velocity vectors around a circular cylinder at $Re=100$ , with forward injection ratio of $U_r=2.0$ . ....	201
7.15: Streaklines for forward injection at $Re=100$ , when a) $U_r=0.$ , b) $U_r=1.498$ , c) $U_r=1.552$ , d) $U_r=2.0$ . ....	202
7.16: Breakdown of the drag and lift coefficient behaviour around a circular cylinder at $Re=100$ , with no forward injection. ....	203
7.17: Breakdown of the drag and lift coefficient behaviour around a circular cylinder at $Re=100$ , with forward injection ratio of $U_r=1.498$ . ....	204

7.18: Vorticity contours around a cylinder at $Re=100$ , without forward injection. ....	205
7.19: Vorticity contours around a circular cylinder at $Re=100$ , with forward injection ratio of $Ur=1.498$ . ....	205
7.20: Vorticity contours around a circular cylinder at $Re=100$ , with forward injection ratio of $Ur=1.552$ . ....	206
7.21: Vorticity contours around a circular cylinder at $Re=100$ , with forward injection ratio of $Ur=2.0$ . ....	206
7.22: Behaviour of main parameters with $Ur$ for turbulent flow with forward injection. ....	210
7.23: Drag and lift time histories with their power spectra for $Re=6.5 \times 10^4$ , with no forward injection. ....	211
7.24: Drag and lift time histories with their power spectra for $Re=6.5 \times 10^4$ , with forward injection at $Ur=0.75$ . ....	211
7.25: Velocity vectors around a circular cylinder at $Re=6.5 \times 10^4$ , with no forward injection. ....	212
7.26: Velocity vectors around a circular cylinder at $Re=6.5 \times 10^4$ , with forward injection at $Ur=0.75$ . ....	212
7.27: Streaklines around a circular cylinder at $Re=6.5 \times 10^4$ , with no forward injection. ....	213
7.28: Streaklines around a circular cylinder at $Re=6.5 \times 10^4$ , with forward injection at $Ur=0.75$ . ....	213
7.29: Vorticity around a circular cylinder at $Re=6.5 \times 10^4$ , with no forward injection. ....	214
7.30: Vorticity contours around a circular cylinder at $Re=6.5 \times 10^4$ , with forward injection at $Ur=0.75$ . ....	214
8.1: Schematics for the rear stagnation jet. ....	217
8.2: Behaviour of drag and lift coefficients with $Ur$ . ....	219
8.3: Time histories of drag & lift before and after rear stagnation jet of $Ur=3$ . ....	221
8.4: Time histories of drag and lift before and after rear stagnation jet of $Ur=10$ . ....	221
8.5: Velocity vectors behind cylinder at rear stagnation jet of $Ur=3$ . ....	222
8.6: Velocity vectors behind cylinder at rear stagnation jet of $Ur=10$ . ....	222
8.7: Streaklines for rear stagnation jet. ....	223
8.8: Zoom in on streaklines for rear stagnation jet. ....	223
8.9: Behaviour of drag, lift, and Strouhal number with $Ur$ . ....	228
8.10: Time histories of drag and lift coefficients for a square cylinder at $Re=14285$ ; showing also the power spectra. ....	228
8.11: Time histories of drag and lift coefficients for a square cylinder at	

Re=14285 with a rear stagnation jet of $U_r=0.1$ ; showing also the power spectra. ....	229
8.12: Time histories of drag and lift coefficients for a square cylinder at Re=14285 with a rear stagnation jet of $U_r=1.0$ ; showing also the power spectra. ....	229
8.13: Streaklines for a square cylinder at Re=14285 without and with rear stagnation jet at jet velocities of a) $U_r=0.0$ , b) $U_r=0.1$ and c) $U_r=1.00$ . ....	230
8.14: Behaviour of drag, lift, and Strouhal number with $U_r$ . ....	232
8.15: Drag and lift time histories and power spectra for the case with no rear stagnation jet at $Re=6.5 \times 10^4$ . ....	234
8.16: Drag and lift time histories and power spectra for the case with rear stagnation jet of $U_r=0.5$ at $Re=6.5 \times 10^4$ . ....	234
8.17: Drag and lift time histories and power spectra for the case with rear stagnation jet of $U_r=1.5$ at $Re=6.5 \times 10^4$ . ....	235
8.18: Drag and lift time histories and power spectra for the case with rear stagnation jet of $U_r=5.0$ at $Re=6.5 \times 10^4$ . ....	235
8.19: Velocity vectors around a circular cylinder at $Re=6.5 \times 10^4$ . ....	236
8.20: Velocity vectors around a circular cylinder at $Re=6.5 \times 10^4$ , with rear stagnation jet of $U_r=0.5$ . ....	236
8.21: Velocity vectors around a circular cylinder at $Re=6.5 \times 10^4$ , with rear stagnation jet of $U_r=1.5$ . ....	237
8.22: Velocity vectors around a circular cylinder at $Re=6.5 \times 10^4$ , with rear stagnation jet of $U_r=5.0$ . ....	237
8.23: Streaklines for a circular cylinder at $Re=6.5 \times 10^4$ without and with rear stagnation jet at jet velocities of a) $U_r=0.$ , b) $U_r=0.5$ , c) $U_r=1.5$ , and d) $5.0$ . ....	238

## **ACKNOWLEDGEMENTS**

I am especially indebted to my supervisor, Dr B.A. Younis for his continuous guidance and support throughout the project and the writing-up of this thesis.

I am grateful to Mr. Vlado Przulj who has never denied to offer his advice when needed. My thanks also to the technical staff of the City University Hydraulics Laboratory for their assistance in the experimental work.

I would like to thank my family and friends for their support and patience. This work is dedicated to my mother for her persistent support and encouragement throughout the years of my study.

## ABSTRACT

The objectives of this thesis are to investigate, experimentally and numerically, vortex shedding from cylinders submerged in laminar and turbulent flows and various means for its control.

The numerical model used is based on the finite-volume method for the discretisation of the governing transport equations. The  $k-\epsilon$  turbulence model with the SMART discretisation scheme are used throughout. In order to validate the methods, predictions were obtained for a number of flows for which extensive experimental results exist. These include single square and circular cylinders, as well as two circular cylinders in tandem. The code was also used in the prediction of very high Reynolds number flows (i.e.  $Re > 9 \times 10^6$ ), for which no experimental results exist.

The predicted values of the mean drag, the fluctuations of drag and lift and the Strouhal number were satisfactory for the laminar flow cases. For the turbulent cases, however, predictions for the circular cylinder slightly underestimated the mean drag while the fluctuating lift and the Strouhal number were slightly overestimated. The square cylinder results were satisfactory for all regimes.

The flow field that develops around two circular cylinders in tandem was investigated numerically in laminar and turbulent flow conditions. The wide range of well established flow phenomena observed experimentally were reproduced.

The techniques considered for the control of vortex shedding consist of the use of control cylinders, injection into both the approach flow and the wake. It must be noted that injection into the flow is a novel method for which no previous research is reported. Experiments were carried out for forward injection to maximise its efficiency for a circular cylinder.

All the control techniques used, showed a complete suppression of vortex shedding behind a circular and square cylinder in laminar flow and a square cylinder in turbulent flow conditions. However, levels of suppression were not as high for the circular cylinder in turbulent flow.

It is hoped that the work reported herein will contribute to the understanding of the physics involved in the control of vortex shedding, and the instabilities it causes.

# NOMENCLATURE

English	Definition
A	Area
$A_{E, W, N, S, P}$	Coefficients containing convective and diffusive fluxes
$A_{nb}$	Coefficients in discretised equation
$A_{inj}$	Injection area
$C_D$	Drag coefficient = $\frac{F_D}{\frac{1}{2}\rho U_o^2 A}$
$\bar{C}_D$	Mean drag
$\tilde{C}_D$	Rms drag
$C_{Di}$	Interference drag
$\tilde{C}_{D,r}$	Ratio of rms drag after control to before control
$C_L$	Lift coefficient = $\frac{F_L}{\frac{1}{2}\rho U_o^2 A}$
$\tilde{C}_L$	Rms lift
$\tilde{C}_{L,r}$	Ratio of rms drag after control to before control
$C_p$	Distributions of the time averaged surface pressure
$C_{\epsilon_1}, C_{\epsilon_2}, C_\mu, C_t$	Empirical constants
d	Control cylinder diameter/height
$d_{hole}$	Diameter of injection hole
f	Frequency (Hz)
$f_{ip}$	Interpolation factor
$f^*$	Non-dimensional frequency scale $\equiv fD/U$
$f_s$	Vortex shedding frequency
$F_D, F_L$	Pressure and viscous forces in the x,y directions
G	Distance (m) from centre to centre of main cylinder to centre of control cylinder
$G_1$	Injection hole geometry number (1) = $d_{hole}/D$
$G_2$	Injection hole geometry number (2) = $h_{c-c}/L$
$h_{c-c}$	Distance from centre to centre of injection holes
H	Height of cylinder
$i, j$	Unit vectors in x,y directions
I	Total flux
k	Turbulent kinetic energy
$\ell$	Turbulence length scale

L	Immersion depth
$\dot{m}$	Injection mass flow rate $=\rho A_{inj}(U_{hol})^2$
M	Total number of control volumes
N	Number of sample points
p	Pressure
P	Distance (m) from centre to centre of two cylinders in tandem
$P_k$	Rate of production of k
$P_\epsilon$	Rate of production of $\epsilon$
q	Total kinetic energy $=k + \frac{1}{2}(U^2 + V^2)$
Re	Reynolds number $=U_o D / \nu$
$R_f$	Reaction force $=\dot{m}U_{hol}$
$S_\phi$	Source term of term $\phi$ ,
S	Streamwise distance from the upstream corner of square cylinder
St	Strouhal number $=f_s D / U_o$
t	Time (s)
$t^*$	Non-dimensional time scale $\equiv tU/D$
T	Period of oscillation, and Lateral distance from the top side of square cylinder
$T_u$	Turbulence intensity at inlet
u, v, w	Fluctuating velocity components x,y,z directions
U, V, W	Mean velocity in components the x,y,z directions
$U_{hol}$	Injection velocity
$U_{inj}$	Forward injection velocity
$U_o$	Approach velocity
$U_p$	Wall shear stress
$U_r$	Injection ratio $=U_{inj}/U_o$
$U_{sj}$	Stagnation jet velocity
$U_\tau$	Friction velocity $=\sqrt{\tau_w / \rho}$
V	Volume
$V_r$	Change in rms voltage
W	Square cylinder height
x, y, z	Orthogonal coordinates
$y_+$	Dimensionless normal distance of the first grid point above surface

## Greek

$\alpha$	Angle from centre plane of main cylinder to control cylinder
$\beta$	Empirical coefficient
$\Gamma_\phi$	Exchange coefficient for variable $\phi$
$\delta_{ij}$	Kronecker's delta
$\delta n$	Distance from cylinder
$\Delta n$	Size of small cell next to cylinder
$\Delta t$	Time-step (s)
$\Delta t^*$	Non-dimensionalised time-step = $U_0 \Delta t / H$
$\theta$	Angle
$\kappa$	Von Karman's constant
$\lambda_w$	Coefficient to evaluate wall shear stress
$\mu$	Dynamic viscosity
$\nu$	Kinematic viscosity
$\nu_t$	Turbulent (eddy) viscosity = $C_\mu \frac{k^2}{\epsilon}$
$\rho$	Density of fluid
$\epsilon$	Kinetic-energy dissipation rate $\approx \frac{k^{3/2}}{\ell}$
$\sigma_k, \sigma_\epsilon$	Empirical coefficients
$\tau_w$	Wall shear stress
$\tau_{ij}$	Viscous stress tensor
$\phi$	General dependent variable
$\omega$	Vorticity = $\frac{\partial U}{\partial y} - \frac{\partial V}{\partial x}$
$\Omega$	Rotation parameter

## Other

$\bar{\quad}$	Mean value
$\wedge$	Instantaneous values
rms	Root mean square

## Definitions

Angle from centre plane of main cylinder to control cylinder
Empirical coefficient
Exchange coefficient for variable $\phi$
Kronecker's delta
Distance from cylinder
Size of small cell next to cylinder
Time-step (s)
Non-dimensionalised time-step = $U_0 \Delta t / H$
Angle
Von Karman's constant
Coefficient to evaluate wall shear stress
Dynamic viscosity
Kinematic viscosity
Turbulent (eddy) viscosity = $C_\mu \frac{k^2}{\epsilon}$
Density of fluid
Kinetic-energy dissipation rate $\approx \frac{k^{3/2}}{\ell}$
Empirical coefficients
Wall shear stress
Viscous stress tensor
General dependent variable
Vorticity = $\frac{\partial U}{\partial y} - \frac{\partial V}{\partial x}$
Rotation parameter

## Definition

Mean value
Instantaneous values
Root mean square

# CHAPTER ONE: INTRODUCTION

## 1.1 Introductory Remarks

The flow of a fluid around a structure is often accompanied by periodic shedding of vortices that alter the surrounding pressure field and induce forces that can cause destructive vibrations. The study of the suppression of vortex shedding from a circular cylinder has received much attention, since practical application is expected in various areas of engineering. The complexity of the phenomenon arises from its sensitivity to Reynolds number, turbulence intensity levels, surface roughness, three dimensionality, and elastic response. As such, a wide variety of aerodynamic and hydrodynamic means for suppressing the shedding of vortices have been developed.

This chapter presents a review of the phenomenon of vortex shedding from circular and square cylinders and of methods to suppress them.

The cylinder is a bluff body, i.e. one from which the flow separates over a large portion of the surface. Most civil engineering structures, such as bridge piers, offshore platform legs and chimneys are bluff bodies. The primary purpose of these structures is not to utilise the resulting lift and drag forces (as it is with aircraft structures), but rather to bear loads. These structures tend not to be aerodynamically optimised and flow-induced vibrations are usually regarded as a secondary design consideration, at least until a failure occurs.

When the response to vortex shedding produces unacceptable stresses, consideration must be given to reducing the amplitude of this response by suppressing the formation and subsequent shedding of vortices. This suppression can be achieved by using either mechanical or fluid dynamic means.

The mechanical means of suppression involves changes in either the member physical properties or the structural detailing. Thus, increases in natural frequency, stiffness or damping will generally reduce the oscillation amplitude. Generally, these alterations would be considered at the design stage.

The fluid dynamic approach to suppression involves the use of aerodynamic spoilers which reduce the amplitude of response to the fluid processes involved in vortex shedding. Add-on devices such as helical strakes, shrouds, and splitter plates and

control cylinders, are examples of aerodynamic spoilers. The fluid dynamic approach would be considered if in-situ problems were encountered.

## 1.2 Basic Definitions

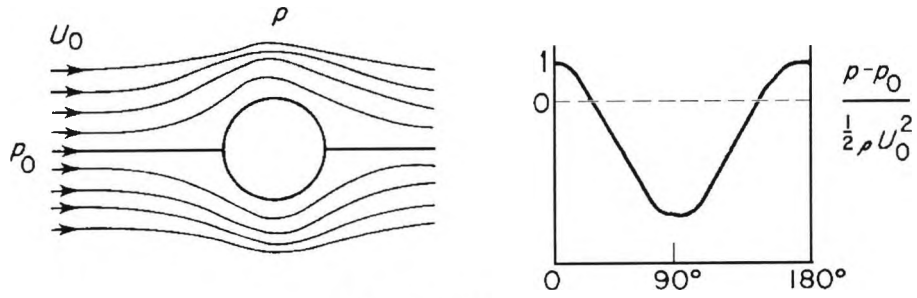
It is often the case that structures shed vortices in fluid flows. The resulting vortex street tends to be very similar regardless of the geometry of the structure. As the vortices are shed from one side and then the other, periodic surface pressures are imposed on the structure.

Vortex shedding from a smooth, circular cylinder in steady flow is a function of Reynolds number; defined as:

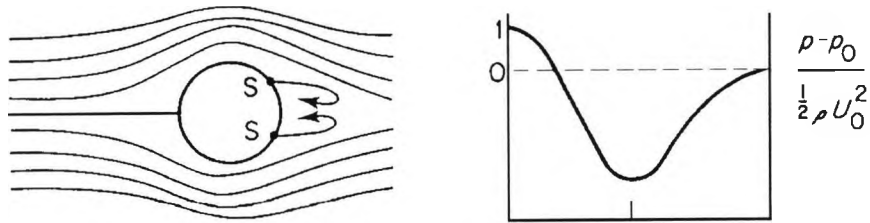
$$\text{Re} = U_0 D / \nu \quad (1.1)$$

Where  $\nu$  is the kinematic viscosity of the fluid,  $U_0$  is the free stream velocity and  $D$  is the cylinder diameter.

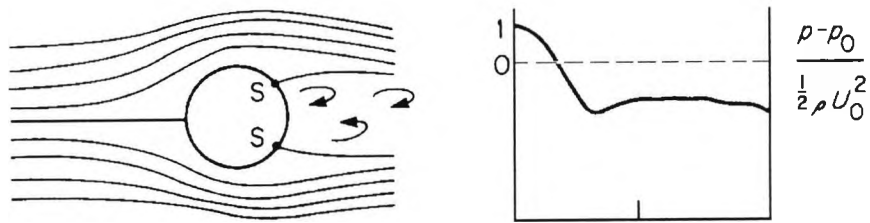
The major Reynolds number regimes of vortex shedding from a smooth cylinder are shown in Figure 1.1 (Douglas et al., 1985). At very low values of  $\text{Re}$ , i.e. below 0.5, the inertia effects are negligible and the flow pattern is very similar to that for an ideal flow. The flow remains symmetric downstream of the cylinder and the pressure recovery is nearly complete. Thus, pressure drag is negligible and the profile drag is nearly all due to skin friction. Figure 1.1a shows the flow pattern and the associated pressure distribution. At increased  $\text{Re}$ , between around 2 and 30, separation of the boundary layer occurs at point  $S$  as indicated in Fig 1.1b. Two symmetrical eddies, rotating in opposition to one another, are found. Further increase of  $\text{Re}$  tends to elongate the fixed eddies, which then begin to oscillate at about  $\text{Re} \approx 90$ . Depending upon the free stream turbulence level, they break away from the cylinder as shown in Fig 1.1c. This occurs alternately from either side of the cylinder, the eddies being washed away by the main stream. This process is known as vortex shedding. It is intensified by a further increase of  $\text{Re}$ , whereby the shedding of vortices from alternate sides of the cylinder is continuous, thus forming in the wake two discrete rows of vortices (Fig 1.1d). This is known as the vortex street or von Karman vortex street. Regular vortex shedding is a dominant feature of two dimensional bluff body wakes and is present irrespective of whether the separating boundary layers is laminar or turbulent (Fig 1.1e).



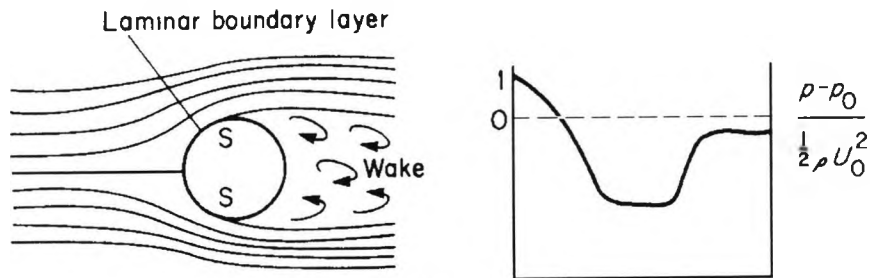
(a)  $Re < 0.5$



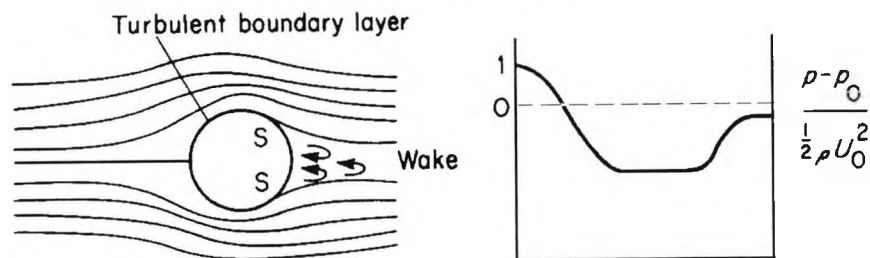
(b)  $2 < Re < 30$



(c)  $90 < Re < 10^3$



(d)  $10^3 \leq Re \leq 2 \times 10^5$



(e)  $Re > 2 \times 10^5$

Figure 1.1: Flow past a circular cylinder.

Due to the shedding vortices, a cylinder in cross flow will be acted upon by a fluctuating lift and fluctuating drag force. The dominant frequency of the former will be one half that of the latter. This is because it takes two of the alternating vortices to produce a full cycle of the lift fluctuations, and only one for a full cycle of the drag fluctuations.

If  $F_D$  is the force in the flow direction and  $F_L$  is the force in the direction normal to it, then the dimensionless lift and drag coefficients can be defined thus:

$$C_D = \frac{F_D}{\frac{1}{2}\rho U_o^2 A} \quad (1.2)$$

$$C_L = \frac{F_L}{\frac{1}{2}\rho U_o^2 A} \quad (1.3)$$

Where  $\rho$  is the density of fluid;  $U_o$  is the incident velocity, and  $A$  is the projected area, which in 2-D flow is the same as the cylinder diameter. Figure 1.2 shows the time history of  $C_D$  and  $C_L$  and defines  $T$  as one lift period of oscillations for a bluff body.

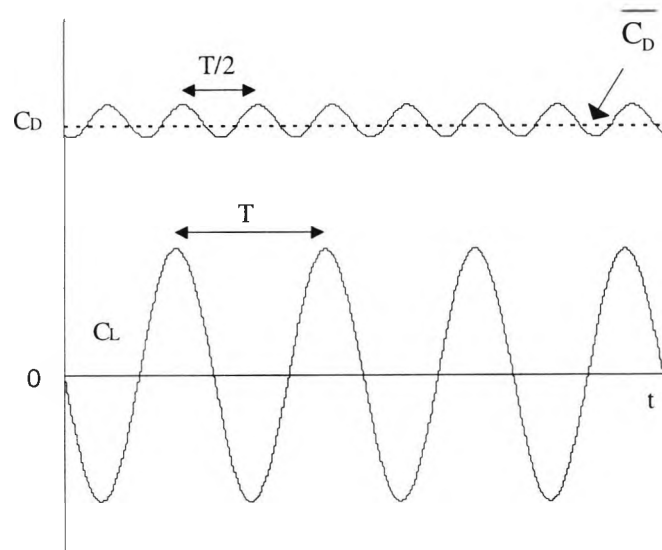


Figure 1.2: Typical time history for drag and lift coefficients over time  $t$ .

A measure of the strength of the lift and drag fluctuations is given in terms of the root mean square, where:

$$\tilde{C}_D = \sqrt{\frac{1}{N} \sum_{n=1}^N (C_D - \bar{C}_D)^2} \quad (1.4)$$

$$\tilde{C}_L = \sqrt{\frac{1}{N} \sum_{n=1}^N (C_L - \bar{C}_L)^2} \quad (1.5)$$

Where:  $N$  = Number of sample points,  $\bar{C}_D$  = Mean  $C_D$ , and  $\bar{C}_L$  = Mean  $C_L$ .

Figure 1.3 shows the relationship between Reynolds number and the time averaged coefficient of drag ( $C_D$ ). This figure is explained in more detail in Chapter Three.

Experiments show that the frequency of shedding ( $f_s$ ) is given in terms of the Strouhal number ( $St$ ), named after Vincent Strouhal (1850-1922). The Strouhal number is an appropriate combination of flow and geometry parameters to render  $f_s$  dimensionless. It is defined as follows:

$$St = \frac{f_s D}{U_o} \quad (1.6)$$

Where  $f_s$  is the vortex shedding frequency;  $St$  is the Strouhal Number

Figure 1.4 shows the relationship between Strouhal number and Reynolds number for a circular cylinder. This figure is explained in more detail in Chapter Three.

Vortex shedding from a stationary cylinder at very high Reynolds numbers does not occur at a single distinct frequency, but rather it wanders over a narrow band of frequencies with a range of amplitudes. Furthermore, it is not uniform along the span.

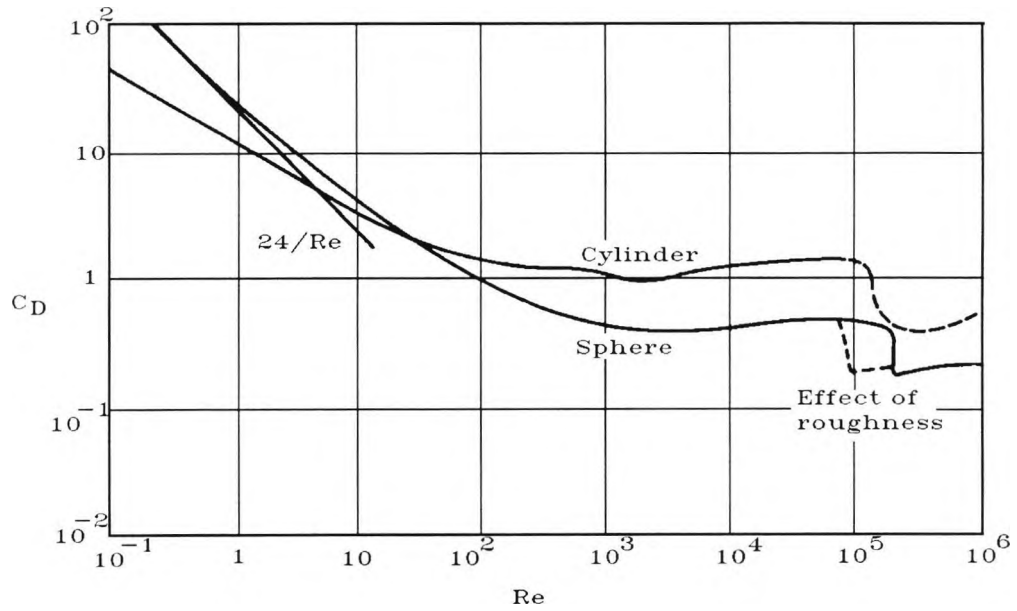


Figure 1.3: Drag coefficient for a sphere and a cylinder.

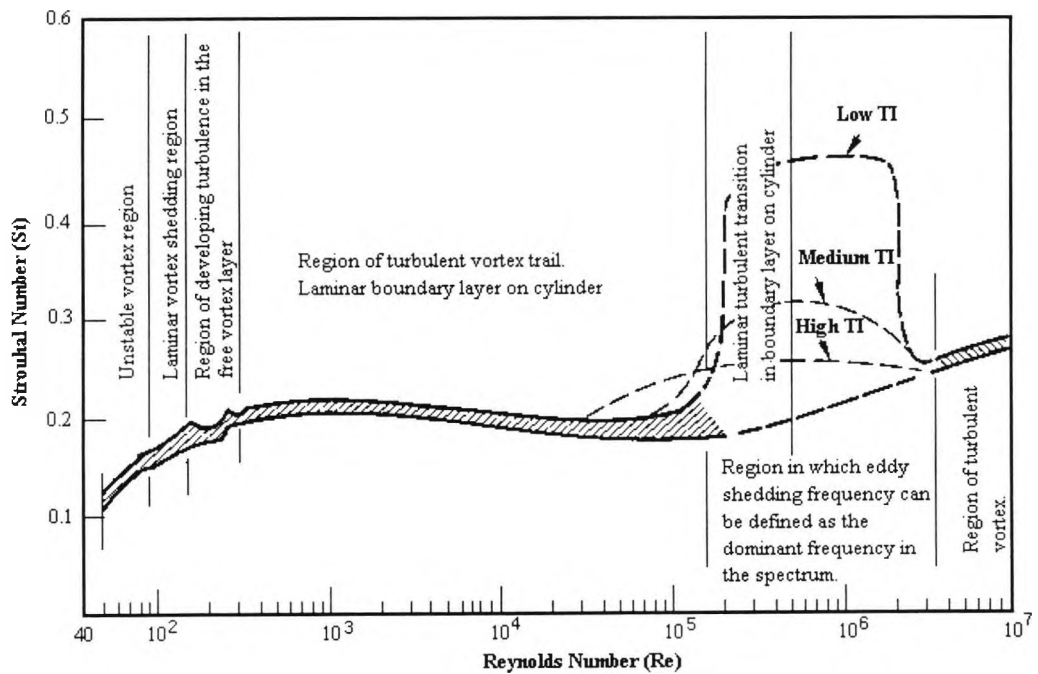


Figure 1.4: Reynolds number versus Strouhal number for circular cylinders (Shin and Wambsganss, 1977) and (Jendrzejczyk and Chen, 1985).

Flows at high Reynolds numbers occur quite frequently in nature, as can be seen from Table 1.1 (Griffin, 1982). Vibrations at these Re numbers are of particular interest with respect to the vibration of the structural components.

Type Of Flow	Location	Reynolds No.	Tracer
Wind past an ocean island	Jan Mayen	$10^{11}$	Clouds
	Guadeloupe	$10^{10}$	Clouds
Water past a ship aground	Nantucket Island	$10^7-10^8$	Oil
Water past a marine pile	English Coast	$10^8$	None
Water past a drill casing pipe	North Sea	$10^5$	None
Water past a model pile	Laboratory channel	$10^4$	Dye
Wake of a sphere towed in water	Towing channel	$3 \times 10^3$	Dye
Wake of an inclined plate	Water channel	$10^3$	Aluminium particles
Air past a circular cylinder	Wind tunnel	$2 \times 10^2$	Aerosol

*Table 1.1: Visualisation of vortex trails and Karman Vortex Streets.*

## 1.3 Suppression Techniques

Numerous methods have been devised to suppress the conditions leading to the flow-induced vibrations of cylinders. These techniques rely on modifying either the geometry or the flow conditions. Below is a brief summary of some of these techniques.

### a) Streamlining the Cross Section

According to Blevins (1990), vortex shedding can be suppressed if separation from the structure is minimised. This also reduces the mean drag. For streamlining the downstream side to be effective, an aspect ratio of about 6 would be required, or an included angle of the taper no bigger than 8 to 10 degrees. Hanco (1967) discusses the reduction of vortex-induced vibration of a pier by tapering. Streamlining is most effective when the direction of flow is fixed relative to the structure and the structure has sufficient stiffness to avoid flutter.

### b) Add-On Vortex Suppression Device

Zdravkovich (1981), Wong and Kokkalis (1982), Every et al. (1982), Hafen and Meggit (1971), and Rogers (1983) review add-on devices for the suppression of vortex-induced vibration of cylindrical structures in wind and marine applications. Zdravkovich classifies these structures into three categories:

- **Surface Protrusions:**

- i) Turbulence Promotion

Prandtl (1914) demonstrated that the developing boundary layer can be 'tripped' (i.e. forced to be turbulent) by a wire fixed on the surface around a sphere. Small drag coefficients typical of critical Reynolds numbers are then obtained with fairly low Reynolds numbers. Fage and Warsap (1929) made a detailed study of the effect of a tripping wire attached to a circular cylinder on prematurely promoting the critical regime. Price (1956) concluded that neither straight tripping wires nor the most effective helical ones were effective in suppressing large-amplitude vibrations.

- ii) Helical Strakes

Scruton and Walshe (1957) developed efficient surface protrusions for avoiding wind-excited oscillations of cylindrical structures. Three plates of sharp edged rectangular section were wound as helical strakes around the surface of the cylinder, with a pitch of 15D. It was found that the attachment of strakes was

effective in reducing the aerodynamic excitation. Woodgate and Maybrey (1959) determined an optimum pitch of  $5D$ , whilst the height of the strakes remained at  $0.09D$ .

- **Shrouds:**

- i) Perforated shrouds with circular holes

Price (1956) carried out an extensive study of the effect of various surface modifications on reducing oscillations of a circular cylinder submerged in water. Price also tried to change the cross-sectional area of the model locally by fitting concentric bushings  $1.25D$  in diameter and  $1.5D$  apart. He subsequently detached them from the surface and thus formed a perforated shroud. According to Price, the “shroud would break up the flow into a large number of small vortices with the result of minimising the periodic asymmetry of the flow about the cylinder.” The shroud proved to be an effective means for vortex suppression, irrespective of the stiffness of the tested cylinder.

- ii) Shrouds with square holes

Walshe and Wootton (1970) found that square holes are more effective than circular ones. Wootton and Yates (1970) carried out drag measurements to separate the drag exerted on the shroud from that experienced by the cylinder. They found that the drag coefficient of the shroud was  $0.7$  and for the enclosed cylinder  $0.2$  (both based on the cylinder diameter).

- **Near wake Stabilisers:**

- i) Splitter Plates

Appelt et al. (1973) carried out tests with long and short splitter plates, attached or detached, behind a circular cylinder. Short splitter plates attached to the circular cylinder significantly modified the flow around them. The drag coefficient was reduced below the original value, even by a very short splitter plate. Reductions by as much as  $31\%$  were obtained when the length of the splitter plate was equal to the cylinder diameter.

- ii) Guide Vanes

Grimminger (1945) tried to stabilise the near wake behind a circular cylinder by placing guide vanes along its boundary, consisting of two flat plates (being  $\sim 1D$  long) fitted along the sides of the cylinder and parallel to each other and the cylinder axis. The guide vanes reduced the drag coefficient from  $1.06$  measured on the original cylinder to  $0.83$ . Oscillations were reduced to low amplitudes.

### **c) Active Control**

Rockwell (1990) discussed the possibility of controlling instabilities in bluff body flows by subjecting the entire body to a prescribed motion. He also discussed the concept of local control, involving localised application of unsteady blowing/suction or heating at specified positions on the surface. Some of these methods are presented here:

- **Minimisation of cross-stream spacing of vortex street:**

Tokumara and Dimotakis (1989) showed that substantial reduction in both transverse and in-line oscillations can be attained by purely rotational motion of the cylinder. Mean  $C_D$  at  $Re=1.5 \times 10^4$  was reduced by a factor of six. Griffin and Ramberg (1976) demonstrated that streamwise oscillations of a cylinder could produce a street of vortices having essentially zero cross-stream spacing. Griffin and Ramberg (1974) showed that with cross-stream oscillations, much higher displacement amplitudes are required to approach a zero value of transverse spacing of the vortex street.

- **Oscillations in the streamwise direction:**

This method subsequently produces small scale symmetrical vortices (Couder and Basdevant, 1989). By applying small amplitude oscillations at a frequency slightly less than twice the Karman frequency, Berger and Schumm (1988) were able to suppress the large-scale Karman mode in low values of Reynolds number.

- **Generation of complex modal structure of vortex street:**

Williamson and Roshko (1988), provide an overview of the possible modes of response due to cross-stream oscillation of a cylinder over a wide range of excitation frequency and amplitude. A variety of vortex patterns can be generated in the near-wake, which substantially alter the fluctuating lift and drag, as well as the spectral content and coherence of the downstream wake.

- **Mode competition of near-wake vortices:**

There are ranges of excitation parameters for which phase-locked response is not attainable. These ranges correspond to cylinder oscillations in the cross-stream direction. Mode competition, whereby the wake vortex pattern alternates between symmetrical and asymmetrical patterns are described by Ongoren and Rockwell (1988). By switching between these symmetric and anti-symmetric modes of vibration with appropriate excitation, it is possible to disrupt phase-locked patterns in the near wake.

#### **d) Base Bleed**

Wood (1964) studied the effect of 'base bleed' on an airfoil section with a blunt trailing edge. This method reduces drag by shifting the vortex formation region further downstream. Igarashi (1978) modified a circular cylinder by introducing a slit cut along the whole span. Thus self-bleed of fluid into the near wake was achieved by high pressure around the stagnation region and low pressure around the base. The self-bleed rate can be altered by rotating the cylinder with the slit so that the slit axis becomes inclined to the free stream velocity up to  $30^\circ$ . Igarashi measured the drag coefficient and Strouhal number for two widths of the slit,  $0.08D$  and  $0.185D$ , at  $Re=4.5 \times 10^4$ . The drag coefficients were 0.9 and 0.75 and Strouhal numbers 0.26 and 0.32, respectively.

#### **e) Control Cylinder**

Kovaszany (1949) indicated that a hot wire probe positioned with supports aligned parallel to the flow caused an upstream propagating instability. Subsequently, Strykowski and Sreenivasan (1990) investigated the control of vortex shedding behind a cylinder by the placement of a second, much smaller cylinder in the near wake of the main cylinder. This effect will be discussed in much more detail in Chapter Five.

#### **f) Injection Into The Free Stream**

The possibility of the suppression of vortex induced vibrations by injection into the free stream was postulated by Dr B.A. Younis who suspected its existence from some flow visualisation pictures. A number of experiments were carried out (Razavi, 1992 and Younis & Razavi, 1996) to quantify the extent to which suppression can be achieved. This method will be discussed in more detail in Chapters Six (experimental work), and Seven (computational results).

#### **g) Rear Stagnation Jet**

Mo and Duke (1993) investigated the numerical simulation of cylinder wake flow with a rear stagnation jet. Their main finding was that a rear stagnation jet forces a symmetrical wake flow pattern, thus eliminating the lateral force. They also observed that the pressure on the cylinder surface drops significantly, more so on the downstream side of the cylinder. This effect will be discussed in more detail in Chapter Eight.

## 1.4 Computational Fluid Dynamics

The steady increase in the speed of computers and in the memory size has made the use of computational fluid dynamics (CFD) more practicable. This branch of fluid dynamics complements experimental and theoretical fluid dynamics by providing an alternative cost-effective means of simulating real flows. CFD provides three main advantages compared with physical model tests:

- (i) Design and development times are significantly reduced.
- (ii) Flow conditions not reproducible in experimental model tests can be simulated.
- (iii) CFD provides more detailed and comprehensive information.

The governing equations (Chapter Two) for flows of practical interest cannot be solved analytically to obtain an exact solution and so it is necessary to seek an approximate, numerical solution. Computational techniques replace the governing partial differential equations with a system of algebraic equations, so that a computer can be used to obtain the solution.

For local methods, like the finite volume method used in this project, the algebraic equations link together values of the dependent variables at adjacent grid points. A grid of discrete points is distributed throughout the computational domain, in time and space. Consequently, one refers to the process of converting the continuous governing equations to a system of algebraic equations as discretisation. The required number of grid points for an accurate solution depends on the dimensionality of the problem, the geometric complexity and the severity of the gradients of the dependent variables. Since the governing equations for most classes of fluid dynamics are non-linear, the computational solution proceeds iteratively.

The mathematical aspects of the modelling technique used in this project are presented in Chapter Two.

## 1.5 Motivation and Objectives of Present Study

The previous sections have introduced the concept of vortex shedding, some of the techniques used to suppress the vibrations caused by it, and the use of computational fluid dynamics to simulate flow problems. The interest in the subject of vortex shedding past cylinders stems mainly from its relevance to various practical applications, such as dynamics of stacks, piles, chimneys, periscopes, and cables. Oscillations excited by vortex shedding can lead to amplitudes as large as two cylinder diameters, an occurrence which is not acceptable in most engineering situations.

Control of such oscillations is consequently a worthwhile area of study. Assessment of different suppression techniques relies heavily on experiments, but the gathering and recording of experimental data is a cumbersome and expensive process. It is with this in mind that the use of numerical modelling becomes an effective tool in enhancing experimental data, and thus aiding in the understanding of this important phenomenon.

The main objective of the present work is to investigate, experimentally and numerically, vortex shedding from cylinders submerged in laminar and turbulent flows and various means for its control.

This will be achieved by the following tasks:

1. The capability of the k- $\epsilon$  method in modelling the range of vortex shedding regimes for a single cylinder, both square and circular will be assessed through comparisons with available experimental data and with other numerical techniques in terms of accuracy of computed results. This is presented in Chapter Three. Dependence of the computed results on grid and choice of scheme are discussed and evaluated. To determine the limits of the model, very high mean-flow Reynolds numbers of the order  $>10^7$  are simulated, for the first time to our knowledge.
2. The flow field around a pair of rigid circular cylinders is very complex and depends on the spacing and the Reynolds number. The interference on the downstream cylinder is of importance when considering suppression techniques, as the drag may be reduced, depending on the spacing between cylinders. Predictions of this phenomenon in the laminar and turbulent flow regimes are presented in Chapter Four.

3. Three methods of vortex suppression were selected for detailed study. The first one is the use of control cylinders. A small control cylinder is placed near the main cylinder to reduce or eliminate oscillations caused by vortex shedding on the main cylinder. Results for square and circular cylinders with control cylinders placed at different points in the flow are discussed in Chapter Five.
4. The second method of suppression is a novel one and consists of the injection of fluid into the approach flow. Experimental results are reported in Chapter Six. Consequently, this phenomenon is investigated numerically in Chapter Seven over a range of Reynolds numbers, and injection rates, which were not possible in the experimental set-up.
5. The third method of suppression to be investigated is the introduction of a rear stagnation jet, acting in a similar way to a splitter plate behind the cylinder. This phenomenon has not been investigated extensively in the past. A study of this technique by modelling it numerically for a circular and square cylinder and thus showing its effectiveness over a range of Reynolds numbers and jet flow rates is presented in Chapter Eight.

It is expected that the results obtained from this work will improve the current state of knowledge in the area of the prediction of vortex shedding and its suppression. By understanding the physics of suppression, engineers and designers can find the best solutions to their problems.

# CHAPTER TWO: MATHEMATICAL FORMULATION

## 2.1 Introductory Remarks

This chapter briefly describes the basis of the computational code used in the present study. The governing equations are first presented followed, by the averaged equations. Section 2.4 describes Boussinesq's eddy viscosity concept used to close the time-averaged equations. Section 2.5 provides the basis of the k- $\epsilon$  turbulence model and the modification necessary to handle vortex shedding.

The code used throughout the present work is based on the finite-volume method for the discretisation of the transport equations governing laminar or turbulent flows, which was originally advanced by Peric (1985). This method is described in Section 2.6. The algebraic form of the discretised transport equation is presented in Section 2.7. An interpolation scheme is required to obtain the value of a dependent variable on the cell faces from knowledge of the value at surrounding nodes. The choice of interpolation schemes is presented in Section 2.8.

The iterative SIMPLE algorithm of Patankar and Spalding (1972), used to couple the pressure and velocity calculations, is introduced in Section 2.9. The boundary conditions are treated in Section 2.10 and details of the solution algorithm and convergence criterion provided in Section 2.11.

## 2.2 Governing Equations

The laminar or turbulent motion of a fluid can be described by the conservation equations for momentum (the Navier-Stokes equations) and mass (continuity equation). Using Cartesian tensor notation, these equations are:

Continuity:

$$\frac{\partial}{\partial x_i}(\rho \hat{U}_i) = 0 \quad (2.1)$$

Momentum:

$$\frac{\partial(\rho \hat{U}_i)}{\partial t} + \frac{\partial}{\partial x_j}(\rho \hat{U}_i \hat{U}_j - \hat{\tau}_{ij}) = \frac{-\partial \hat{p}}{\partial x_i} \quad (2.2)$$

Where  $\rho$  is the fluid density;  $U_i$  represents the components of the velocity vector in the Cartesian coordinate directions  $x_i$ ;  $p$  is the pressure; and:

$$\hat{\tau}_{ij} = \mu \left( \frac{\partial \hat{U}_i}{\partial x_j} + \frac{\partial \hat{U}_j}{\partial x_i} \right) \quad (2.3)$$

are the components of the viscous stress tensor, expressed through the velocity gradients and dynamic viscosity  $\mu$ . In the above equations  $\hat{\phantom{x}}$  indicates instantaneous values of the flow quantities. Equations 2.1 to 2.3 are valid for all types of flow but are often solved in a simplified form arrived at by recognising a special feature of the flow. For incompressible flows, for example, the density ( $\rho$ ) is constant and therefore it can be taken out of the derivatives.

For the purpose of modelling separated flows, it is noted that the influence at a point in the flow spreads in all directions. Therefore two-way coordinates apply throughout i.e. the conditions at a given location in that coordinate are influenced by changes in conditions on either side of that location (Patankar, 1980). The simulation of elliptic flows requires an iterative, whole field approach. Thus, the governing equations are solved, simultaneously, over the whole flow field since the direction of influence at a particular point is not known *a priori*. Moreover, because of the non-linearity of the governing equations, an iterative solution is necessary, based on repeated guess-and-correct cycles.

## 2.3 Averaged Equations

In practice, turbulent flows can be simulated directly by solving the full 3-D Navier-Stokes equations for the full range of the turbulent motions from the smallest dissipation scales to the largest, corresponding to the physical dimensions of the flow. Unfortunately, the present-day computing resources only enable such *Direct Numerical Simulation* (DNS) for the simplest geometries and then only for low Reynolds Numbers. It is thus necessary to use some sort of averaging to render the equations soluble.

Reynolds (1883) proposed a decomposition of the instantaneous variables (e.g. pressure, velocity, density) into mean and fluctuating components:

$$\begin{aligned}\hat{U} &= U + u \\ \hat{V} &= V + v\end{aligned}\tag{2.4}$$

The mean component is simply the long-time average of the instantaneous value, defined thus:

$$U_i = \lim_{t \rightarrow \infty} \frac{1}{\Delta t} \int_t^{t+\Delta t} \hat{U}_i(t) \cdot dt\tag{2.5}$$

The above averaging is only applicable to statistically stationary flows. For the present applications, we interpret the Reynolds-averaging process to mean:

$$U_i = \frac{1}{\Delta t} \int_t^{t+\Delta t} \hat{U}_i(t) \cdot dt\tag{2.6}$$

where  $\Delta t$ , the time interval, is greater than the time-scale of the turbulent fluctuations but is much smaller than the period of the vortex shedding ( $T$ ). Typically, in this work,  $\Delta t$  is taken as  $T/2000$  seconds.

By introducing the above definitions into the instantaneous Navier-Stokes equations and averaging the results:

$$\frac{\partial \rho U_i}{\partial t} + \frac{\partial}{\partial x_j} (\rho U_i U_j) = \frac{\partial}{\partial x_i} (-\rho \overline{u_i u_j}) - \frac{\partial p}{\partial x_i}\tag{2.7}$$

Where  $\overline{u_i u_j}$  is the Reynolds-stress tensor, defined as:

$$\overline{u_i u_j} = \begin{pmatrix} \overline{u^2} & \overline{uv} & \overline{uw} \\ \overline{vu} & \overline{v^2} & \overline{vw} \\ \overline{wu} & \overline{wv} & \overline{w^2} \end{pmatrix}\tag{2.8}$$

Because of the non-linearity of the convection terms in the Navier-Stokes equations, the averaging process introduces some unknown turbulence correlations. These are known as the Reynolds stresses. Physically, they represent the rate at which momentum is transported by turbulent fluctuations. Their magnitude is many times greater than their molecular (laminar) counterparts which explains mixing associated with turbulent flows and the absence of molecular diffusion in Equation 2.7.

The original Navier-Stokes equations form a closed set of equations but the unknown Reynolds stresses, introduced by the averaging process, render the equations insoluble. There are more unknowns than there are equations. This is what is known as the *closure* problem.

## 2.4 Boussinesq's Eddy Viscosity Concept

A solution to the closure problem is to use a turbulence model, which consists of a set of differential equations and/or algebraic formulae, which allow the determination of the Reynolds stresses and thus close the time-averaged equations.

Boussinesq (1887) proposed that the Reynolds stresses may be modelled as being proportional to the mean rates of strain; the proportionality coefficient defining the turbulent or eddy viscosity, thus:

$$-\overline{u_i u_j} \equiv \nu_t \left( \frac{\partial U_i}{\partial x_j} + \frac{\partial U_j}{\partial x_i} \right) - \frac{2}{3} \delta_{ij} k \quad (2.9)$$

Where  $k$  is the turbulent kinetic energy and  $\delta_{ij}$  is the Kronecker's delta.

Unlike its molecular counterpart,  $\nu_t$  is not a function of the fluid but rather of the flow. It is zero in laminar flows, while in turbulent flows it varies from point to point depending on the local level of turbulence activity.

By dimensional analysis:

$$\nu_t = \text{Coefficient} \times \text{Velocity Scale} \times \text{Length Scale} \quad (2.10)$$

The turbulence model will provide values for the eddy viscosity from Equation 2.10, which will then be used to evaluate the turbulent stresses from Boussinesq's hypothesis (Equation 2.9). Once the stresses are determined, they will be substituted in the time-averaged flow equations (Equation 2.7).

## 2.5 The k - ε Turbulence Model

In the two-equation model, the eddy viscosity is evaluated from the solution of two differential equations: one for k and another for its dissipation rate (ε) which is related to the turbulence length scale (ℓ) as:

$$\varepsilon \approx \frac{k^{3/2}}{\ell} \quad (2.11)$$

The exact equation for ε, which is derived from the Navier-Stokes equations (Tennekes and Lumley, 1972), is too complex and contains many unknowns. In terms of physical processes, the ε equations represents a balance between the rate of transport of ε by the mean flow and the rate of its diffusion by the turbulence fluctuations, its generation by vortex stretching and finally, its destruction by the action of viscosity.

The diffusion term is modelled via the gradient-transport hypothesis, thus:

$$\text{Diffusion } (\varepsilon) = \frac{\partial}{\partial x_i} \left( \frac{v_t}{\sigma_\varepsilon} \frac{\partial \varepsilon}{\partial x_i} \right) \quad (2.12)$$

Where  $\sigma_\varepsilon$  is an empirical coefficient. The sources of ε (production and dissipation) are modelled collectively, thus:

$$\text{Source } (\varepsilon) = C_{\varepsilon_1} \frac{\varepsilon}{k} P_k - C_{\varepsilon_2} \frac{\varepsilon^2}{k} \quad (2.13)$$

Where  $C_{\varepsilon_1}$  and  $C_{\varepsilon_2}$  are empirical constants and  $P_k$  is the rate of production of k and described as:

$$P_k = -\overline{u_i u_j} \frac{\partial U_i}{\partial x_j} \quad (2.14)$$

The complete k-ε model equations are as follows:

$$v_t = C_\mu \frac{k^2}{\varepsilon} \quad (2.15a)$$

$$\frac{\partial k}{\partial t} + U_i \frac{\partial k}{\partial x_i} = \frac{\partial}{\partial x_i} \left( \frac{v_i}{\sigma_k} \frac{\partial k}{\partial x_i} \right) + P_k - \epsilon \quad (2.15b)$$

$$\frac{\partial \epsilon}{\partial t} + U_i \frac{\partial \epsilon}{\partial x_i} = \frac{\partial}{\partial x_i} \left( \frac{v_i}{\sigma_\epsilon} \frac{\partial \epsilon}{\partial x_i} \right) + C_{\epsilon_1} \frac{\epsilon}{k} P_k - C_{\epsilon_2} \frac{\epsilon^2}{k} \quad (2.15c)$$

The model contains five coefficients that are determined both from reference to experimental data (e.g. for decay of turbulence behind a grid or for ratio of  $\overline{uv}/k$  in equilibrium flows) and from computer optimisation (Launder and Spalding, 1974). The most widely accepted set of coefficients are:

$C_\mu$	$C_{\epsilon_1}$	$C_{\epsilon_2}$	$\sigma_k$	$\sigma_\epsilon$
0.09	1.44	1.92	1.0	1.3

The standard k- $\epsilon$  model is known not to yield accurate predictions for the unsteady turbulent flows dominated by strong organised structures for example when predicting vortex shedding flows (Younis, 1987). In order to take explicit account of the presence of vortex shedding, Younis (1987) proposed that the  $\epsilon$  production term be redefined as follows:

$$P_\epsilon = C_{\epsilon_1} P_k \frac{\epsilon}{k} \left( 1 + C_t \frac{k}{\epsilon} \left| \frac{\partial}{\partial t} (q) \right| \right) \quad (2.16)$$

Where  $q$  is the total kinetic energy of ensemble mean flow:

$$q = k + \frac{1}{2} (U^2 + V^2) \quad (2.17)$$

A new coefficient  $C_t=0.38$  is introduced, its value being obtained by computer optimisation. This is discussed in more detail in Section 3.4.4.

## 2.6 Finite Volume Discretisation

The basis of the finite volume methodology is the division of the calculation domain into a finite number of control volumes and then the integration of these equations over each control volume. This procedure enables satisfaction of integral balances of quantities like mass, momentum or energy over each cell and, consequently, over the entire domain.

A typical control volume in two dimensions, which may be non-orthogonal, is shown in Figure 2.1 (Demirdzic and Peric, 1988). The computational nodes (storage locations for all variables) are located in the centre of the control volume.

The governing equations can be seen as special cases of the general transport equations:

$$\frac{\partial}{\partial t}(\rho\phi) + \frac{\partial}{\partial x_j} I_j = S_\phi \quad (2.18)$$

Where the total flux  $I_j$  contains convective and diffusive fluxes as:

$$I_j = I_j^C + I_j^D = (\rho\phi U_j) - \Gamma_\phi \frac{\partial\phi}{\partial x_j} \quad (2.19)$$

The variable  $\phi$  can be  $U_i$ ,  $k$ ,  $\epsilon$ , etc.; and  $\Gamma_\phi$  is the exchange coefficient equal to the effective viscosity in momentum equations and to the effective diffusivity of  $k$  and  $\epsilon$ . All terms not appearing on the left side of Equation 2.18 are included in the source term  $S_\phi$ . In the continuity equation  $\phi$  takes the value of unity, and there is no diffusion and source terms.

Using Gauss' divergence theorem, integration of Equation 2.18 over any control volume (with volume  $V$  and surface  $A$ ) in physical space yields the integral conservation law:

$$\int_V \frac{\partial}{\partial t}(\rho\phi) dV + \oint_A I_j dA_j = \int_V S_\phi dV \quad (2.20)$$

Where  $dA_j$  is the surface vector normal to the surface  $A$  and directed outward. The evaluation of three distinct parts of the above equation, namely rate of change, the net flux, and the net source of transport variable, will be discussed below.

### 2.6.1 Rate of Change - temporal discretisation

It is assumed that the value of the variable  $\phi$  at the centre of the control volume (point P in Figure 2.1) represents an average over the cell. Thus for a non-moving control volume, the rate of change is:

$$\int_V \frac{\partial}{\partial t}(\rho\phi) dV = \frac{d}{dt} \int_V (\rho\phi) dV \approx \frac{\rho\Delta V}{\Delta t}(\phi^n - \phi^o) \quad (2.21)$$

where superscripts 'n' and 'o' indicate the new and old time levels over the time interval  $\Delta t$ . A fully implicit temporal discretization is chosen. With this choice, the net fluxes and the source term in Equation 2.20 are evaluated at the new time level (the superscript 'n' is omitted hereafter).

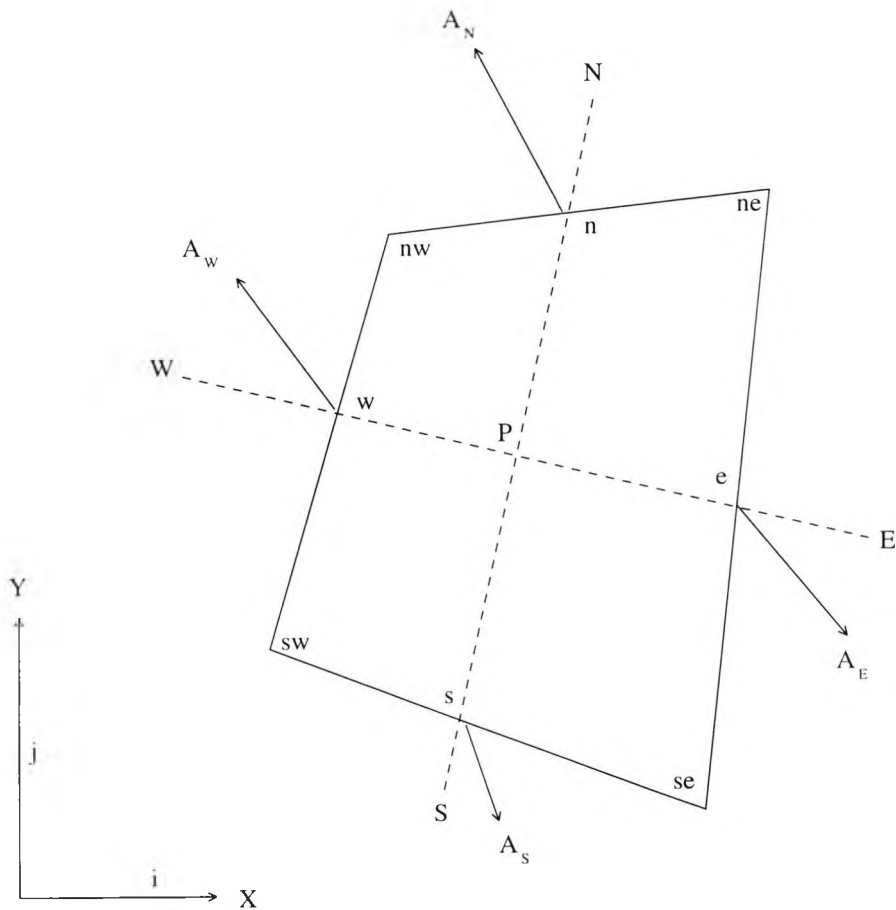


Figure 2.1: Two-dimensional control volume.

## 2.6.2 Convection and diffusion fluxes

The net flux through the control volume faces (e)ast, (w)est, (s)outh and (n)orth in Figure 2.1 can be expressed as:

$$\oint_{\Lambda} I_j dA_j = I_e + I_w + I_n + I_s \quad (2.22)$$

Since the control volume vertices are connected by straight lines, the integrals can be approximated by the scalar product of the flux vector and the surface vector, each taken at the cell face centre. Note that the outward flux through 'e'-cell face  $I_e$  is the inward flux through the 'w'-cell face of the neighbour control volume, so only  $I_e$  and  $I_n$  are calculated in the code through solving for the convection and diffusion fluxes.

## 2.6.3 Sources

The source terms on the right side of Equation 2.20 are integrated by assuming that the integral is given as the product of the specific source at the control volume centre P and the CV volume:

$$S_{\phi} = \int_V S_{\phi} dV = S_{\phi,p} \Delta V_P \quad (2.23)$$

When the volumetric source depends on the variable  $\phi$  itself, it is linearised in the usual way:

$$S_{\phi} = S_{\phi}^C - S_{\phi}^P \phi_P \quad (2.24)$$

If the source term contains a negative part, but no explicit dependence on  $\phi_P$ , it is useful to introduce this dependence artificially by multiplying and dividing the term by  $\phi_P$ .

## 2.7 Algebraic Form Of The Discretised Transport Equations

After introducing the fluxes through all CV faces and sources into the integral transport Equation 2.20, the discretised transport equation for each CV can be written in the conventional algebraic form:

$$A_P \phi_P = \sum_{nb} A_{nb} \phi_{nb} + S_\phi^C \quad (2.25)$$

where  $\phi_{nb}$  are the neighbour values of  $\phi_P$ , i.e.  $nb=E, W, N,$  and  $S$ . The coefficients  $A_{nb}$ , contains contributions from the implicitly treated parts of convection (F) and diffusion (D) fluxes:

$$\begin{aligned} A_E &= D_e + \max(-F_{1e}, 0), & A_W &= D_w + \max(-F_{1w}, 0) \\ A_N &= D_n + \max(-F_{1n}, 0), & A_S &= D_s + \max(-F_{1s}, 0) \end{aligned} \quad (2.26)$$

By employing the discretised continuity equation, the coefficient  $A_P$  is given as:

$$A_P = A_P^0 + \frac{(\rho \Delta V)_P}{\Delta t}, \quad A_P^0 = \sum_{nb} A_{nb}^0 + S_\phi^P \quad (2.27)$$

For the whole computational domain, a system of  $M$  equations like Equation 2.25 ( $M$  is the total number of control volumes) can be solved by the Strongly Implicit Procedure (SIP) of Stone (1968).

## 2.8 Choice of Interpolation Scheme

An interpolation scheme is required to obtain the value of a dependent variable on the cell face from knowledge of the values at surrounding grid nodes. The choice of interpolation scheme has a profound influence on the stability of the numerical algorithm and the accuracy of the computed solution. This choice is governed by various requirements which include robustness, economy and accuracy for a given grid density. Various schemes were tested for the present work (see Section 3.4). Below is an outline of their main features:

### 2.8.1 Central Differencing Scheme

In this scheme, the value of  $\phi$  at the east cell face is obtained from the expression:

$$\phi_e = \phi_E f_{1P} + \phi_P (1 - f_{1P}) \quad (2.28)$$

Where  $f_{1P}$  is an interpolation factor given by:

$$f_{1P} = \frac{\overline{Pe}}{\overline{Pe} + \overline{eE}} \quad (2.29)$$

$\overline{Pe}$  is the distance between the central point P and point e in the centre of the east cell face and  $\overline{eE}$  is the distance between e and E at the centre of the east neighbouring volume. If this scheme is used to evaluate the convective parts of the coefficients  $A_{nb}$ , then the result is:

$$A_E^C = -F_{1e} f_{1P} \quad (2.30)$$

and for the west side:

$$A_W^C = F_{1w} (1 - f_{1w}) \quad (2.31)$$

It is clear from the above that the convective parts of the coefficients may become large and negative leading to the whole coefficient  $A_{nb}$  to become negative with undesirable consequences to the stability of the solution process. For this reason, and for flows dominated by convection, this scheme is abandoned in favour of the following scheme.

### 2.8.2 Upwind-Differencing Scheme

In this scheme, the cell-face values are obtained from the following expressions:

$$\begin{aligned} \phi_e &= \phi_P \quad \text{if } F_{1e} > 0 \\ \phi_e &= \phi_E \quad \text{if } F_{1e} < 0 \end{aligned} \quad (2.32)$$

If a new operator is defined by  $\text{MAX}[a,b]$  to denote the greater of a and b, the convective parts of the coefficient  $A_{nb}$  can be written as:

$$A_E^C = \text{MAX}[0, -F_{1e}] \quad (2.33)$$

or, for the west face, as:

$$A_w^c = \text{MAX}[0, F_{1w}] \quad (2.34)$$

This scheme is formally only first-order accurate thus requiring relatively fine grids for accurate solutions. On the other hand, it is stable, since it does not allow the coefficients to become negative.

### 2.8.3 Linear-Upwind Differencing Scheme

In this scheme, the value at the cell-face is obtained by linear extrapolation of the values at the two nodes upwind of it, thus:

$$\begin{aligned} \phi_e &= \phi_p + (\phi_p - \phi_w)(1 - f_{1w}) \quad \text{if } F_{1e} > 0 \\ \phi_e &= \phi_E + (\phi_E - \phi_{EE})(1 - f_{1w}) \quad \text{if } F_{1e} < 0 \end{aligned} \quad (2.35)$$

With this definition, the convective parts of the coefficient  $A_{nb}$  may be written for the east face as:

$$\begin{aligned} A_E^c &= \text{MAX}[0, -F_{1e}](1 + f_{1E}) + \text{MAX}[0, -F_{1w}]f_{1P} \\ A_{EE}^c &= -\text{MAX}[0, -F_{1e}]f_{1E} \end{aligned} \quad (2.36)$$

and, for the west face as:

$$\begin{aligned} A_w^c &= \text{MAX}[0, F_{1w}](2 - f_{1ww}) + \text{MAX}[0, F_{1e}](1 - f_{1w}) \\ A_{ww}^c &= -\text{MAX}[0, F_{1w}](1 - f_{1ww}) \end{aligned} \quad (2.37)$$

In this scheme, therefore, the coefficient  $A_p$  now contains additional contributions from nodes lying beyond the ones immediately surrounding it, thus:

$$A_p^c = \sum_{nb} A_{nb}^c \quad nb = E, W, N, S, EE, WW, NN, SS \quad (2.38)$$

This scheme is second-order accurate but it is also unbounded which means that the interpolated values may take on values greater or less than those at the neighbouring nodes.

### 2.8.4 The SMART Scheme

Some schemes are non-monotonic. This means that they may give rise to unphysical oscillations, typically in the vicinity of steep gradients of the quantity to be resolved. In strongly coupled and non-linear situations at high Reynolds numbers these numerical oscillations tend to grow in an unbounded manner, which may prevent solutions from converging.

It is more convenient to work with the normalised variable,  $\hat{\phi}$ , rather than the dimensional  $\phi$ , used above, where:

$$\hat{\phi} = \frac{\phi - \phi_w}{\phi_E - \phi_w} \quad (2.39)$$

Based on normalised variable analysis, Gaskell and Lau (1988) formulated a Convection Bounded Criterion (CBC) for implicit steady-state flow calculations. Figure 2.2 shows a Normalised Variable Diagram (NVD) representing the different schemes used here. CBC states that for a scheme to have the boundedness property, the cell face values  $\hat{\phi}_e$  should lie within the shaded area in Figure 2.2 in the range  $0 < \hat{\phi}_p < 1$ , and on the line of  $\hat{\phi}_e = \hat{\phi}_p$ .

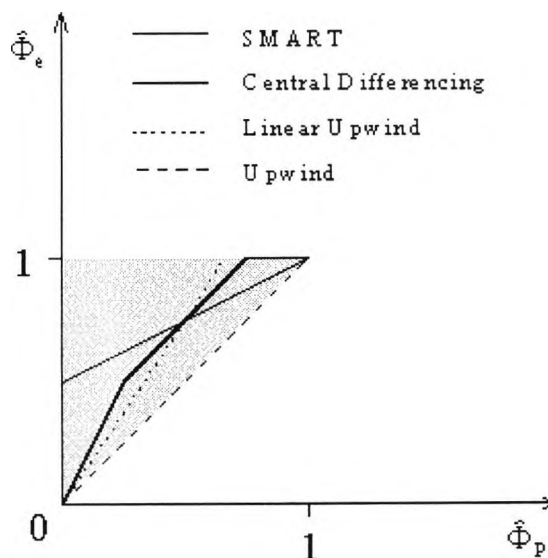


Figure 2.2: Normalised Variable Diagram for different interpolation schemes

Of the above mentioned schemes, only the first-order Upwind Differencing Scheme satisfies boundeness. A number of schemes satisfying CBS have been proposed. Gaskell and Lau (1988) proposed the SMART Scheme (Sharp and Monotonic Algorithm for Realistic Transport) which is expressed in terms of the normalised variable  $\hat{\phi}_p$  and through flux limiters, which determine the path taken on the NVD diagram. The SMART scheme removes unphysical numerical oscillations by switching from one scheme to another. Further details may be found in the original reference.

## 2.9 Pressure - Velocity Coupling

The numerical methods for compressible flows traditionally employ the continuity equation as a conservation equation for density. Pressure is then linked to the density via an equation of state. However, in the case of incompressible flows, the pressure-density coupling is negligible because of very small density changes. In these situations, the continuity equation has no explicit link to the pressure and it acts as a constraint on the velocity field. Since the unknown pressure gradients appear in the momentum equations, there is no obvious equation for the pressure. Mathematically speaking the pressure field should be determined in such a way that the velocities satisfy the continuity and momentum equations simultaneously. In the present approach, pressure is a primary variable and the above requirement is achieved using the SIMPLE (Semi-Implicit Method for Pressure-Linked Equations) algorithm devised by Patankar and Spalding (1972).

In the SIMPLE algorithm, a pressure-correction equation is derived from the discretized equations of momentum and continuity. This technique was adapted by Rhie and Chow (1983) for co-located grid storage used here, whereby all the dependent variables are stored at the same location.

## 2.10 Treatment Of Boundary Conditions

Boundaries of the computational domain can be generally identified as *inlet*, *outlet*, *symmetry axis* or *planes* and *solid walls*. Two types of boundary conditions may be specified; known values (Dirichlet type), and unknown boundary fluxes (von Neumann type). The first type typically applies to the inlet boundaries and the solid walls.

### 2.10.1 Inlet Boundaries:

Profiles of all the variables are prescribed at the inlet to the solution domain. Here, the U-velocity component is set to the value appropriate to the Reynolds number of interest. The V-velocity component at the inlet is set to zero. The turbulent quantities can be calculated using the relative turbulence level and turbulence viscosity.

$$k_{in} = 1.5(T_u U_o)^2 \quad (2.40)$$

$$\epsilon_{in} = \frac{C_\mu k_{in}^2}{v_t}$$

Where  $T_u$  is the relative turbulence intensity at inlet, usually taken as 3%.  $U_o$  is the inlet velocity,  $C_\mu$  is set to 0.09 and  $v_t$  is the eddy viscosity, which is prescribed as:

$$v_t = 100\nu \quad (2.41)$$

Where  $\nu$  is the kinematic viscosity of the fluid.

### 2.10.2 Outlet Boundaries

A zero streamwise gradient condition ( $\partial\phi/\partial x = 0$ ) is valid if the flow is fully developed. It is also appropriate for outlet boundaries located sufficiently far downstream from the region of interest.

### 2.10.3 Planes or Axes of Symmetry

Along the symmetry plane or axis, the normal velocity component is equal to zero, while the gradients of other variables normal to it are set to equal zero.

### 2.10.4 Solid Walls

In laminar flows, the boundary conditions used at the wall are simply that the velocities there are zero. In turbulent flows, the computational grid does not normally extend into the viscous sub-layer but only to a point outside it, in the fully-turbulent region of the flow. For the velocity component parallel to the wall, a flux boundary condition is used. The momentum flux at the wall, the wall shear stress, is obtained from the log-law:

$$U_p = \frac{U_\tau}{\kappa} \ln(Ey_p^+) \quad (2.42)$$

where  $E$  is a constant whose value depends on the wall roughness (for smooth walls,  $E$  is taken to be equal to 9) and von Karman's constant  $\kappa$  is equal to 0.41.  $U_\tau$  is the friction velocity ( $=\sqrt{\tau_w / \rho}$ ).  $U_p$  is the velocity component parallel to the wall at point  $P$ , lying at distance  $\delta n$  from the wall.  $y^+$  is the normal distance in wall coordinates, defined as:

$$y^+ = \frac{\rho U_\tau \delta n}{\mu} \quad (2.43)$$

The wall shear stress may be expressed as:

$$\bar{\tau}_w = -\lambda_w \bar{U}_p \quad (2.44)$$

where  $\lambda_w$  is a coefficient evaluated differently depending on whether the computational point lies in the laminar or fully-turbulent parts of the flow, thus:

$$\lambda_w = \frac{\mu}{\delta n} \quad \text{if } y^+ < 11.63 \text{ (laminar sublayer)} \quad (2.45)$$

$$\lambda_w = \frac{\rho U_\tau \kappa}{\ln(Ey^+)} \quad \text{if } y^+ > 11.63 \text{ (turbulent layer)}$$

The flux of  $k$ , the turbulence kinetic energy, at the wall is taken to be zero and its value at the wall-adjacent node is obtained from the solution of its equation with the production rate evaluated from:

$$P_k = \tau_w \frac{\partial U_p}{\partial n} \quad (2.46)$$

## 2.11 Time-Step Size

The time-step size depends on the grid spacing, which should be small enough to resolve accurately the velocity gradients, particularly for the near-wall cells. The time-step size  $\Delta t$  should be smaller than the local convective time scale  $T_{\text{con}}$  and viscous time scale  $T_{\text{vis}}$ :

$$\Delta t = \min(T_{\text{con}}, T_{\text{vis}})$$

$$T_{\text{con}} = \min\left(\frac{\Delta x}{|U|}, \frac{\Delta y}{|V|}\right) \quad (2.47)$$

$$T_{\text{vis}} = \frac{1}{2} \frac{\Delta x^2 \Delta y^2}{\nu(\Delta x^2 + \Delta y^2)}$$

Replacing  $\Delta x$  and  $\Delta y$  with the smallest grid spacing  $\Delta n$ , and  $U$  and  $V$  by the reference velocity  $U_0$ , the Courant-Friedrichs-Lewy conditions can be arrived at:

$$\Delta t^* \leq \frac{\Delta n}{H} \quad (2.48)$$

and Fourier-number condition:

$$\Delta t^* \leq \frac{1}{4} \left(\frac{\Delta n}{H}\right)^2 \text{Re} \quad (2.49)$$

where

$$\Delta t^* = \frac{\Delta t U_0}{H} \quad (2.50)$$

is the non-dimensionalised time step and  $H$  is the dimensions of the bluff body. By reducing the time-step size below the Courant-Friedrichs-Lewy or Fourier-number conditions there was no need to use underrelaxation factors. For the computations in this work,  $\Delta t^*$  was kept below 0.6. This required at least 1000 time-steps to cover one vortex shedding cycle. The number of time-steps per vortex shedding cycle is given by:  $1 / \Delta t^* S_l$ . Typically, 3 to 5 outer iterations per time-step were required once a periodic solution was achieved.

## 2.12 Flow-Solver Outline

The overall solution procedure can be summarised as follows:

1. Provide the numerical grid (see Chapter Three) and the initial field values of the dependent variables.
2. In the case of unsteady flow store the current variable values for the time  $t=t_0$  as old ones.
3. Assemble and solve the momentum equations to get  $U_i$  using the latest available values for the pressure  $p$  and mass fluxes  $F_i$ .
4. Calculate the cell face velocities by the momentum interpolation practice, and determine the mass imbalance.
5. Assemble and solve the pressure correction equation.
6. Update the pressure field and correct the velocities and mass fluxes.
7. In case of turbulent flow assemble and solve the transport equations for  $k$  and  $\epsilon$  and update the turbulent viscosity.
8. Repeat steps 3 to 7 until the converged solution for the current time level is reached. The convergence criterion adopted here is that the sum of the absolute values of the residuals for all variables, normalised by the appropriate inlet flux, should drop below a pre-specified level (set to  $5 \times 10^{-4}$  here).
9. Advance the time step  $\Delta t$  and return to step 2; continue until the prescribed number of time steps is performed.

## 2.13 Overall Flow Chart

The computations throughout this work were conducted on a SUNSPARC10 Workstation. The programmes used were written in the FORTRAN language, with GINO extensions for pre- and post-processing purposes. Figure 2.3 shows a flow chart of the three main stages, described below with the FORTRAN program and data file names:

1. Pre-processing: A grid generation code (*grid.f*) is used to set up a grid with control over shape, size, and density, detailed in a grid input file (*circ-in.dat* or *sq-in.dat*). The resulting grid is output into a grid file (*grid.dat*).
2. Flow solver: The flow solver code used (*flow.f*), reads data created by the grid generator, and uses the input data from file (*fs-in.dat*), to set up boundary conditions, time step limits, and other criteria, in order to solve the problem.
3. Post-processing: Several output files are created by the flow solver. These are used to assess the cyclic features of important parameters such as drag, lift, pressure, velocity, turbulence intensity, and others in the flow field.

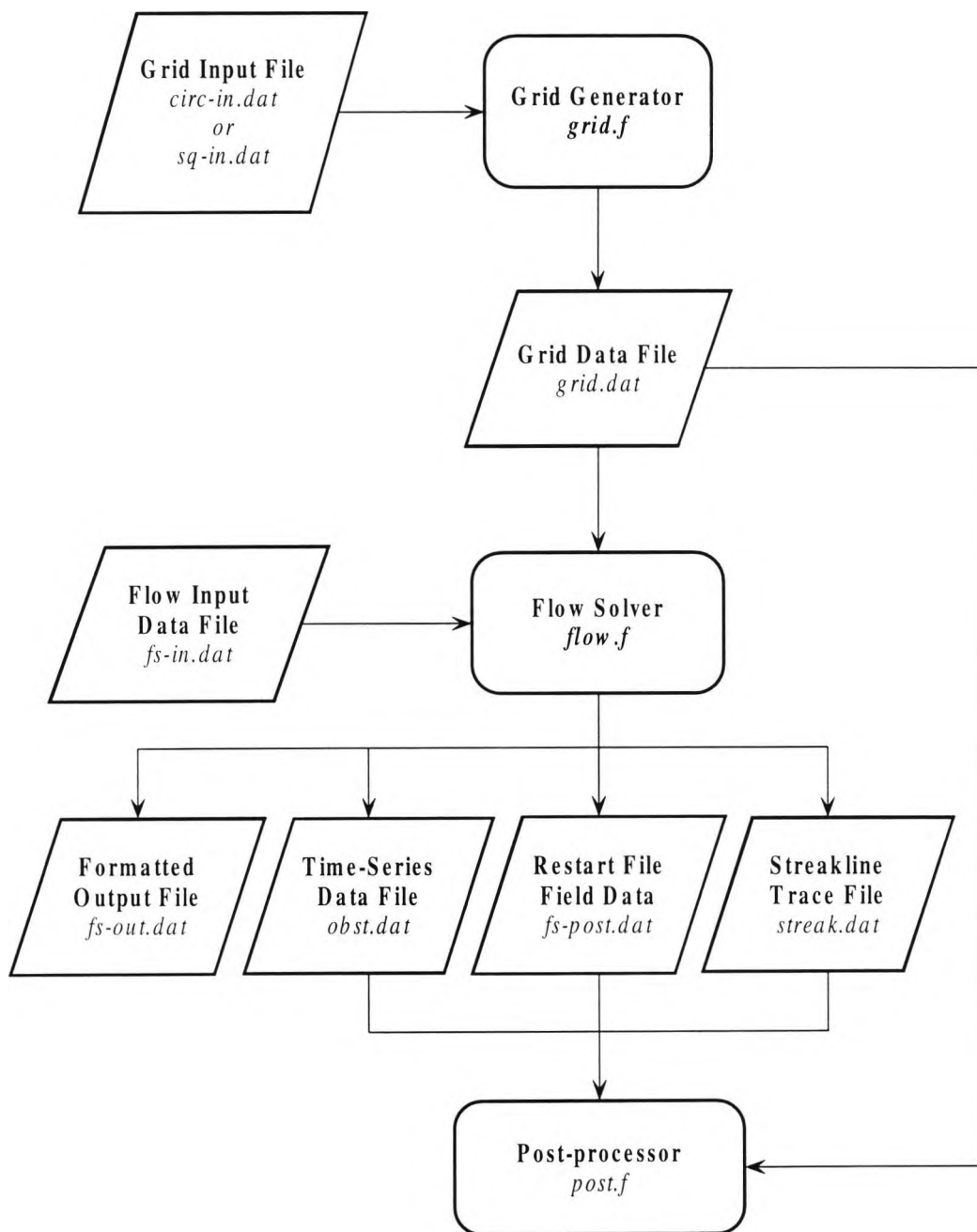


Figure 2.3: Flow chart of programmes and data flow in the project with FORTRAN names.

# CHAPTER THREE: APPLICATION TO SINGLE CYLINDERS

## 3.1 Introductory Remarks

The ability of the  $k-\varepsilon$  model to capture the main features of vortex shedding from a single cylinder, either square or circular in shape is checked in this chapter. Comparisons are made with measured data on the mean drag, lift and Strouhal number at different Reynolds numbers. The sensitivity of the computed results to the choice of interpolation scheme and the size of the computational grid is determined.

A review of experimental results and previous predictions are presented in Sections 3.2 and 3.3. The computational details are presented in Section 3.4 with an outline of the grid generation process. Grid and time-step dependence tests for a square and circular cylinder are presented in Section 3.5. A variety of interpolation schemes are evaluated for a square and circular cylinder in laminar flow in Section 3.6. The choice of turbulence model and the sensitivity of the results to the choice of an empirical coefficient are investigated in Section 3.7. The dependence of the predicted vortex shedding parameters on Reynolds number is presented in Section 3.8 with emphasis on application to very high Reynolds number (i.e.  $Re > 9 \times 10^6$ ) cases, for which no experimental results exist.

## 3.2 Review of Experimental Findings

A large number of experimental studies have been carried out on vortex shedding from single cylinders (Bearman, 1984), but detailed knowledge of the unsteady flow field is rather limited owing to the considerable effort involved in taking unsteady measurements in such flows. This is why vortex shedding has attracted the attention of numerical analysts. In the following a summary of some of these experimental studies for circular and square cylinders is presented.

### 3.2.1 Circular Cylinders

The flow parameters (e.g. drag, lift, and Strouhal number) are dependent on the Reynolds number. Figure 3.1(a) shows the relationship between measured mean drag coefficient ( $\overline{C}_D$ ), and Re for a smooth circular cylinder. The major identifiable regions are shown (labelled A,B,C and D). As pointed out by Farell (1981), defining different flow-regime terminology can be “very confusing”. Most investigators appear to prefer their own terminology. In this project, we adopt the terminology of Roshko (1961) which is (ref. Figure 3.1(a)):

Range	Terminology
A	Subcritical
B	Transition Range
C	Supercritical
D	Transcritical

*Table 3.1: Terminology according to Roshko (1961) for flow regimes defined in Fig 3.1(a).*

The many experimental measurements of vortex shedding at subcritical Reynolds numbers are in fairly good agreement. At higher Reynolds numbers however, there is little agreement (Chen, 1987). One reason is the sensitivity of the flow to small perturbations arising from, for example, small changes in the flow velocity or turbulence intensity.

At small Re (say  $<5$ ), inertia forces are negligible compared with viscous forces and the drag is almost directly proportional to the incident velocity. When separation of the boundary layer occurs, pressure drag becomes a larger contributor, and the slope of the curve becomes less steep. By  $Re=200$ , the von Karman vortex street is well established and the pressure drag accounts for nearly 90% of the total drag. With increasing Re, the drag coefficient decreases to a minimum of 0.9 at  $Re \approx 2000$  and then rises slightly to 1.2 at  $Re \approx 3 \times 10^4$ . The *subcritical regime* (A) is defined by the range  $2000 < Re < 1 \times 10^5$ . The main feature of this regime is the upstream movement of the point of transition, from laminar to turbulent flow, with increasing Reynolds number. Laminar separation on the surface of the cylinder occurs at a maximum of  $80^\circ$  from the stagnation point. At about  $Re=10^4$ , this point of transition is close to the point of separation, and the major portion of the free shear layer is turbulent. For  $10^4 < Re < 1 \times 10^5$  there is minimal

movement of the transition point and the flow field is essentially unchanged. Consequently,  $\bar{C}_D$  is reasonably independent of  $Re$  in the subcritical regime above about  $10^4$ .

The *transition* (B) from subcritical to supercritical behaviour takes place in the range  $1 \times 10^5 < Re < 2 \times 10^5$ . In this range the value of  $\bar{C}_D$  drops suddenly. This effect is usually called the *drag crisis*. The explanation of this behaviour is found to be in the appearance of turbulent flow in the downstream areas of the boundary layer, and a consequential readjustment of the wake. The wake contracts and this leads to a temporary reduction in drag.

As  $Re$  is increased beyond  $2 \times 10^5$ , the *supercritical regime* (C) is entered. As  $Re$  is increased in this regime the point of transition, from laminar to turbulent flow moves upstream until it reaches the point of separation.  $\bar{C}_D$  attains its minimum in this range. Once transition precedes separation, the *transcritical regime* (D) is entered. Further increase in Reynolds number leaves the wake relatively unaffected so that the drag force changes little from this point onwards. At  $Re > 10^7$  the value of  $\bar{C}_D$  appears to be independent of  $Re$ .

A summary of some of the measurements of Strouhal numbers ( $St$ ) for smooth circular cylinders are shown in Figure 3.1(b). Strouhal number is obtained from the power spectra of the lift fluctuations. Numerous measurements have been made of  $St$  in the subcritical regime. The shaded area encompasses measurements from many sources compiled by Lienhard (1966). In common with  $\bar{C}_D$  in this regime, the Strouhal number displays relatively little scatter. The Strouhal number remains nearly constant at about 0.2 within the range of Reynolds number from 300 to  $2 \times 10^5$ .

The large increase in the value of  $St$  that occurs at the transition from subcritical to supercritical is related to the position of the final separation. This is the farthest downstream that final separation takes place and is usually preceded by laminar separation and reattachment. As the Reynolds number is further increased to about  $3.5 \times 10^5$ , the Strouhal number seems to increase depending on the turbulence intensity of the incoming flow. However, vortex shedding in this region is much weaker and defining an accurate shedding frequency is often difficult. The transcritical regime measurements show an increasing  $St$  value with increasing  $Re$ .

Compared with the mean drag coefficient and Strouhal number, the root mean square (rms) of the lift coefficient  $\tilde{C}_L$  is not well established. Measurements of  $\tilde{C}_L$  display

scatter. Part of the scatter can be attributed to the fact that more sophisticated instrumentation techniques are required for measuring  $\bar{C}_L$  (Basu, 1985). Figure 3.1(c) summarises some available experimental measurements of  $\bar{C}_L$  as a function of  $Re$  for smooth circular cylinders. According to West and Appelt (1993), the large variation in the magnitude of  $\bar{C}_L$  illustrates their sensitivity to aspect ratio, blockage, turbulence intensity and end conditions. Very small-scale turbulence can apparently amplify  $\bar{C}_L$  dramatically.

### 3.2.2 Square Cylinders

In the case of a sharp edged body like a square cylinder, where the separation points are fixed at the corners, the aerodynamic characteristics are said to be relatively insensitive to Reynolds number (Okajima, 1982). At extremely low Reynolds numbers, the flow is known to separate at the trailing edges rather than the leading edges where the separation, if it occurs, is indiscernible owing to immediate reattachment. With an increase of Reynolds number, the flow separation at the leading edge becomes more established, and the steady reattachment becomes impossible. On the other hand, the phenomenon of transition from laminar to turbulent flow, which occurs in the flow near the cylinder at certain values of the Reynolds number, should be taken into consideration.

Consequently, there exists a certain range of Reynolds numbers where the flow characteristics, the Strouhal number in particular, of a square cylinder change rapidly. This occurs in the range of  $Re \approx 500$  and  $1000$ . In consequence, the Strouhal number sharply decreases at these Reynolds numbers. Beyond  $Re \approx 10^4$ ,  $\bar{C}_D$  and Strouhal number for the square cylinder have nearly constant values. These trends can be seen from the experimental measurements for a smooth square cylinder as plotted in Figure 3.2.

Compared with the circular cylinder, there are only a few experimental studies reported for the square cylinder. The relatively large discrepancies between the various tests point to experimental uncertainties. In particular, the sharpness of the cylinder corners can influence the shedding frequency.

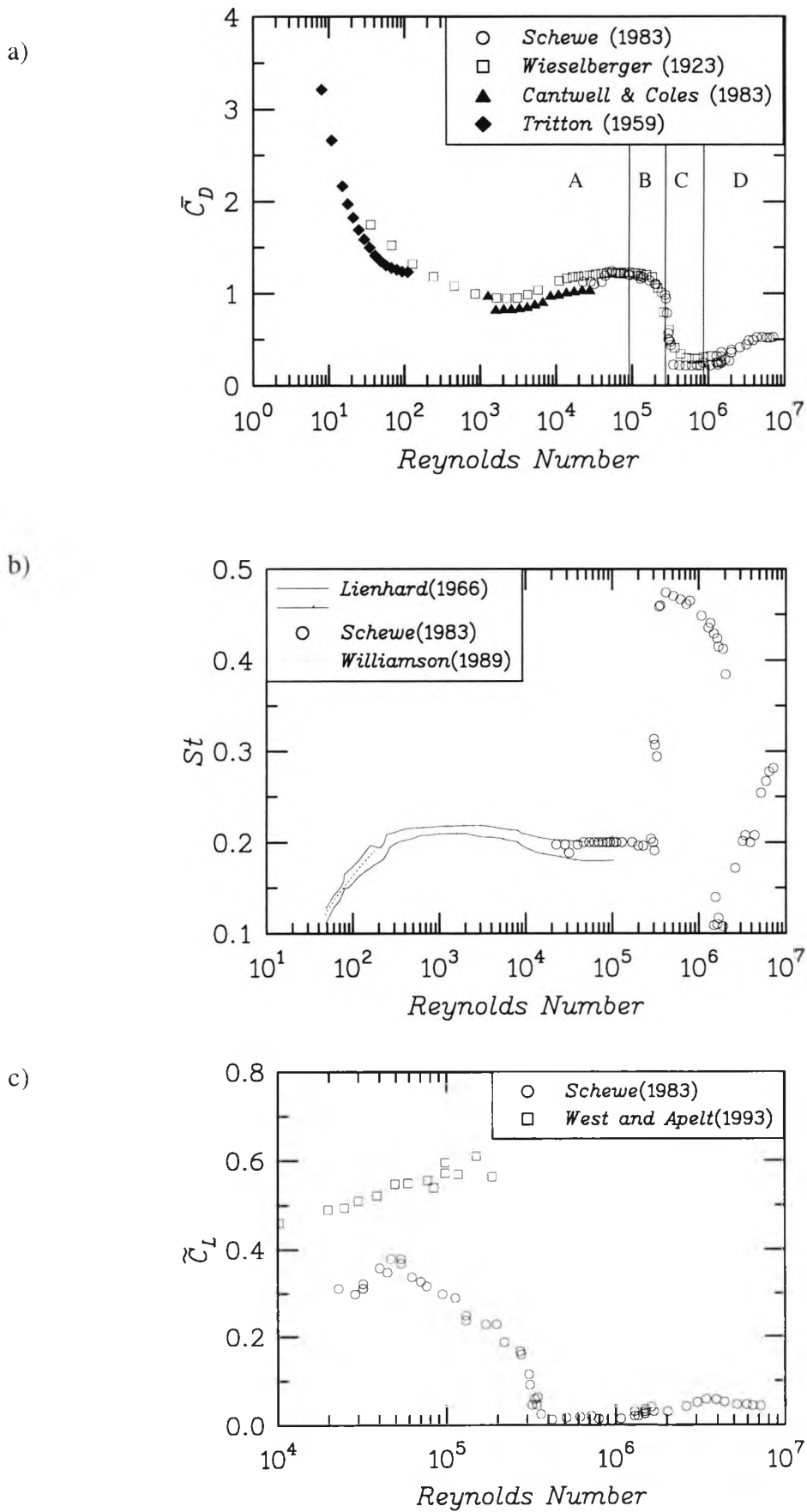


Figure 3.1: Experimental data for a smooth circular cylinder for a) Mean Drag Coefficient; b) Strouhal number; c) RMS Lift Coefficient.

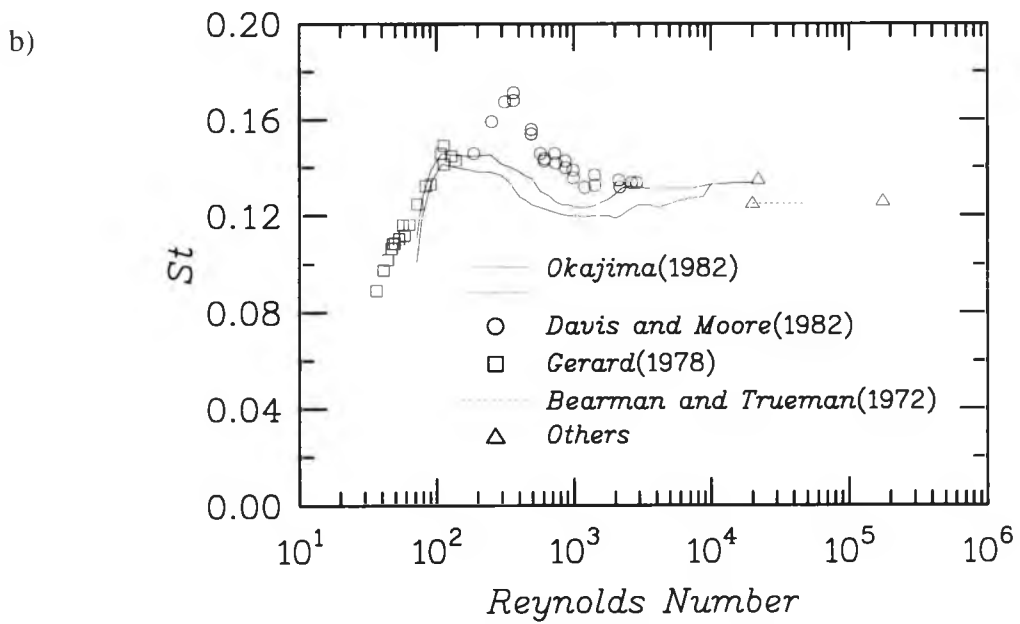
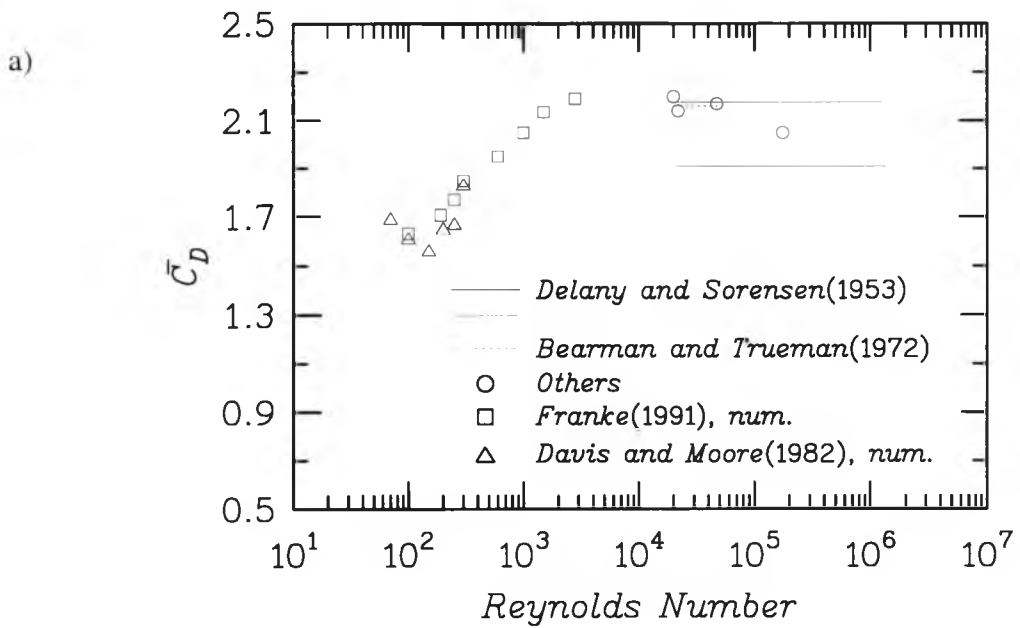


Figure 3.2: Experimental and numerical data for a square cylinder for a) Mean Drag Coefficient; b) Strouhal number.

### 3.3 Review Of Previous Predictions

Before presenting some past work on predicting vortex shedding, it is worth first mentioning some of the features that should characterise these predictions. The computations should exhibit a clear periodic behaviour in the lift and drag coefficients, with a drag frequency twice that of the lift. Moreover, and for all Reynolds numbers, the maximum and minimum values of lift and drag should show no cycle-to-cycle variation while the long-time average of  $C_L$  must be zero.

The accuracy of the numerical results depends strongly on the resolution of the boundary layer near the cylinder walls. According to Franke et al. (1990), one of the most common problems with the numerical study of vortex shedding flow past cylinders is the presence of numerical diffusion, which effectively reduces the Reynolds number and may even inhibit the self-excitation of vortex shedding.

Many basic but important features of turbulent separated flows are not captured fully by current turbulence models. For example, the size of the recirculation region behind a backward-facing step is typically unpredicted by up to 20%, or the point of flow separation from a circular cylinder is delayed by up to 25 degrees (Basara and Younis, 1995). The use of a non-linear stress-strain relationship, such as that proposed by Speziale (1987), in place of Boussinesq's original linear relationship leads to much improved predictions (Basara and Younis, 1992 and 1993). Nevertheless, some differences remain in the recovery zone further downstream.

Younis (1987) found that vortex shedding from a square cylinder can be predicted using the  $k-\epsilon$  model of turbulence with log-law assumptions. In sharp contrast, Franke and Rodi (1991) reported that 'the calculations with the  $k-\epsilon$  model using wall functions yielded a steady solution and no vortex shedding'.

Song and Yuan (1990) modelled vortex shedding over a circular cylinder, based on the weakly compressible flow equations with a simple subgrid scale turbulence model. An explicit finite volume method was used. A subcritical and a supercritical case were computed. They showed that the large-scale vortex-shedding phenomenon, the primary vortices, and the related oscillatory lift and drag can be calculated fairly well with a grid system coarser than the boundary layer thickness. The secondary vortices and the related higher frequency oscillations were also calculated using a somewhat finer grid.

Celik et al. (1985) proposed a two-parameter irrotational flow model for the calculation of mean flow past smooth circular cylinders. This method takes into account the displacement thickness of the boundary layer, by which the location of separation is predicted. The boundary layer effect was shown to be important in the supercritical flow regime. This is presumably due to the rapid thickening of the boundary layer in the extensive pressure-rise region in this regime.

There are two alternative approaches to conventional turbulence modelling: Large Eddy Simulations (LES), and Direct Numerical Simulation (DNS). Neither is viable for the practical simulation of vortex shedding flows. In LES, a sub-grid approach is used to model the dissipation that occurs through the unresolved small-scale motions, but the computed results are known to be sensitive to the choice of such model while the computational efforts involved are quite prohibitive, particularly for the high Reynolds number conditions encountered in engineering practice. The DNS method requires excessive computing resources to capture the viscous dissipation associated with the small-scale motions without which turbulence would grow without bounds.

In the following sections, results obtained from present predictions are compared with some of the above methods.

### 3.4 Grid Generation

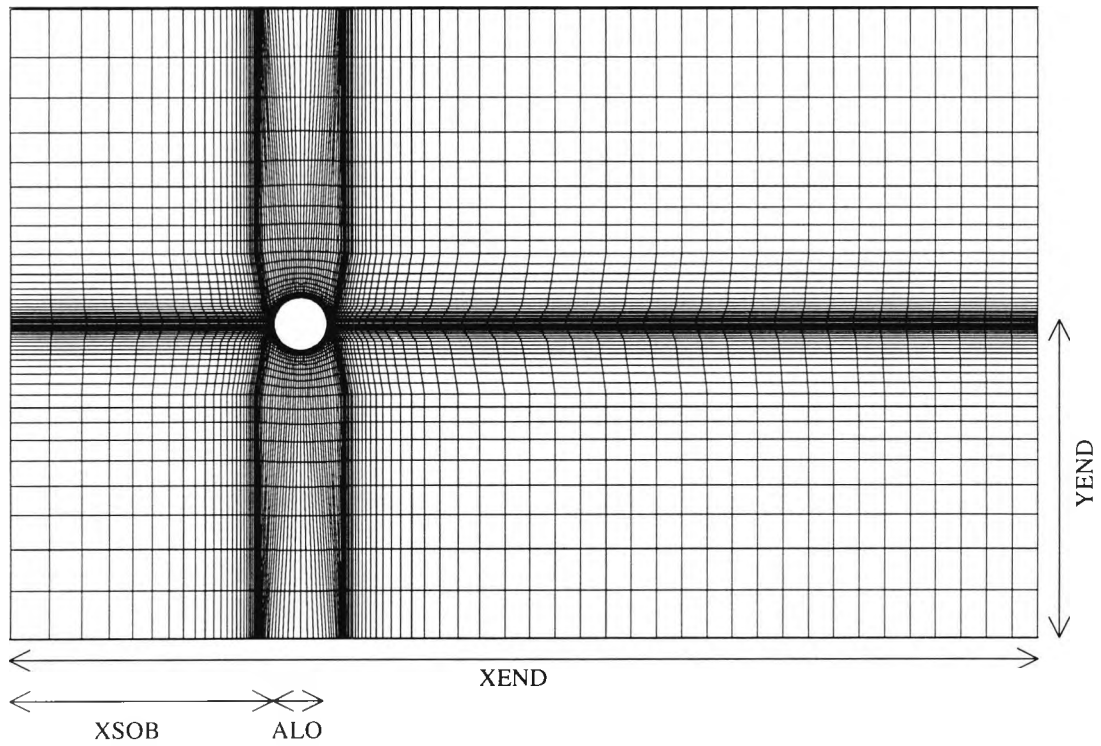
For the purposes of this project, a two-dimensional non-orthogonal structured mesh, consisting of quadrilaterals is used. The computational mesh, subdivides the solution domain into a finite number of discrete volumes - *control volumes* (CV). Each CV is defined by its four vertices. These are connected by straight-line segments. In the present flow solver, all variables ( $U, V, p, k,$  and  $\epsilon$ ) are stored at the geometric centre of the CV. Transport equations are solved only for interior computational points (nodes). i.e. for the nodes which do not coincide with the boundary of the solution domain. The boundary nodes are thus used for the implementation of boundary conditions.

A pair of two indices ( $i$  and  $j$ ) indicates the position of a CV on the numerical mesh. A simplified version of the discrete transfinite mapping method has been used in the grid generation code. The method is algebraic and is based on a simple idea of similar distribution of control-volume vertices along straight lines connecting two opposite boundaries. In addition, a function that gives the distribution of points along the straight lines is prescribed.

In the case of complex geometries, for example when a cylinder is present within the solution domain, the above practice can be applied to regions obtained by subdividing the solution domain into several subdomains. Thus, the grid for the whole solution domain is the result of merging corresponding subgrids. In the case of a circular cylinder, it is also necessary to define the grid splitting lines. Grid line smoothing is also applied. Figure 3.3(a) shows a  $148 \times 102$  grid used for a single circular cylinder, with a close-up of the cylinder region in Figure 3.4. Table 3.2 shows a typical list of parameters which are used in the grid generation program to control the shape and size of the grid.

For the square cylinder, there is no need for subdomains. A geometric expansion series is used to calculate the distribution of cell vertices along the boundaries. Figure 3.3(b) shows a  $121 \times 110$  grid used for a square cylinder, with a close-up of the cylinder region in Figure 3.5. Table 3.3 shows a typical list of parameters which are used in the grid generation program to control the shape and size of the grid.

a)



b)

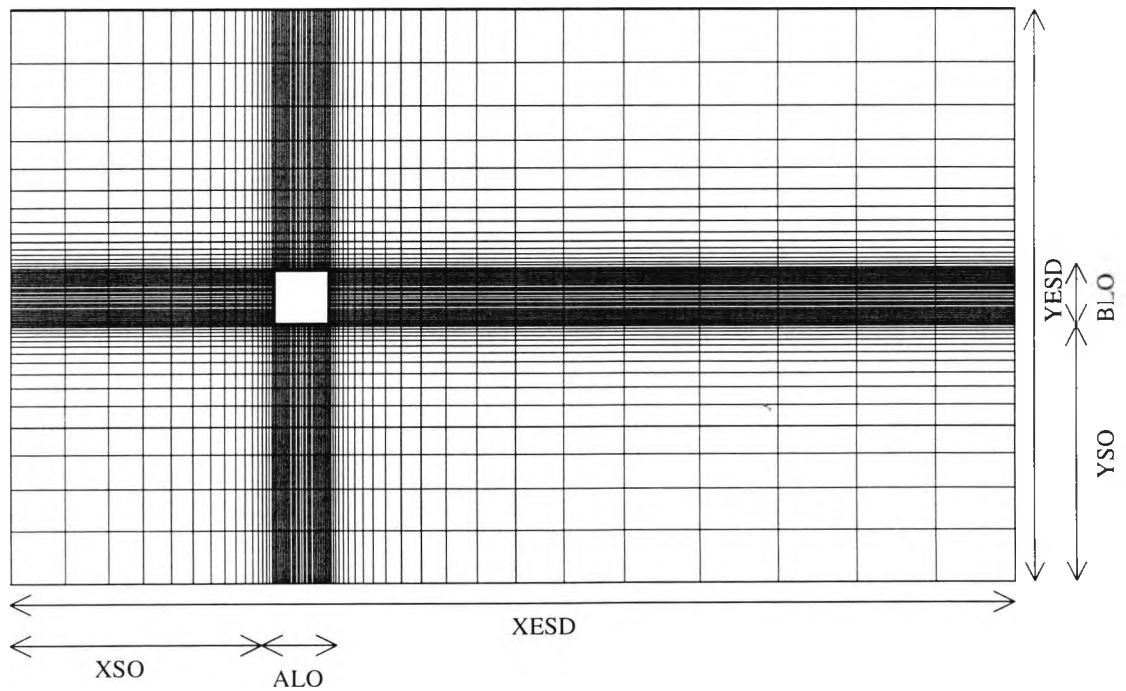


Figure 3.3: Typical grid arrangements used to model single a) Circular (148x102) and b) Square cylinder (121x110).

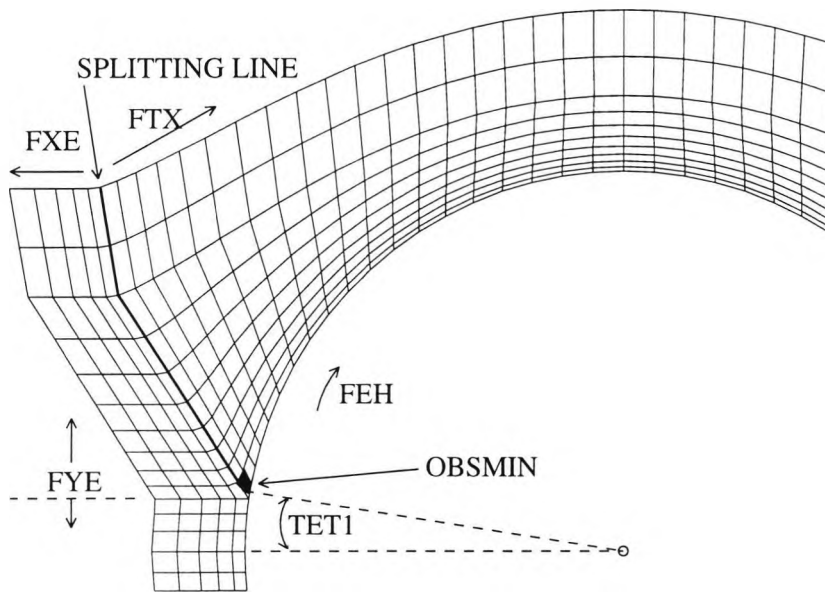


Figure 3.4: Close up of circular cylinder with important parameters highlighted.

Parameter	Value	Meaning
ALO	1	Diameter of cylinder.
XSOB	14	Distance from inlet of the computational domain to cylinder face.
XEND	48	Total length of the computation domain (in x-direction).
YEND	12	Total width of the computation domain (in y-direction).
OBSMIN	0.02	Smallest cell size next to cylinder.
FXE	1.2	Expansion factor in x-direction.
FYE	1.2	Expansion factor in y-direction.
FTX	1.2	Expansion factor for the region between grid splitting lines (above cylinder).
FTXK	1.2	Similar to FTX but for subdomains downstream of cylinder.
FEH	1.2	Expansion factor along cylinder wall.
NSUB	4	Number of subdomain.
TET1	18	Angle that determines beginning of the grid splitting lines at the cylinder face.

Table 3.2: Geometric data used in the grid code to generate a grid for a circular cylinder (all measurements are in metres).

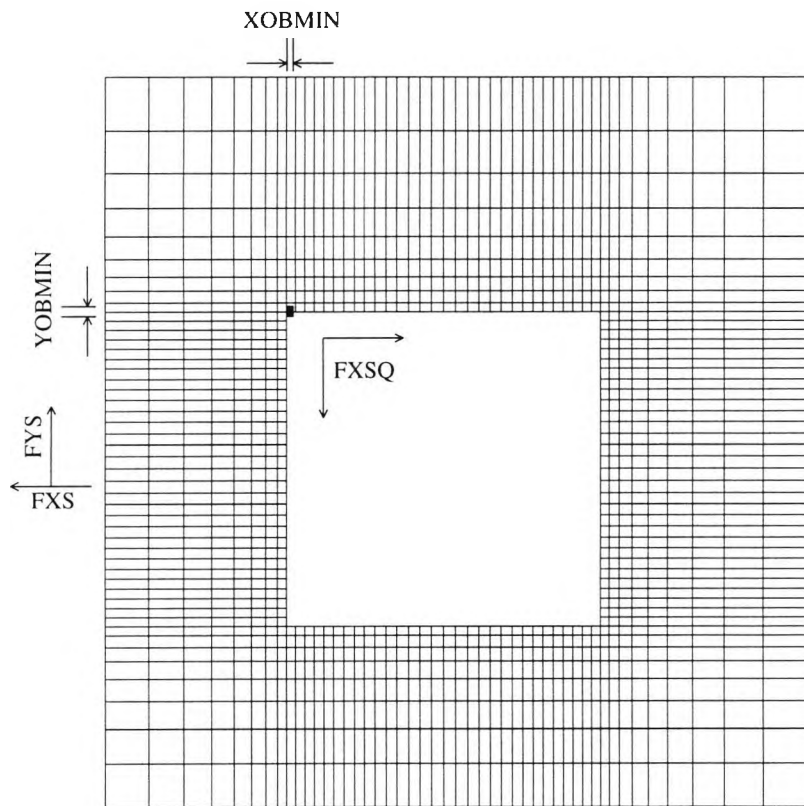


Figure 3.5: Close up of square cylinder with important parameters highlighted.

Parameter	Value	Meaning	
ALO	1	Width of cylinder.	
BLO	1	Height of cylinder.	
XSO	10	Distance from inlet of the computational domain to cylinder face.	
YSO	11.5	Distance from the bottom boundary to the cylinder base.	
XESD	1	Total length of the computation domain (in x-direction).	
YESD	40	Total width of the computation domain (in y-direction).	
XOBMIN	24	Smallest cell size (in x-direction) adjacent to cylinder.	
YOBMIN	0.03	Smallest cell size (in y-direction) adjacent to cylinder.	
FXS	0.03	Expansion factor in x-direction.	
FYS	1.1	Expansion factor in y-direction.	
FXSQ	1.1	Expansion factor (in both x- and y-direction) for cells on the cylinder wall.	

Table 3.3: Geometric data used in the grid code to generate a grid for a square cylinder (all measurements are in metres).

## 3.5 Grid and Time-step Dependence

Grid and time-step dependence test are necessary in order to separate numerical errors from turbulence-model defects. The usual way to achieve this is to repeat a computation on a grid with a finer concentration of nodes and again on a grid with coarser concentration, and repeat for larger and smaller time-steps.

This is done for both the circular and square cylinders in laminar and turbulent flows:

### 3.5.1 Circular Cylinder

The outcome of the grid and time-step size dependence checks for a circular cylinder at  $Re=100$  are summarised in Table 3.4. Experimental data and other CFD results are also shown there for reference. The present predictions are in good accord with the experimental data. Mean drag and Strouhal number are well within the experimental range. The results show that for the number of nodes used, there is very little effect on the mean drag or Strouhal number, even with a 40% reduction in the number of grid nodes (as for RUN 1 and RUN 3). The same is true for the time step value. It does not have any effect on the value of mean drag or Strouhal number when reduced to 40% its original value (as for RUN 1 and RUN 5).

The results show that with the number of nodes used, the present predictions are fairly insensitive to the choice of grid density and time-step. Refining the grid will very often produce a better accuracy. However, the execution time must be taken into consideration when making choices for the grid density.

Table 3.5 shows the number of time-steps and CPU time on a SUNSPARC10 Workstation (in minutes) needed to obtain data for one cycle of the lift coefficient for the RUNs in Table 3.4.

The results show that RUN 1 represents a reasonable balance between accuracy and computational efficiency. For this reason, all consequent computations for a single circular cylinder in laminar flow will be conducted with this grid. Figure 3.8 shows thirteen cycles for the lift coefficient of RUN 1. This was obtained in 910 minutes, although more time was needed in the preliminary stage to achieve a periodic solution. Table 3.6 shows grid and time-step dependence checks for turbulent calculations for a circular cylinder at  $Re=65000$ , obtained with the modified k- $\epsilon$  model and the SMART

scheme. Note that the experimental results of Schewe (1983) are for  $Re=62438$ . RUN 1, which had the same grid density as for the laminar flow case, showed an inadequacy in predicting the mean drag, which is well below the experimental data. In RUN 2, the grid density was increased by 1.2 times that in RUN 1. The results show a better prediction of mean drag, although Strouhal number increased further. No improvements were observed by halving the time step from RUN 2 to RUN 3. Mean drag dropped slightly when halving the time step again in RUN 4.

It is shown here that grid resolution is of crucial importance, since there is a need for more resolution around the cylinder. The results show that RUN 2 represents a reasonable balance between accuracy and computational efficiency. For this reason, all consequent computations for a single circular cylinder in turbulent flow will be conducted with this grid.

For the turbulent flow calculations, the computational time is increased due to the need to perform extra calculations to solve for the  $k$  and  $\epsilon$  equations. The twelve lift cycles shown in Figure 3.12 for  $Re=65000$  took 1440 CPU minutes to obtain.

There is another grid-related factor affecting solution accuracy. The viscous sublayer of a boundary layer is so thin that it is difficult to use enough grid points to resolve it. This problem is avoided by using wall functions, which rely on the existence of a logarithmic region in the velocity profile. The validity of the wall function depends on the value of  $y_+$  (dimensionless normal distance of the first grid point above surface). Grid-insensitive computations can be obtained provided  $30 < y_+ < 1000$ . If the value of  $y_+$  drops out of this range, then the flow departs from the assumed logarithmic distribution. This criterion can be achieved by monitoring the value of  $y_+$  when calculations are made and then by increasing or decreasing the smallest cell size next to the cylinder in the grid as appropriate.

For both the laminar and turbulent flow calculations, the results are not time step dependent as long as the conditions set out in Section 2.11 are met, and thus will be set according to the Reynolds number.

Runs	St	$\bar{C}_D$	Grid Nodes	$\Delta t^*$
1	0.173	1.451	148x102=15096	0.054
2	0.1745	1.449	124x104=12648	0.054
3	0.174	1.448	97x62=6014	0.054
4	0.174	1.449	148x102=15096	0.041
5	0.1744	1.451	148x102=15096	0.021
<b>Experiment:</b>				
Lienhard (1966)	0.155-0.173	1.35-1.49	-	-
<b>Other Predictions:</b>				
Gresho et al. (1984)	0.180	1.76	1852	0.05
Braza et al. (1986)	0.160	1.28	13530	0.02
Engleman (1990)	0.173	1.41	14000	N/A
Li et al. (1991)	0.163	1.35	826	0.5
Behr et al. (1991)	0.170	1.41	4749	0.007

Table 3.4: Grid and time step dependence for a circular cylinder in laminar flow ( $Re=100$ ).

RUN	Number of time-steps	CPU time required in minutes
1	1010	70
2	850	60
3	700	50
4	1330	95
5	2600	183

Table 3.5: Number of time-steps and CPU time required per cycle for RUNs 1 to 5.

RUNs	St	$\overline{C}_D$	Grid Nodes	$\Delta t^*$
1	0.288	0.675	148x102=15096	0.001
2	0.292	1.025	195x98=19110	0.001
3	0.292	1.025	195x98=19110	0.0005
4	0.292	1.008	195x98=19110	0.00025
<b>Experiments:</b>				
Schewe (1983)	0.2004	1.222	-	-
Sakamoto & Haniu (1994)	0.209	1.24	-	-

Table 3.6: Grid and time step dependence for a circular cylinder in turbulent flow ( $Re=65,000$ ).

### 3.5.2 Square Cylinder

The outcome of the grid and time-step size dependence checks for a square cylinder at  $Re=100$  are summarised in Table 3.7. Experimental and other CFD results are shown there for reference. The predicted Strouhal number is well within the experimental range. The present results are in good comparison to previous predictions (there are no experimental results for the mean drag coefficient). The results show that grid density does not have a significant effect on the value of mean drag or Strouhal number, even if the number of grid nodes are increased to 1.2 times their original value (as for RUN 1 and RUN 3), or decreased to 70% of their original value (as for RUN 1 and RUN 4). The same is true for the time step value. It does not have any effect on the value of mean drag or Strouhal number when reduced to 50% its original value (as for RUN 1 and RUN 2).

Table 3.8 shows the number of time-steps and CPU time on a SUNSPARC10 Workstation (in minutes) needed to obtain data for one cycle of the lift coefficient for the RUNs in Table 3.7.

The results show that RUN 1 represents a reasonable balance between accuracy and computational efficiency. For this reason all consequent computations for a single square cylinder in laminar flow will be conducted with this grid. Figure 3.10 shows eleven cycles for the lift coefficient of RUN 1. This was obtained in 880 minutes, although more time was needed in the preliminary stage to achieve a periodic solution.

Table 3.9 shows grid and time-step dependence checks for turbulent calculations for a square cylinder at  $Re=20000$ , obtained with the modified  $k-\epsilon$  model and the SMART scheme. RUN 1, which had the same grid density as for the laminar flow case, showed an inadequacy in predicting the mean drag, which is below the experimental data. In RUN 2 the grid density was increased by 1.2 times that in RUN 1. The results show a better prediction of mean drag and Strouhal number. No improvements were observed by halving the time step from RUN 2 to RUN 3, and again in RUN 4.

It is shown here, as in the case of the circular cylinder, that grid resolution is of crucial importance, since there is a need for more resolution around the cylinder. The results are not time-step dependent though. The results show that RUN 2 represents a reasonable balance between accuracy and computational efficiency. For this reason all consequent computations for a single square cylinder in turbulent flow will be conducted with this grid.

For the turbulent flow calculations, the computational time is increased due to the need to perform extra calculations to solve for the  $k$  and  $\epsilon$  equations. Eight lift cycles of RUN 2, took 1536 CPU minutes to obtain.

As in the case of the circular cylinder, both the laminar and turbulent flow predictions, gave results which were not time step dependent as long as the conditions set out in Section 2.11 are met, and thus will be set according to the Reynolds number. The number of grid nodes, however need to be larger in order to capture the flow characteristics, depending on the Reynolds number. It is important to note that the value of  $y_+$  was kept within the range  $30 < y_+ < 1000$  for the square cylinder calculations.

RUNs	St	$\overline{C_D}$	Grid Nodes	$\Delta t^*$
<b>1</b>	0.150	1.476	121x110=13310	0.01
<b>2</b>	0.145	1.472	121x110=13310	0.005
<b>3</b>	0.145	1.470	136x118=16048	0.005
<b>4</b>	0.141	1.517	93x98=9114	0.01
<b>Experiments:</b>				
Davis & Moore (1982)	0.155	-	-	-
Okajima (1982)	0.146	-	-	-
<b>Other Predictions:</b>				
Davis & Moore (1982)	0.165	1.770	3162	0.05
Franke et al. (1990)	0.154	1.610	6688	0.025
Kelkar & Patankar (1992)	0.126	1.820	6400	0.12

Table 3.7: Grid and time-step dependence for a square cylinder in laminar flow ( $Re=100$ ).

RUN	Number of time-steps	CPU time required in minutes
<b>1</b>	1060	80
<b>2</b>	2350	163
<b>3</b>	2530	180
<b>4</b>	980	70

Table 3.8: Number of time-steps and CPU time required per cycle for RUNs 1 to 5.

Runs	St	$\bar{C}_D$	Grid Nodes	$\Delta t^*$
1	0.150	1.850	121x110=13310	$2.28 \times 10^{-3}$
2	0.132	2.104	136x118=16048	$2.28 \times 10^{-3}$
3	0.132	2.100	136x118=16048	$1.14 \times 10^{-3}$
4	0.132	2.100	136x118=16048	$5.7 \times 10^{-4}$
<b>Experiments:</b>				
Bearman & Trueman (1972)	0.123	2.190	-	-
Sarpakaya & Ihrig (1986)	0.125	2.150	-	-
Lee (1975)	0.126	2.050	-	-
Bearman & Obasaju (1982)	0.130	-	-	-
Lyn (1989)	0.135	-	-	-
Durao et al. (1988)	0.138	-	-	-
<b>Previous Predictions:</b>				
Kato & Launder (1993)*	0.145	2.050	104x70=7280	N/A
Bosch & Rodi (1996)*	0.146	2.108	106x75=7950	0.02
Franke & Rodi (1991)	0.136	2.150	N/A	N/A
Deng et al. (1994)	0.115	1.978	121x94=11374	0.05*

Table 3.9: Grid and time step dependence for a square cylinder in turbulent flow at  $Re=20,000$ .

Note: \* Reynolds number modelled at 22,000.

\* Time step in the form of  $\Delta t^*$ .

## 3.6 Laminar Flow Results

The present results for a single cylinder are divided into laminar and turbulent flows, depending on the Reynolds number. According to Braza et al. (1986), and Bloor (1964), turbulent fluctuations start to influence the flow in the wake of a circular cylinder in the Reynolds number range 400-1400. In order to account for these effects, a turbulence model has to be introduced. In this work, flows with Reynolds numbers above 1400 are treated as turbulent.

### 3.6.1 Circular Cylinder

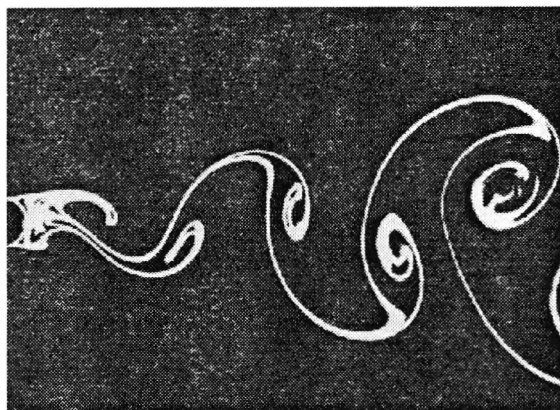
Figure 3.6 shows a typical vortex street, formed behind a circular cylinder at  $Re=140$ , taken from van Dyke (1982). It is possible to predict such a figure by releasing massless particles in the flow, and performing numerical integration of the local velocity vectors over time, and thus plotting the streaklines. The predictions reported below were obtained on a grid of  $148 \times 102$  (see Figure 3.3(a)) and a Reynolds number of 100. The non-dimensional time step ( $\Delta t^*$ ) used in these simulations was 0.054.

Figure 3.7 shows the computed streaklines for three different interpolation schemes. The upwind scheme, which is only first order accurate, is extremely diffusive, leading to serious numerical errors in the computed field. This is evidenced here by the dispersion of the released particles and the distortion of the resulting vortices. The Linear Upwind scheme is formally second-order accurate and is seen here to produce a von Karman vortex street with regions of concentrated vorticity preserved well downstream of the shedding points. The centres of vorticity are displaced from the centre plane, which is in accord with flow visualisation (see Figure 3.6). The SMART scheme is formulated to be of third-order accuracy, dropping to second-order if necessary to preserve boundness.

Figure 3.8 shows the time histories of  $C_D$  and  $C_L$  obtained when using the SMART scheme. Several cycles are plotted ( $t^*$  is non-dimensional time scale  $\equiv tU/D$ ). The vortex shedding frequency ( $f_s$ ) is evaluated by analysing the time histories of  $C_D$  and  $C_L$  with a standard Fast Fourier Transform (FFT) routine. The frequency  $f_s$  is that which corresponds to the highest amplitude. It is of importance to note that the frequency of  $C_L$  is half the frequency of  $C_D$ , as expected. Also shown in Figure 3.8, is the power spectra of the drag and lift coefficients, over a non-dimensional frequency spectrum ( $f^* \equiv fD/U$ ).

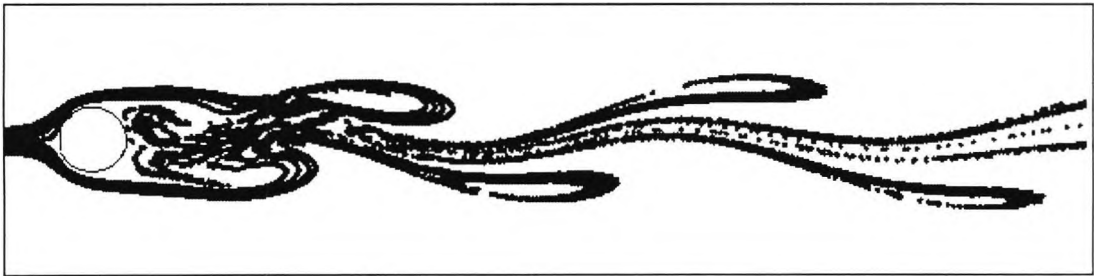
Overall evaluation of the flow solver can only be made by comparing predicted and measured values of the important parameters characterising vortex shedding presents this data for a circular cylinder at  $Re=100$ . Table 3.10 presents the results obtained with the three schemes, experimental data and other predictions. The results show that the choice of scheme does affect the value of mean drag, and Strouhal number. The upwind and linear-upwind schemes underpredict both the mean drag and Strouhal number. The SMART scheme, however achieves the closest value of mean drag and Strouhal number to those obtained experimentally.

That the computed solutions obtained with these schemes and other numerical results are different is not surprising since some may still be grid-dependent. The effect of numerical (rather than physical) parameters such as accuracy and boundness are quite obvious and suggest that the bounded, third-order accurate, SMART scheme is the most appropriate for the present applications.

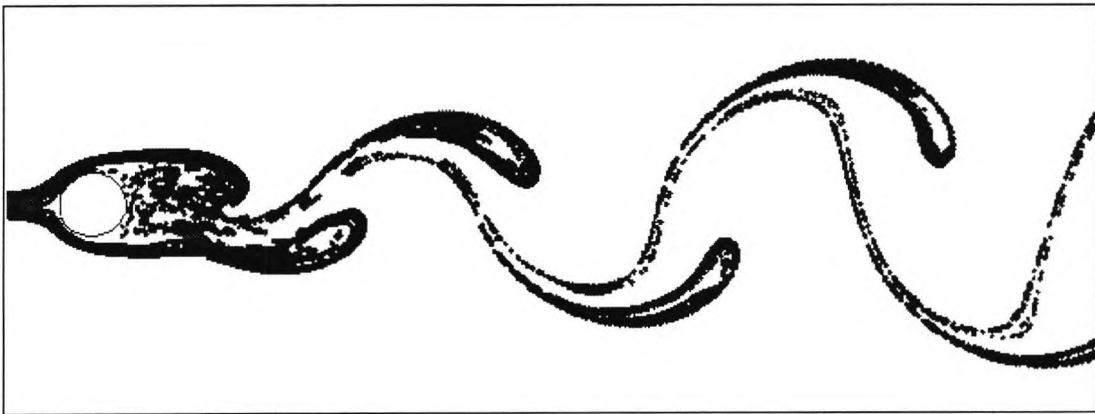


*Figure 3.6: Flow visualisation of vortex shedding from a circular cylinder at Reynolds number of 140.*

UPWIND



Linear UPWIND



SMART

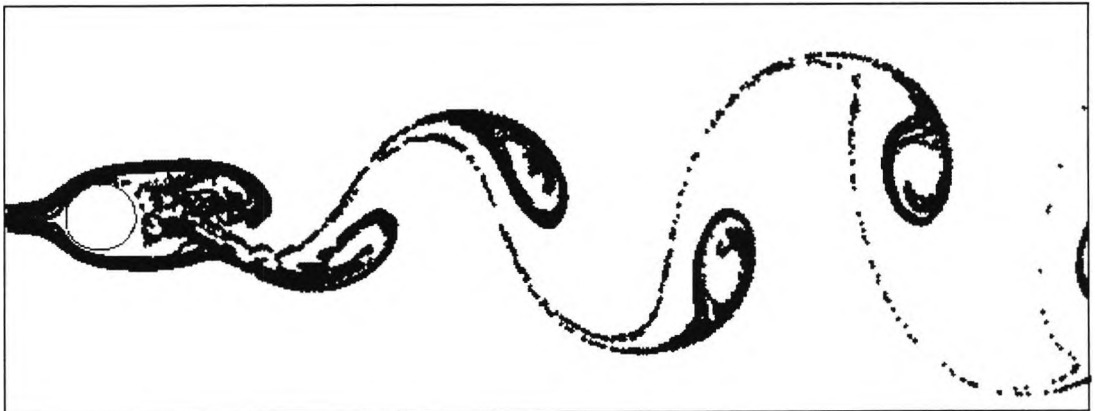


*Figure 3.7: Streaklines behind a circular cylinder at  $Re=100$  as obtained with the SMART scheme.*

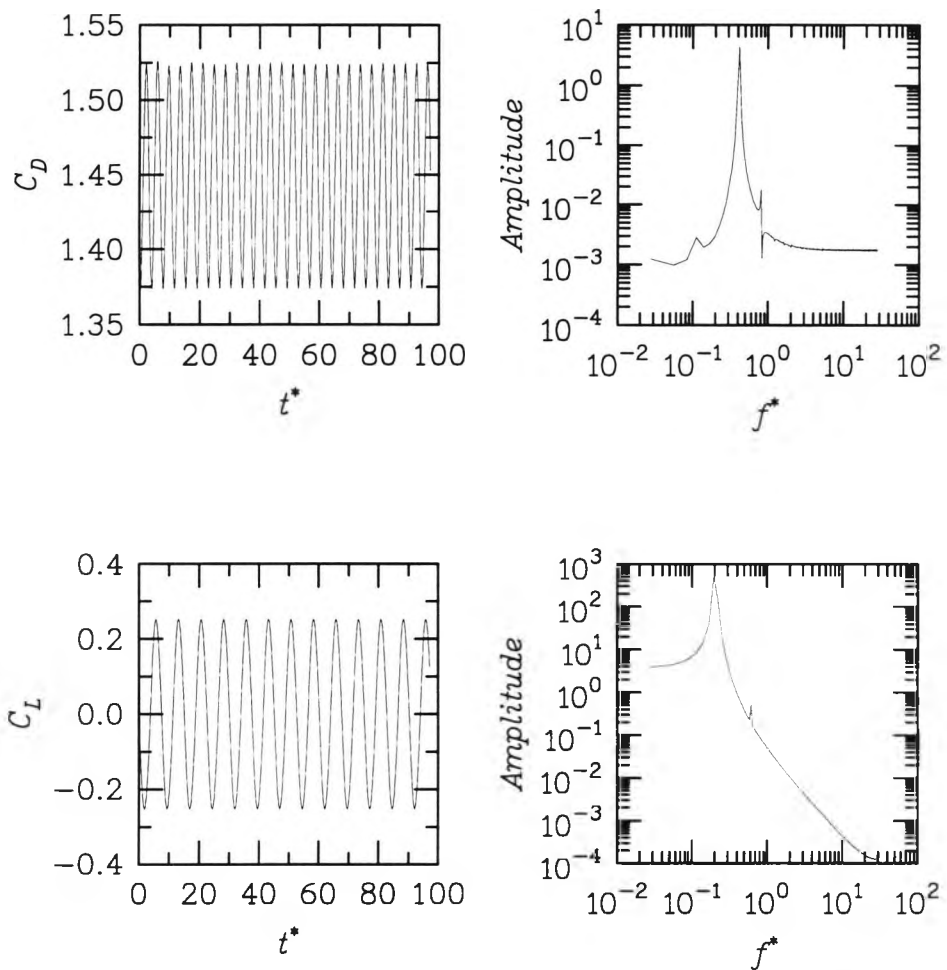


Figure 3.8: Time histories of drag and lift for a circular cylinder at  $Re=100$ ; showing also the power spectra.

	St	$\bar{C}_D$	Grid Nodes	$\Delta t^*$
<b>Experiments:</b>				
Lienhard (1966)	0.155-0.173	1.35-1.49	-	-
<b>Predictions:</b>				
Present (Upwind)	0.120	1.231	148x102	0.054
Present (Lin-Upwind)	0.145	1.289	148x102	0.054
Present (Smart)	0.173	1.451	148x102	0.054
Gresho et al. (1984)	0.180	1.76	1852	0.05
Braza et al. (1986)	0.160	1.28	13530	0.02
Engleman (1990)	0.173	1.41	14000	N/A
Li et al. (1991)	0.163	1.35	826	0.5
Behr et al. (1991)	0.170	1.41	4749	0.007

Table 3.10: Results for a circular cylinder at  $Re=100$ .

### 3.6.2 Square Cylinder

A grid of 121x110 was used (see Figure 3.3(b)). The Reynolds number was set to 100, with a  $\Delta t^*$  of 0.01. Figure 3.9 shows the computed streaklines for three different interpolation schemes. As in the case of the circular cylinder, the SMART scheme predictions show the centres of vorticity displaced from the centre plane, which is in accord with a typical von Karman vortex streets (Figure 3.6).

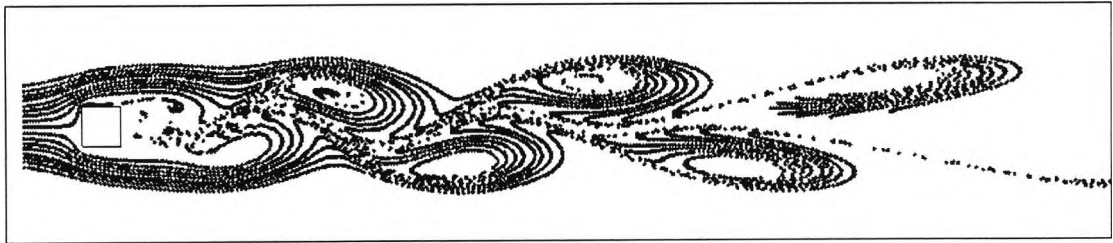
Figure 3.10 shows the time histories of  $C_D$  and  $C_L$  obtained when using the SMART scheme. Several cycles are presented over a non-dimensional time scale ( $t^*$ ). Also shown, is the power spectra of the drag and lift coefficients, over a non-dimensional frequency spectrum ( $f^*$ ). It is of importance to note that the frequency of  $C_L$  is half the frequency of  $C_D$ , as expected.

Overall evaluation of the flow solver can only be made by comparing predicted and measured values of the important parameters characterising vortex shedding. Table 3.11 presents this data for a square cylinder at  $Re=100$ . It is evident that the Strouhal number results are in good agreement with the experimental results. No such comparison can be made for  $\overline{C_D}$  as there are no experimental results for this Reynolds number.

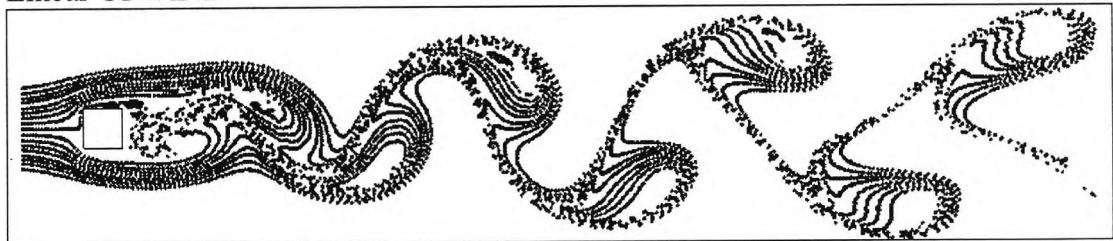
The table also shows that the choice of scheme does not affect  $\overline{C_D}$ , but has a substantial influence on the predicted Strouhal number. The SMART scheme achieves the closest value of  $St$  to those of experiments and other numerical results.

Again, as in the case of the circular cylinder, the effect of numerical (rather than physical) parameters such as accuracy and boundness are quite obvious and suggest that the bounded, third-order accurate, SMART scheme is the most appropriate for the present applications.

UPWIND



Linear UPWIND



SMART

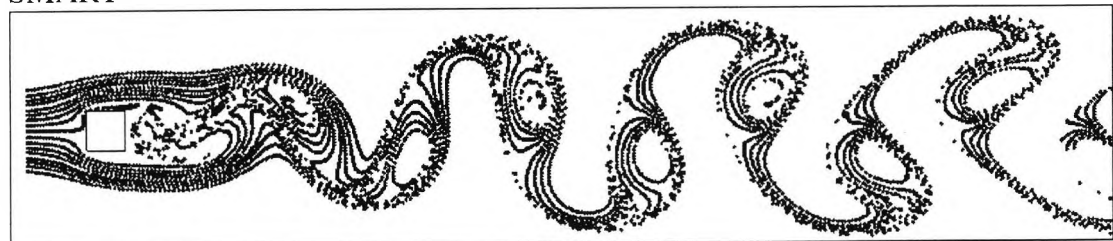


Figure 3.9: Streaklines behind a square cylinder at  $Re=100$  as obtained with alternative interpolation schemes.

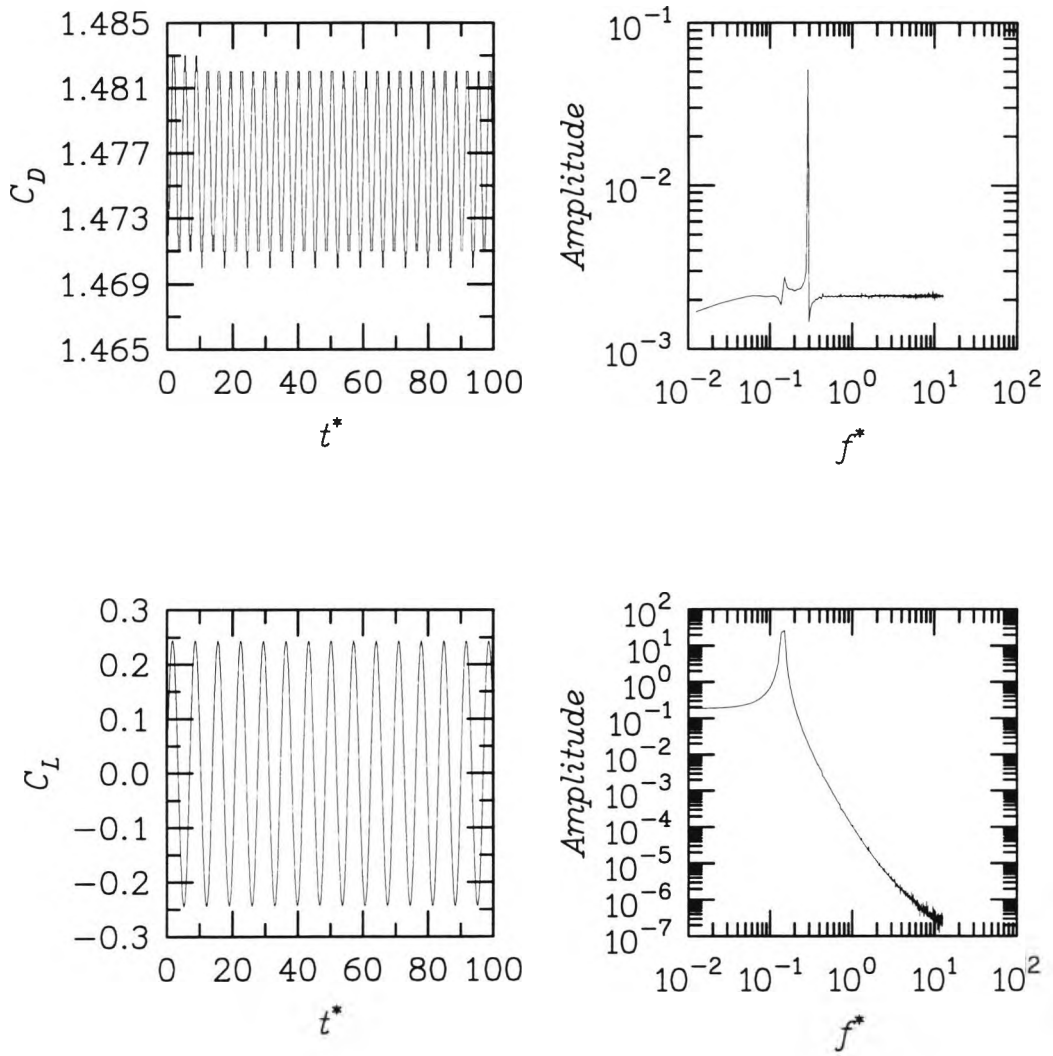


Figure 3.10: Time histories of drag and lift for a square cylinder at  $Re=100$ ; showing also the power spectra.

	St	$\overline{C_D}$	Grid	$\Delta t^*$
<b>Experiments:</b>				
Davis & Moore (1982)	0.155	-	-	-
Okajima (1982)	0.146	-	-	-
<b>Predictions:</b>				
Present (Upwind)	0.110	1.478	121x110	0.01
Present (Lin-Upwind)	0.132	1.478	121x110	0.01
Present (SMART)	0.150	1.476	121x110	0.01
Davis & Moore (1982)	0.165	1.770	51x62	0.05
Franke et al. (1990)	0.154	1.610	88x76	0.025
Kelkar & Patankar (1992)	0.126	1.820	80x80	0.12

Table 3.11: Results for a square cylinder at  $Re=100$ .

### 3.7 Turbulent Flow

Turbulence models are mainly developed with reference to steady flows, whereas the flows associated with vortex shedding cause organised mean-flow periodicity to be superimposed on the random turbulent fluctuations. This is shown by experiments; e.g. by Durao et al. (1988) who measured the turbulence energy spectrum in the unsteady wake of a square cylinder, and found discrete peaks of energy input occurring at the vortex shedding frequency. The presence of those peaks invalidates a fundamental assumption in turbulence modelling; namely that of spectral equilibrium which implies that the rate of energy dissipation by the small scales (ie  $\epsilon$ ) is equal to the rate of energy input at the large scales. While adequate for steady flows, this assumption becomes inappropriate in the presence of the discrete energy peaks and this suggests that the  $\epsilon$  equation may not be sufficiently sensitive to the imposed oscillations.

A proposal made by Younis (1987) and Przulj & Younis (1993) for accounting for the effects of periodicity on the energy-transfer process is to redefine the 'production of dissipation' term in the  $\epsilon$  equation to include an additional term to represent the extra energy input into the turbulent motions. Various corrections were considered and the best improvement was obtained by redefining the  $\epsilon$  production term thus:

$$P_{\epsilon} = C_{\epsilon 1} P_k \frac{\epsilon}{k} \left( 1 + C_t \frac{k}{\epsilon} \frac{\left| \frac{\partial}{\partial t} (q) \right|}{q} \right) \quad (3.1)$$

where  $q$  is the total (i.e. mean plus turbulent) kinetic energy defined as:

$$q = k + \frac{1}{2}(U^2 + V^2) \quad (3.2)$$

A new coefficient ( $C_t=0.38$ ) is introduced; its value is obtained by computer optimisation.

### 3.7.1 Square Cylinder

Results of the simulations at  $Re=20,000$  for a square cylinder, using the modified  $k-\varepsilon$  model, are presented in Table 3.12. Here, the parameter  $\bar{C}_D$  is also presented. This is the root mean square value of  $C_D$ , which shows the extent of the fluctuation of the Drag coefficient. The experiments were conducted at different Reynolds numbers, and thus some of the discrepancies in the results may be due to Reynolds number effects.

There is good correlation with the experimental results: Strouhal number, mean drag, and rms lift are well within the measured range, while rms drag is overpredicted.

The consequences of the use of the modified  $k-\varepsilon$  model on both the average and the peak-to-peak levels of lift and drag coefficient are clear from Figure 3.11. The figure shows the effect of switching off the modification from  $t^*=11$ , for a square cylinder. It is clear that vortex shedding is drastically suppressed. The results presented in Table 3.12 also confirm this, where all the coefficients are reduced, except for the Strouhal number, which is unaffected.

An alternative to the Younis (1987) and Przulj & Younis (1993)  $k-\varepsilon$  modification is one introduced by Kato & Launder (1993). To reduce the excessive production of  $k$  in the stagnation regions in front of a cylinder, due to an unrealistic representation of the normal stresses in eddy-viscosity models, they proposed to replace the production term by:

$$P_k = C_\mu \varepsilon S \Omega, \quad S = \frac{k}{\varepsilon} \sqrt{\frac{1}{2} \left[ \frac{\partial U_i}{\partial x_j} + \frac{\partial U_j}{\partial x_i} \right]^2}, \quad \Omega = \frac{k}{\varepsilon} \sqrt{\frac{1}{2} \left[ \frac{\partial U_i}{\partial x_j} - \frac{\partial U_j}{\partial x_i} \right]^2} \quad (3-3)$$

The quantity  $\Omega$  is a rotation parameter. In simple shear flows,  $S$  and  $\Omega$  are equal, but in stagnation flows,  $\Omega=0$  and  $S>0$ , resulting in the reduction of the  $k$ -production. Predictions were performed using this modification to compare with the  $k-\varepsilon$  modification and the results obtained by Kato & Launder (1993) and Bosch & Rodi (1996). Table 3.13 shows the grid and time-step sizes used in this comparison. There is a discrepancy between the present results obtained with the Kato & Launder modification and those of Kato & Launder (1993) themselves, especially in the rms value of lift. This can be attributed to the finer grid used here. The time-step from Kato & Launder (1993) is not known. There is better agreement between the present results and those carried out by Bosch & Rodi (1996) using the Kato & Launder modification. It shows that the present grid is more refined and the time-steps smaller, therefore the

field is resolved more accurately. Comparing the present k- $\epsilon$  modification of Younis (1987) and Przulj & Younis (1993) with the different reproductions of the Kato & Launder model, it is apparent that the Strouhal number, mean drag and rms lift show reasonable results, while rms drag is overpredicted. Therefore, the present k- $\epsilon$  modification is preferred.

The Kato & Launder modification failed to converge for the case of a circular cylinder. Periodic vortex shedding could not be achieved using any of the differencing schemes available.

Therefore, considering the square cylinder results and the failure of the Kato & Launder modification to model the case of the circular cylinder, the Younis (1987) and Przulj & Younis (1993) modification to the k- $\epsilon$  model is appropriate for use throughout this work.

The predictions of Franke and Rodi (1991) [Table 3.12] were obtained using the Reynolds Stress Model (RSM) and are seen to give good results. Deng et al. (1994) used the Baldwin-Lomax model, which is a version of the eddy-viscosity model, and also reported good results with a fine grid.

Overall, the results obtained for the square cylinder were in satisfactory agreement with the experimental data. This is because the separation points (which are normally difficult to predict) are fixed in this flow.

### 3.7.2 Circular Cylinder

The flow over a circular cylinder is more difficult to predict in the subcritical regime, since the flow is not fully turbulent. Results for  $Re=65,000$ , using the modified k- $\epsilon$  model are presented in Table 3.14. It is clear that the Strouhal number and  $\bar{C}_L$  are overestimated compared to the data, while  $\bar{C}_D$  is underestimated. The main reason for this is that the separation angle which should not be far greater than  $90^\circ$ , is obtained here at around  $130^\circ$ . It then follows that the separated wake is narrower, and thus  $\bar{C}_D$  is lower than the measured value.

Figure 3.12 shows time histories of  $C_D$  and  $C_L$ , with the k- $\epsilon$  modification up to  $t^*=15.5$  and without the modification, thereafter. It is again apparent that vortex shedding is drastically suppressed when the standard k- $\epsilon$  model is used.

The results in Table 3.14 quantify this outcome, where it is clear that all the coefficients are reduced, except for the Strouhal number, which is unaffected. Note that the case of  $C_t=0.0$  is in effect the standard  $k-\epsilon$  model.

The coefficient in Equation 3.1 used for the  $k-\epsilon$  modification is  $C_t=0.38$ . This value was obtained by Przulj (PhD Thesis in Preparation) by computer optimisation for a square cylinder. The prime difference between modelling a square and a circular cylinder is that for the square cylinder, the position of separation is fixed. For a circular cylinder, however, this position is not fixed, but depends on Reynolds number. It was therefore deemed necessary to carry out a parametric study in order to find the optimum value of  $C_t$  for a circular cylinder.

Two values of Reynolds numbers were chosen: 65,000, which is in the subcritical range, and  $5 \times 10^6$ , which is in the transcritical range. A grid of  $195 \times 98$  was used for these calculations. Figure 3.13 and Figure 3.14 show the variation of mean drag with different values of  $C_t$ , compared to experimental results by Schewe (1983).

Table 3.14 presents the predictions for  $Re=65,000$  and experimental results. Strouhal number is overpredicted for all values of  $C_t$ . The mean drag shows good results for values of  $C_t$  above and equal to 0.38. The rms drag is well predicted above  $C_t = 0.15$ , while rms lift is overpredicted above  $C_t = 0.15$ . Above  $C_t = 0.76$ , all parameters seem to be unchanged.

Table 3.15 details the results for  $Re=5 \times 10^6$  and experimental results of Schewe (1983) which are for  $Re=5.1 \times 10^6$ . The Strouhal number is again overpredicted for all values of  $C_t$ . Mean drag is now underpredicted, although the results flatten out for  $C_t \geq 0.38$ . No comparisons can be made of the predicted value of rms drag and lift, but their values seem to be constant above  $C_t = 0.15$ . This parametric study has shown that the results are not significantly improved by adopting a value of  $C_t$  different from 0.38, and therefore this value will be used throughout. Note the behaviour of the parameters when  $C_t$  is very small (0.15). This has the effect of suppressing vortex shedding. At small values, the unsteady modification is effectively turned off.

Similar results were obtained by Deng et al. (1994) for Reynolds numbers ranging from  $6 \times 10^3$  to  $3.6 \times 10^6$ , using the Baldwin-Lomax model and a  $(121 \times 115)$  grid, which is coarser than the present grid. Mean drag in the subcritical and transcritical regimes was overpredicted, while the drag crisis was not found. Their Strouhal number results seem independent of Reynolds number.

	St	$\bar{C}_D$	$\tilde{C}_D$	$\tilde{C}_L$
<b>Experiments:</b>				
Bearman & Trueman (1972)	0.123	2.190		
Sarpakaya & Ihrig (1986)	0.125	2.150		
Lee (1975)	0.126	2.050	0.180	1.320
Bearman & Obasaju (1982)	0.130			1.200
Lyn (1989)	0.135			
Durao et al. (1988)	0.138			
<b>Predictions:</b>				
Present (Standard k- $\epsilon$ )	0.137	1.745	0.194	0.381
Present (Modified k- $\epsilon$ )	0.132	2.104	0.291	1.321
Present (Kato & Launder)	0.136	2.098	0.103	1.393
Kato & Launder (1993)*	0.145	2.050	-	0.917
Bosch & Rodi (1996)*	0.146	2.108	-	1.463
Franke (1991)	0.136	2.150	-	-
Deng et al. (1994)	0.115	1.978	0.224	1.965

Table 3.12: Predicted and measured parameters for a square cylinder at  $Re=20,000$ .

\*Using Kato & Launder modification with wall function at  $Re=22,000$ .

Predictions	Grid	$\Delta t$
Present	136x118	$2.28 \times 10^{-3}$ *
Kato & Launder (1993)	104x70	Not Known
Bosch & Rodi (1996)	106x75	0.02*
Deng et al. (1994)	121x94	0.05

Table 3.13: Grid and time-step arrangements for predictions of square cylinder.

\*number is in the form  $\Delta t$ \*

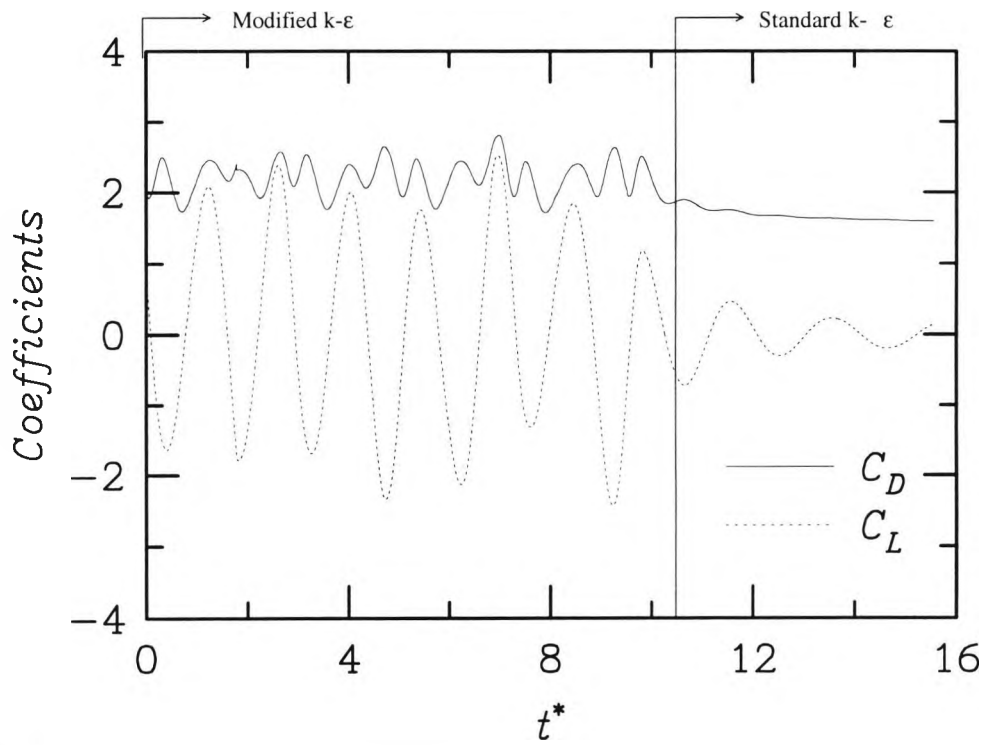


Figure 3.11: Predicted drag and lift coefficients with and without the  $k-\epsilon$  model modification for a square cylinder at  $Re=20,000$ .

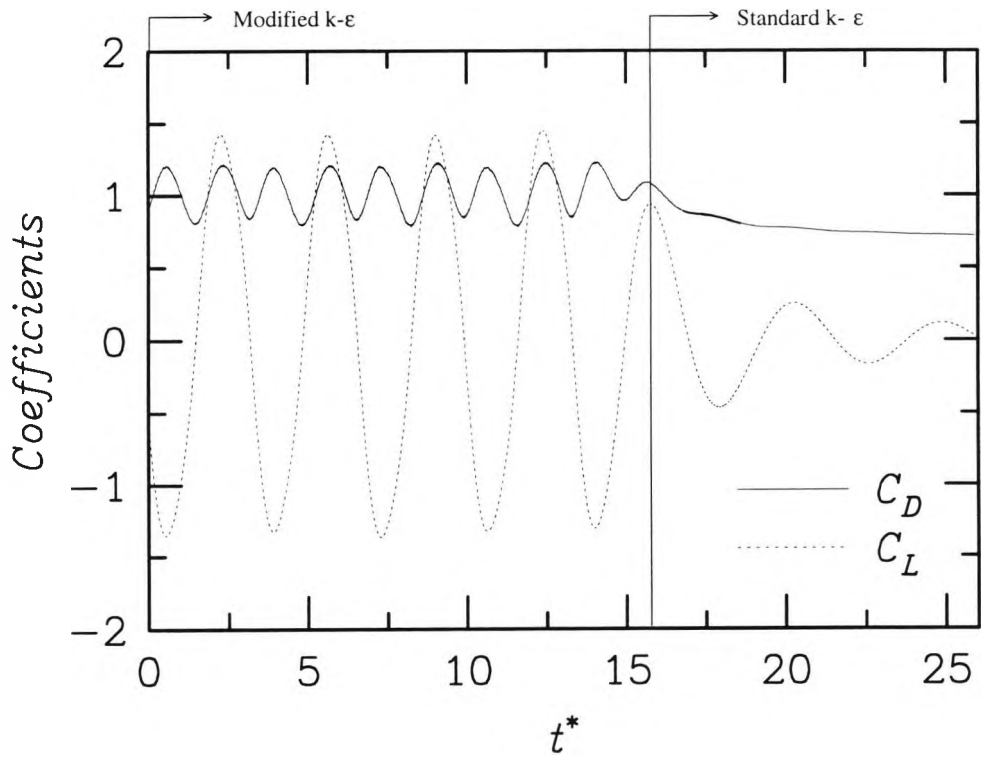


Figure 3.12: Predicted drag and lift coefficients with and without the  $k-\epsilon$  model modification for a circular cylinder at  $Re=65,000$ .

	Re	St	$\bar{C}_D$	$\tilde{C}_D$	$\tilde{C}_L$
<b>Experiments:</b>					
Schewe (1983)	62438	0.2004	1.222		0.338
Wieselberger (1923)	66205		1.223		
Sakamoto & Haniu (1994)	65000	0.2009	1.240	0.12	0.460
Lienhard (1966)	61094	0.1800 - 0.2010			
West & Apelt (1993)	59034				0.550
<b>Predictions:</b>					
Present (k- $\epsilon$ , $C_t=0.0$ )	65000	0.294	0.630	0.106	0.104
Present (k- $\epsilon$ , $C_t=0.15$ )	65000	0.292	0.834	0.118	0.205
Present (k- $\epsilon$ , $C_t=0.38$ )	65000	0.292	1.025	0.139	0.995
Present (k- $\epsilon$ , $C_t=0.76$ )	65000	0.298	1.083	0.158	1.022
Present (k- $\epsilon$ , $C_t=1.52$ )	65000	0.291	1.144	0.151	1.044
Deng et al. (1994)	65000	0.251	1.100	-	-

Table 3.14: Predicted and measured parameters for a circular cylinder at  $Re \approx 65,000$ .

	Re	St	$\bar{C}_D$	$\tilde{C}_D$	$\tilde{C}_L$
<b>Experiment:</b>					
Schewe (1983)	$5.1 \times 10^6$	0.254	0.526	-	0.047
<b>Predictions:</b>					
Present (k- $\epsilon$ , $C_t=0.0$ )	$5 \times 10^6$	0.371	0.100	$1.00 \times 10^{-2}$	0.200
Present (k- $\epsilon$ , $C_t=0.15$ )	$5 \times 10^6$	0.389	0.195	$1.75 \times 10^{-2}$	0.295
Present (k- $\epsilon$ , $C_t=0.38$ )	$5 \times 10^6$	0.375	0.216	$1.5 \times 10^{-2}$	0.306
Present (k- $\epsilon$ , $C_t=0.76$ )	$5 \times 10^6$	0.378	0.215	$1.65 \times 10^{-2}$	0.317
Present (k- $\epsilon$ , $C_t=1.52$ )	$5 \times 10^6$	0.391	0.200	$1.82 \times 10^{-2}$	0.387
Deng et al. (1994)	$3.6 \times 10^6$	0.255	0.800	-	-

Table 3.15: Predicted and measured parameters for a circular cylinder at  $Re \approx 5 \times 10^6$

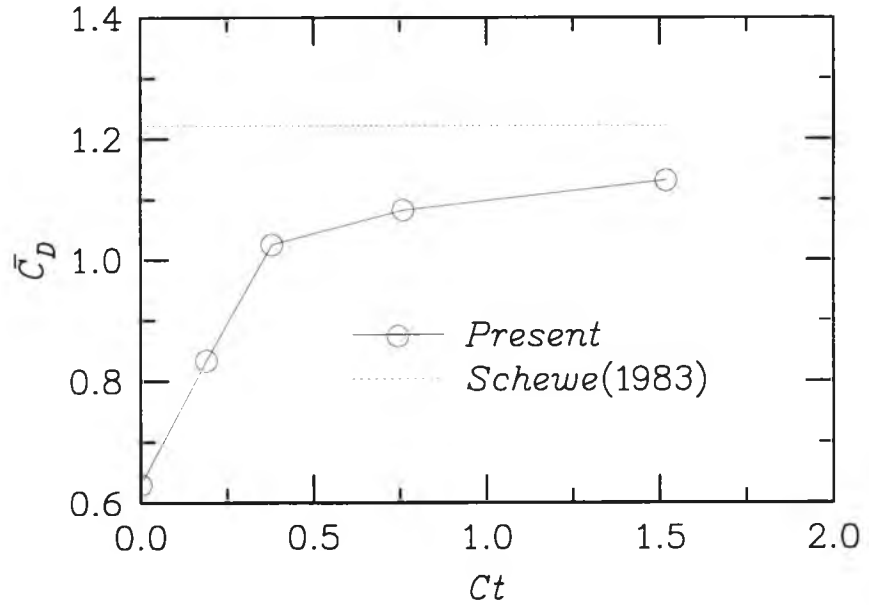


Figure 3.13: Parametric study of  $C_D$  coefficient for  $Re=65,000$ .

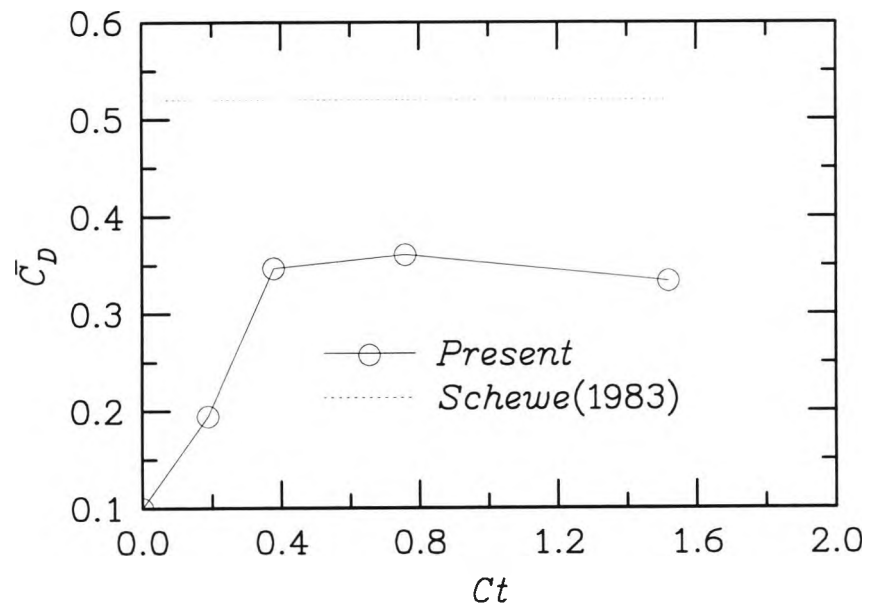


Figure 3.14: Parametric study of  $C_D$  coefficient for  $Re=5 \times 10^6$ .

### 3.8 Reynolds Number Dependence

The prediction of the dependence of the vortex shedding parameters on Reynolds number is shown in Figure 3.15 and Figure 3.16 where mean drag, and Strouhal number are plotted over a range of Reynolds numbers, for a circular and square cylinder. Figure 3.15 also shows the values of fluctuating lift over a range of Reynolds numbers for the circular cylinder. Also shown on the same figures are experimental results and other predictive methods.

For the square cylinder, the present simulations seem to be able to better capture the different regimes for the mean drag and the Strouhal number.

For a circular cylinder in the subcritical regime ( $Re < 1 \times 10^5$ ),  $\overline{C_D}$  and  $St$  are well predicted. From a Reynolds number of 20000 up to the transition region, mean drag is slightly underestimated, and Strouhal number slightly overestimated. Like other predictive methods (e.g. Franke and Rodi, 1991), the present method overestimates both  $C_D$  and  $St$  at high values of  $Re$  presumably because of three-dimensionality effects which could not be captured with a two-dimensional code.

Attempts were made to simulate the transition and the supercritical regimes with no success. The present simulations failed to capture the drag crisis. Deng et al. (1994) also failed to predict these regimes.

Full-scale data on the response of cylinders to transcritical flows are limited due to the problems encountered in producing high Reynolds numbers in the laboratory environment. On site experiments would not be feasible either due to difficulties in data acquisition.

Experimental results show that the mean drag becomes constant in the transcritical regime at around 0.5. Figure 3.15 shows that the measurements of Strouhal number are scattered in this regime. Predictions were performed for three Reynolds number in the transcritical regime. The results are presented in Table 3.16. The results for the first two show an underestimation of mean drag. Whilst the Strouhal number and  $\overline{C_L}$  are constant in predictions and overestimate the measurements of Schewe (1983) as can be seen in Figure 3.15. The separation point is estimated at around  $145^\circ$ , which conforms to experimental results. It can be seen from Table 3.16 that the time step was altered and shown not to affect the results. In addition, the standard k- $\epsilon$  model was used for

the case of  $Re=9 \times 10^6$ , where it produces suppression of the mean drag and fluctuating lift.

For  $Re=5 \times 10^7$  Reynolds number case, a very dense grid of  $479 \times 180$  was used, with the size of smallest cell next to cylinder set to 0.001 of the cylinder diameter, in order to keep  $y_+$  in the acceptable range. Due to the density of the grid, the results were very slow to obtain: approximately two weeks to obtain one cycle. The results show that mean drag is kept at 0.165 with the Strouhal number falling to 0.21, therefore vortex shedding is predicted to exist at this Reynolds number. Incidentally  $\tilde{C}_L$  drops considerably to 0.1, which is on the same level as the transcritical levels shown by experiments.

The significance of the  $Re=5 \times 10^7$  simulation is that it shows that the model used here does predict a constant mean drag between  $9 \times 10^6$  and  $5 \times 10^7$  (i.e. in the transcritical regime).

Re	Grid	$\Delta t^*$	$\bar{C}_D$	$\tilde{C}_L$	St
$5 \times 10^6$	195x98	$5.7 \times 10^{-3}$	0.216	0.306	0.375
$5 \times 10^6$	195x98	$2.85 \times 10^{-3}$	0.215	0.306	0.375
$9 \times 10^6$	195x98	$4.12 \times 10^{-3}$	0.172	0.260	0.375
$9 \times 10^6$	195x98	$2.06 \times 10^{-3}$	0.173	0.262	0.375
$9 \times 10^6^*$	195x98	$4.12 \times 10^{-3}$	0.119	$7.19 \times 10^{-2}$	0.437
$5 \times 10^7$	479x180	$1.1 \times 10^{-4}$	0.165	0.1	0.21

Table 3.16: Results a circular cylinder in the transcritical regime.

\*Predictions carried out with the standard  $k-\epsilon$  model



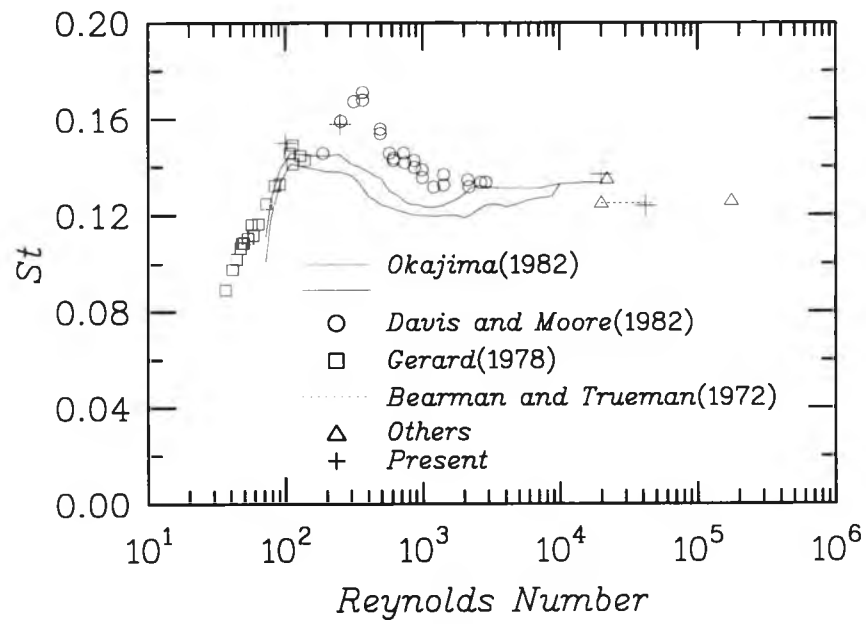
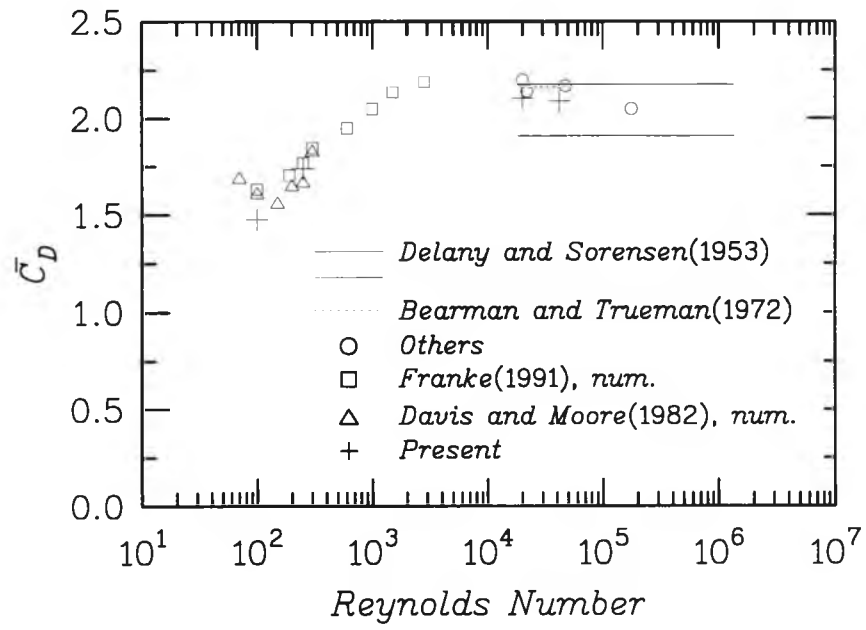


Figure 3.16: Variation of mean drag and Strouhal number with Reynolds number for a single square cylinder.

### 3.9 Conclusions

In this chapter, predictions were carried out for single circular and square cylinders over a range of Reynolds numbers. The results show that by using the modified  $k$ - $\epsilon$  model with the computational details described in this chapter, it is possible to obtain acceptable results for the main parameters characterising vortex shedding from single cylinders of circular and square shapes.

In all the cases studied, both  $C_D$  and  $C_L$  were predicted to vary smoothly with time and the frequency of  $C_D$  was predicted to be twice that of  $C_L$ , as expected. Streaklines were computed and found to present a view of the flow field which is in accord with published flow visualisations.

Grid and time-step dependence checks were carried out. It is shown that laminar flow calculations are independent of grid effects. The grid does have to be refined in order to capture the turbulent aspects of the flow when simulating at higher Reynolds numbers, with the cell size next to the cylinder small enough so that  $y_+$  is in the appropriate range. The results showed the insensitivity of the solutions to the time-step size, as long as the value of the latter is smaller than that required by the non-dimensionalised time step criteria set out in Section 2.11.

Predictions were obtained using the Upwind, Linear Upwind and SMART schemes for a square and circular cylinder at  $Re=100$ . The results showed that the third order bounded SMART scheme provides the most accurate results for a given grid and will be used henceforth.

The  $k$ - $\epsilon$  turbulence model was used when simulating Reynolds numbers higher than 1400. The Younis (1987) and Przulj & Younis (1993) modification, which accounts for the effects of periodicity on the turbulence spectrum was tested against the standard  $k$ - $\epsilon$  model and the Kato & Launder (1993) modification. It was found that the standard  $k$ - $\epsilon$  model underpredicts the strength of the shedding. For the square cylinder, the Younis (1987) and Przulj & Younis (1993) modification gave better results than the Kato & Launder (1993) model. For the circular cylinder, the Kato & Launder (1993) modification did not converge.

The value of the coefficient ( $C_1$ ) in the Younis (1987) and Przulj & Younis (1993) modification was investigated for a circular cylinder in subcritical and transcritical

regimes. A value of  $C_f=0.38$  presented the best results and will thus be used throughout the present work.

The flow over a circular cylinder goes through four distinct regimes depending on the Reynolds number. In the lower end of the subcritical regime, when the flow is fully laminar, mean drag and Strouhal number are predicted accurately. At higher values, above  $Re=20000$ , the present method underestimates the mean drag and overestimates the Strouhal number. The present method also fails to capture the drag crisis and the supercritical regime. The transcritical regime was investigated. It was found that the mean drag is underestimated and the fluctuating lift and Strouhal number overestimated with respect to the data of Schewe (1983). The predicted mean drag remains constant at  $Re=5 \times 10^7$ , while the fluctuating lift and Strouhal number fall significantly.

# CHAPTER FOUR: APPLICATION TO TWO CIRCULAR CYLINDERS IN TANDEM

## 4.1 Introductory Remarks

While numerous investigations have been made of the flow past single obstacles of various shapes, few studies have been made of the wake interference and the vortex shedding processes associated with complex configurations consisting of multiple obstacles. When two similar bluff bodies are sufficiently apart, they behave in a similar or even identical manner to a single bluff body in isolation. However, when the two bodies are at close proximity to each other, the integral parameters such as the drag and lift forces, the shedding frequency and the vortex-shedding patterns are considerably different from the case of a single body. This is because their wakes interfere in a complex manner, depending on the arrangement of the bodies and the spacing between them.

There has been some previous experimental and numerical work on the case of two cylinders in tandem and a review of that is presented in Sections 4.2 and 4.3.

The changes to the drag caused on the downstream cylinder is of importance when considering suppression techniques, as the drag may be increased or reduced, depending on the spacing between the cylinders. This chapter presents numerical results for this phenomenon in the laminar and turbulent regimes.

The computational details are presented in Section 4.4. The laminar flow simulations are given in Section 4.5 and the turbulent flow simulations in Section 4.6.

## 4.2 Review of Experimental Results

There exist critical values of the spacing between cylinders arranged in tandem, where the flow patterns abruptly change over, producing different aerodynamic characteristics. These critical spacings are thought to have a close relation with the size of the vortex formation region.

Bierman and Hernstein (1933) measured the drag forces on struts (with circular and aerofoil sections) arranged in tandem at Reynolds numbers of  $0.6 \times 10^5$  to  $1.6 \times 10^5$ . A new parameter was introduced to compare the drag coefficient of the cylinder in question with the drag of a single cylinder in isolation. This is called the Interference Drag ( $C_{Di}$ ), defined as:

$$C_{Di} = C_D \text{ for cylinder} - C_D \text{ for single cylinder} \quad (4.1)$$

The data for two circular cylinders up to 9 diameters apart are reproduced in Figure 4.1. The Figure shows that the drag of the downstream cylinder is decreased in the presence of the upstream cylinder, while the drag of the upstream cylinder is not greatly affected by this interaction. For spacings less than 3 diameters, the downstream cylinder experiences a thrust (i.e. negative drag) and the net drag on both cylinders is less than that of a single cylinder. For spacings between 3 to 4 diameters, the drag of the downstream cylinder rapidly increases with increase in spacing. The magnitude of the interference does not change for spacings greater than around 4 diameters.

The portion of the curve where a dip in the interference drag coefficient ( $C_{Di}$ ) occurs represents the critical spacing. Its value cannot be determined accurately, but seems to be about 3 to 3.5 diameters.

Curve C in Figure 4.1 represents the combined interference drag coefficient. This is defined as  $C_{Di}$  of the upstream cylinder plus  $C_{Di}$  of the downstream cylinder. This quantity appears to be negative for all spacing which means that the overall drag of cylinders in tandem is less than twice the value of the drag for a single cylinder.

Hori (1959) measured the vortex shedding frequency, the surface pressure distribution and the wake velocity behind two cylinders in tandem. He observed that the interference of the two cylinders was strong and dependent on Reynolds number, even at large spacings. Furthermore, he found that a thrust acted on the downstream cylinder for small spacing distances.

Thomas and Kraus (1964) observed vortex street eddies shed from two cylinders at low Reynolds numbers ( $Re = 62$  to  $500$ ) by a smoke visualisation technique.

Strouhal frequencies for two cylinders in tandem were measured by Oka et al. (1972) and Jendrzejczyk and Chen (1986). In general, the vortex shedding frequencies behind

the two cylinders were found to be different. No distinct vortex shedding frequency was found behind the upstream cylinders up to  $P/D = 3.8$ . For separations greater than 3.8, the vortex shedding frequency reached the value for an isolated cylinder. Vortex shedding was observed for the whole range of spacings behind the downstream cylinder. It decreased with  $P/D$  in the range  $1 < P/D < 3.8$ , then jumped to higher values at  $P/D \approx 3.8$ , which is the same spacing at which the vortex shedding appeared behind the upstream cylinder.

Zdravkovich (1977) compiled drag coefficients for various Reynolds numbers. He showed a jump in the drag coefficient for the upstream cylinder at  $P/D$  between 3 and 4. Regardless of the Reynolds number, the drag coefficient reached the value for a single cylinder once the spacing was larger than the critical  $P/D$ . The downstream cylinder showed a stronger dependence on the Reynolds number.

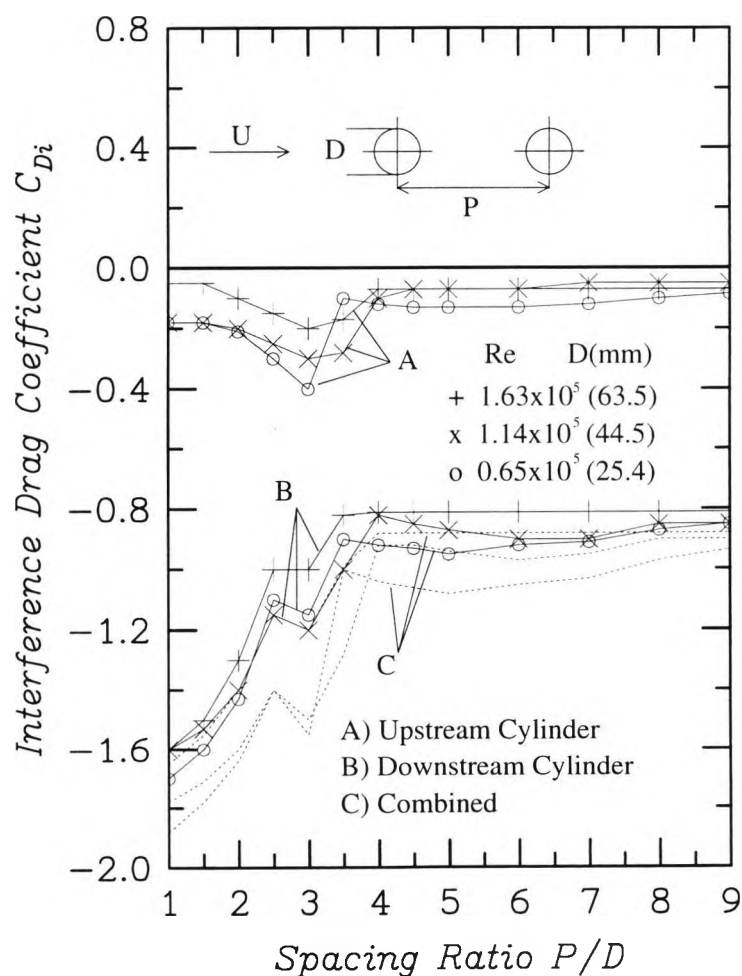


Figure 4.1: Interference Drag Coefficient for two cylinders in tandem (data from Bierman and Hernstein (1933)).

The flow around two cylinders in tandem may be characterised by two distinct regimes depending on the critical spacing. For spacings up to the critical range of  $P/D$ , the vortex street is suppressed behind the upstream cylinder. Beyond this critical spacing range, vortex streets may be formed from both cylinders. Igarashi (1981) examined the flow structure around two cylinders in detail and subdivided the first regime into four flow patterns. From his results, Zdravkovich (1985) showed schematic flow patterns as shown in Figure 4.2. The subdivisions are as follows:

- a) When the spacing is very small, less than 1.1, the two cylinders behave as a single slender body with a high Strouhal number. The region between the two cylinders is stagnant and the shear layers separated from the upstream cylinder cannot reattach on the downstream one and a vortex street is formed only behind the downstream one.
- b) When the spacing is between  $1.1 < P/D < 1.6$  an alternate reattachment of the shear layers takes place on the front side of the downstream cylinder in the frequency of the vortex shedding of the latter.
- c) When the spacing is between  $1.6 < P/D < 2.4$  quasi-steady reattachment of separated shear layers is observed on the downstream cylinder.
- d) When the spacing is between  $2.5 < P/D < 3.4$ , occasionally one of the reattachment points is disrupted, but there is no regular vortex shedding behind the upstream cylinder yet.
- e) A bistable range exists around the critical spacing where the vortex shedding behind the upstream cylinder persists for some time and then is intermittently suppressed and replaced by the reattachment flow regime.
- f) Beyond  $P/D = 3.8$ , which is over the critical spacing, the separated shear layers from the upstream cylinder roll up alternately and form vortices behind the cylinder. Two vortex streets are synchronistically formed behind the two cylinders. Further, for large values of the spacing, over  $P/D = 5$ , drag coefficient of only the downstream cylinder is affected.

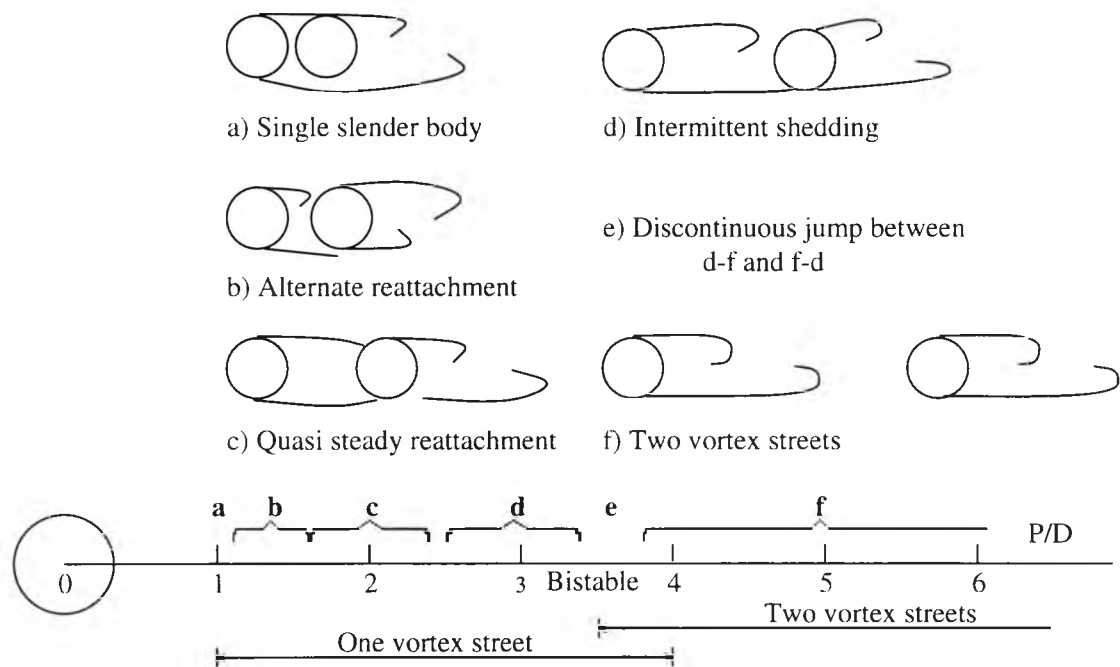


Figure 4.2: Classification of regimes for two circular cylinders in tandem.

### 4.3 Review of Previous Predictions

Li et al. (1991) used a Crank-Nicolson finite element method to simulate the flow past two circular cylinders in tandem. At  $Re=100$ , a perturbation was applied in order to make the field asymmetric and hasten the occurrence of vortex shedding. For small spacings ( $P/D < 3$ ), the vortex street formed behind the downstream cylinder only. Parameters such as the drag, the lift, and the Strouhal number were found to be lower than experimental data, mainly because of the use of a coarse grid. Ren and Blachen (1993) investigated laminar flow past two cylinders in tandem, again using the finite element method. This was done for  $Re=250$  and  $P/D=2$  and  $5$ . Their results show only the flow patterns around the cylinders. Values of the drag and lift coefficients, and the Strouhal number were not given.

Stansby and Slaouti (1991) applied a random vortex method to two-dimensional laminar flow around two cylinders arranged in transverse and in tandem at  $Re=200$ . Qualitative and quantitative results were obtained and the well known result that, below the critical spacing, the combined drag is less than twice the drag on a single cylinder, was reproduced. They found the critical spacing between  $3.4 < P/D < 3.8$ . They also found a thrust acting on the downstream cylinder up to  $P/D=3.0$ .

Jing et al. (1992) studied the oscillations of a cylinder in the wake of an upstream cylinder using Direct Numerical Simulation (DNS). They found that at small cylinder spacings, the shear layers separating from the upstream cylinder reattached to the downstream one. As a consequence, the formation of vortex street between the two cylinders was inhibited. This is referred to as the 'vortex suppression' regime. At large spacings, the vortex street behind the upstream cylinder has sufficient room to develop. The intensity of the transverse oscillations becomes stronger thus, leading to an even stronger vortex street behind the downstream cylinder. This is referred to as the 'vortex formation' regime.

Sun et al. (1993) applied a finite element method to investigate the flow regimes and frequency of vortex shedding of two circular cylinders in tandem. They found the critical spacing, where flow changes from the 'vortex suppression' regime to the 'vortex formation' regime, to be around  $P/D \approx 3.7$  for  $Re=80$  and  $P/D \approx 3.0$  for  $Re=100$ . They found the circumferential pressure profiles of the downstream cylinder as well as drag and lift coefficient variations on both cylinders with respect to cylinder spacings.

#### 4.4 Computational Details

The same grid generation program used for the single cylinder is used here to generate grids with two cylinders in tandem. This is done by introducing a new subdomain in the grid and repeating the same process for the downstream cylinder as that for the upstream cylinder. A limitation of this method is that the diameter of the downstream cylinder has to be the same as that of the upstream cylinder. Two new parameters are introduced in the input to the grid generation program to determine the position of the downstream cylinder and the grid density between the cylinders:

- XCIL Distance between the centres of the two cylinders.
- XGAP Expansion in the x-direction for the region in between the two cylinders.

Figure 4.3 defines the boundaries and quantities used in generating grids for two cylinders. Figure 4.4, 4.5, and 4.5 show examples of grids used in the present work.

The flow solver is modified so that the distances of the near boundary nodes from the east and west of the obstacle boundary are stored for the downstream cylinder. The north and south boundary node distances are taken from the upstream cylinder. These are then used in the flow solver to specify the boundary conditions for the  $u$ ,  $v$ ,  $k$  and

$\epsilon$  equations for both cylinders. The subroutine that determines the lift and drag coefficients is also modified to account for the presence of two cylinders.

The SMART scheme is used throughout the simulations. The non-dimensionalised time step ( $\Delta t^*$ ) was set at the minimum required to obtain convergence with 3-4 iterations, with no under-relaxation. No time-step dependence checks were conducted as it was shown in Section 3.5 that the solutions are fairly independent of this parameter.

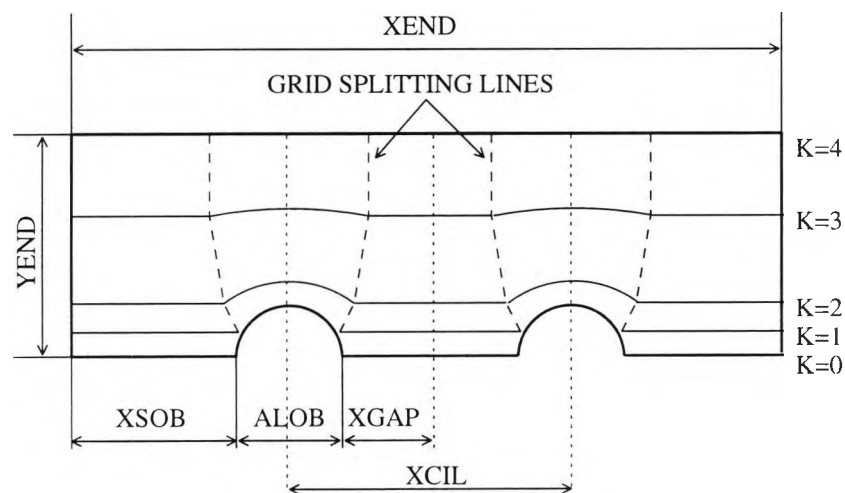


Figure 4.3: Definitions of quantities involved in generating grids.

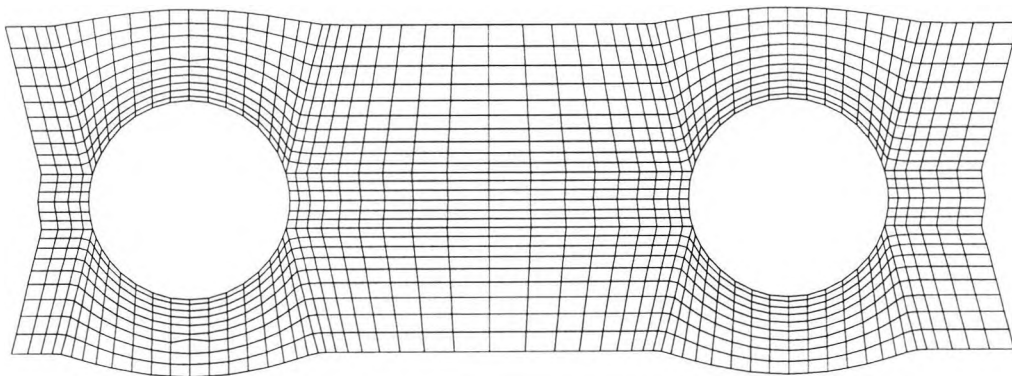
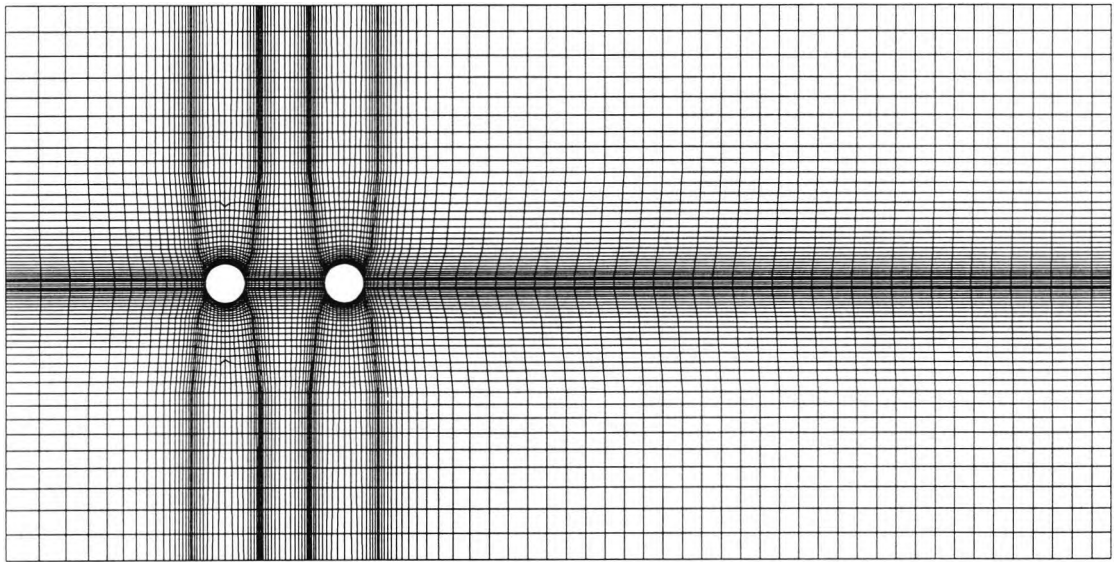
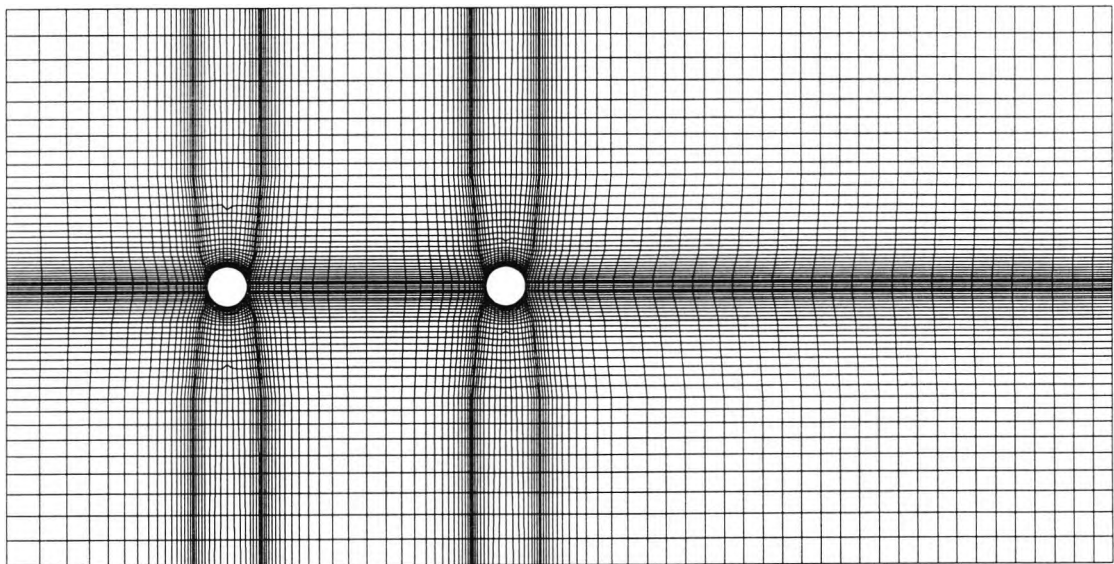


Figure 4.4: The area around the two cylinders, with a separation of three diameters.



*Figure 4.5: A grid of 115x78 used for two cylinders in tandem at three diameters spacing.*



*Figure 4.6: A grid of 111x66 used for two cylinders in tandem at seven diameters spacing.*

## 4.5 Laminar Flow Simulations

Two geometries were investigated in the laminar flow regime for  $P/D=3$  and 7. Two values of Reynolds number were used:  $Re=100$  and 300. For the case of  $P/D=3$ , a grid of  $115 \times 78$  (Figure 4.5) was used. For the case of  $P/D=7$ , a grid of  $111 \times 66$  (Figure 4.6) was used. The time step was fixed at a value corresponding to  $\Delta t^* = 3.42 \times 10^{-3}$ . The SMART scheme was used throughout the simulations.

Time histories for the drag and lift coefficients are shown in Figure 4.7 and Figure 4.9, for  $P/D=3$  and 7, respectively. The streaklines for  $P/D=3$  and 7 at  $Re=300$  are shown in Figure 4.8 and Figure 4.10, respectively.

It is evident from the streaklines that a separation of  $P/D=3$  (Figure 4.8) confirms the existence of the 'vortex suppression' regime, where the vortices do not have enough room to grow, develop, and shed in between the two cylinders. Since the downstream cylinder is in the attached vortex region of the upstream cylinder, its equivalent 'free-stream' velocity is weaker. This leads to an even weaker wake behind it.

When the spacing between the two cylinders is sufficiently greater than the critical value, the 'vortex formation' regime appears and vortex streets form behind both cylinders. This can be seen from the streaklines of  $P/D=7$  (Figure 4.10).

These findings are in agreement with the computational results of Jing et al. (1992), who also found the 'vortex suppression' and 'vortex formation' regimes.

The mean drag, and the rms of the lift coefficients of the upstream and downstream cylinders were calculated and compared with the numerical results of Sun et al. (1993) at  $Re=100$ . The results for the mean drag are shown in Figure 4.11(a) at  $Re=100$ . Figure 4.11(b) shows the results at  $Re=300$ , for which no other experimental or numerical results were available. Also included there are the present numerical results for a single cylinders at these Reynolds numbers.

It can be seen that the present results follow the same trends as those of Sun et al. (1993). The mean drag of the upstream cylinder is less influenced by the change of the flow regime, since the incoming flow remains unchanged.

The mean drag of the downstream cylinder at  $P/D=3$  is very small, consistent with the presence of the 'vortex suppression' regime. This quantity can even become negative,

as in the case of  $Re=300$ . This happens on the downstream cylinder when the pressure at the base is higher than its value at the stagnation point, so that its drag coefficient may be negative. This result was also obtained by Sun et al. (1993) and Stansby and Slaouti (1991).

At the larger separation of  $P/D=7$  (Figure 4.11), the mean drag coefficient on the upstream cylinder reverts to levels appropriate to an isolated cylinder at the same Reynolds number. The effects of the wake interaction on the downstream cylinder, on the other hand, are quite profound. From the results it is obvious that the downstream cylinder experiences a 'shielding' effect evidenced by the marked reduction in the mean value of its drag coefficient.

The results for the rms lift coefficient are shown in Figure 4.12(a) for  $Re=100$  and Figure 4.12(b) for  $Re=300$ . The rms lift coefficients of both cylinders jump from almost zero, at  $P/D<3$  to a large value approaching that of a single cylinder. At the larger separation of  $P/D=7$ , the 'shielding' effect does not extend to the rms lift, which shows a marked increase for the downstream cylinder.

The vortex shedding frequency of the upstream and downstream cylinders were also calculated, thus establishing the Strouhal number of each cylinder. This was then compared to the Strouhal number for a single cylinder at the same Reynolds number. Figure 4.13 shows the ratio of the Strouhal number of each cylinder to that of a single isolated cylinder. Also included in the figure are the numerical results of Li et al. (1991) at  $Re=100$ . The present results are generally in close agreement with the previous numerical results.

At the separation of  $P/D=3$ , the Strouhal number of the upstream cylinder is at its minimum, since a distinct vortex street does not exist between the cylinders.

At the larger spacing of  $P/D=7$ , the occurrence of vortex shedding between the two cylinders creates oscillatory oncoming flow in front of the downstream cylinder, and in turn this leads to a stronger oscillatory flow behind it. The vortex street between the two cylinders develops more freely (and is stronger) than at smaller spacings. The value of the Strouhal number approaches that of an isolated cylinder.

It is also clear from Figure 4.11 that the combined drag on the two cylinders is always less than twice the drag of an isolated cylinder.

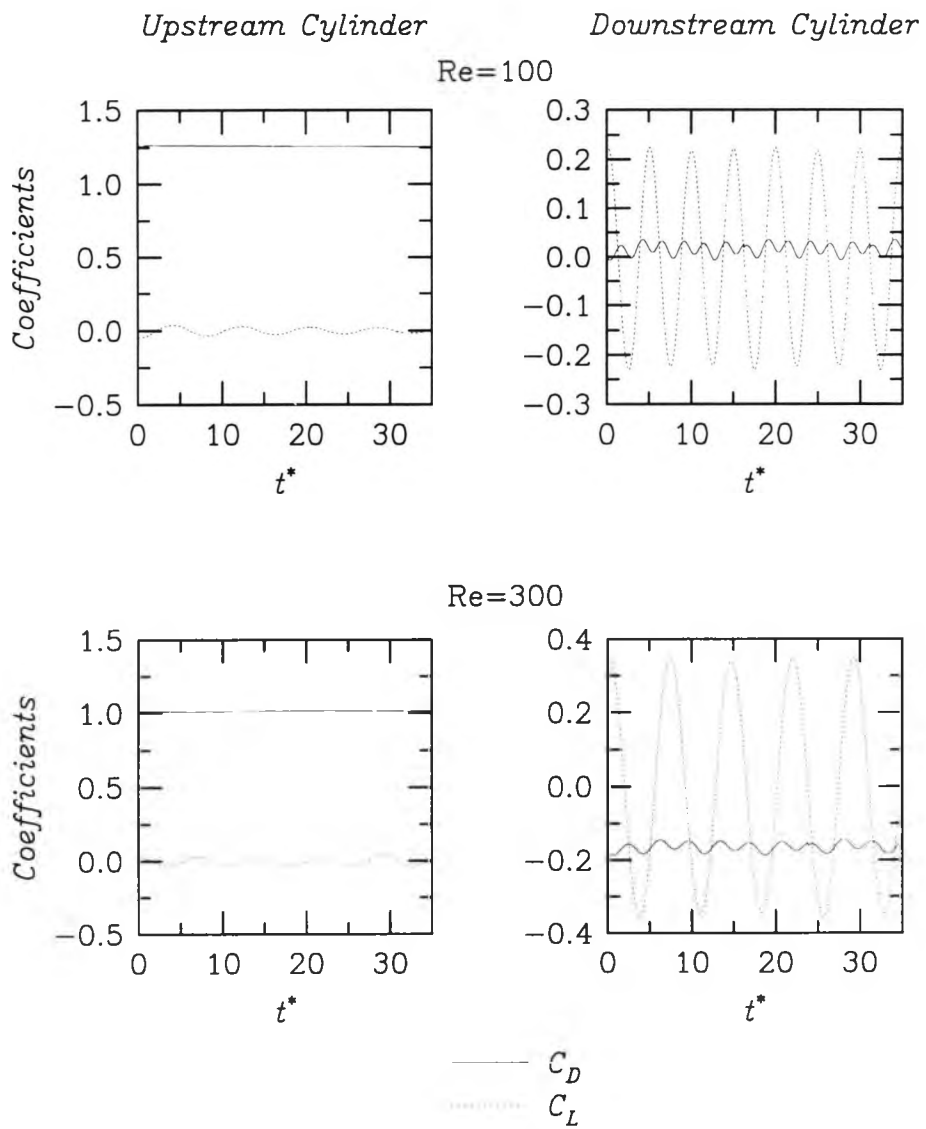


Figure 4.7: Time histories for drag and lift coefficient of two circular cylinders in tandem at  $P/D=3$  at  $Re=100$  and  $300$ .

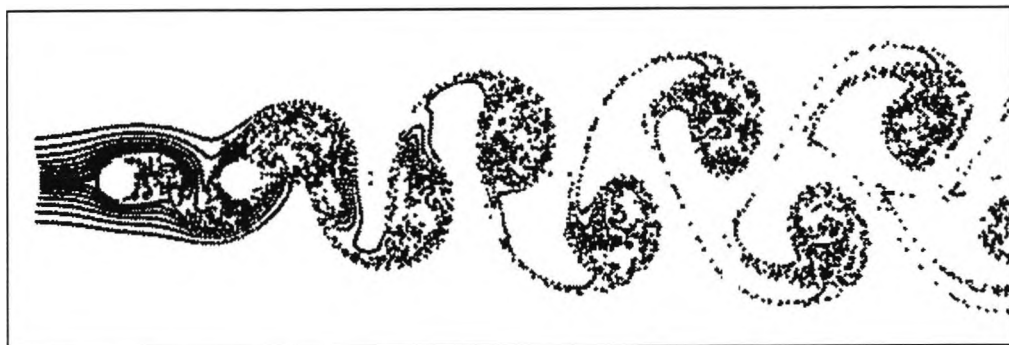


Figure 4.8: Streaklines for two cylinders in tandem at  $P/D=3$  with  $Re=300$ .

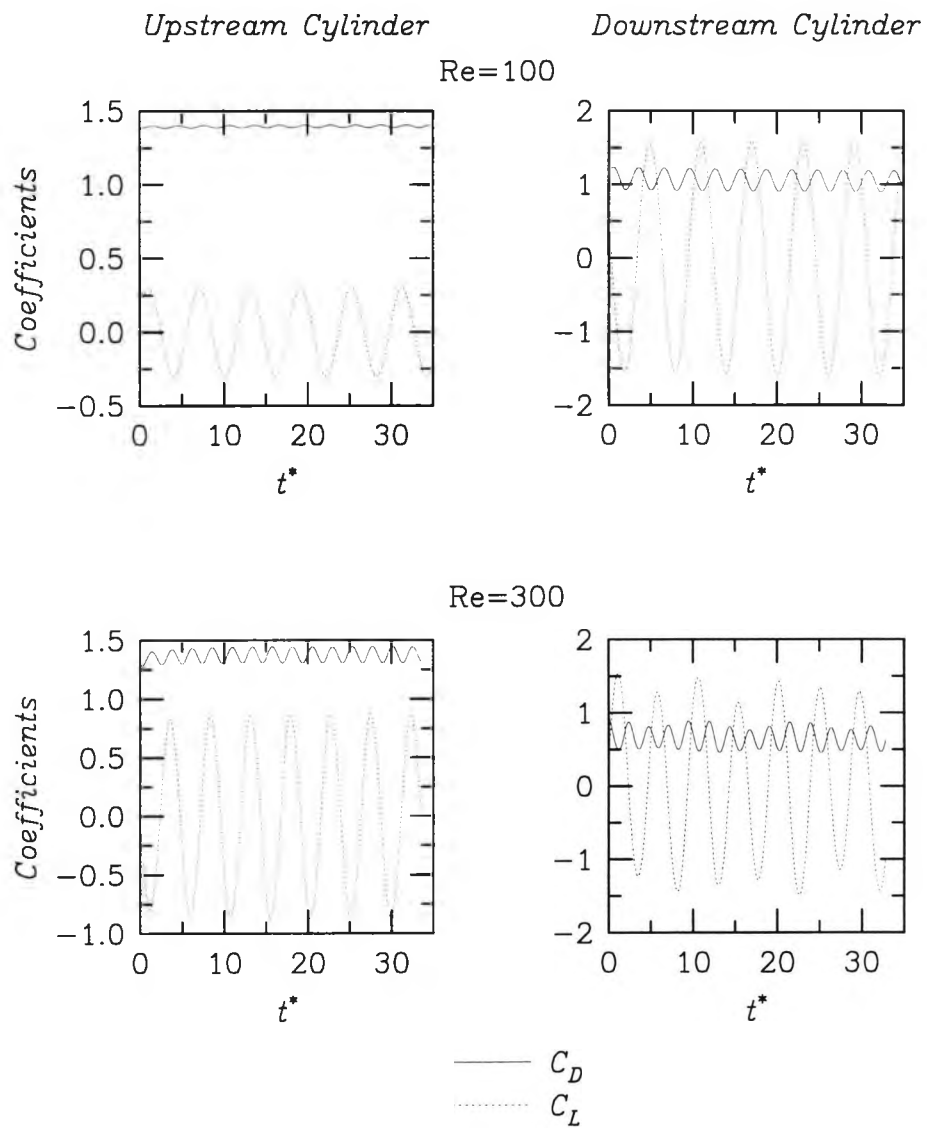


Figure 4.9: Time histories for drag and lift coefficient of two circular cylinders in tandem at  $P/D=7$  at  $Re=100$  and  $300$ .

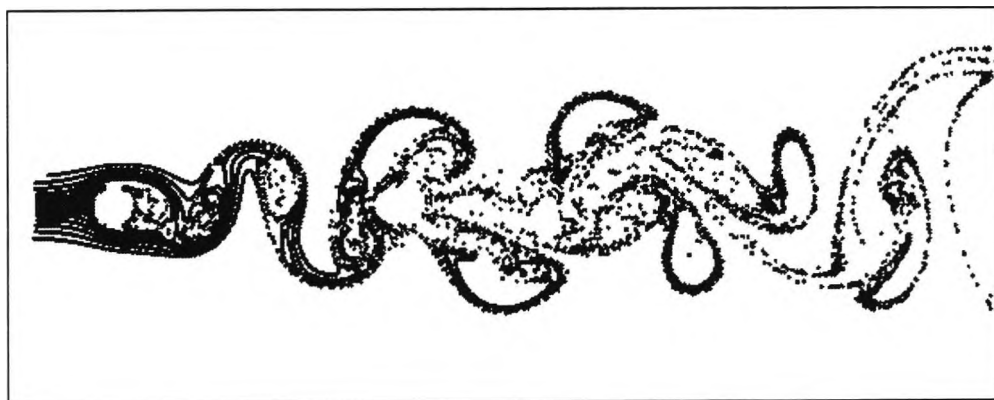


Figure 4.10: Streaklines for two cylinders in tandem at  $P/D=7$  with  $Re=300$ .

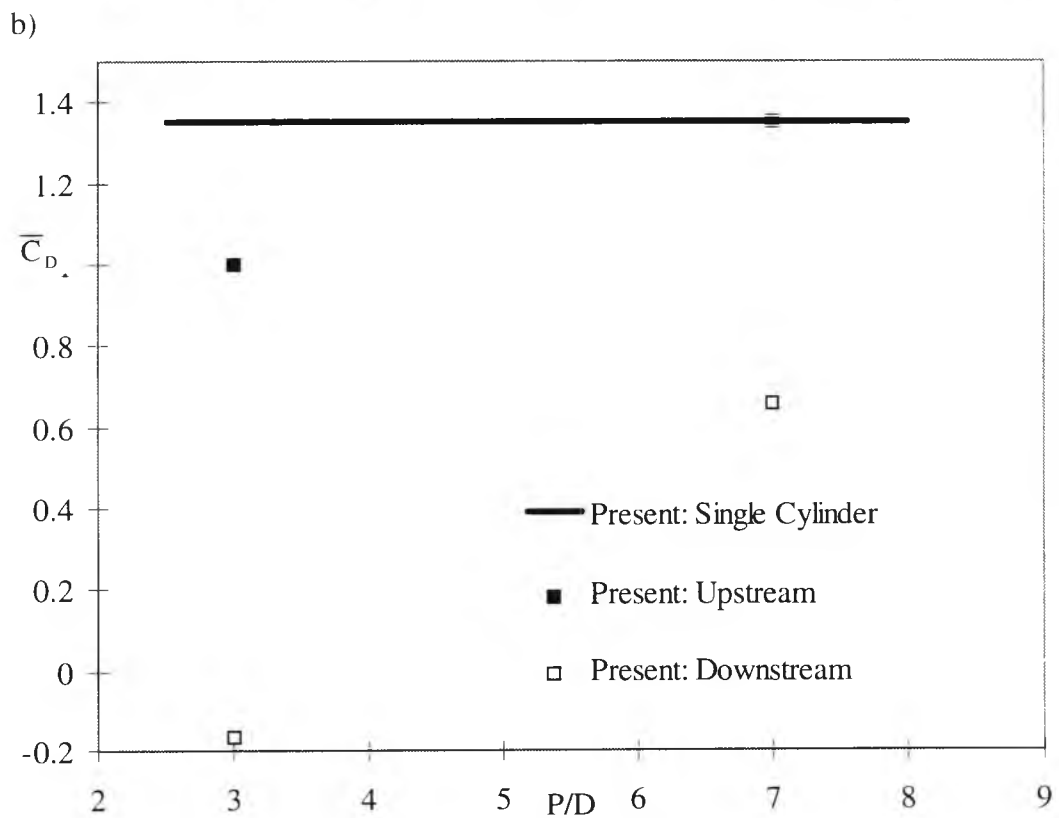
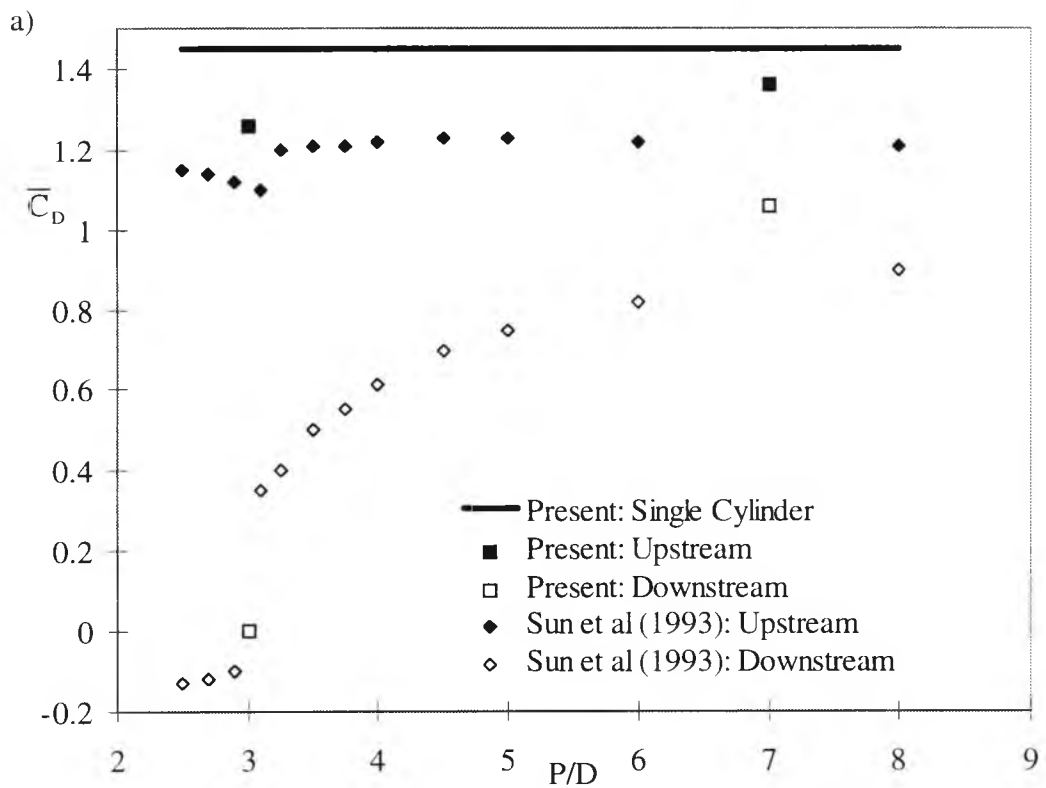
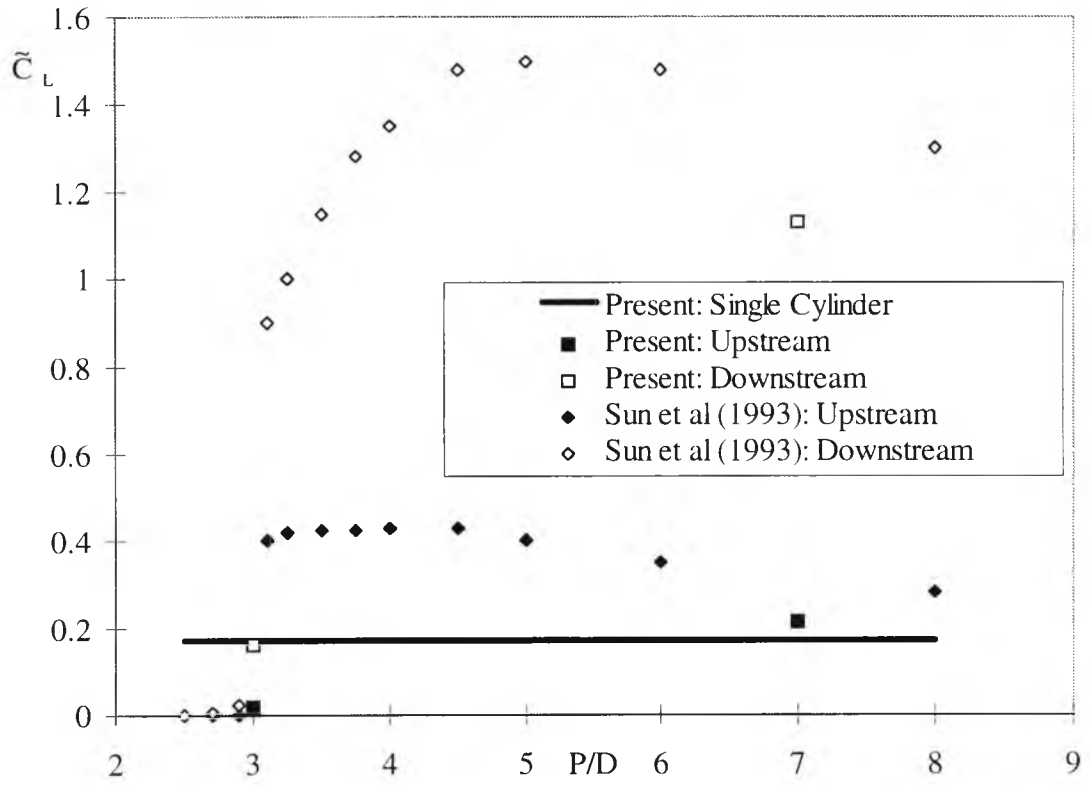


Figure 4.11: Mean drag coefficient for different cylinder spacing ( $P/D$ ) at  
 a)  $Re=100$  and b)  $Re=300$ .

a)



b)

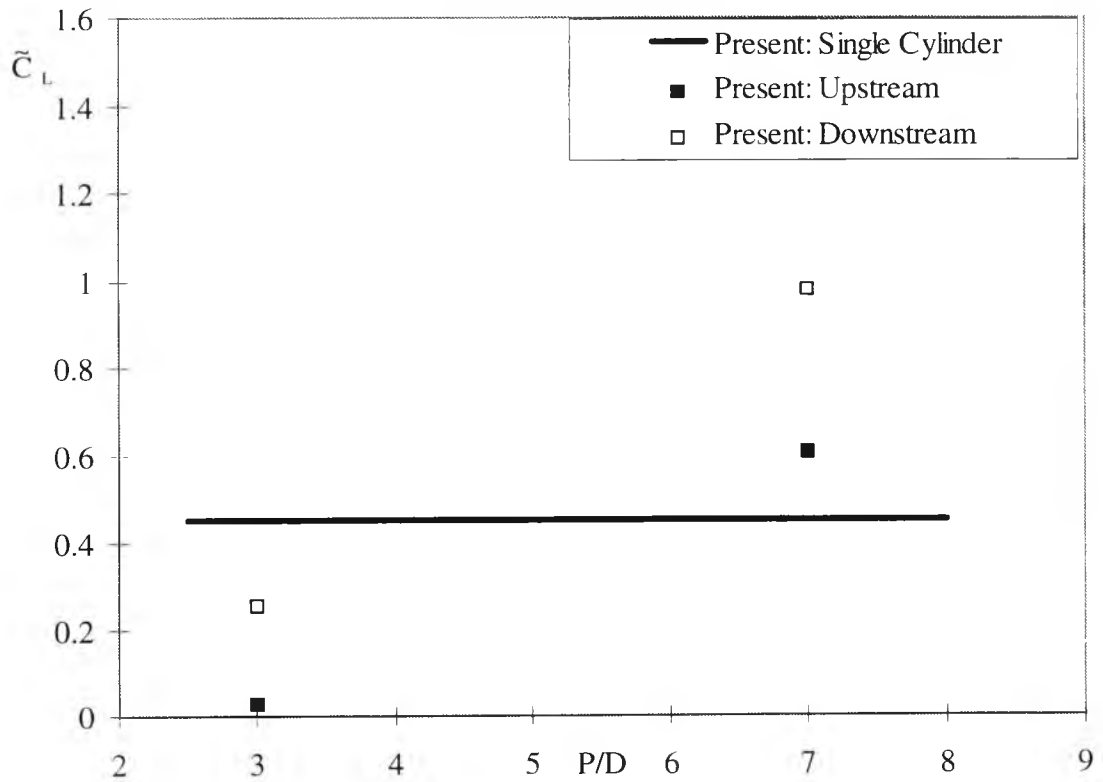
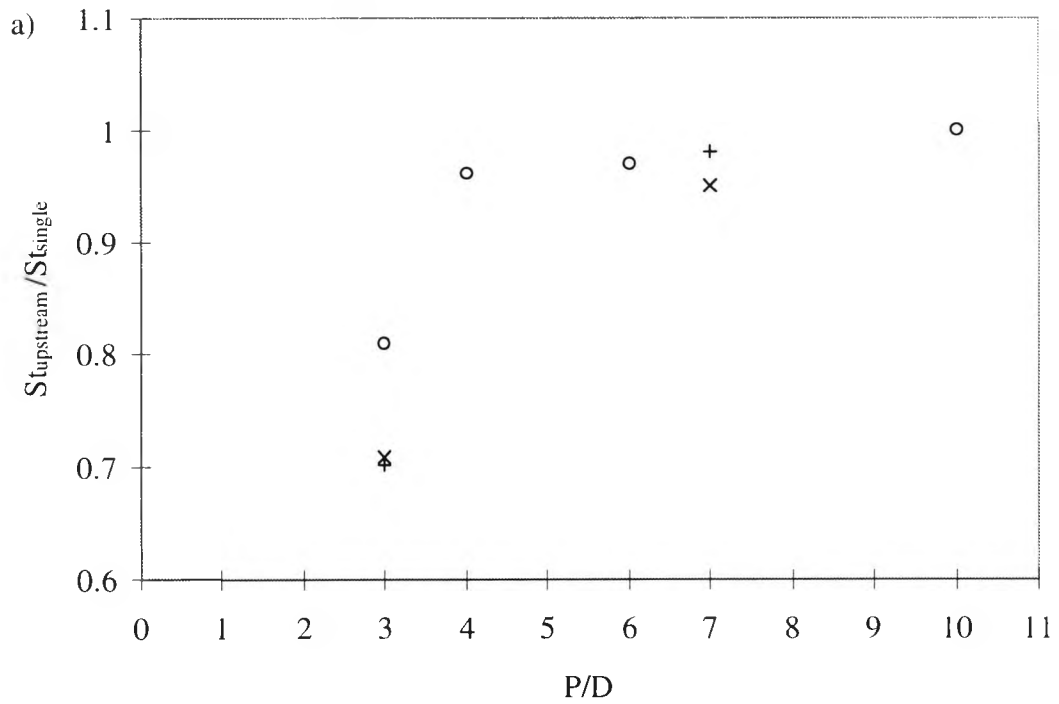


Figure 4.12: RMS lift coefficient for different cylinder spacing ( $P/D$ ) at  
a)  $Re=100$  and b)  $Re=300$ .



× Present Calculations (Re=100)      + Present Calculations (Re=300)  
 o Calculations of Li et al. (1991); Re=100

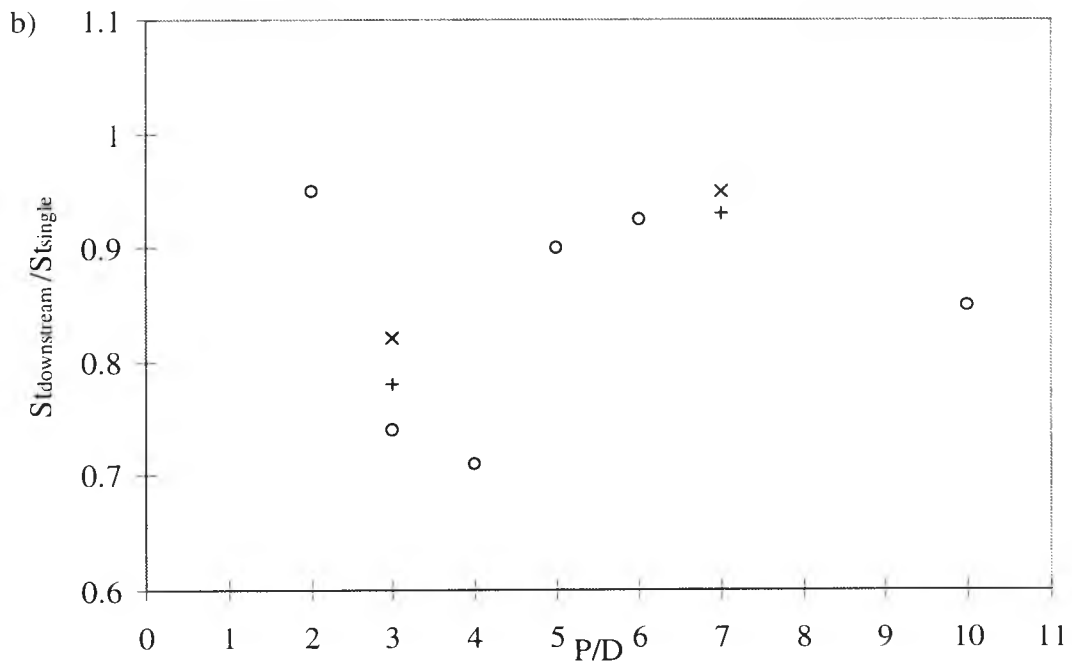
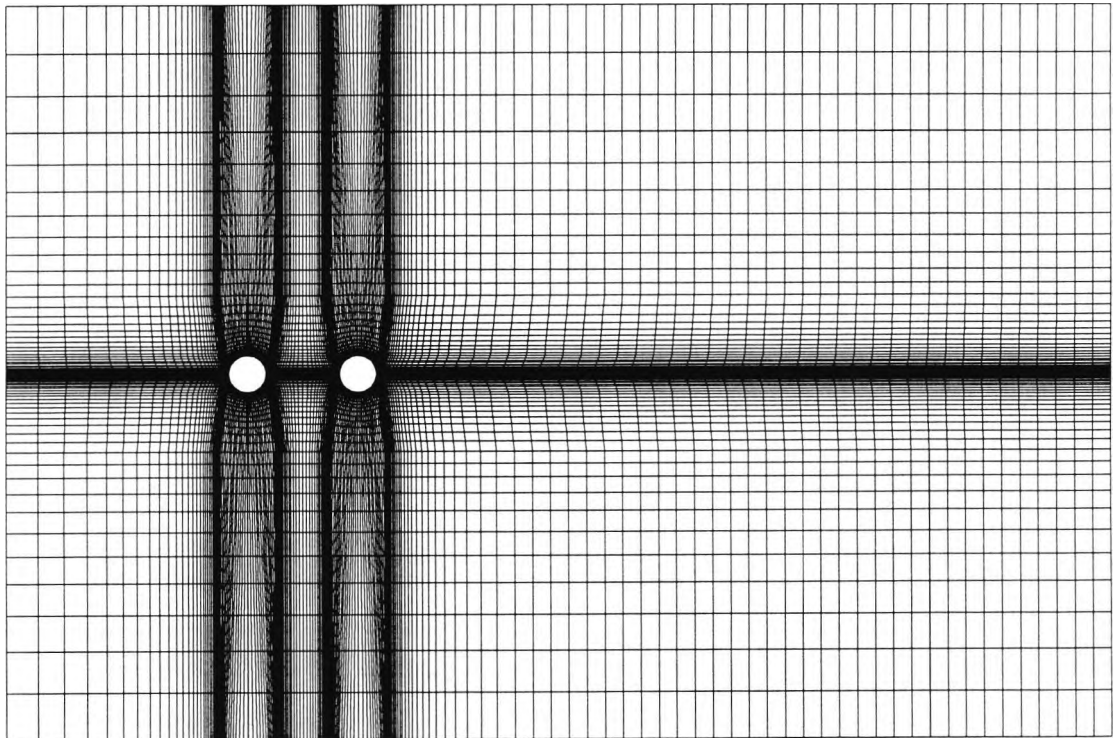


Figure 4.13: Strouhal number ratio for different cylinder spacing ( $P/D$ ) for the  
 a) Upstream cylinder and b) Downstream cylinder.

## 4.6 Turbulent Flow Simulations

Bierman and Hernstein (1933) conducted experiments to determine the critical value of spacing in turbulent flow conditions. In this section, their data are used to check calculations performed for a Reynolds number of  $6.5 \times 10^4$ . This Reynolds number was chosen because it coincides with the value appropriate to the investigations of Sakamoto and Haniu (1994) for the suppression of vortex shedding using a control cylinder (see Chapter 5).

There is no need to make further modifications to the code except for introducing the boundary conditions for  $k$  and  $\epsilon$  on the downstream cylinder. The grid used was finer than for the laminar calculations in order to capture the turbulent boundary layer. Figure 4.14 shows a  $191 \times 72$  grid used in the present simulations of the  $P/D=3$  conditions.



*Figure 4.14: Grid used for turbulent flow simulations of two cylinder in at  $P/D=3$ .*

Spacing Ratio (P/D)	Grid Size
1.35	178x72
2	178x72
2.5	187x72
3	195x72
4	200x72
5	235x72
6	250x72
7	275x72

*Table 4.1: Grid arrangements for two cylinders in tandem in turbulent flow.*

Eight values of P/D were investigated, each with a different grid. Table 4.1 shows the grid sizes for each spacing ratio. As can be seen, the larger the distance between the cylinders, the more grid nodes were used in the x-direction. The number of grid nodes in the y-direction was unchanged. The non-dimensionalised time step ( $\Delta t^*$ ) was set equal to  $1 \times 10^{-3}$  throughout the computations. The SMART scheme was used.

The computations were carried out with the Younis (1987) and Przulj & Younis (1993) k- $\epsilon$  turbulence model modification discussed in Chapters 2 and 3. In order to investigate its validity for two cylinders in tandem, the RUN with P/D=5 was performed with and without the modification. The time histories of the drag and lift coefficients are shown in Figure 4.15. The modification was removed at  $t^*=10.25$ . There is a reduction in mean and fluctuating drag and fluctuating lift associated with the use of the standard k- $\epsilon$  model. It is obvious that the use of the standard k- $\epsilon$  model causes the vortex shedding to be drastically suppressed as was the case for single cylinder. Therefore, the present modification was used throughout the computations. It is important to note that even though the drag coefficient for the downstream cylinder is very small, its mean does not equal zero.

The present predictions of the interference drag coefficient and the mean drag are compared with the measurements of Biermann and Herrnstein (1933) in Figure 4.16 (a) and (b).

The jumps in both the interference drag and the mean drag are captured by the present predictions. The critical spacing ratio is predicted to be in the range  $2.5 < P/D < 4$ , which is in accordance with the data. Once the spacing ratio is larger than the critical value, the drag coefficient increases monotonically to the value for a single cylinder. It

is worth noting that even at high values of  $P/D$ , the sum of the drag on the cylinders (about 1.05) is less than twice the predicted value for a single cylinder (about 2.05).

The vortex shedding frequency of the upstream and downstream cylinders were also calculated, thus establishing the Strouhal number of each cylinder. This was then compared to the Strouhal number for a single cylinder at the same Reynolds number. Figure 4.17 shows the ratio of the Strouhal number of each cylinder to that of a single isolated cylinder. Also included in the figure are the experimental data of Oka et al. (1972) at  $Re=51,000$  and Jendrzejczyk & Chen (1986) at  $Re=65,000$ . The present results are in good agreement with the experimental data, and show the same behaviour of the Strouhal ratio for both upstream and downstream cylinders with respect to the  $P/D$  value.

The power spectra of the lift for  $P/D < 2.5$  show that no distinct vortex shedding frequency was found behind the upstream cylinder. When the interval was greater than this value, a distinct vortex shedding frequency was attainable behind the upstream cylinder and its frequency gradually approached its limiting value corresponding to the case of a single cylinder.

Vortex shedding was shown to exist behind the downstream cylinder for the whole range of  $P/D$  values. Below the critical value, the Strouhal number decreased continuously to its minimum level: the two cylinders then behave as a single slender body, with a prominent vortex street behind the downstream cylinder. For high values of  $P/D$ , the Strouhal numbers is seen to asymptote to the single cylinder value.

Three key regimes of the flow around two circular cylinders in tandem are shown in Figure 4.18. Plotted there are the velocity vectors around the cylinders at  $Re=65,000$ . The maximum velocity in the field, represented by the longest arrow, is 1 m/s.

Figure 4.18(a) shows the arrangement for  $P/D=1.35$  which is below the critical spacing range. Two vortices are formed behind the upstream cylinder. These are almost symmetric and thus do not result in alternate vortex shedding. At this small cylinder spacing the shear layers separating from the upstream cylinder reattach on the downstream cylinder. As a consequence, the formation of a vortex street between the two cylinders is inhibited. The oncoming flow to the downstream cylinder is very weak and leads to an equally weak vortex street behind the downstream cylinder. This is evident from the small values of mean drag shown in Figure 4.16(b). Note that for this spacing, the drag on the downstream cylinder is actually thrust.

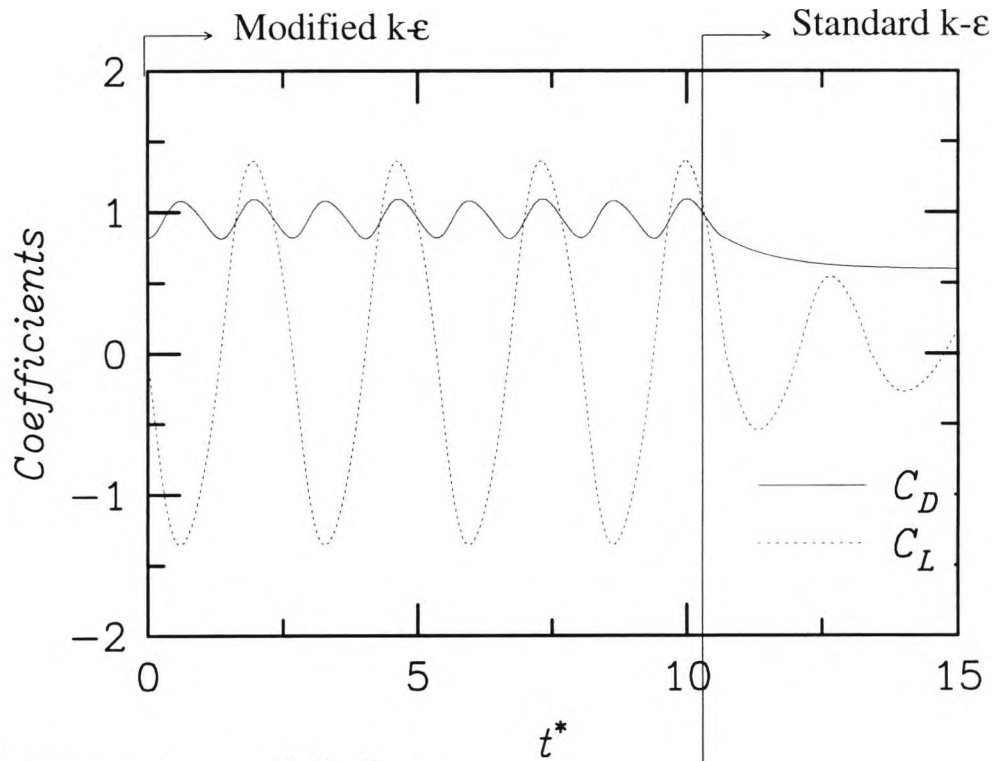
is evident from the small values of mean drag shown in Figure 4.16(b). Note that for this spacing, the drag on the downstream cylinder is actually thrust.

Figure 4.18(b) shows the flow field for  $P/D=2.5$ . This is at the onset of the critical regime. There are alternate vortices behind the upstream cylinder, although it is obvious from the figure that they do not constitute an organised vortex street. The Strouhal number for the downstream cylinder is at its minimum.

Figure 4.18(c) shows the flow that exists at a spacing of  $P/D=5$ . At this large spacing, which is beyond the critical regime, the vortex street behind the upstream cylinder has enough room to develop. Both cylinders now form vortex streets. The asymmetry in the oncoming flow causes vortex shedding from the downstream cylinder.

The above three findings are in accordance with three of the regimes as described by Zdravkovich (1985) (reproduced in Figure 4.2) and namely; b) Alternate reattachment, d) Intermittent shedding streets, and f) Two vortex streets.

**a) Upstream Cylinder**



**b) Downstream Cylinder**

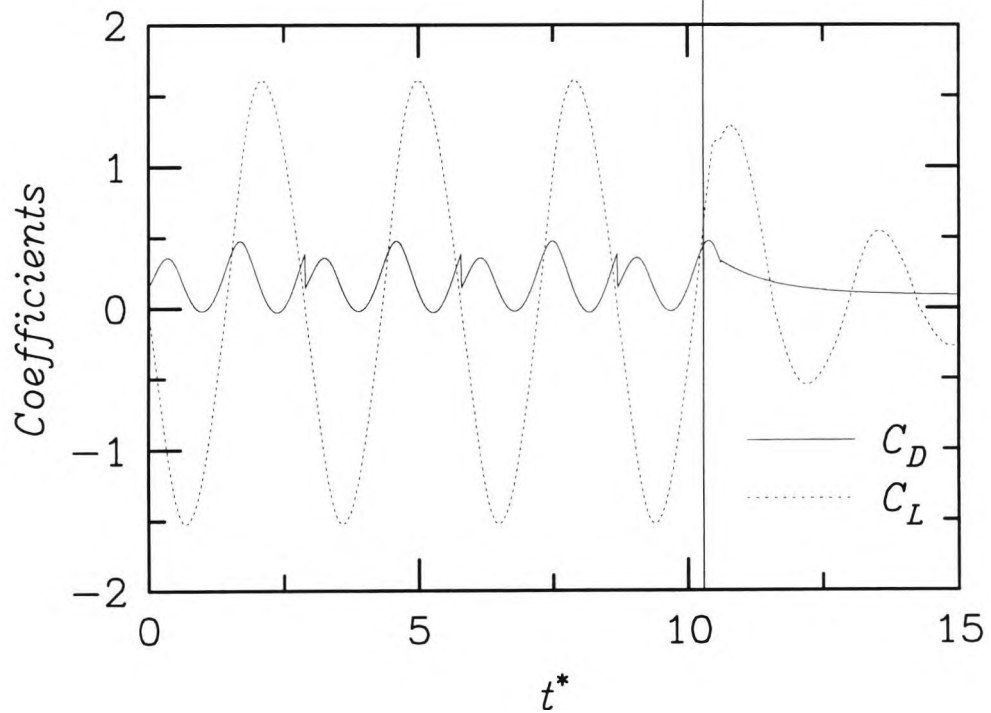


Figure 4.15: a) Upstream and b) downstream cylinder time histories of the drag and lift coefficients for two cylinder in tandem with a separation of  $P/D=5$  at  $Re=6.5 \times 10^4$  with and without the k- $\epsilon$  modification.

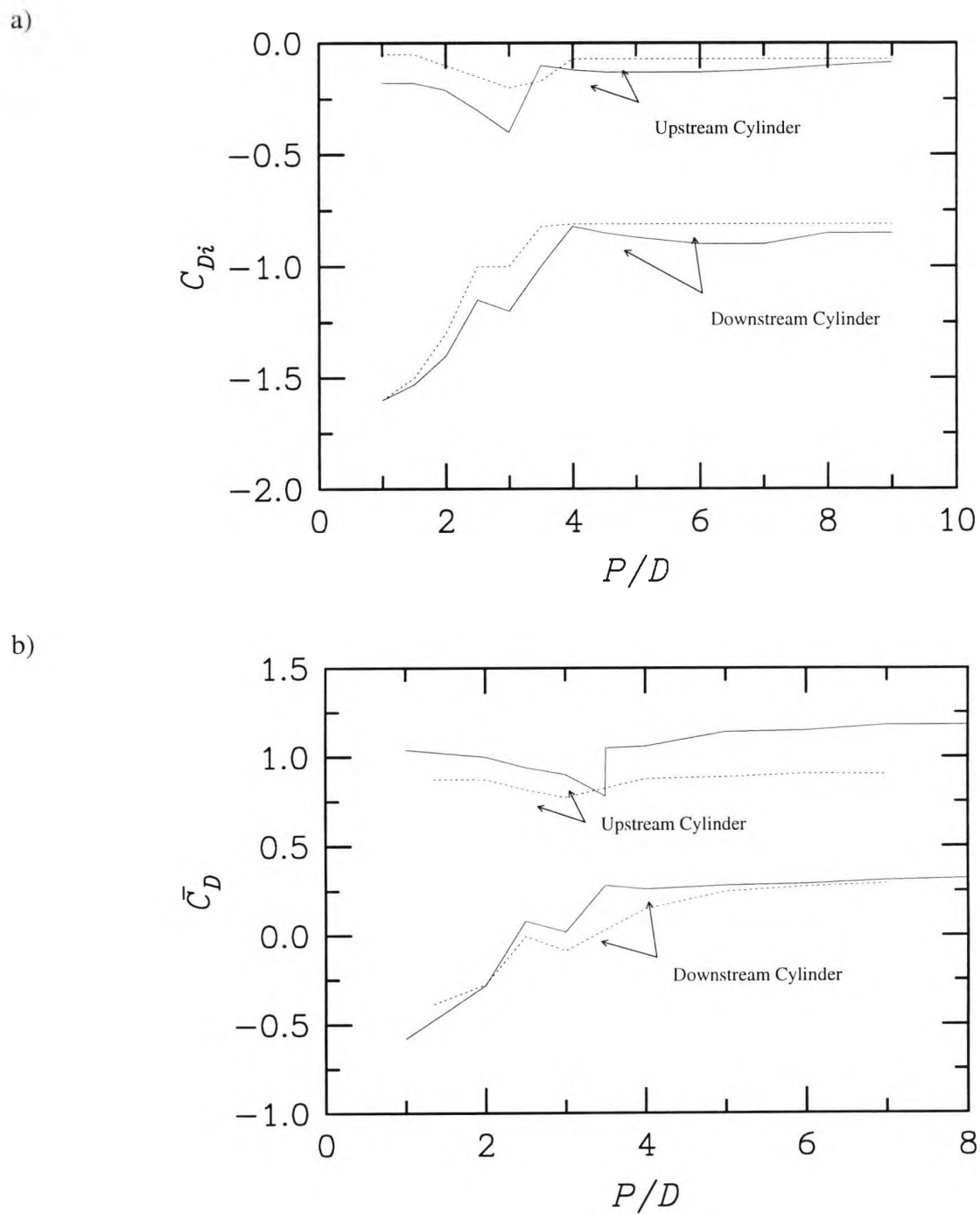
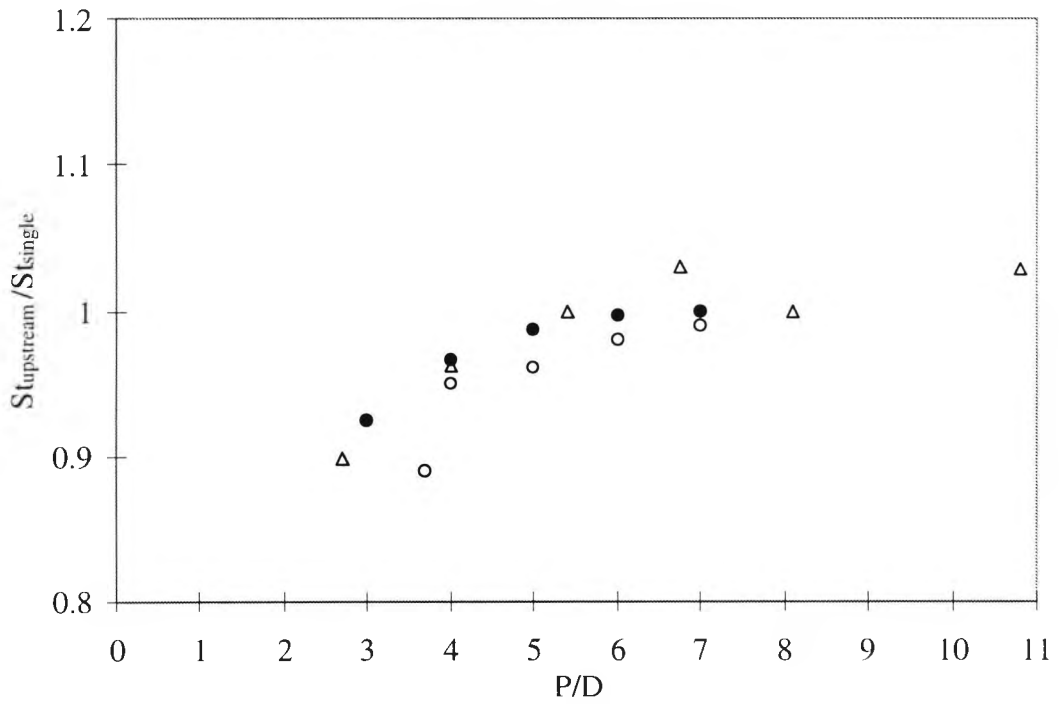


Figure 4.16: Two cylinders in tandem, showing a) interference drag, and b) mean drag in turbulent flow. (Experimental — and Numerical .....).

a) Upstream Cylinders



- Present Calculations at Re=65,000
- Data of Oka et al. (1972) at Re=51,000
- △ Data of Jendrzejczyk and Chen (1986) at Re=65000

b) Downstream Cylinders

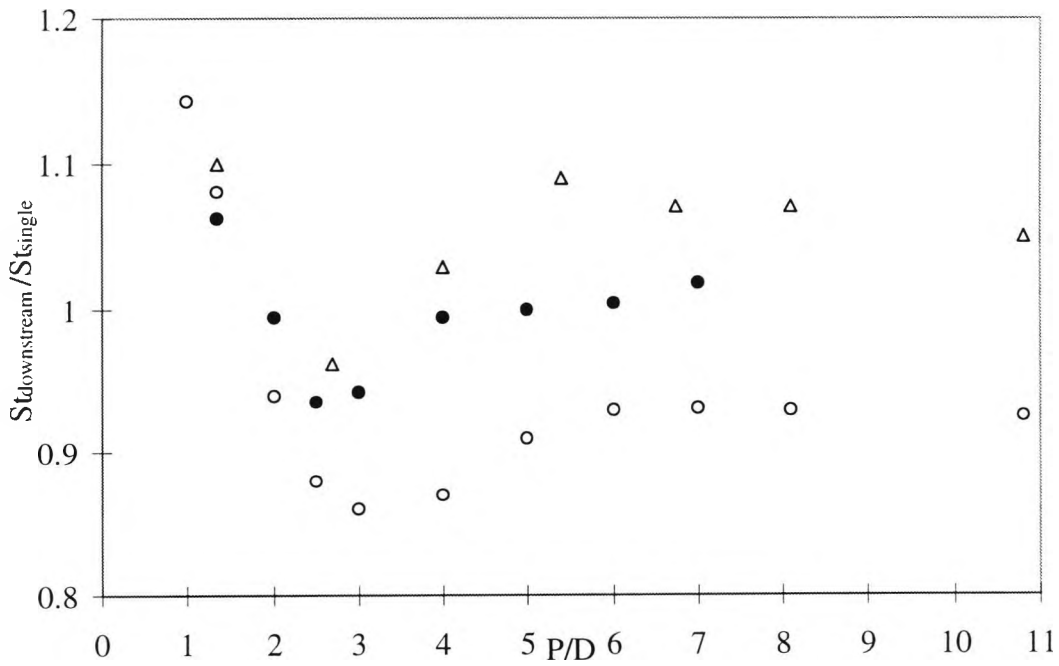


Figure 4.17: Strouhal number analysis for two cylinders in tandem at  $Re=6.5 \times 10^4$ .

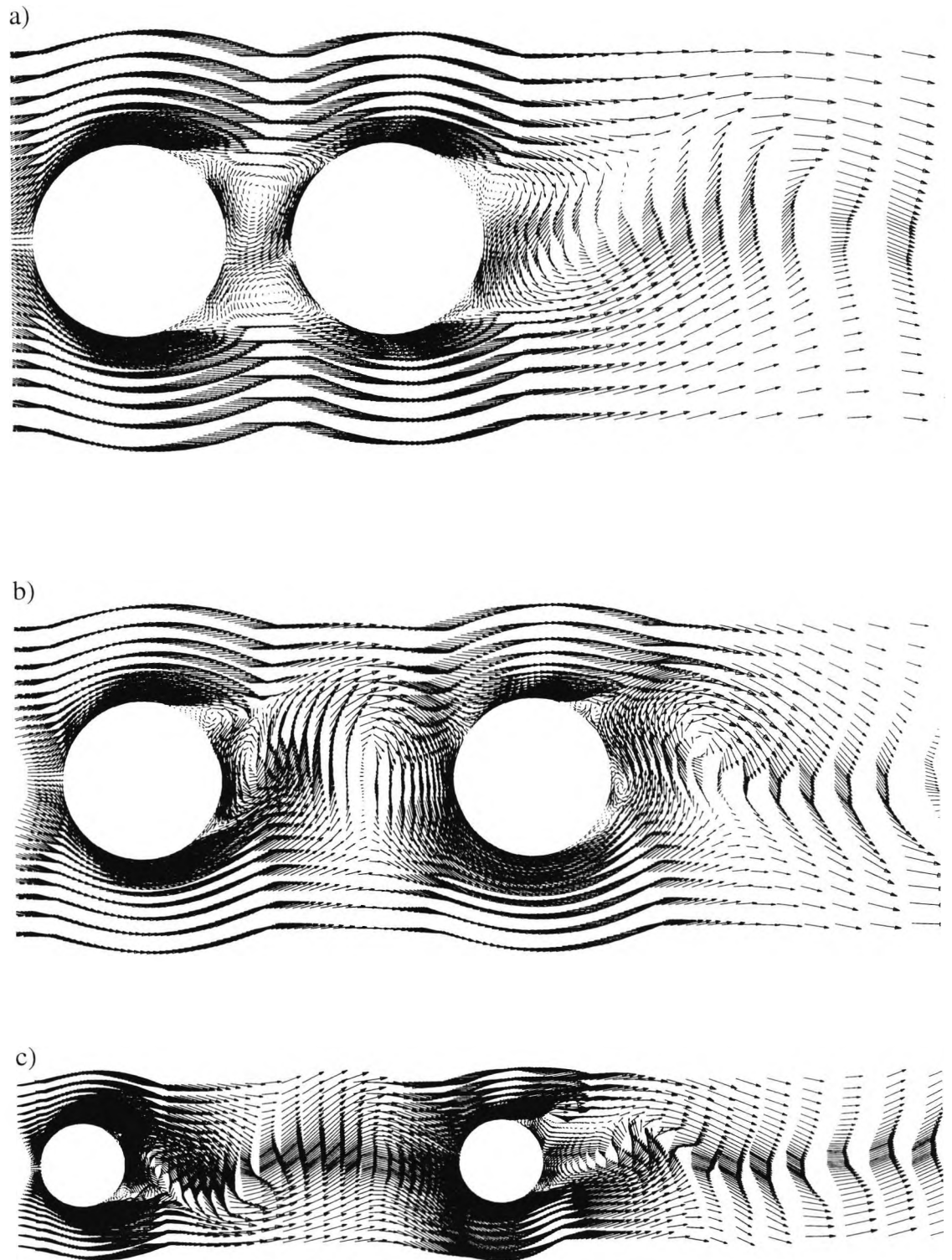


Figure 4.18: Velocity vectors for two cylinders in flow of  $Re=65,000$  at different separation: a)  $P/D=1.35$ , b)  $P/D=2.5$ , c)  $P/D=5$ .

(Longest vector represents 1 m/s).

## 4.7 Conclusions

The present prediction method was used to investigating the flow field that develops around two cylinders in tandem in laminar and turbulent flow regimes. The method reproduces the wide range of well established flow phenomenon observed experimentally.

All previous predictions of these flows, were in the laminar regime. To the author's knowledge, this is the first study of the flows around cylinders in tandem to be conducted in the turbulent regime. The present study extended the investigation into the turbulent flow regime by modelling at  $Re=65,000$ , using the modified  $k-\epsilon$  method, with satisfactory results

In the laminar flow calculations, the experimentally observed 'vortex suppression' regime at  $P/D=3$  and the 'vortex formation' regime at  $P/D=7$  were found at  $Re=100$  and  $300$ . At a small spacing, there is not enough room between the cylinders for the formation of a vortex street, and since the oncoming flow to the downstream cylinder is weak, the resulting vortex shedding behind it is also weak. At a larger spacing, the occurrence of vortex shedding between the two cylinders creates an oscillatory oncoming flow and this leads to a stronger vortex shedding behind the downstream cylinder. These observations were correctly reproduced in the present predictions.

A wide range of spacings was investigated in the turbulent flow regime. The results were used to show the influence of the downstream cylinder on the flow around the upstream cylinder. Also predicted were the different flow regimes that exist around the cylinders and how these depend on the cylinders spacing. The critical spacing, when the two cylinders stop behaving as one, was predicted to lie in the range  $2.5 < P/D < 4$ .

Three key regimes were shown:

- a) Below the critical spacing ( $P/D=1.35$ ), where there is alternate reattachment of the shear layers separating from the upstream cylinder on the downstream cylinder.
- b) At the critical spacing ( $P/D=2.5$ ), where the flow shifts between two regimes. There are vortices behind the upstream cylinder, but they do not constitute a periodic vortex street.

c) Above the critical spacing ( $P/D=5$ ), where there is enough room between the cylinder for a vortex street, and therefore both cylinders produce vortex street. The mean drag of the upstream cylinder is now approaching that of a single cylinder.

The standard  $k-\epsilon$  model was tested for the case of  $P/D=5$  where it was found to be inadequate.

It was observed that the mean drag of the downstream cylinder can become negative at small spacings in the vortex suppression regime. This constitutes a thrust in this cylinder.

It was also observed that up to the spacing ratios examined ( $P/D=7$ ), the overall drag of the two cylinders in tandem is always less than twice the value of the drag for a single cylinder. Further, it was found that the drag on the upstream cylinder never reaches the value appropriate to a single cylinder.

# CHAPTER FIVE: PREDICTION OF SUPPRESSION BY CONTROL CYLINDER

## 5.1 Introductory Remarks

A number of methods have been developed with the aim of suppressing vortex shedding from square and circular cylinders. These methods generally fall into one of the following three categories (Zdravkovich, 1981):

- i) The control of the boundary layer on the surface with the use of a tripping wire, fin, or blowing nozzle installed on the surface.
- ii) The control of the entrainment process that determines the supply of irrotational fluid necessary for the growth of vortices. This is typically achieved by enclosing the body with a porous flexible plate or multiple rods.
- iii) The control of the wake with the use of a splitter plate, guidevane, or by base-bleed.

We consider three methods of suppression in this study, namely; the control cylinder, forward injection, and rear stagnation jet. In this Chapter, we consider the use of a control cylinder, whereby a small cylinder is placed near the main cylinder to reduce or eliminate oscillations caused by vortex shedding from it. Experimental and previous predictions for this are presented in Section 5.2 and Section 5.3 respectively. The computational details and code modifications are presented in Section 5.4. Results obtained for circular and square cylinders with control cylinders placed at different points in the flow are discussed in Section 5.5 for laminar flow, and Section 5.6 for turbulent flow.

## 5.2 Experimental Results

Strykowski and Sreenivasan (1985) reported that vortex shedding from circular cylinders could be suppressed almost completely by placing a small cylinder in the separated shear layer on one side. This was achieved in the range of low Reynolds numbers (less than  $Re=120$ ) where the shear layers separating from the circular cylinder are thin, and vortex shedding is well established.

Igarashi and Tsutsui (1989) investigated the reduction of the mean drag on a circular cylinder by means of using a small cylinder. They found that the mean drag was considerably reduced by about 20~30%, by forcibly reattaching the separated shear layer back on to the surface of the circular cylinder. They also noted reductions in the fluctuating pressure on the surface.

Sakamoto, Tan and Haniu (1991) investigated the possibility of suppressing vortex shedding from a square prism by means of a small circular cylinder placed in the shear layer. Their investigations were carried out at  $Re=4.2 \times 10^4$ . They found that the maximum reduction of the mean drag and the fluctuating lift and drag forces occurred when the control cylinder was located near the outer boundary of the shear layer.

Strykowski and Sreenivasan (1990) reported on experimental and computational results on the suppression of vortex shedding from a circular cylinder at low Reynolds numbers, using a control cylinder. They stated that while some aspects of the suppression phenomenon might be sensitive to three-dimensionalities, specific end conditions, free-stream turbulence levels, etc., the essentials of the phenomenon are independent of them. They also found that the effects of a control cylinder are negligible except when placed in the near wake region (not further than ~3.5 to 4 diameters downstream of the cylinder).

Sakamoto and Haniu (1994) extended the available results by investigating the suppression of fluid forces on a circular cylinder by using a control cylinder at a higher Reynolds number ( $Re=6.5 \times 10^4$ ). They found that the suppression can be classified into two categories; one is due to the control of the boundary layer along the surface of the circular cylinder; the other is due to the control of the shear layer separated from its surface. The maximum reduction of the mean drag was 50%, and the maximum reduction in the fluctuating lift and drag was 85%. Suppression by this technique is possible behind a variety of objects and over a range of Reynolds numbers.

### 5.3 Previous Predictions

Strykowski and Sreenivasan (1990), applied a finite-difference Galerkin method, developed by Stephens et al. (1984), to compute the vortex shedding patterns after the introduction of a control cylinder. Numerical simulation were carried out for  $Re=55$ , with a relatively small physical domain. This prohibited a detailed quantitative comparison of numerical data with experimental. Their results showed that the vortex street is suppressed soon after inserting the control cylinder, leading to the formation of two standing eddies.

Lin and Wu (1994) numerically investigated two kinds of flow control devices: an attached or detached splitter plate, and a control cylinder behind a circular cylinder. They used an artificial compressibility method, first proposed by Chorin (1967), utilising a high-order upwind method for the space discretisation. The investigations were carried out at low Reynolds numbers ( $46 < Re < 200$ ). For the control cylinder investigations, they found that in steady conditions, mean drag decreases at  $Re=20$  and increases at  $Re=40$ . In unsteady conditions ( $Re=80$ ), the mean drag is reduced by 12%, but mean lift is increased. When the control cylinder is placed further away from the main cylinder, the root mean square (rms) of the lift coefficient is reduced by 70%, and the oscillation of the drag coefficient becomes double-periodic. The shedding frequency is reduced by approximately 52% and the mean of drag is reduced by 7.5%.

### 5.4 Computational Details

It is not straightforward to generate a grid for a small circular control cylinder, and thus an approximation is devised for this study. This involves the use of a quadrilateral body in place of the circular one. For this approximation to be valid, a fine grid is required. This is discussed further in Sections 5.5 and 5.6.

The grid generation technique for a control cylinder is similar to that used for the case of the two cylinders in tandem. The positions of the four vertices of the control cylinder are specified manually and the volumes and the distance of near-boundary nodes from the east, west, north, and south edges of the control cylinder are stored. The sides of the control cylinder quadrilateral are treated as walls and thus the wall boundary conditions are calculated.

The predictions were carried out using the SMART scheme throughout. The modified k- $\epsilon$  turbulence model was used for the turbulent cases.

The predictions start with the simulation of a circular or square cylinder case without a control cylinder. The computed flow field is then stored in a 'start-up' file. The computations are then re-started in the presence of a control cylinder. It was found that the non-dimensionalised time-step  $\Delta t^*$  did not have to be altered when the control cylinder was introduced.

## 5.5 Laminar Flow Simulations

### 5.5.1 Circular Cylinder

The principal experimental results for the circular cylinder with control cylinder at low Reynolds numbers are those collected by Strykowski & Sreenivasan (1990) in the range  $80 \leq Re \leq 120$ . The numerical results of Lin & Wu (1994) were obtained at  $Re=80$ . The numerical simulations presented here will be for  $Re=100$ .

A control cylinder of height  $d$  is introduced, behind and parallel to a main cylinder of diameter  $D$  (Figure 5.1). The  $x$  and  $y$  coordinates are measured from the centre of the main cylinder.

The same grid (148x102) and the start-up file as for the single circular cylinder at  $Re=100$  described in Section 3.5.1 for a circular cylinder were used here. Three arrangements for the positioning of a control cylinder were considered. These are shown in Figure 5.2 to Figure 5.4. Note that grid arrangement (1) refers to the no control cylinder case shown in Figure 3.4. In this work, the control cylinder was approximated as a four-sided obstacle. The ratio of the main cylinder diameter to control cylinder diameter ( $D/d$ ) was not constant due to the non-uniformity of the grid. Three values of  $D/d$  were considered:  $D/d = 4.12, 5.38, \text{ and } 7.78$ . These were located at the distances away from the main cylinder as shown in Figure 5.2 to Figure 5.4. The experiments of Strykowski & Sreenivasan (1990) were for ratios ranging from  $D/d=1$  to 20, although they mainly used  $D/d=7$ .

The SMART differencing scheme was again utilised here. The non-dimensional time-step ( $\Delta t^*$ ) was kept at 0.054, which is the same as for the single circular cylinder at

Re=100. It was not deemed necessary to alter the time-step, as satisfactory results were obtained with the present one. Time histories of the drag and lift coefficients and their power spectra are shown in Figure 5.5 to Figure 5.8. The computed streaklines for the four runs before and after inserting the control cylinder are shown Figure 5.9. The predicted drag and lift coefficients are presented in Table 5.1, together with the results of Lin and Wu (1994) at Re=80. Results for the Strouhal numbers are shown in Table 5.2.

The extent of suppression in the fluctuating drag and lift coefficients is defined in terms of the parameters  $C_{Dr}$  and  $C_{Lr}$ :

$$C_{Dr} = \frac{\tilde{C}_D \text{ after introducing control cylinder (ie for RUN 2 - 3)}}{\tilde{C}_D \text{ before introducing control cylinder (ie for RUN 1)}} \quad (5.1)$$

$$C_{Lr} = \frac{\tilde{C}_L \text{ after introducing control cylinder (ie for RUN 2 - 3)}}{\tilde{C}_L \text{ before introducing control cylinder (ie for RUN 1)}} \quad (5.2)$$

The results show that the conditions of RUN 2 produce complete suppression. The control cylinder is placed one cylinder diameter above and behind the main cylinder. Figure 5.6 shows a reduction in mean drag, with its fluctuations at minimal levels ( $C_{Dr}=4.82 \times 10^{-3}$ ). There is a slight increase in mean lift, but the rms of the lift coefficient is very small ( $C_{Lr}=6.21 \times 10^{-3}$ ). The Strouhal number is negligibly small compared to the case of a single circular cylinder. The streaklines show no sign of vortex shedding, except very far downstream of the cylinder (Figure 5.9).

In the case of the second control arrangement (RUN 3), the control cylinder was placed at half a cylinder diameter behind and one cylinder diameter above the main cylinder. Table 5.1 shows that the mean and fluctuation of drag levels are reduced relative to the uncontrolled case, but not as dramatically as RUN 2. There is a shift into negative mean lift, although fluctuations of lift are still suppressed ( $C_{Lr}=0.118$ ). The Strouhal number is smaller than in the standard case, but significantly larger than RUN 2. The streaklines in Figure 5.9 show some form of vortex shedding with the vortices lengthening in the field.

For RUN 4, the control cylinder was placed above the centre line of the main cylinder at a height of 0.64 diameters of the main cylinder. This position was chosen to show that the introduction of a control cylinder does not necessarily lead to effective

suppression. Table 5.1 shows the mean drag level increasing relative to the uncontrolled case but that its fluctuations are reduced ( $C_{Dr}=0.4$ ). The mean lift is further increased in the negative direction, with the fluctuations enhanced almost three times ( $C_{Lr}=2.778$ ). Strouhal number is closer to the case of standard vortex shedding. The streaklines in Figure 5.9 show a pattern very similar to natural vortex shedding, with the vortex street widening and the entrainment region increasing in size.

The power spectra of the case with no control cylinder are shown in Figure 5.5. A distinct sharp peak is apparent depicting vortex shedding. RUN 2 shows a complete disappearance of the peak which is an indication that no periodic structures exist. RUN 3 shows a wide peak for the lift coefficient, therefore there is some form of shedding, while by RUN 4, the peak is sharper, but still not as sharp as RUN 1.

The findings are very similar to those of Strykowski and Sreenivasan (1990). They did not show detailed drag, lift or Strouhal number analysis. Their findings were based mainly on Hydrogen-bubble visualisations. They found regions of suppression for different values of  $D/d$  at  $Re=80$ . RUN 2 which gave the maximum suppression effect here, is placed in the same zone as their findings for  $D/d=7.5$ . They found that the region of control shrinks essentially to a point with increase in  $D/d$ . They found suppression up to  $Re=100$ , while  $Re=120$  did not show suppression in the vortex street at  $D/d=7$ . Their findings also show that for  $Re=80$ , there is a reduction of 20% in the mean of the drag coefficient. Similarly, the maximum reduction in drag shown here was 17% for RUN 2.

Strykowski & Sreenivasan (1990) also presented numerical simulations for  $Re=55$ . The results were largely qualitative and showed the formation of symmetric eddies behind the main cylinder in the presence of a control cylinder.

The arrangement adopted by Lin and Wu (1994) in numerically simulating a control cylinder was the same as the one shown here. As can be seen in Table 5.1, the control cylinder was placed further away from the cylinder. Their simulations carried out at  $Re=80$ , show a reduction in mean drag and increase in mean lift for RUNs B and C. The fluctuating drag drops to  $C_{Dr}=0.583$  for RUN B but remains at its original value for RUN C. The fluctuating lift is minimum at RUN B ( $C_{Lr}=0.025$ ), but increases slightly to  $C_{Lr}=0.075$  for RUN C. From their results it is obvious that Lin and Wu (1994) did not achieve the same dramatic suppression as in RUN 2 mainly because the control cylinder was placed further away from the cylinder.

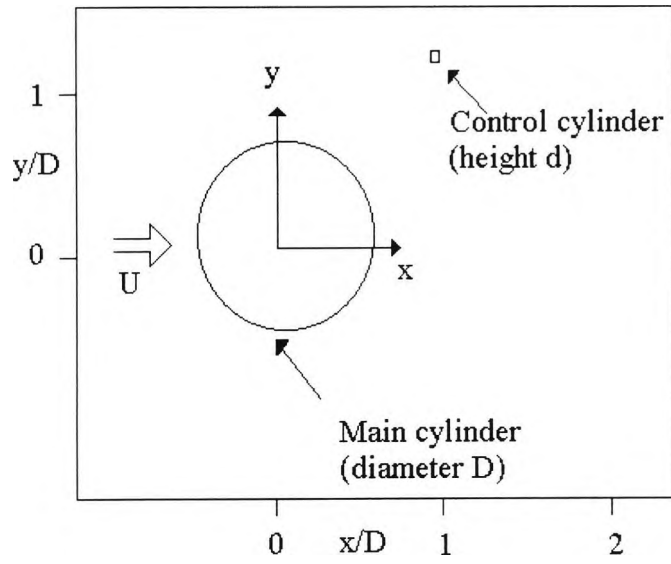


Figure 5.1: Schematics of arrangement for control of vortex shedding.

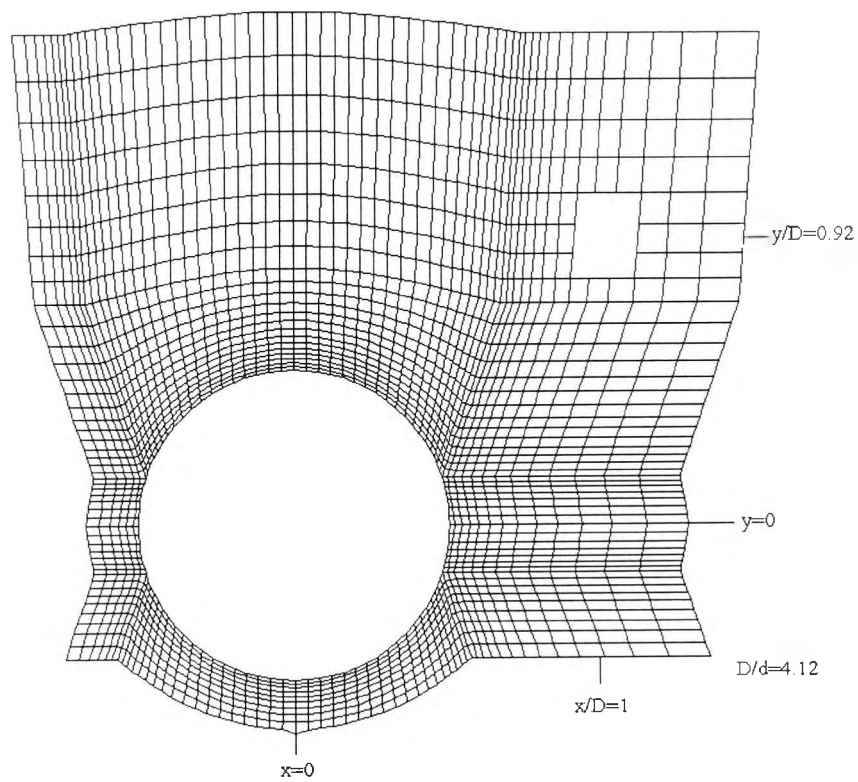


Figure 5.2: Grid arrangement (2) for a circular cylinder with control cylinder.

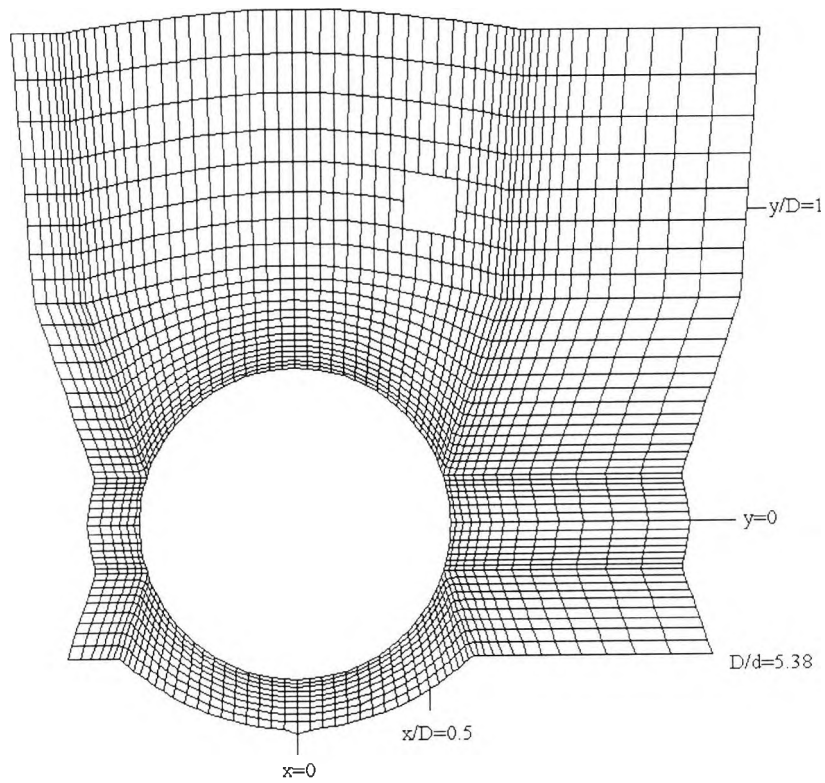


Figure 5.3: Grid arrangement (3) for a circular cylinder with control cylinder.

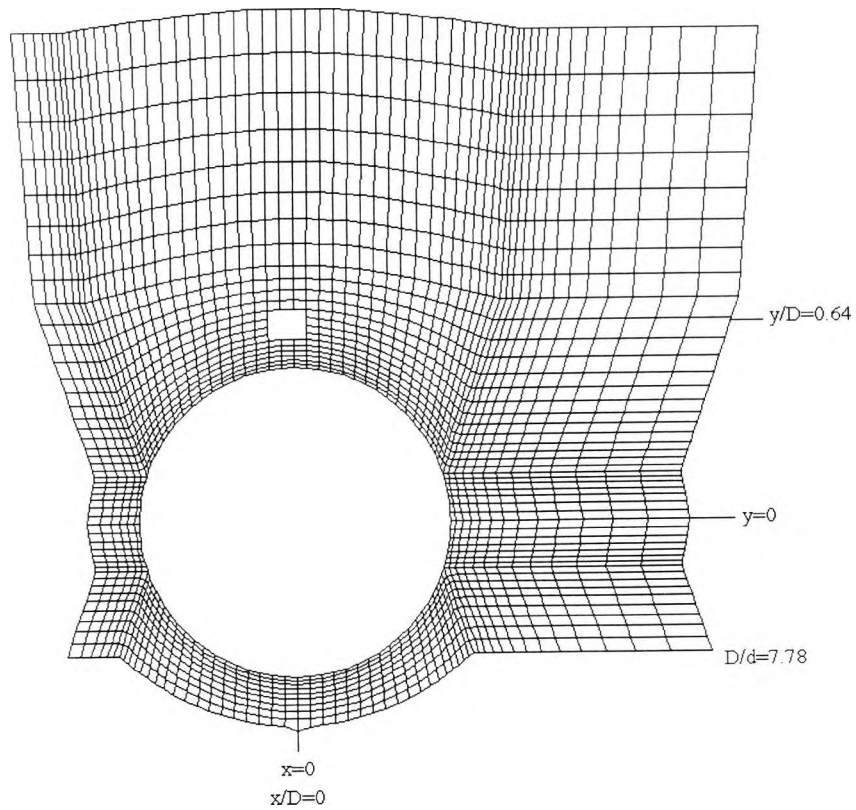


Figure 5.4: Grid arrangement (4) for a circular cylinder with control cylinder.

RUN	D/d	x/D	y/D	$\bar{C}_D$	$\check{C}_D$	$C_{Dr}$	$\bar{C}_L$	$\check{C}_L$	$C_{Lr}$
Present Results Re=100									
1	-	-	-	1.451	0.105	1.000	$-5.9 \times 10^{-3}$	0.161	1.000
2	4.12	1.00	0.92	1.201	$5.07 \times 10^{-4}$	$4.82 \times 10^{-3}$	0.063	0.001	$6.21 \times 10^{-3}$
3	5.38	0.5	1.00	1.256	$3.73 \times 10^{-3}$	0.036	-0.054	0.019	0.118
4	7.78	0.00	0.64	1.695	0.042	0.400	-0.730	0.447	2.776
Results of Lin and Wu (1994) Re=80									
A	-	-	-	1.37	0.012	1.000	0.000	0.189	1.000
B	-	2.15	1.47	1.22	$7 \times 10^{-3}$	0.583	0.063	0.025	0.132
C	-	2.28	1.25	1.27	0.012	1.000	0.035	0.075	0.397

Table 5.1: Results of the behaviour of the drag and lift coefficients with a control cylinder collected by present method at Re=100 and Lin and Wu (1994) at Re=80.

RUN	D/d	x/D	y/D	St
1	-	-	-	0.173
2	4.12	1.00	0.92	0.001
3	5.38	0.5	1.00	0.143
4	7.78	0.00	0.64	0.151

Table 5.2: FFT analysis of the drag and lift coefficients with a control cylinder.

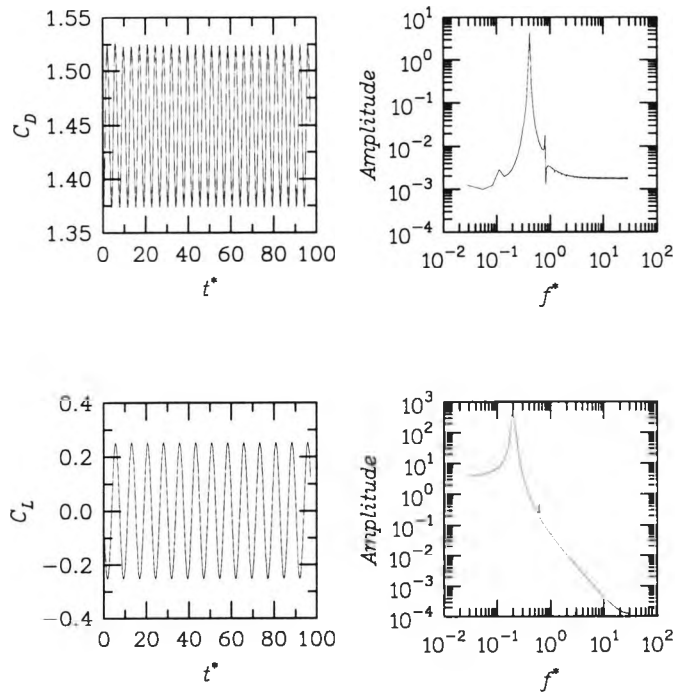


Figure 5.5: Time histories and power spectra for a circular cylinder at  $Re=100$  with no control cylinder (RUN 1).

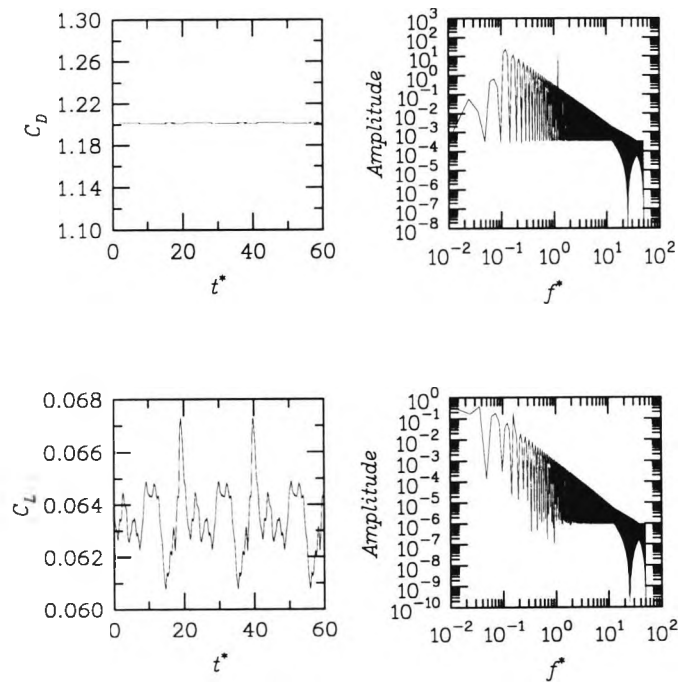


Figure 5.6: Time histories and power spectra for a circular cylinder at  $Re=100$  with control cylinder (RUN 2:  $D/d=4.12$ ,  $x/D=1$ ,  $y/D=0.92$ ).

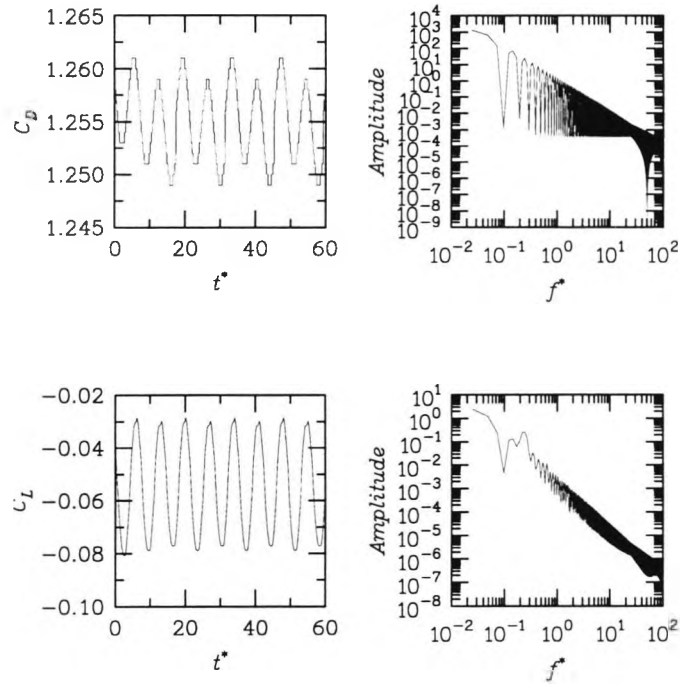


Figure 5.7: Time histories and power spectra for a circular cylinder at  $Re=100$  with control cylinder (RUN 3:  $D/d=5.38$ ,  $x/D=0.5$ ,  $y/D=1$ ).

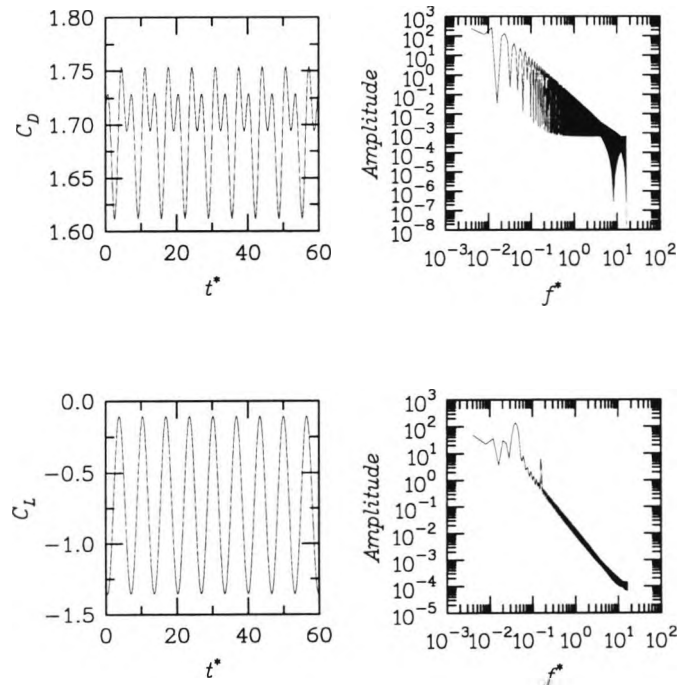
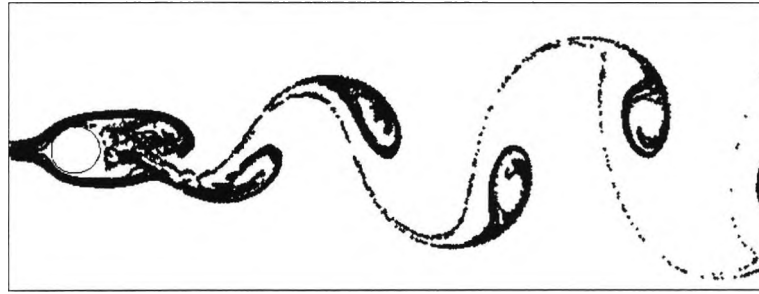
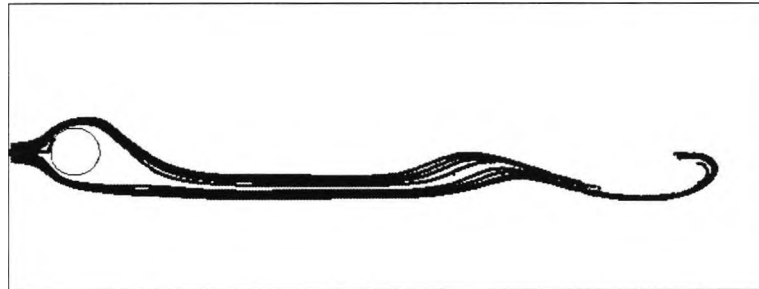


Figure 5.8: Time histories and power spectra for a circular cylinder at  $Re=100$  with control cylinder (RUN 4:  $D/d=7.78$ ,  $x/D=0$ ,  $y/D=0.64$ ).

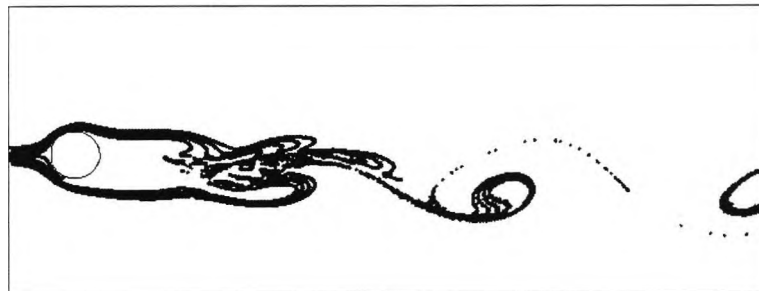
RUN 1



RUN 2



RUN 3



RUN 4

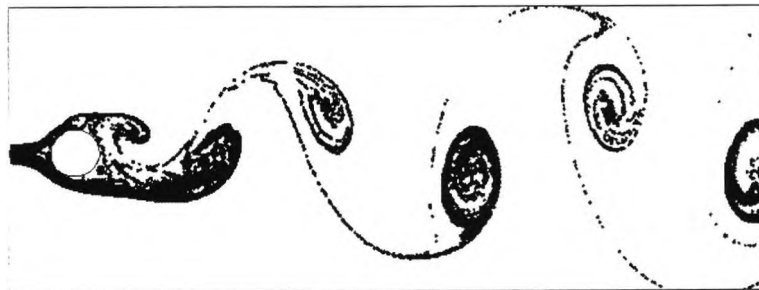


*Figure 5.9: Streaklines for the four runs before and after inserting a control cylinder.*

## 5.5.2 Square Cylinder

Simulations were carried out for a Reynolds number of 100. No experimental data are available for comparison.

A control cylinder of height  $d$  is introduced behind, and parallel to a larger square cylinder of height  $D$  (Figure 5.10). The  $x$  and  $y$  coordinates are measured from the centre of the main cylinder with reference to  $x/D$  and  $y/D$ .

The grid (121x110) and the start-up file described in Section 3.5.2 for a square cylinder at  $Re=100$  were used here. Three arrangements for the positioning of the control cylinder were modelled. These are shown in Figure 5.11 to Figure 5.13. Note that grid arrangement 1 refers to the no control cylinder case shown in Figure 3.5. The ratio ( $D/d$ ) varied slightly, because of the non-uniformity of the grid. The positions of the three cases of control cylinder are shown in Table 5.3.

The simulations were performed with  $\Delta t^*=0.01$ . Time histories of the drag and lift coefficients, and their FFT analysis, are shown in Figure 5.14 to Figure 5.17. Figure 5.18 shows the computed streaklines for the four different positions. The extent of the suppression in the fluctuating drag and lift coefficients is defined in terms of the parameters  $C_{Dr}$  and  $C_{Lr}$ .

The predicted results are presented in Table 5.3 and Table 5.4. From Table 5.3 it is clear that RUN 2 gives the optimum suppression of vortex shedding. In this RUN, the control cylinder is placed approximately one main cylinder height above and behind the main cylinder. The main parameters,  $\overline{C_D}$ ,  $C_{Dr}$ ,  $C_{Lr}$  are at their lowest. The fluctuating drag is almost zero, as can be seen from Table 5.3 and the drag time history in Figure 5.15. This extent of vortex suppression is also clear from the power spectrum of the drag; there is no distinct shedding frequency, and the amplitude is drastically reduced. The mean lift is finite, but its fluctuations are considerably smaller than was the case for RUN 1. The streaklines for RUN 2 (Figure 5.18) show no sign of vortex shedding, except well downstream of the cylinder.

When the control cylinder is brought closer to the main cylinder (RUN 3), the mean drag increases slightly (Table 5.3), but the fluctuations are increased four fold. The mean lift is negative in this case, which means that there is a mean force in the downward direction. The lift fluctuations are also increased. The power spectra show

distinct vortex shedding frequencies at lower values than RUN 1. The streaklines for this case show a fully established vortex shedding field (Figure 5.9).

The conditions of RUN 4 are such that the vortex shedding is enhanced relative to the previous runs. The control cylinder is placed just downstream of the centre of the main cylinder and  $0.8D$  above it. Table 5.3 shows that the mean drag is increased and its fluctuation is enhanced six times relative to the no control cylinder case. The mean lift is increased considerably in the negative direction, while its fluctuations are also higher. The power spectra show a shift in the shedding frequency and thus a considerable increase in Strouhal number. The streaklines (Figure 5.9) show that with this arrangement, the vortex street is widened.

Figure 5.19 to Figure 5.22 show velocity vectors for RUNs 1-4 at the instant of maximum lift. They show that for RUN 2 there are two standing vortices behind the cylinder. RUN 3 shows alternating vortices packed near the rear of the cylinder, and RUN 4 shows that the control cylinder acts as an extension to the main cylinder and thus vortices are shed behind the two as one. This explains the observed widening of the vortex street.

By far the most successful arrangement for suppressing vortex shedding is RUN 2 where the centre of the control cylinder is placed at  $x/D=1.02$  and  $y/D=0.95$  with  $D/d=7.14$ . For this run, the position of the control cylinder is inside the separated shear layer (position of the maximum velocity in the field around the cylinder). For the other arrangements studied, the vortex shedding was actually enhanced in some ways (mean, and fluctuating drag and lift, and Strouhal number). When the control cylinder is placed outside the boundary (RUN 3) of the shear layer and on its border (RUN 4), vortex shedding is enhanced.

RUN	D/d	x/D	y/D	$\bar{C}_D$	$\tilde{C}_D$	$C_{Dr}$	$\bar{C}_L$	$\tilde{C}_L$	$C_{Lr}$
1	-	-	-	1.476	$4.19 \times 10^{-3}$	1.000	$6.41 \times 10^{-3}$	0.171	1.00
2	7.14	1.02	0.95	1.302	$1.15 \times 10^{-1}$	0.027	$2.85 \times 10^{-2}$	$5.27 \times 10^{-4}$	$3 \times 10^{-3}$
3	5.5	0.59	1.21	1.480	$1.67 \times 10^{-2}$	3.978	-0.178	$7.70 \times 10^{-2}$	0.451
4	7.3	0.22	0.76	1.778	$2.50 \times 10^{-2}$	5.959	-0.768	0.356	2.082

Table 5.3: Behaviour of the drag and lift coefficients with a control cylinder.

RUN	D/d	x/D	y/D	St
1	-	-	-	0.150
2	7.14	1.02	0.95	0.148
3	5.5	0.59	1.21	0.138
4	7.3	0.22	0.76	0.261

Table 5.4: FFT analysis of the drag and lift coefficients with a control cylinder for a square cylinder in laminar flow.

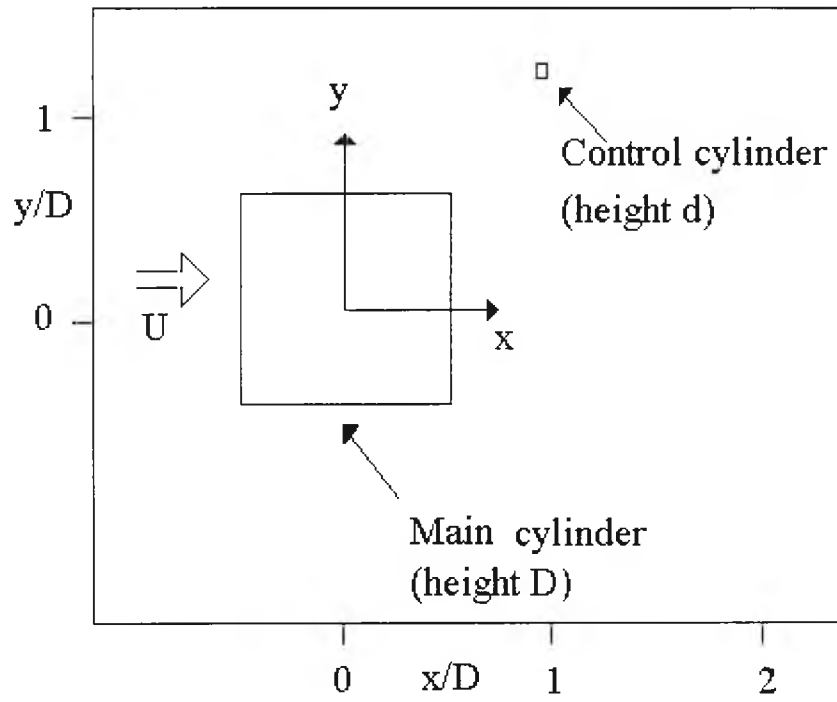


Figure 5.10: Schematics of arrangement for control cylinder.

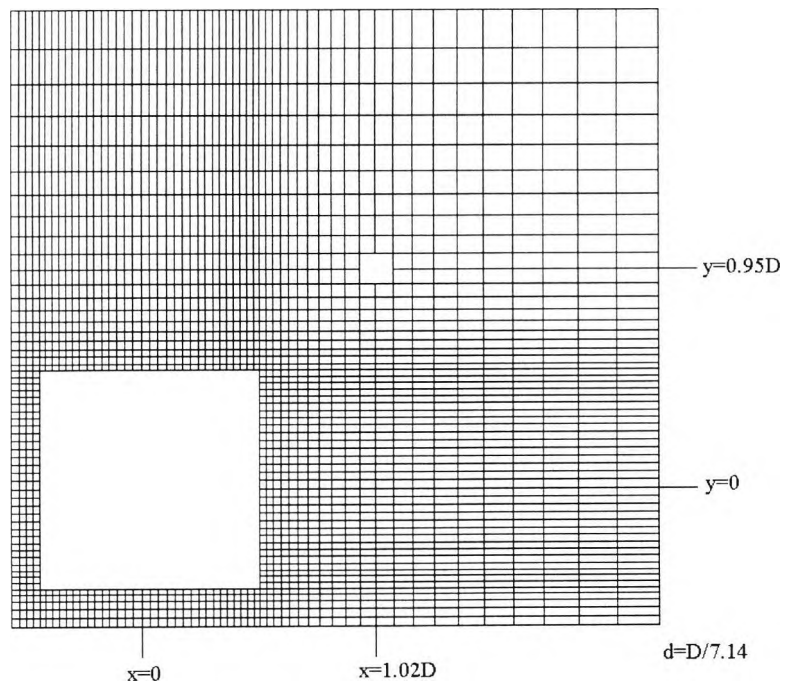


Figure 5.11: Grid arrangement (2) for a square cylinder with control cylinder.

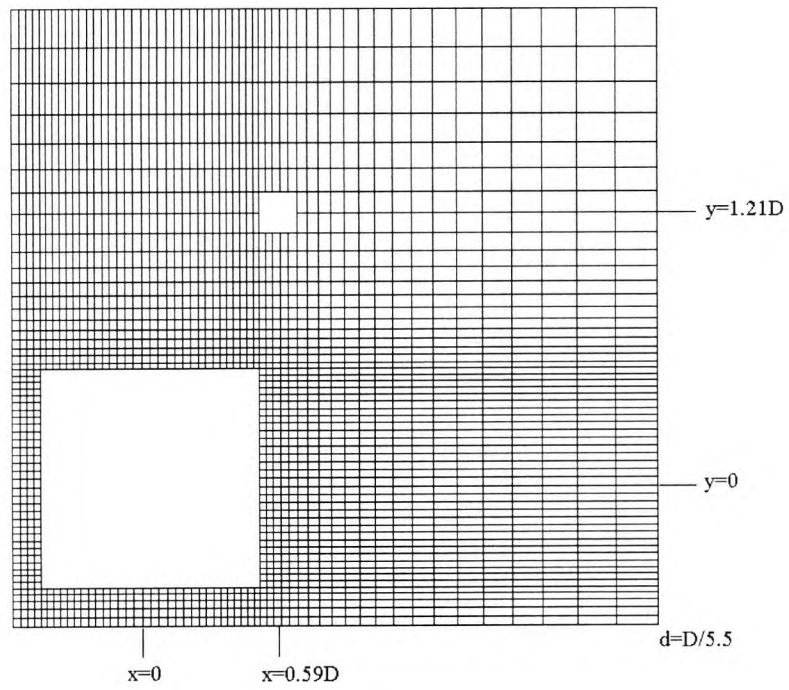


Figure 5.12: Grid arrangement (3) for a square cylinder with control cylinder.

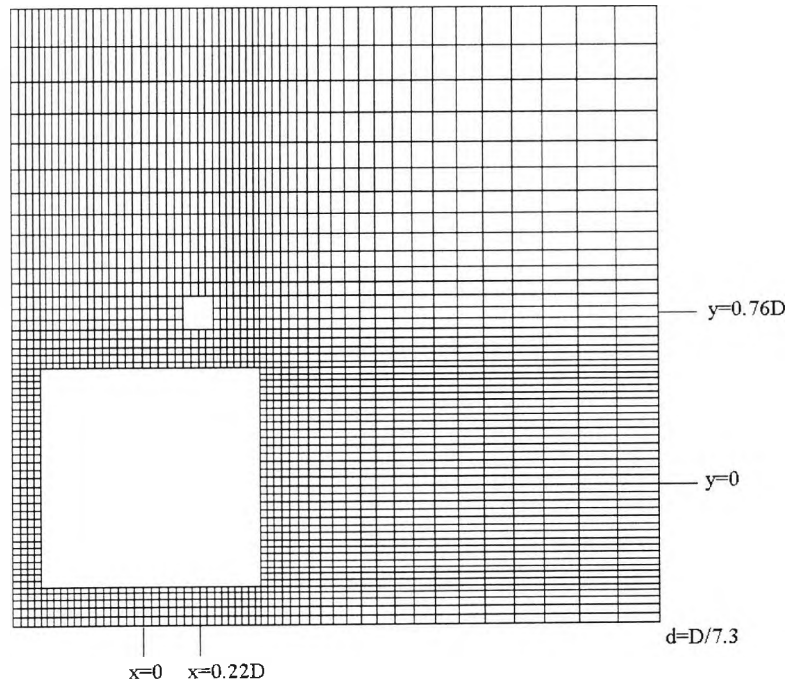


Figure 5.13: Grid arrangement (4) for a square cylinder with control cylinder.

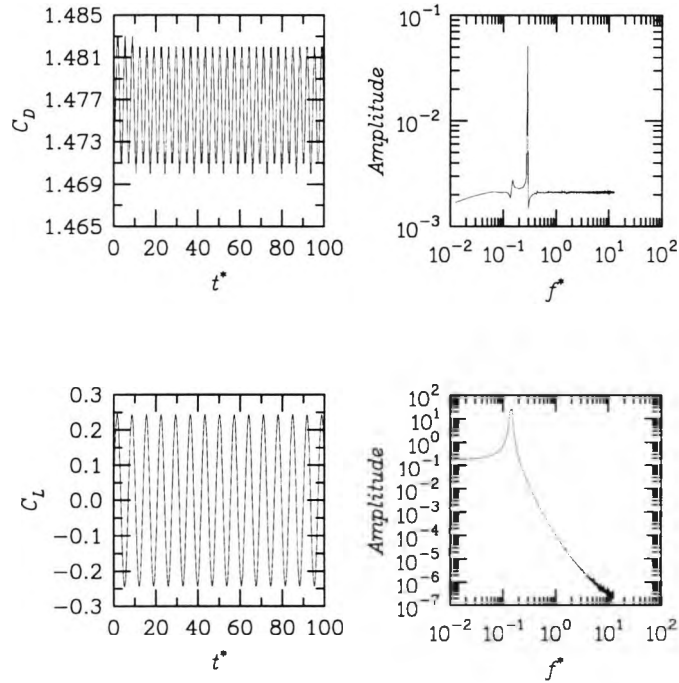


Figure 5.14: Time histories for the drag and lift coefficients for a square cylinder at  $Re=100$  with no control cylinder (RUN 1); showing also the power spectra.

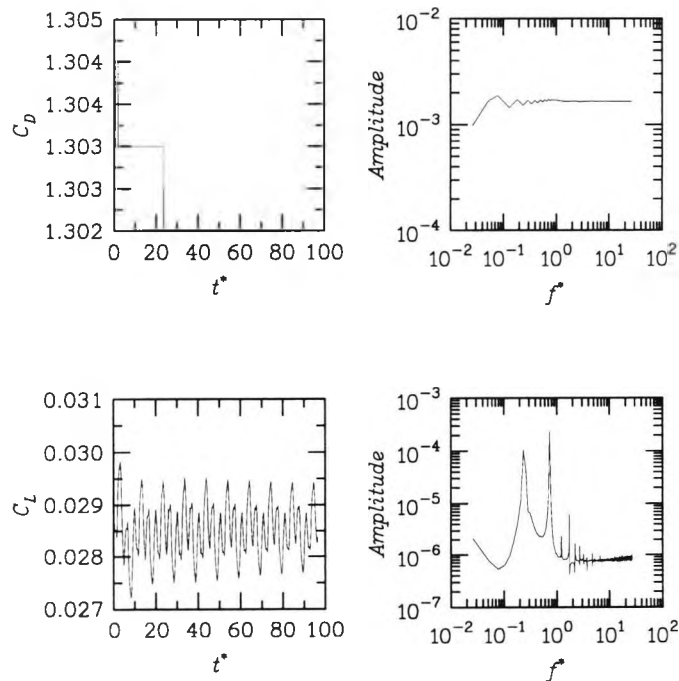


Figure 5.15: Time histories for the drag and lift coefficients for a square cylinder at  $Re=100$  with a control cylinder (RUN 2:  $D/d=7.14$ ,  $x/D=1.02$ ,  $y/D=0.95$ ); showing also the power spectra.

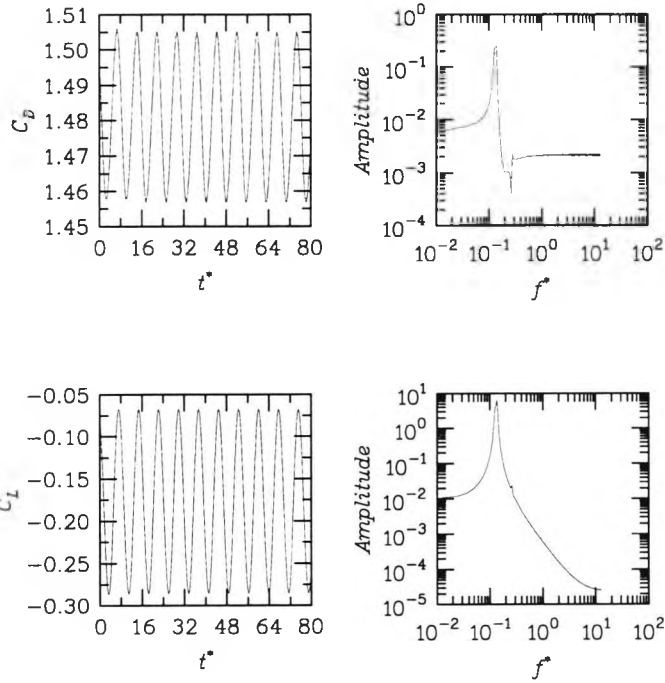


Figure 5.16: Time histories for the drag and lift coefficients for a square cylinder at  $Re=100$  with a control cylinder (RUN 3:  $D/d=5.5$ ,  $x/D=0.59$ ,  $y/D=1.21$ ); showing also the power spectra.

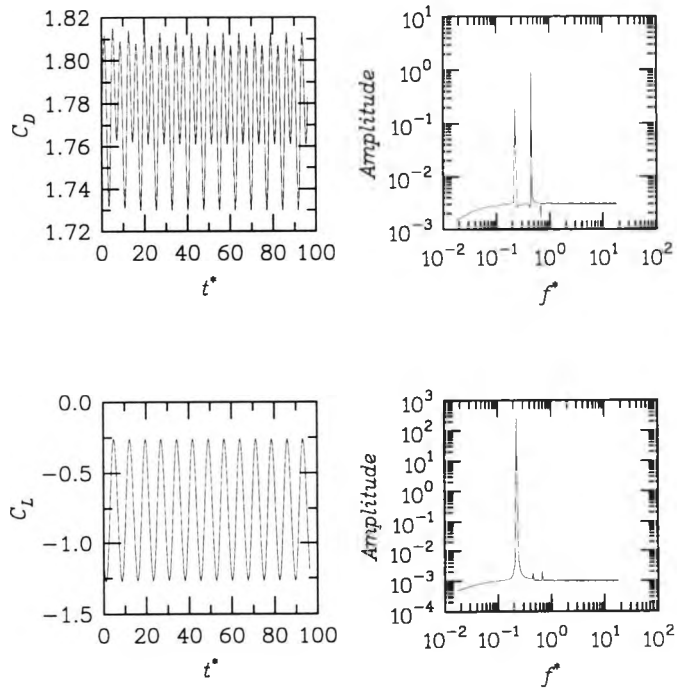
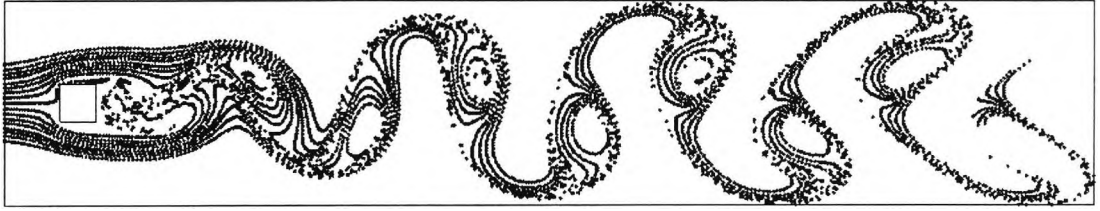
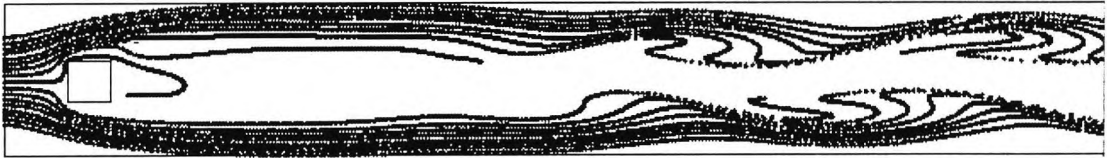


Figure 5.17: Time histories for the drag and lift coefficients for a square cylinder at  $Re=100$  with a control cylinder (RUN 4:  $D/d=7.3$ ,  $x/D=0.22$ ,  $y/D=0.76$ ); showing also the power spectra.

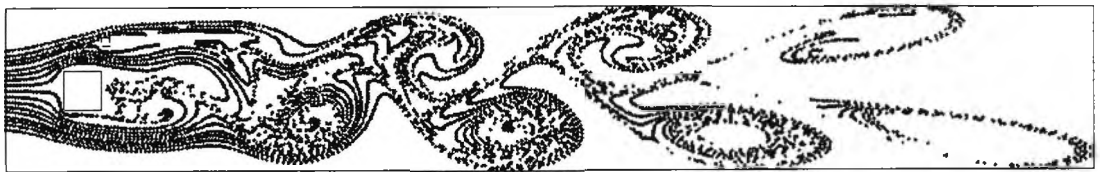
RUN 1



RUN 2



RUN 3



RUN 4

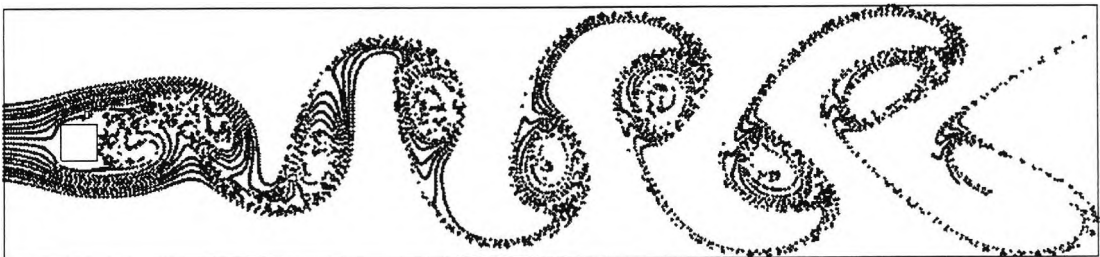


Figure 5.18: Streaklines for the four runs before and after inserting a control cylinders.

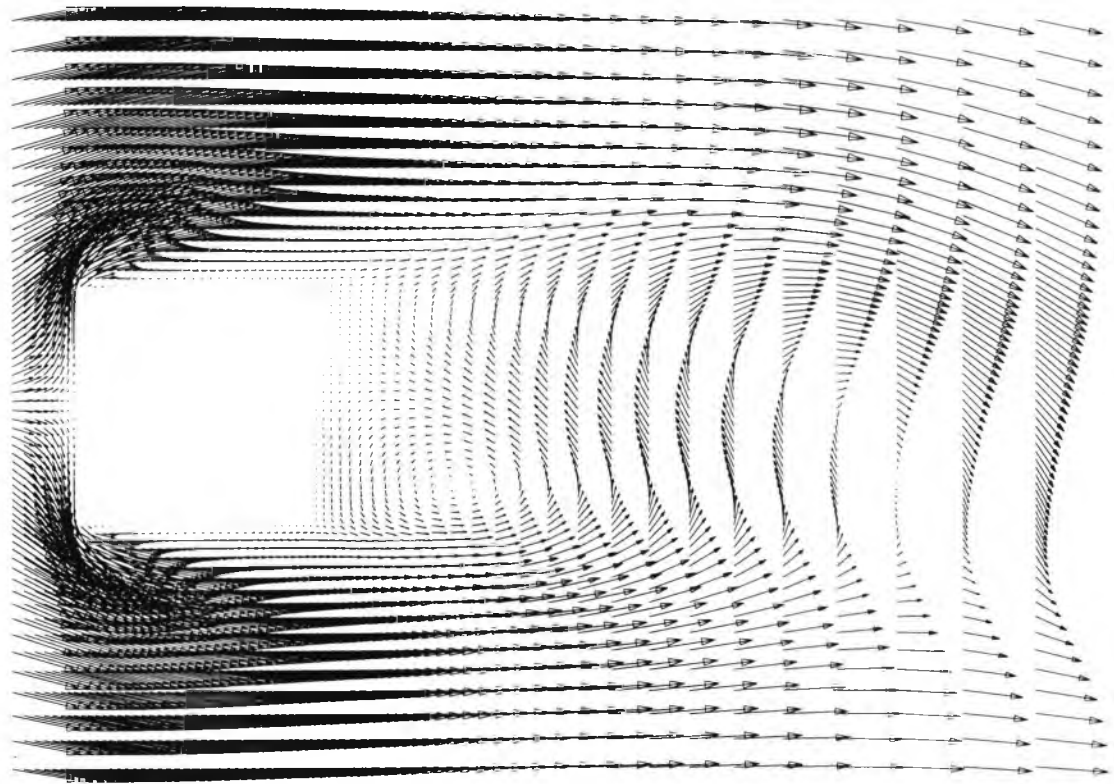


Figure 5.19: Velocity vectors around a square cylinder at  $Re=100$ , with no control.  
 (The largest arrow indicates a velocity of  $1.56 \times 10^{-3}$  m/s)

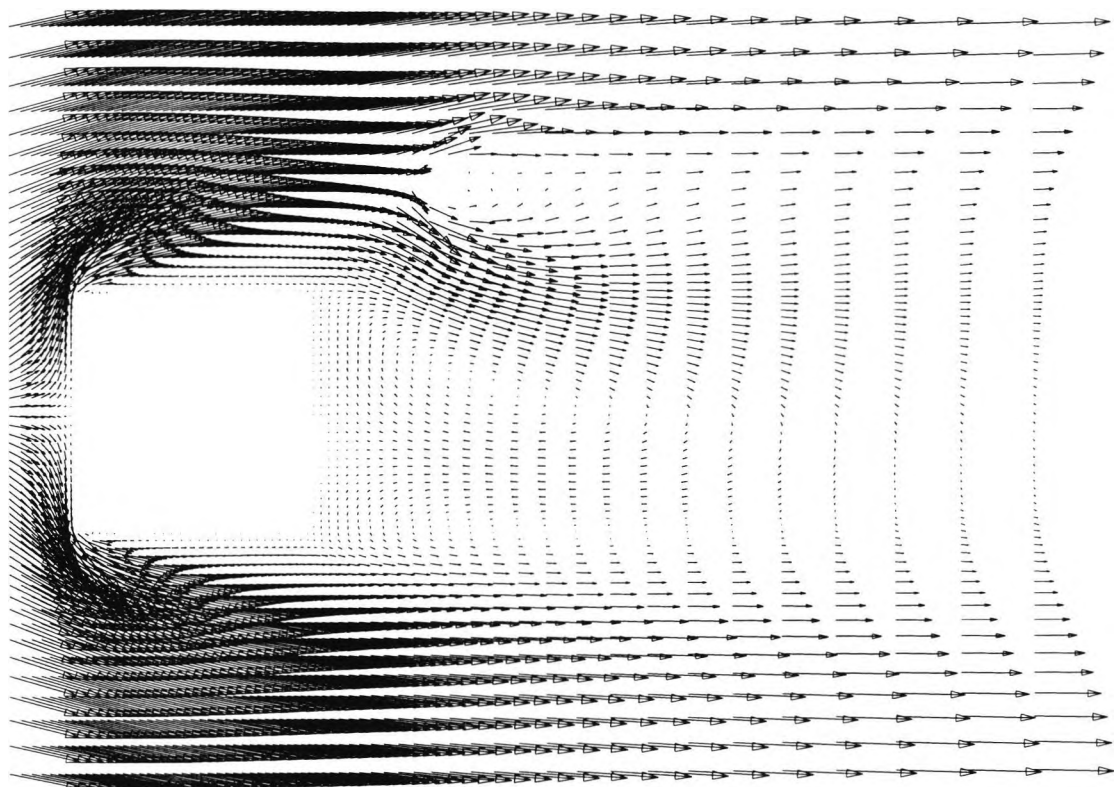


Figure 5.20: Velocity vectors around a square cylinder at  $Re=100$ , with control as in grid arrangement (2).

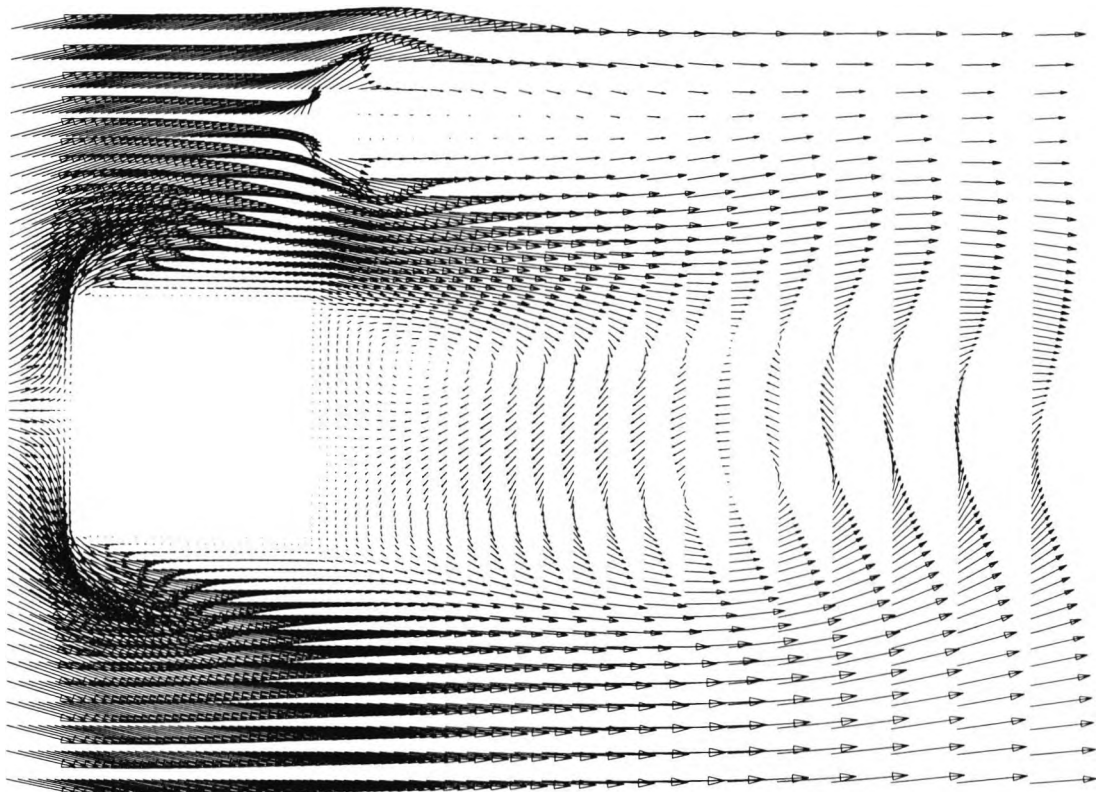


Figure 5.21: Velocity vectors around a square cylinder at  $Re=100$ , with control as in grid arrangement (3).

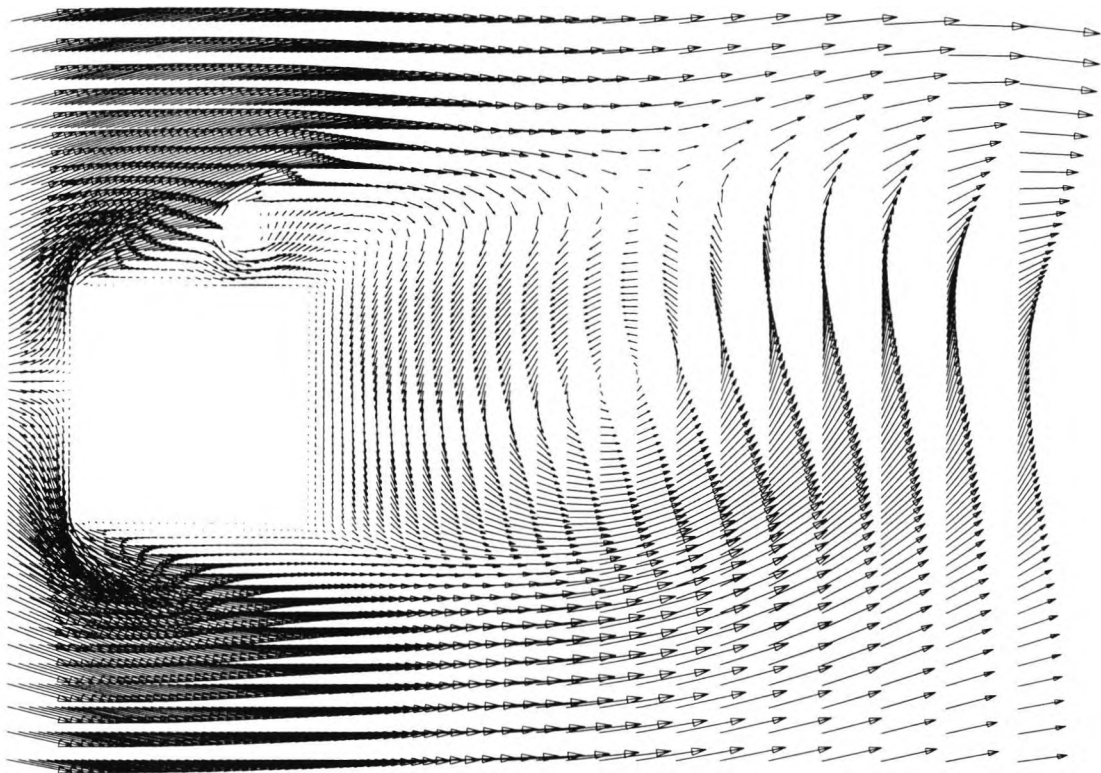


Figure 5.22: Velocity vectors around a square cylinder at  $Re=100$ , with control as in grid arrangement (4).

## 5.6 Turbulent Flow Simulations

No further modifications were necessary in order to simulate a control cylinder in turbulent flow conditions: the control cylinder was treated in exactly the same way as the second cylinder in Chapter Four. Results were obtained for both circular and square cylinders.

### 5.6.1 Circular Cylinder

Sakamoto and Haniu (1994) investigated the suppression of vortex shedding from a circular cylinder by controlling the flow around it using a small-diameter control cylinder placed near the main cylinder. Their experiments were carried out at a Reynolds number of  $6.5 \times 10^4$ . The present investigations were performed for the same Reynolds number.

In order to make comparisons with the experimental data, the same notation and definitions were used. A control cylinder of length ( $d$ ) is introduced, at an angle ( $\alpha$ ) from the centre plane and at a distance  $G$  away from the main cylinder. The main cylinder is of diameter ( $D$ ). Figure 5.23 shows the definition sketch and coordinate system. In the experiments of Sakamoto and Haniu (1994), the position of the control cylinder was varied in the region of  $G=0.2$ - $10$ mm (i.e.  $G/D=0.004$ - $0.20$ ). For the present purposes, two values of  $G/D$  were studied, namely  $0.082$  and  $0.122$ . These correspond to values of  $G = 4$  and  $6$ mm respectively.

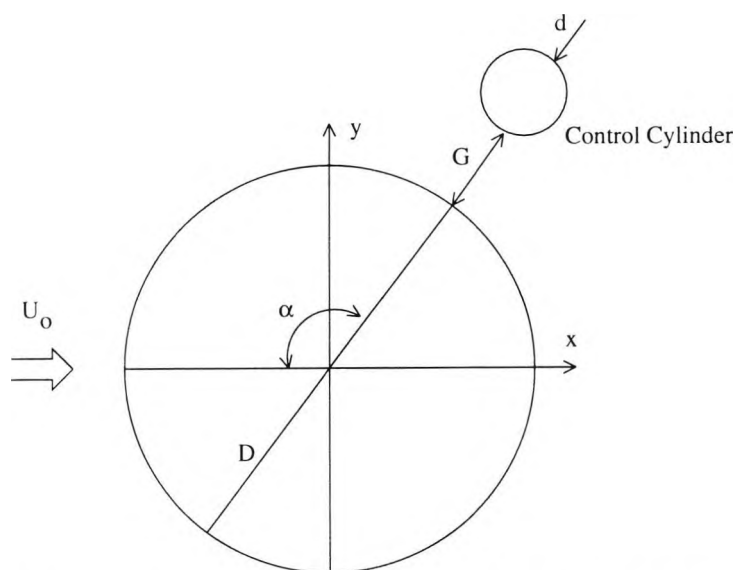
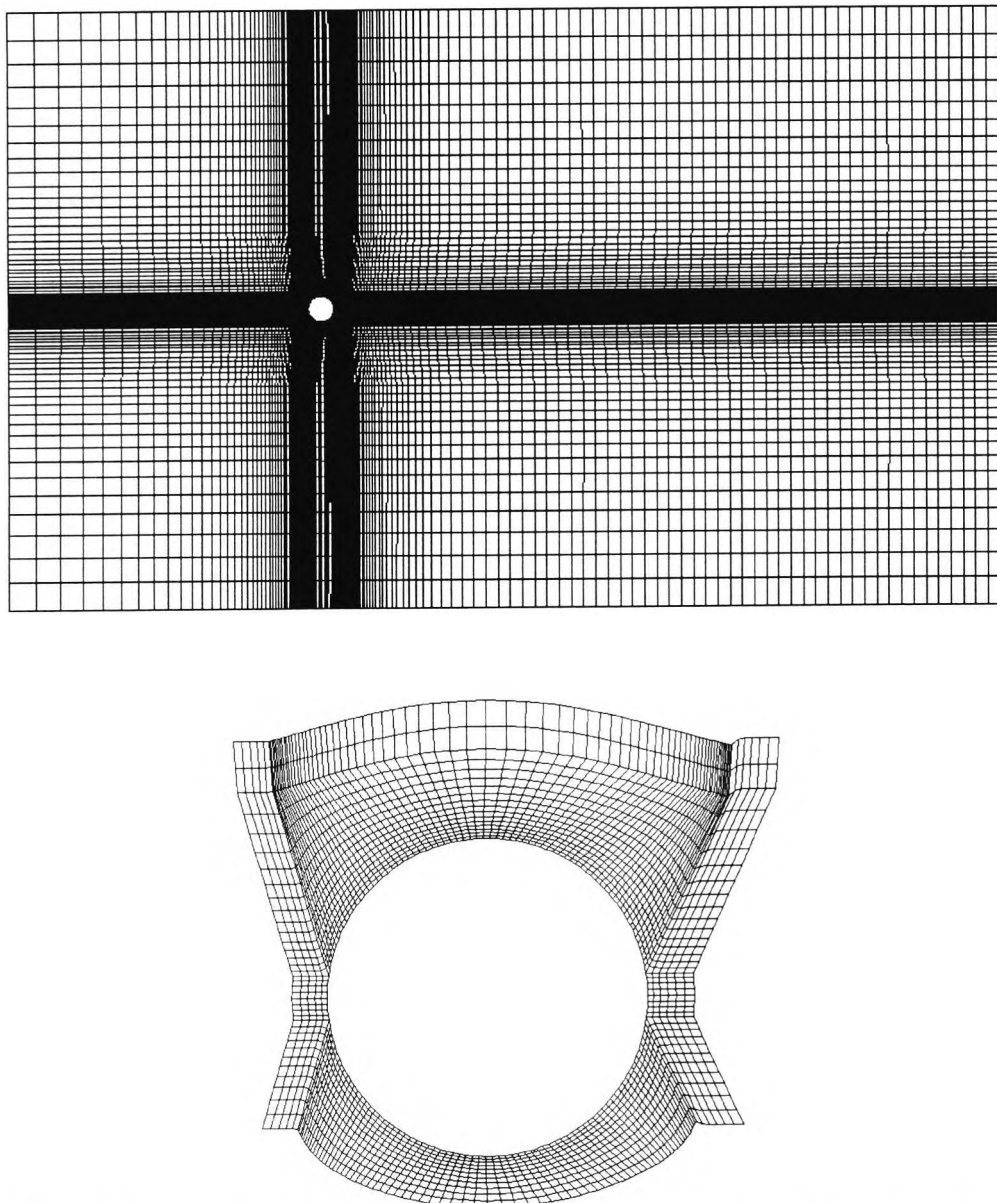


Figure 5.23: Definition sketch and coordinate system.

In the experiments, the diameter of the main cylinder was  $D=49\text{mm}$  and that of the control cylinder was  $d=3\text{mm}$ , i.e.  $D/d=17$ . In the predictions, due to the limitations of the grid-generation code,  $D/d$  was not constant. Two values were selected: 0.06 and 0.09. In the experiments, the angle between the main cylinder and control cylinder was in the range  $\alpha=0^\circ-180^\circ$ . Three values of angles of  $\alpha$  were computed, namely:  $60^\circ$ ,  $90^\circ$ , and  $120^\circ$ . Six grids were created in total to model the control cylinder. The whole grid, and close up of the main cylinder is shown in Figure 5.24. Figure 5.25 (a) to (f) show close ups of the main cylinder and the six control cylinder configurations. The grid used consisted of  $195 \times 98$  nodes.



*Figure 5.24: Grid without control cylinder and close up of the main cylinder.*

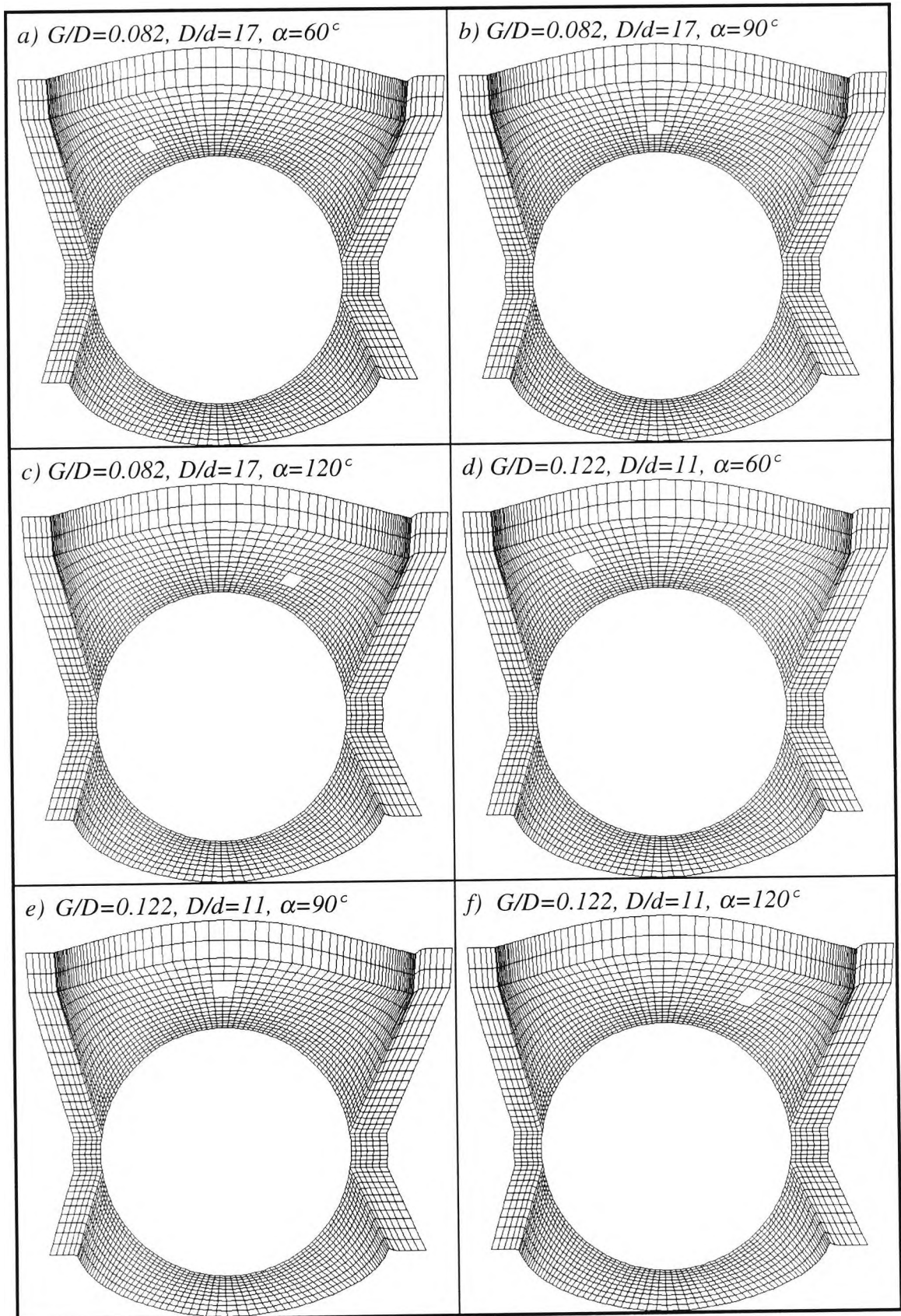


Figure 5.25: Grid arrangements for the runs with control cylinder.

The modified k- $\epsilon$  model and the SMART scheme were used, with  $\Delta t^*=0.001$ . These are the same condition as in Section 3.7.2. The present predictions of the main parameters are presented in Table 5.5.

The time histories of the drag and lift coefficients and their power spectra, with and without a control cylinder, are shown in Figure 5.26-Figure 5.31. The figures and the table show that the minimum values of  $\overline{C}_D$  are obtained when the control cylinder is positioned at  $\alpha=60^\circ$  and  $\alpha=120^\circ$  (i.e. RUNs 2,4,5, and 7) . The value of  $\overline{C}_L$  takes a maximum value when  $\overline{C}_D$  is at its lowest. This occurs at  $\alpha=60^\circ$  for RUN 2 and at  $\alpha=120^\circ$  for RUN 4. At  $\alpha=60^\circ$ , the separation point is moved downstream due to the accelerated flow in the gap between the main cylinder and the control. At  $\alpha=120^\circ$ , the reattached shear layer on the main cylinder remains attached until near the rear stagnation point. As a result, a large lift force is generated, because the pressure on the upper surface is considerably lower than that on the lower surface.

It can be seen from Table 5.5 that maximum reduction of fluctuating drag is achieved for RUN 2, where  $C_{Dr}=0.245$  and RUN 4, where  $C_{Dr}=0.692$ . At other positions the fluctuating drag remains the same as for an isolated cylinder. The fluctuating lift is reduced for all positions, but mostly for RUN 2, where  $C_{Lr}=0.087$ . When the control cylinder is placed at the locations for RUNs 2 and 4, it is possible to suppress the vortex shedding completely. This is evident from the disappearance of the peaks in the power spectra and the reduction of the Strouhal number to 0.004 and 0.007 respectively.

Figure 5.33 (a) and (b) show the predicted distributions of the time averaged surface pressure coefficient ( $C_p$ ) for the main cylinder, for different positions of the control cylinder. It can be seen from both figures that when  $\alpha=60^\circ$ , the separation point is displaced downstream, from around  $120^\circ$  where it occurs for the isolated cylinder. This confirms the supposition of Sakamoto and Haniu (1994) that the mechanism of flow control is associated with the displacement of the separation point.

Sakamoto and Haniu (1994) identified four regions for placing the control cylinder. Region I, where  $0^\circ < \alpha < 70^\circ$ , is when the mean drag decreases. Region II, where  $70^\circ < \alpha < 110^\circ$ , is when the mean drag increases. Region III, where  $110^\circ < \alpha < 135^\circ$ , is when the mean drag decreases again and region IV, where  $135^\circ < \alpha < 180^\circ$ , is when the mean drag does not vary. The present predictions were carried out in the first three regions, as region IV seems not to affect the flow conditions.

Figure 5.34 shows the predicted and measured values of mean drag for the two values of  $G/d$ . As explained in section 3.7.2, the present predictions underestimate the value of mean drag for the single isolated cylinder, therefore the predictions of the case where a control cylinder is present are also on the low side. However, the predictions for each region exhibit similar trends as the experimental data. In region I, the effectiveness of the control cylinder is attributed to the control of the boundary layer on the main cylinder. In regions II and III, the effectiveness of the control cylinder is attributed to the control of the free shear layer. Maximum suppression of mean drag is achieved in region I, at  $\alpha=60^\circ$ .

In region II, mean drag increases compared with the region I. This is due to the fact that the shear layer is forced to bend by the control cylinder. The rolling up of the shear layer is intensified and the base pressure increases, as shown in Figure 5.33 (a) and (b).

In region III, the shear layer which separated earlier is forcibly reattached and remains so until near the rear stagnation point. The base pressure is then decreased relative to the isolated cylinder, as shown in Figure 5.33 (a) and (b).

Figure 5.35 shows the computed streaklines for an isolated circular cylinder at  $Re=6.5 \times 10^4$ . Figure 5.36 and Figure 5.37 show computed streaklines for the control cylinder cases discussed above. For RUN 2 (Figure 5.36(a)), the separation point is moved downstream and a complete breakdown of vortex shedding patterns is evident. For RUN 3 (Figure 5.36(b)), vortex shedding is restored. For RUN 4 (Figure 5.36(c)), an unstable flow pattern is produced with a major reduction in all the coefficients. Figure 5.37 (a) to (c) show similar patterns, but since the control cylinder is placed further away from the main cylinder (i.e.  $G/D=0.122$ ), the effects are less pronounced as before.

Grid	G/D	$\alpha$	$\bar{C}_D$	$\tilde{C}_D$	$C_{Dr}$	$\bar{C}_L$	$\tilde{C}_L$	$C_{Lr}$	St
Experiments of Sakamoto and Haniu (1994) (no control cylinder)									
-	-	-	1.240	0.120	-	0	0.460	-	-
Present Predictions									
1	-	-	1.025	0.139	1.000	-0.006	0.995	1.000	0.292
2	0.082	60°	0.600	0.034	0.245	0.331	0.087	0.087	0.007
3	0.082	90°	0.948	0.142	1.022	-0.022	0.456	0.458	0.195
4	0.082	120°	0.874	0.096	0.691	0.321	0.443	0.445	0.004
5	0.122	60°	0.771	0.150	1.079	0.006	0.544	0.557	0.220
6	0.122	90°	1.014	0.152	1.094	0.280	0.480	0.482	0.147
7	0.122	120°	0.757	0.154	1.108	0.211	0.470	0.472	0.147

Table 5.5: Results for the circular cylinder with control cylinder at  $Re=6.5 \times 10^4$ .

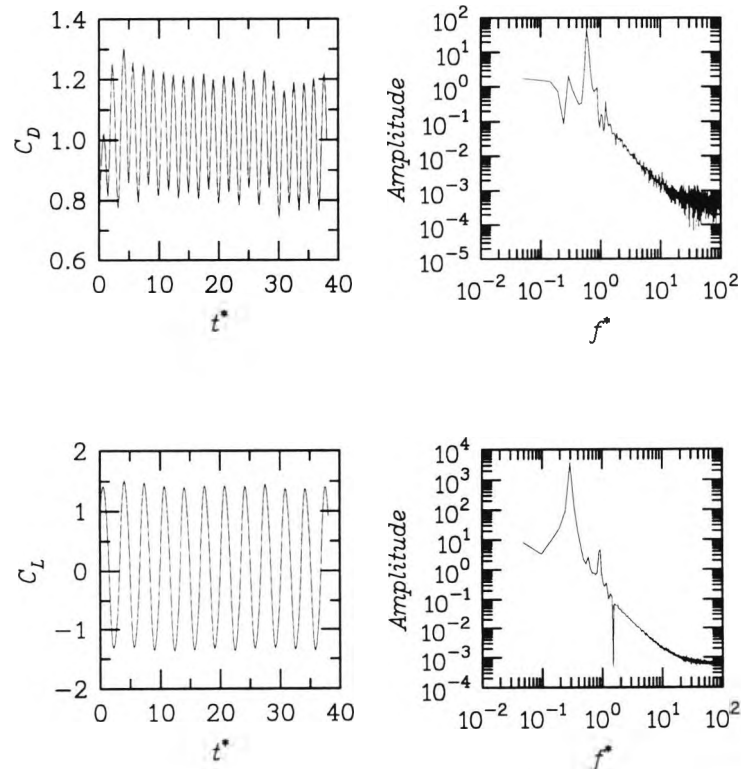


Figure 5.26: Drag and lift time histories and power spectra for RUN 1 (the case with no control cylinder).

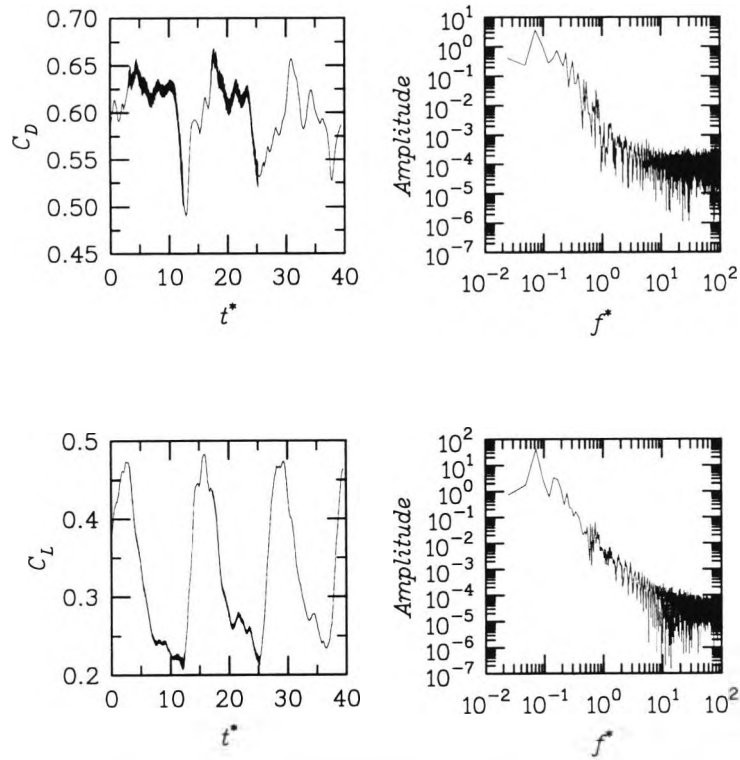


Figure 5.27: Drag and lift time histories and power spectra for RUN 2  
( $G/D=0.082$ ,  $D/d=17$ ,  $\alpha=60^\circ$ ).

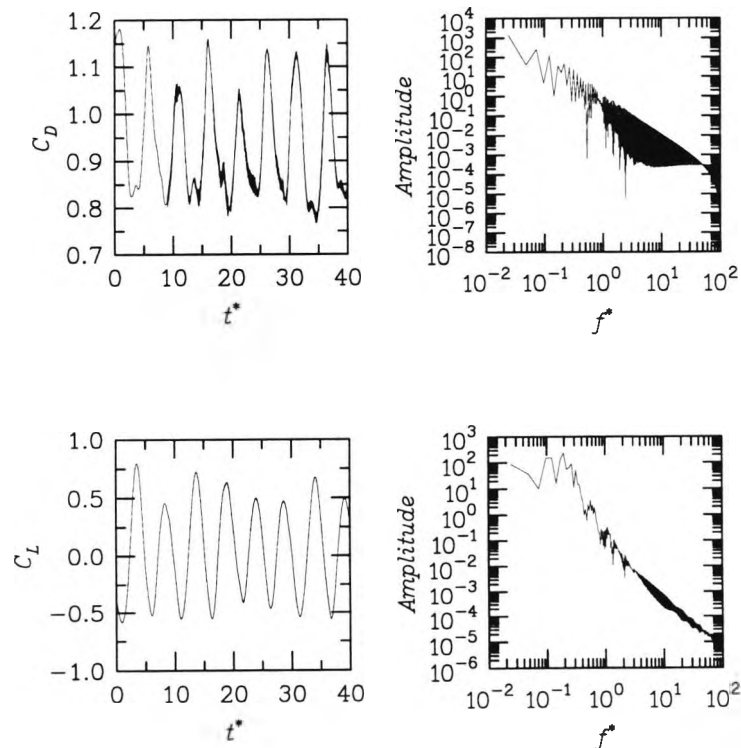


Figure 5.28: Drag and lift time histories and power spectra for RUN 3  
( $G/D=0.082$ ,  $D/d=17$ ,  $\alpha=90^\circ$ ).

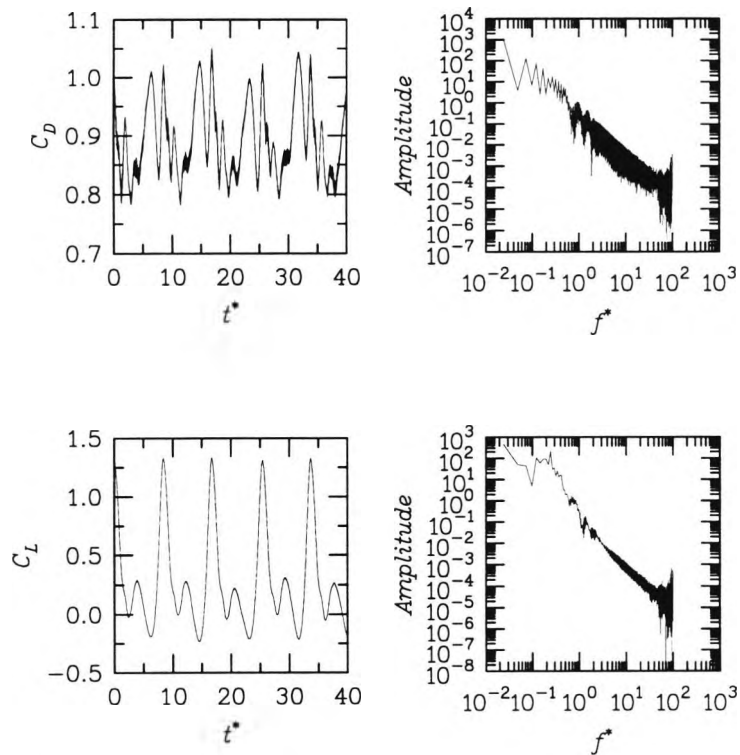


Figure 5.29: Drag and lift time histories and power spectra for RUN 4  
 ( $G/D=0.082$ ,  $D/d=17$ ,  $\alpha=120^\circ$ ).

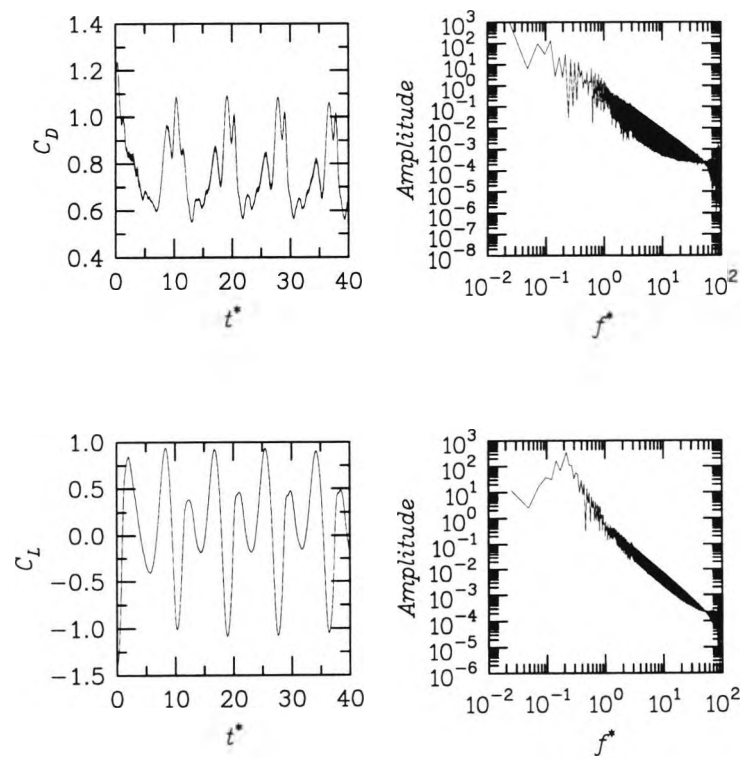


Figure 5.30: Drag and lift time histories and power spectra for RUN 5  
 ( $G/D=0.122$ ,  $D/d=11$ ,  $\alpha=60^\circ$ ).

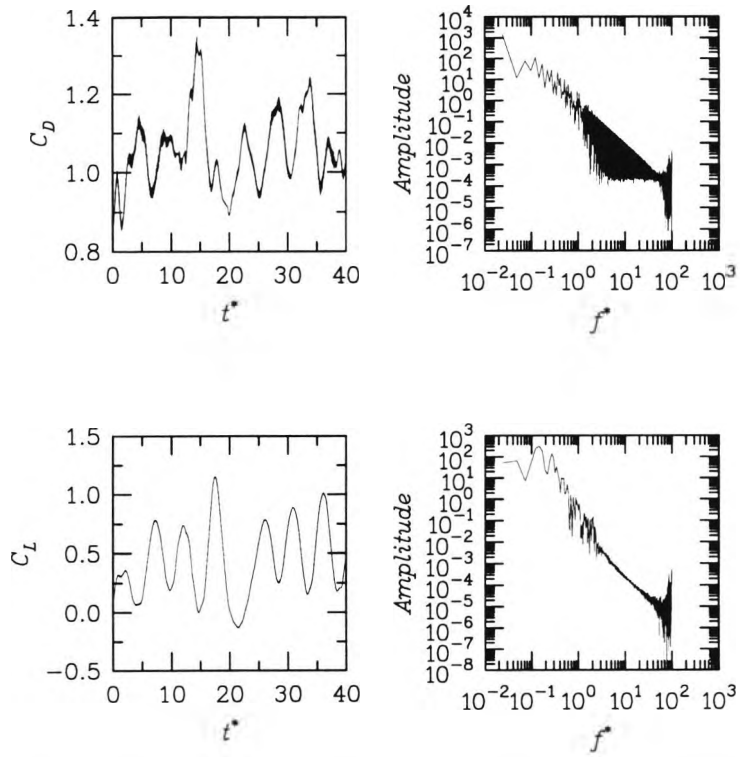


Figure 5.31: Drag and lift time histories and power spectra for RUN 6 ( $G/D=0.122$ ,  $D/d=11$ ,  $\alpha=90^\circ$ ).

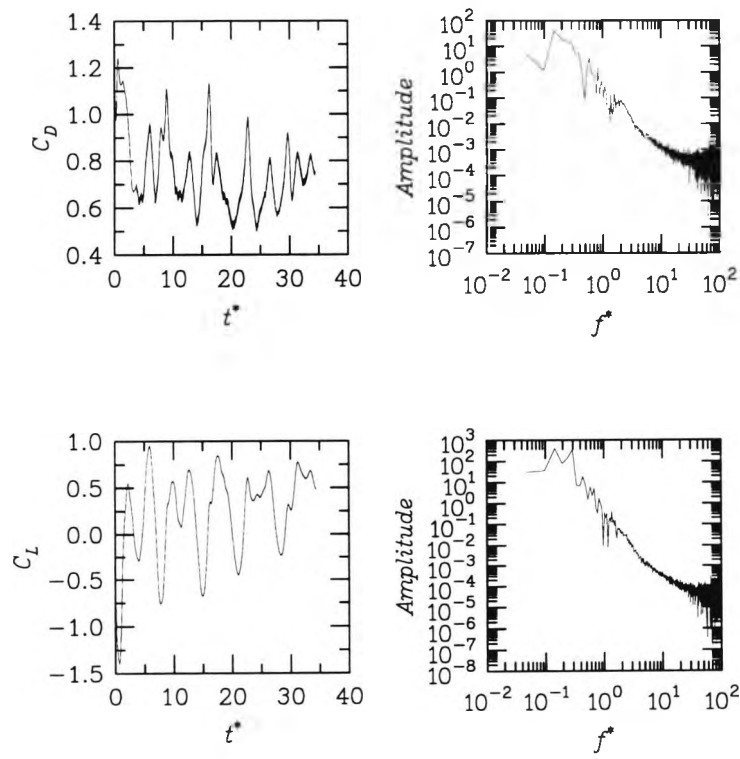
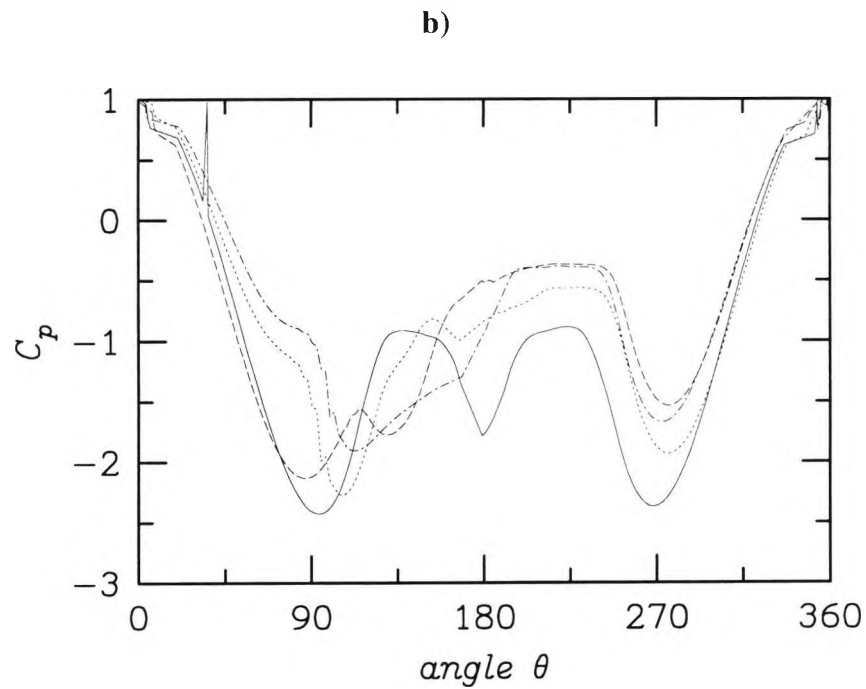
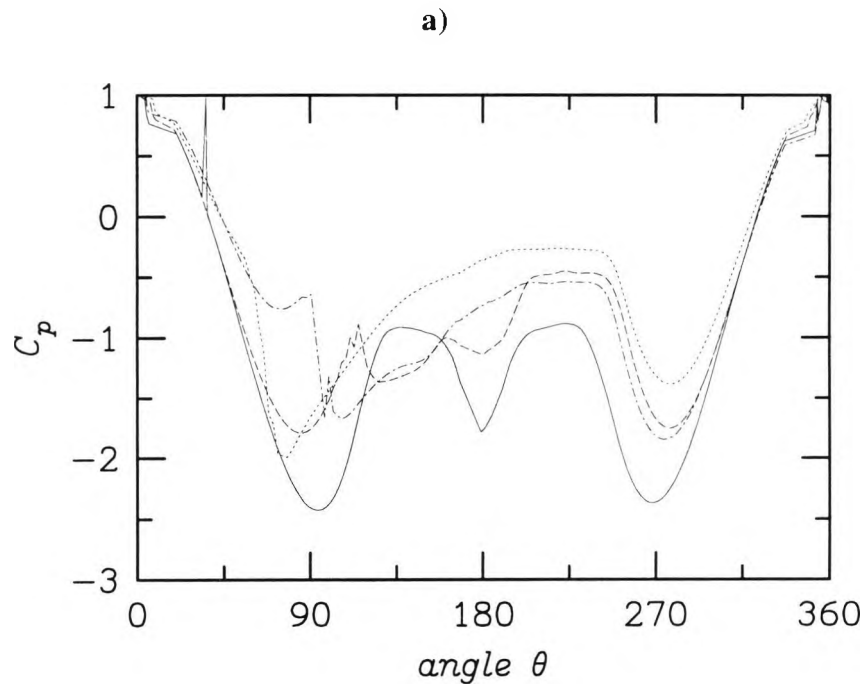


Figure 5.32: Drag and lift time histories and power spectra for RUN 7 ( $G/D=0.122$ ,  $D/d=11$ ,  $\alpha=120^\circ$ ).



- No Control
- - -  $\alpha=60^\circ$
- · ·  $\alpha=90^\circ$
- · -  $\alpha=120^\circ$

Figure 5.33: Predicted distribution of the time averaged pressure coefficient ( $C_p$ ) for  
a)  $G/D=0.082$  and b)  $G/D=0.122$

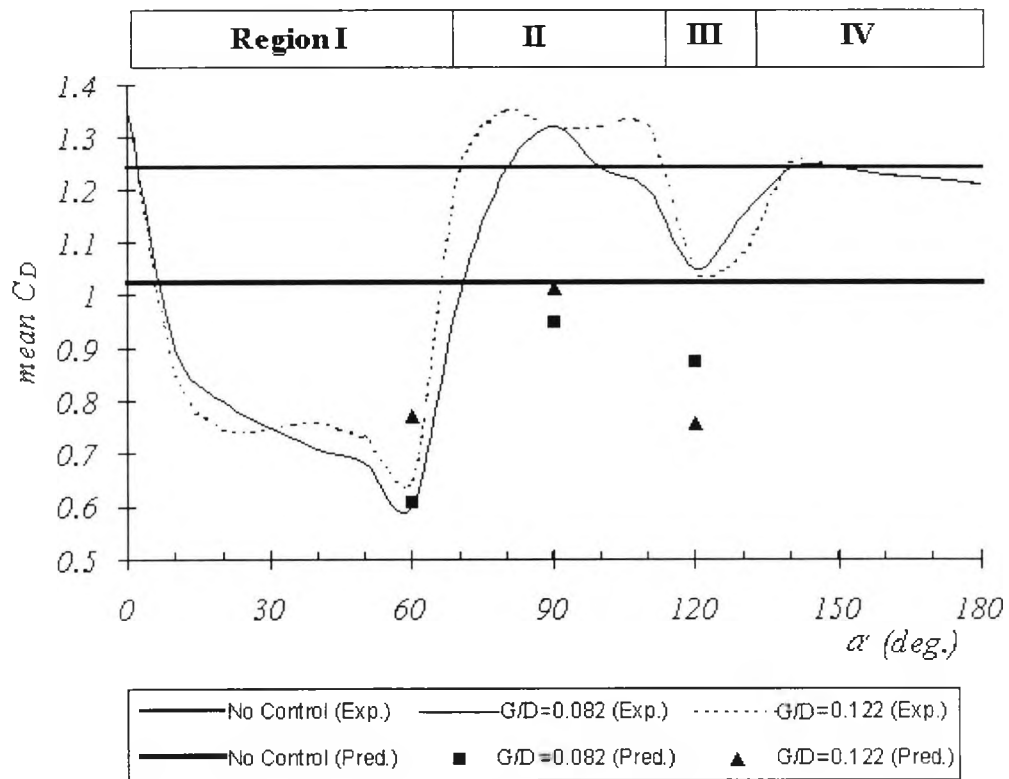


Figure 5.34: Distribution of mean  $C_D$  for different positions of the control cylinder, showing comparisons between the results of Sakamoto and Haniu (1994) and the present predictions.

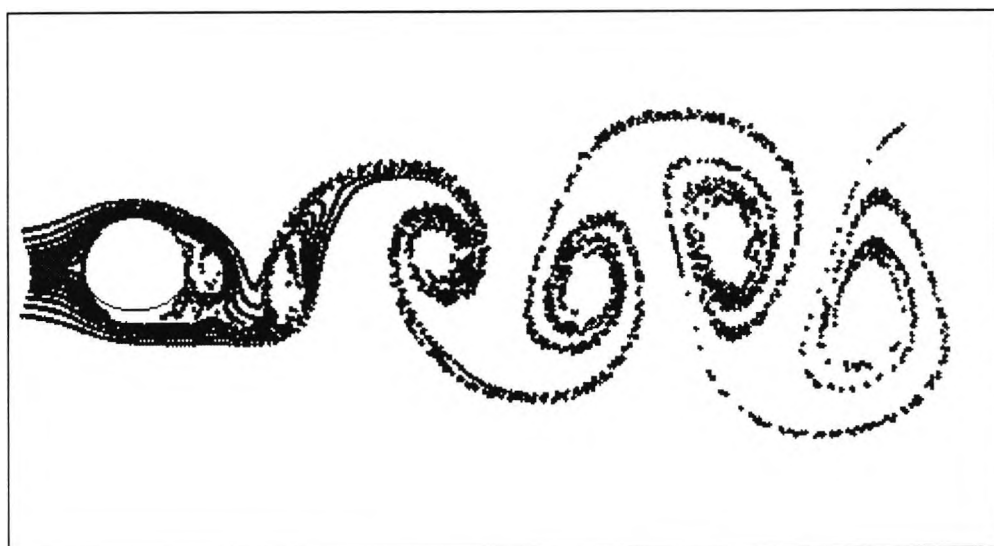
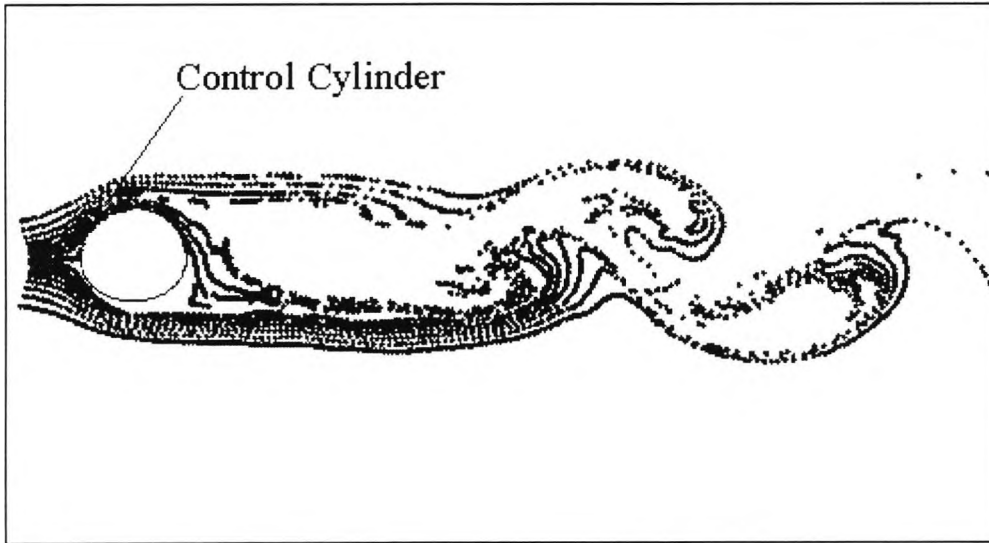
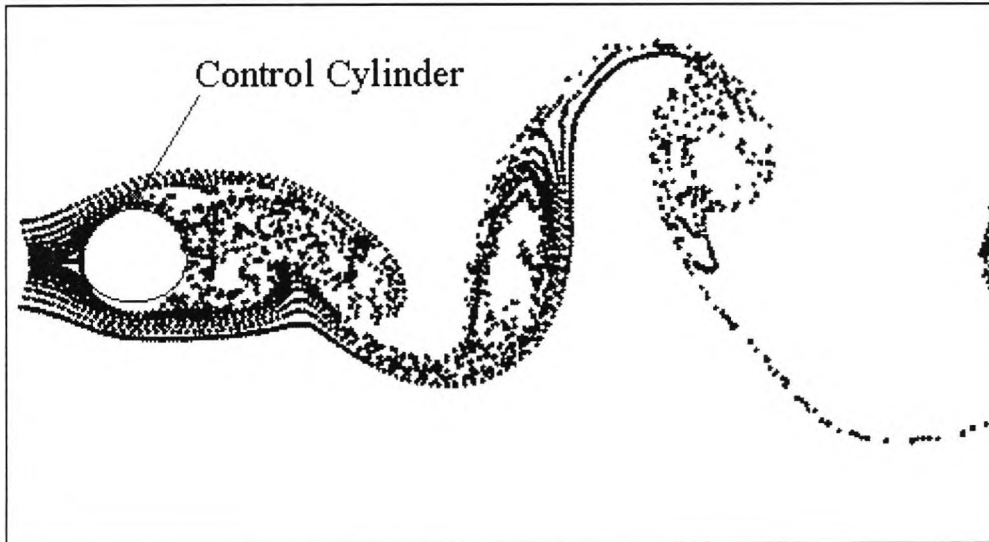


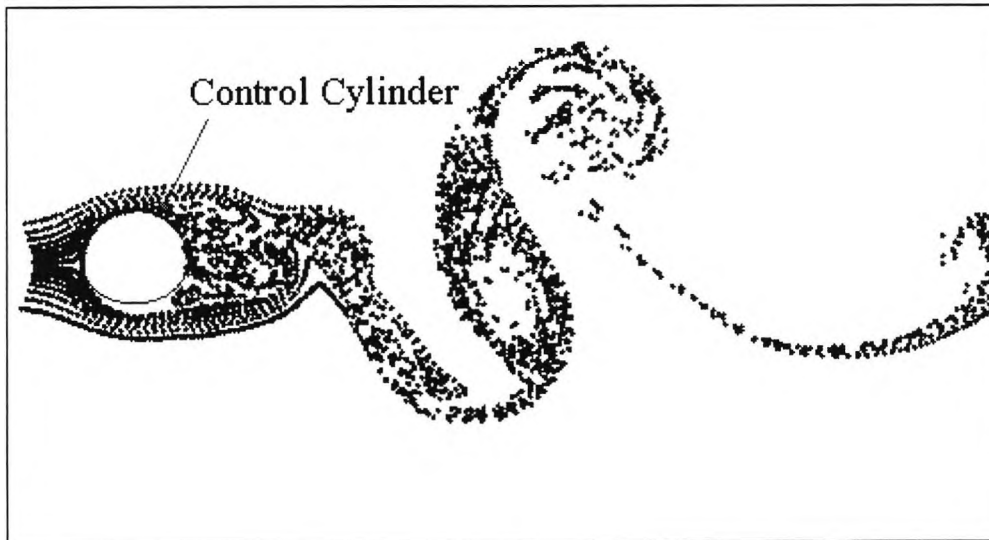
Figure 5.35: Streaklines with no control cylinder (RUN 1).



a)

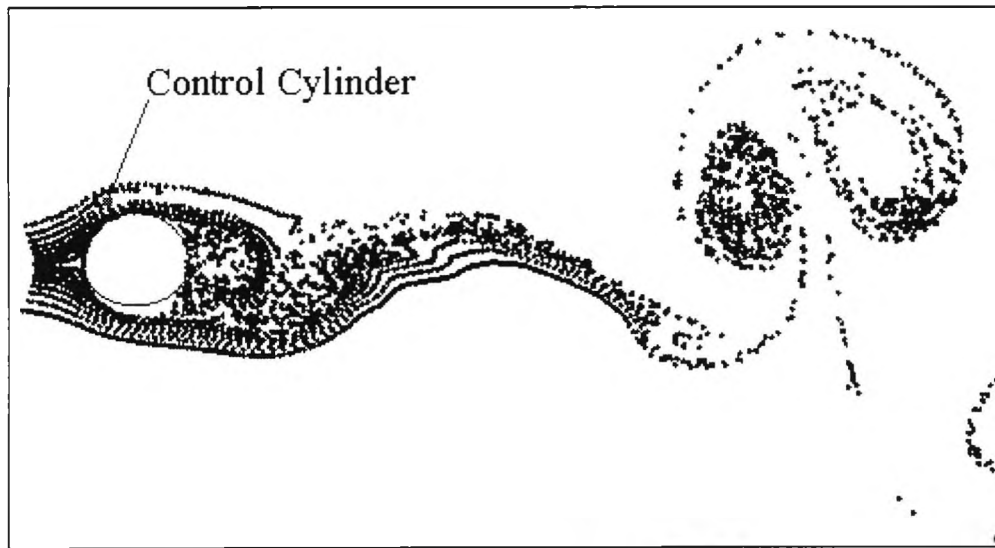


b)

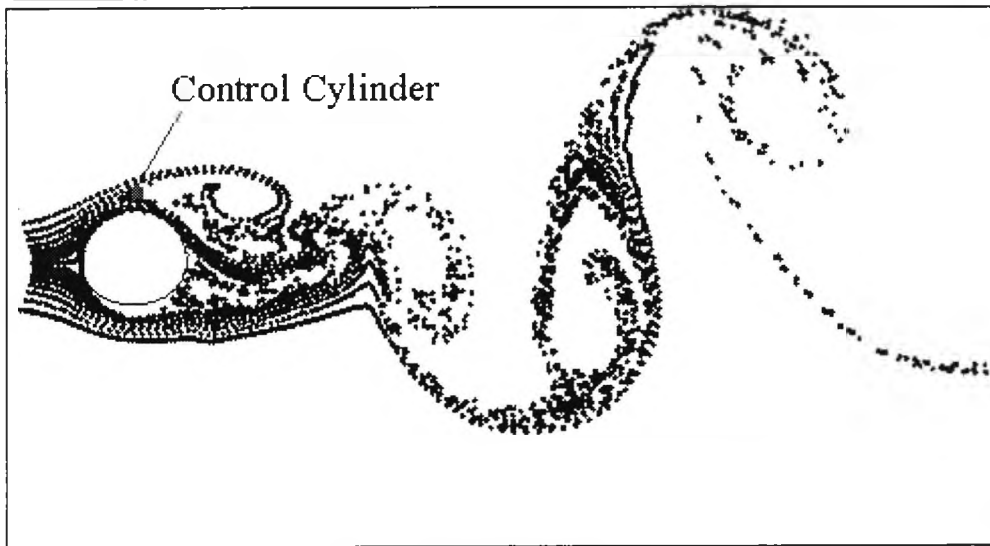


c)

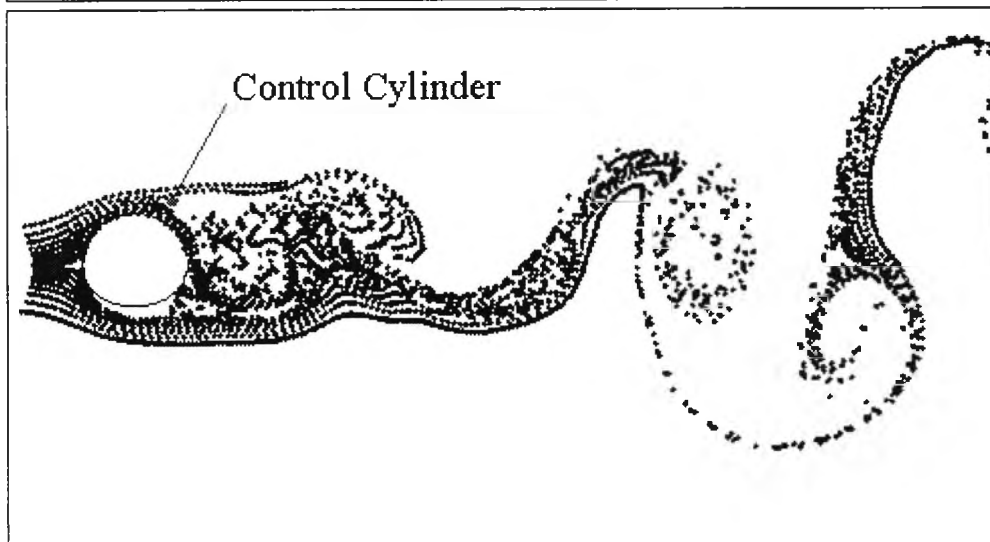
Figure 5.36: Streaklines with control cylinder for a) RUN 2 ( $G/D=0.082$ ,  $D/d=17$ ,  $\alpha=60^\circ$ ); b) RUN 3 ( $G/D=0.082$ ,  $D/d=17$ ,  $\alpha=90^\circ$ ) and c) RUN 4 ( $G/D=0.082$ ,  $D/d=17$ ,  $\alpha=120^\circ$ ).



a)



b)



c)

Figure 5.37: Streaklines with control cylinder for a) RUN 5 ( $G/D=0.122$ ,  $D/d=11$ ,  $\alpha=60^\circ$ ); b) RUN 6 ( $G/D=0.122$ ,  $a/d=0.09$ ,  $\alpha=90^\circ$ ) and c) RUN 7 ( $G/D=0.122$ ,  $D/d=11$ ,  $\alpha=120^\circ$ ).

## 5.6.2 Square Cylinder

Sakamoto, Tan and Haniu (1991) obtained experimental data on the suppression of vortex shedding from a square cylinder by means of a small circular control cylinder at  $Re=4.2 \times 10^4$ . The present investigations were carried out for the same Reynolds number.

A control cylinder of height ( $d$ ) is introduced, above and parallel to a square cylinder of height  $W$  (see Figure 5.38). The position of the control cylinder is fixed via the ratios  $S/W$  and  $T/W$ , where  $S$  is the streamwise distance from the upstream corner and  $T$  is the lateral distance from the top side. The coordinates are measured from the top left hand corner of the main cylinder. In the experiments of Sakamoto, Tan and Haniu (1991), a circular control cylinder was used, but in the present simulations a square obstacle is used, due to the limitations in the grid-generation method.

The same grid (136x118) described in section 3.5.2 and used to model an isolated square cylinder, was used here. The modified  $k-\epsilon$  model, with the SMART scheme was used, with a  $\Delta t^*$  of 0.007. Table 5.6 compares the predicted values of the main parameters compared with the ones obtained experimentally by Sakamoto, Tan and Haniu (1991) at  $Re=4.2 \times 10^4$ , without a control cylinder. The results show a good comparison for mean drag and Strouhal numbers. The values of rms drag and lift however are overestimated in the predictions.

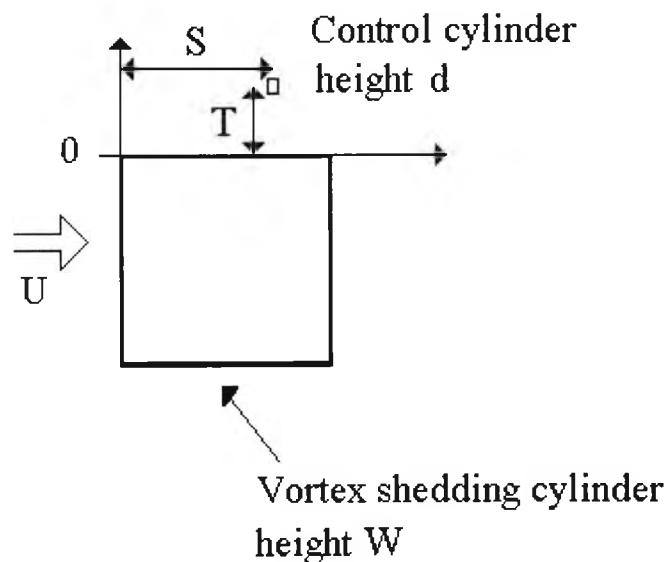


Figure 5.38: Definition sketch and coordinate system.

The ratio of main cylinder to control cylinder heights ( $W/d$ ) was not kept constant, but varied in the range 7-17 depending on the many position where the control cylinder was placed in order to arrive at optimum suppression. In the experiments, the ratio of  $W/d$  ranged between 7 and 14. Twenty nine different positions were explored along the top side of the cylinder to determine the optimum position for the control cylinder to suppress vortex shedding.

The main effect of a control cylinder on the main cylinder is that it reduces the fluid forces acting on the latter by controlling the separated shear layer from it. It is therefore necessary to identify the position of this layer. Two experimental methods exist for locating it. Fage and Johansen (1927) defined the position of the outer and inner boundaries of this layer as the points where the time-averaged velocity becomes greatest and least, respectively. Sasaki and Kiya (1984) measured the turbulence intensity in the shear layer and indicated that a position with the greatest turbulence intensity is the approximate centre of the shear layer.

Figure 5.39 shows the position of the maximum time-averaged velocity as predicted in the absence of a control cylinder. The figure also shows (open circles) the positions where a control cylinder was placed. Generally the fluid forces on the body are dependent on the characteristics of the outer boundary of the shear layer, where the maximum velocity occurs, rather than at the centre of the shear layer, where the turbulence intensity is largest (Bearman and Trueman, 1972).

Table 5.7 shows the results obtained for all twenty nine control cylinder positions modelled. It is evident that the position of the control cylinder suppressing most of the fluid forces coincides with the outer boundary of the shear layer representing maximum velocity. RUNs 3, 6, 9, 13, 17, 23, and 27 are positioned nearest to the outer boundary of the shear layer along each segment of  $S/W$ . It can be seen that the mean and fluctuating drag and fluctuating lift are most suppressed for these RUNs. Mean lift however is negative for most of these RUNs. The Strouhal number is also increased for these RUNs. This is because the growth of the shear layer is prevented, so that the rolling up of the shear layer weakens. This leads to a decrease in the width of the wake, and thus an increase in the Strouhal number. The reverse occurs when the control cylinder is placed outside the shear layer. Then the width of the wake increases because the rolling-up of the shear layer is intensified, so that the Strouhal number decreases.

Thus it is considered most effective to set the control cylinder near the outer boundary of the shear layer as shown. This is in complete accord with the results of Sakamoto

Tan and Haniu (1991), who also found it more effective to place the control cylinder near the outer boundary of the shear layer, for suppressing the fluid forces.

Figure 5.40(a) shows the predicted mean drag on the main cylinder as a function of  $S/W$ . The control cylinder was moved along the line of maximum velocity (i.e. the outer boundary of the shear layer). The experimental results of Sakamoto Tan and Haniu (1991) are shown in Figure 5.40(b), for various values of control cylinder diameter. The value of mean drag is decreased as  $S/W$  increases beyond the leading edge, perhaps due to the transition between laminar and turbulence. When the control cylinder is placed inside the trailing edge, where the shear layer is supposed to start the rolling-up into the vortex formation region, mean drag is reduced. However, as the distance  $S/W$  increases beyond 1 (ie the trailing edge of the cylinder), the drag reduction is not so remarkable.

Figure 5.41 and Figure 5.42 show the rms drag and lift of the main cylinder, as a function of  $S/W$ . Again, the control cylinder was moved along the line of maximum velocity. In the predictions, the values of  $\tilde{C}_D$ , and  $\tilde{C}_L$  are overestimated, but the predicted trends are similar to that observed in the experiments. Again maximum reduction in  $\tilde{C}_D$  and  $\tilde{C}_L$  occur when the control cylinder is placed inside the two edges of the main cylinder. Figure 5.43 and Figure 5.44 show the time histories for the drag and lift coefficient and the power spectra without and with a control cylinder respectively. In the latter case, the control cylinder is placed near the leading edge of the main cylinder along the outer boundary of the shear layer (RUN 6). This is the position that produced the most suppression in the mean drag and rms drag and lift.

	$\bar{C}_D$	$\tilde{C}_D$	$\tilde{C}_L$	St
Present predictions	2.373	0.324	1.526	0.139
Sakamoto, Tan and Haniu (1991)	2.300	0.168	1.120	0.128

Table 5.6: *Predictions and experimental values of the main parameters for a square cylinder at  $Re=4.2 \times 10^4$ .*

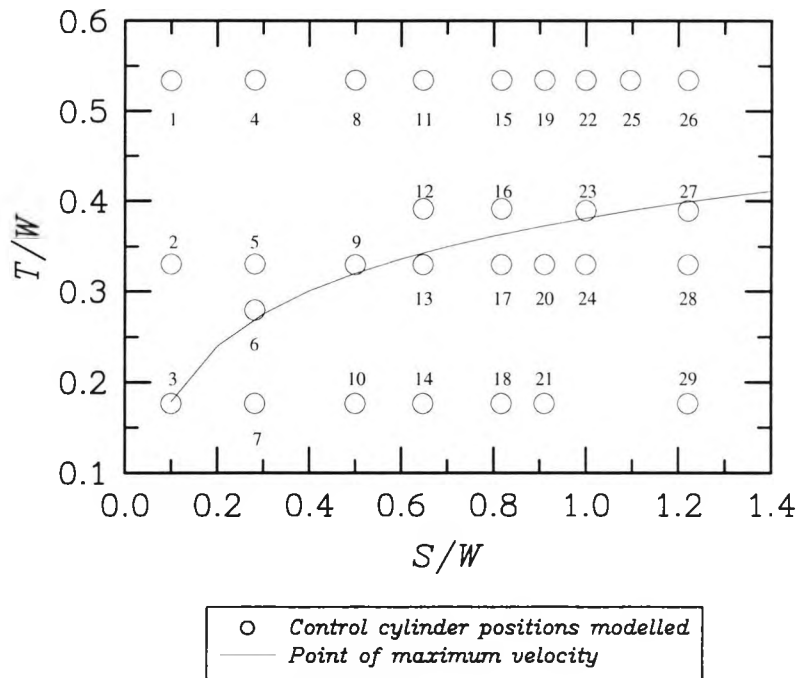


Figure 5.39: Position of maximum velocity along the cylinder, and positions of control cylinder modelled, highlighting the optimum positions.

RUN	S/W	T/W	$\bar{C}_D$	$\tilde{C}_D$	$C_{Dr}$	$\bar{C}_L$	$\tilde{C}_L$	$C_{Lr}$	St
1	0.100	0.535	2.310	0.480	1.481	-0.300	0.678	0.444	0.128
2	0.100	0.330	2.300	0.450	1.389	-0.203	0.750	0.491	0.130
<b>3</b>	<b>0.100</b>	<b>0.177</b>	<b>2.210</b>	<b>0.300</b>	<b>0.926</b>	<b>-0.105</b>	<b>1.310</b>	<b>0.858</b>	<b>0.140</b>
4	0.282	0.535	2.295	0.470	1.451	-0.295	0.667	0.437	0.120
5	0.282	0.330	2.004	0.250	0.772	-0.110	0.504	0.330	0.130
<b>6</b>	<b>0.282</b>	<b>0.280</b>	<b>1.859</b>	<b>0.167</b>	<b>0.515</b>	<b>0.017</b>	<b>0.560</b>	<b>0.367</b>	<b>0.150</b>
7	0.282	0.177	2.562	0.329	1.015	-0.422	1.445	0.947	0.130
8	0.500	0.535	2.292	0.463	1.429	-0.354	0.664	0.435	0.122
<b>9</b>	<b>0.500</b>	<b>0.330</b>	<b>2.128</b>	<b>0.232</b>	<b>0.716</b>	<b>-0.210</b>	<b>0.849</b>	<b>0.556</b>	<b>0.140</b>
10	0.500	0.177	2.598	0.275	0.849	-0.394	1.590	1.042	0.122
11	0.648	0.535	2.232	0.434	1.340	-0.430	0.570	0.374	0.122
12	0.648	0.392	2.103	0.293	0.904	-0.142	0.740	0.485	0.138
<b>13</b>	<b>0.648</b>	<b>0.330</b>	<b>2.103</b>	<b>0.243</b>	<b>0.750</b>	<b>-0.262</b>	<b>0.948</b>	<b>0.621</b>	<b>0.140</b>
14	0.648	0.177	2.554	0.259	0.800	-0.355	1.553	1.018	0.134
15	0.817	0.535	2.087	0.414	1.278	-0.157	0.470	0.308	0.122
<b>16</b>	<b>0.817</b>	<b>0.392</b>	<b>2.232</b>	<b>0.264</b>	<b>0.815</b>	<b>-0.200</b>	<b>1.108</b>	<b>0.726</b>	<b>0.140</b>
<b>17</b>	<b>0.817</b>	<b>0.330</b>	<b>2.087</b>	<b>0.252</b>	<b>0.778</b>	<b>-0.134</b>	<b>0.819</b>	<b>0.537</b>	<b>0.145</b>
18	0.817	0.177	2.483	0.272	0.840	-0.255	1.426	0.934	0.128
19	0.911	0.535	2.283	0.361	1.114	0.063	0.502	0.329	0.128
20	0.911	0.330	2.171	0.249	0.769	0.403	1.113	0.729	0.130
21	0.911	0.177	2.457	0.288	0.889	-0.319	1.349	0.884	0.128
22	1.000	0.535	1.995	0.322	0.994	-0.236	0.670	0.439	0.122
<b>23</b>	<b>1.000</b>	<b>0.390</b>	<b>1.876</b>	<b>0.184</b>	<b>0.568</b>	<b>0.063</b>	<b>0.589</b>	<b>0.386</b>	<b>0.140</b>
24	1.000	0.330	2.576	0.280	0.865	-0.105	1.059	0.694	0.122
25	1.100	0.535	2.036	0.307	0.948	-0.105	0.624	0.409	0.115
<b>26</b>	<b>1.221</b>	<b>0.535</b>	<b>2.122</b>	<b>0.462</b>	<b>1.426</b>	<b>-0.126</b>	<b>0.793</b>	<b>0.520</b>	<b>0.122</b>
<b>27</b>	<b>1.221</b>	<b>0.390</b>	<b>2.022</b>	<b>0.303</b>	<b>0.935</b>	<b>-0.120</b>	<b>1.206</b>	<b>0.790</b>	<b>0.135</b>
28	1.221	0.330	2.092	0.343	1.059	-0.040	1.243	0.815	0.128
29	1.221	0.177	2.233	0.346	1.068	0.004	1.343	0.880	0.130

Table 5.7: Behaviour of drag, lift and Strouhal number with a control cylinder.

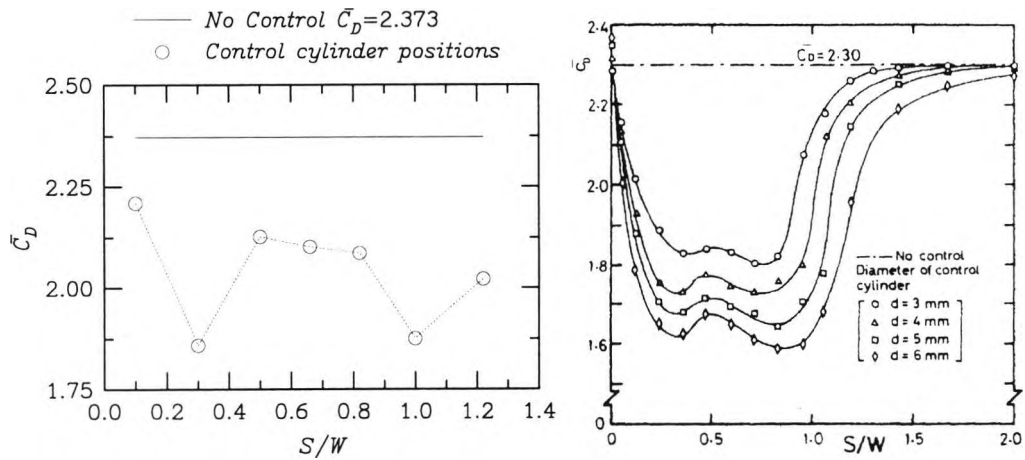


Figure 5.40: a) Predicted and b) Experimental\* values of minimum mean drag along  $S/W$  at the point of maximum velocity.

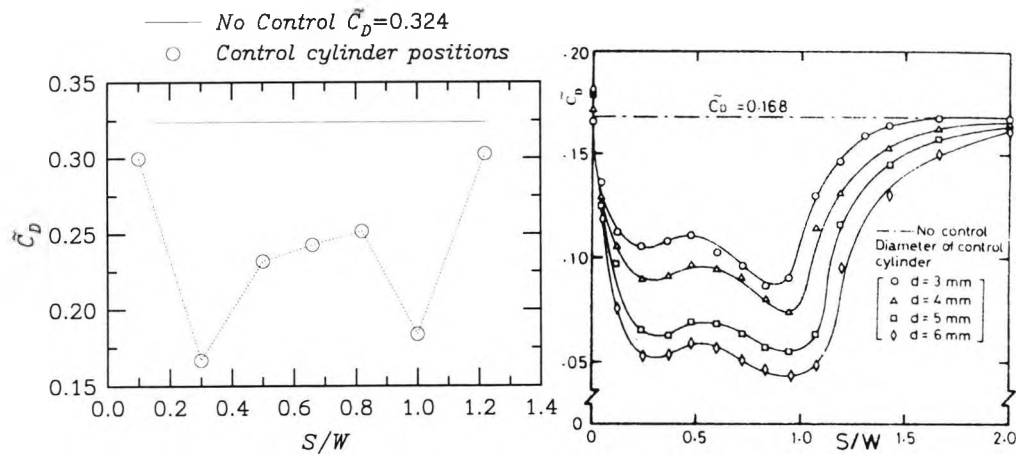


Figure 5.41: a) Predicted and b) Experimental\* values of minimum fluctuating drag along  $S/W$  at the point of maximum velocity.

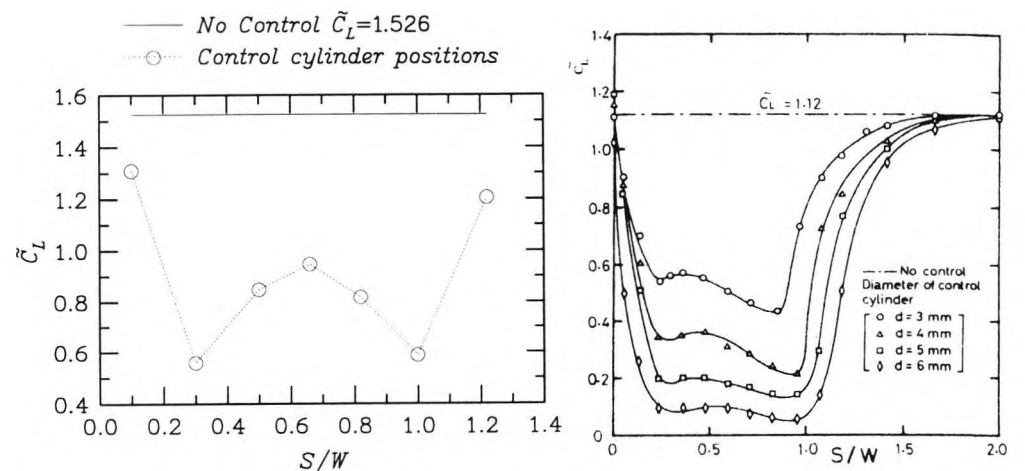


Figure 5.42: a) Predicted and b) Experimental\* values of fluctuating lift along  $S/W$  at the point of maximum velocity.

\* Experimental results presented are from Sakamoto, Tan and Haniu (1991)

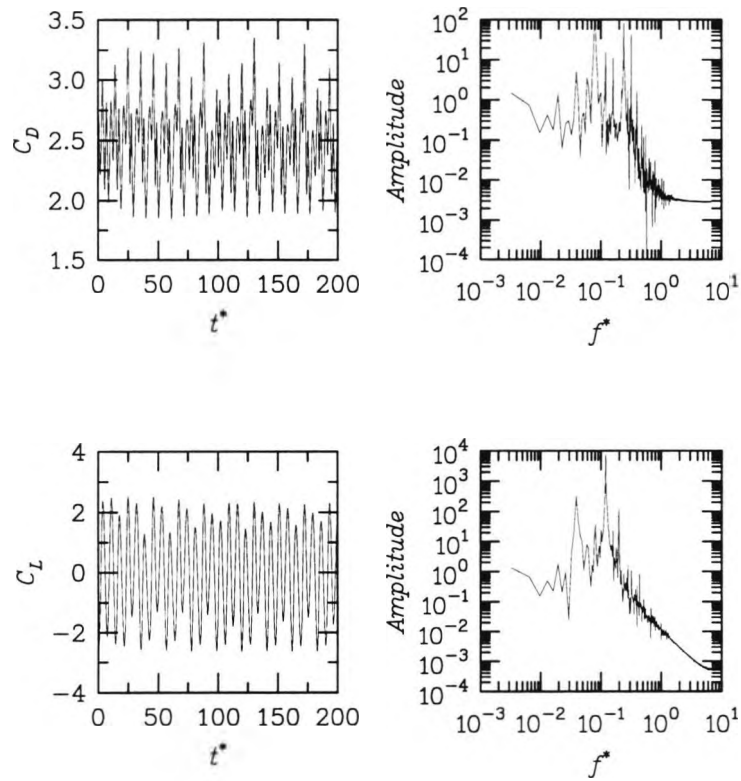


Figure 5.43: Time histories for the drag and lift coefficients for a square cylinder at  $Re=4.2 \times 10^4$  with no control cylinder; showing also the power spectra.

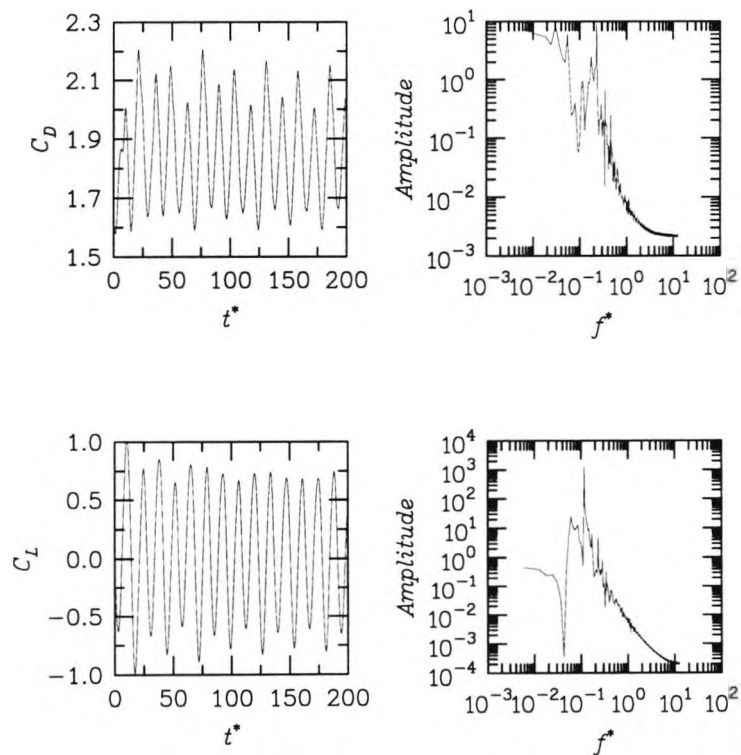


Figure 5.44: Time histories for the drag and lift coefficients for a square cylinder at  $Re=4.2 \times 10^4$  with control cylinder at  $S/W=0.282$ ,  $T/W=0.280$  (RUN 6); showing also the power spectra.

Interference with the separated shear layer can cause different flow patterns, depending on the position of the control cylinder. Figure 5.45 shows the computed streaklines for the case with no control. Figure 5.46 (a) to (c) show the streaklines around the main cylinder for different positions of the control cylinder. When the control cylinder is placed inside the separated shear layer Figure 5.46(a), it is seen to exert no influence on the behaviour of the main cylinder (RUN 10).

Figure 5.46(b) shows the case of maximum suppression (RUN 6). This is when the control cylinder is placed inside the leading edge, on the outer boundary of the shear layer. The rolling up of the shear layer is forced downwards, so that the width of the wake becomes narrower. Figure 5.46(c) shows the case when the shear layer is forcibly bent by the control cylinder when it is placed outside the boundary of the shear layer (RUN 22). In this case the strength of the rolling up of the shear layer is intensified.



*Figure 5.45: Streaklines around a square cylinder at  $Re=4.2 \times 10^4$ .*

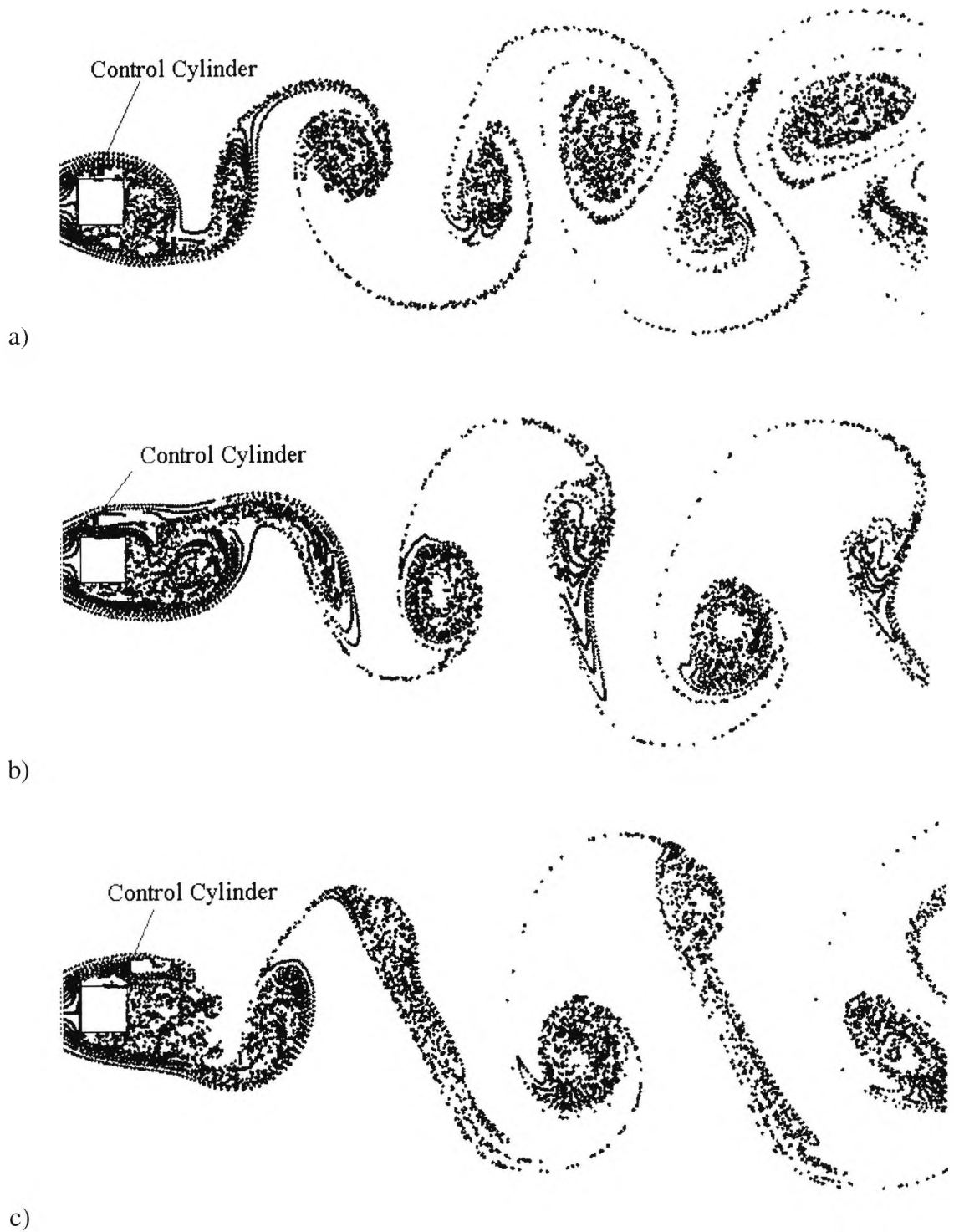


Figure 5.46: Streamlines around a square cylinder at  $Re=4.2 \times 10^4$  a) without control cylinder, and with control cylinder at b)  $S/W=0.5$   $T/W=0.177$  (RUN 10); c)  $S/W=0.282$ ,  $T/W=0.280$  (RUN 6); and d)  $S/W=1.0$ ,  $T/W=0.535$  (RUN 22).

## 5.7 Conclusions

The results in this Chapter have demonstrated that for the first time, it is possible to capture the effects of suppression of vortex shedding from square and circular cylinders, in both laminar and turbulent regimes, by using a control cylinder placed in the vicinity of the main one.

A circular cylinder in laminar flow was simulated at  $Re=100$ , to compare to the experimental and numerical results of Strykowski & Sreenivasan (1990) and Lin & Wu (1994). It was shown that complete suppression is achieved when a control cylinder of size  $D/d=4.12$  is placed at  $x/D=1$  and  $y/D=0.92$ . Fluctuating drag and lift coefficients were reduced to 0.5% and 0.1% of their original values. There were no dominant shedding frequencies in the power spectra, and the streaklines showed no sign of vortex shedding. This complies with the results of Strykowski & Sreenivasan (1990). The mechanism of suppression is by forcibly reattaching the separated shear layer. The simulations of Lin & Wu (1994), carried out at  $Re=80$  did not achieve the same extent of suppression as the present study.

There are no previous experimental or numerical results for a square cylinder in laminar flow with a control cylinder. The present simulations were carried out at  $Re=100$ . It was shown that it is possible to suppress vortex shedding almost completely when a control cylinder of size  $D/d=7$  is placed above and behind the main cylinder (at  $x/D=1.02$  and  $y/D=0.95$ ). In this case, the fluctuating drag is reduced to about 3% of its original value, and fluctuating lift is reduced to 0.3% of its original value.

The flow over a circular cylinder at  $Re=6.5 \times 10^4$  was investigated experimentally by Sakamoto and Haniu (1994). Even though the predictions of single circular cylinder in turbulent flow underestimate mean drag and overestimate the rms of the drag and lift coefficients, the extent of suppression and its mechanism were satisfactorily reproduced when a control cylinder was present. Two types of suppression mechanism were found; one arises when the boundary layer along the surface of the circular cylinder is controlled. This gives the most suppression. The other arises when the separated shear layer is controlled. The fluctuating drag and lift are reduced to 25% and 9% of their original values respectively. The suppression effect is highly visible through the wake pattern, as visualised by streaklines.

A square cylinder at  $Re=4.2 \times 10^4$  was investigated experimentally by Sakamoto Tan and Haniu (1991). The present simulations, carried out with the modified k- $\epsilon$  model, confirmed that the best position for the control cylinder is on the outer boundary of the shear layer, and inside the leading edge. Vortex shedding was not completely suppressed in turbulent flow, as shown by the streaklines in the flow field. Along the shear layer, the fluctuating drag and lift coefficients dropped by 50% and 36% of their original values respectively.

# CHAPTER SIX: EXPERIMENTATIONS ON SUPPRESSION BY FORWARD INJECTION

## 6.1 Introductory Remarks

The possibility of suppressing vortex-induced vibrations by the injection of fluid into the approach stream was postulated by Dr B.A.Younis who suspected its existence from flow visualisations. A number of preliminary experiments were carried out (Razavi, 1992 and Younis & Razavi, 1996), and are extended in the present study.

The experimental set-up is described in Section 6.2. A number of parameters were varied, such as the number of holes, their diameter, and the distance between their centres, in order to find the geometric arrangement yielding optimum suppression. A data reduction method was devised to minimise the number of experiments. This is explained in Section 6.3. The results are presented in Section 6.4. A number of tests were carried out in order to maximise the effect and quantify it. The penetration length of the injected fluid was also examined, as was the sensitivity of the suppression to yaw.

## 6.2 Experimental Set-up

Figure 6.1 illustrates the experimental set-up. A picture of the laboratories and the set-up is shown in Figure 6.2. All the experiments were carried out using copper cylinders, 1.3m long with an outer diameter of 12mm. The cylinders were placed in a 16m long water channel at a distance of 5.7m from the inlet. The immersion depth was set to 0.32m. The flow rates in the channel were in the range 18-85 litres per second as measured via the pressure drop along the channel. The bottoms of the cylinders were capped, and holes were drilled on the cylinders' side facing the incoming flow. Two accelerometers were placed on a perspex mounting, and screwed onto the cylinder at a height of 0.5m from the base. This was done in order to determine the in-line and transverse accelerations of the cylinder. In order to record vibrations caused by vortex shedding, the accelerometers were connected to an amplifier, which was then connected via an analogue-digital converter to a computer. The cylinder was then rigidly clamped at 1m height from the base to a stand, thus creating a cantilever. A hosepipe was connected to the top of the cylinder to inject

water into the cylinder and out of the holes into the free stream. The maximum injection flow rate possible was 0.229  $\ell/s$ .

A data analysis method was also devised. Vibrations from the cylinder caused the accelerometers to register two signals, which were picked up by the amplifier. Through the A/D converter, these signals were then converted to voltage readings, which were stored on a computer. The data file thus created was then analysed using a FORTRAN program, to determine the root mean square and the power spectrum of each signal.

Since there are many variables involved in describing the extent of suppression, dimensional analysis was used to group the variables and reduced the number of experiments necessary to quantify their effect. The following non-dimensional groupings were considered as relevant:

**a) Reynolds number:**

As was shown earlier, vortex shedding from a smooth circular cylinder in steady flow is a function of Reynolds number. The flow parameters (e.g. drag, lift, and Strouhal number) are dependent on the Reynolds number (see Chapters 1 and 3). Reynolds number is also used to quantify the approach flow. The average velocity in the channel was deduced from the flow rate in the channel, which in turn was measured by pressure tapings in the channel bed.

**b) Strouhal number:**

The Strouhal number is an appropriate combination of flow and geometry parameters to render the vortex shedding frequency dimensionless (see Chapters 1 and 3).

**c) Geometry number ( $G_1$ ):**

This number was introduced to scale the hole diameter:

$$G_1 = \frac{d_{\text{hole}}}{D} \quad (6.1)$$

where  $d_{\text{hole}}$  is the diameter of drilled holes and  $D$  is the cylinder diameter.

**d) Geometry number ( $G_2$ ):**

This number was introduced to scale the spacing between holes:

$$G_2 = \frac{h_{c-c}}{L} \quad (6.2)$$

where  $h_{c-c}$  is the distance from centre to centre, and  $L$  is the immersion depth.

In order to establish the optimum criterion for suppression, the values of  $G_1$  and  $G_2$  had to be varied with respect to a range of Reynolds numbers. The outcome of this exercise fixes the optimum geometry and allows further experiments to be carried out in order to understand the relationship between Strouhal number and Reynolds number.

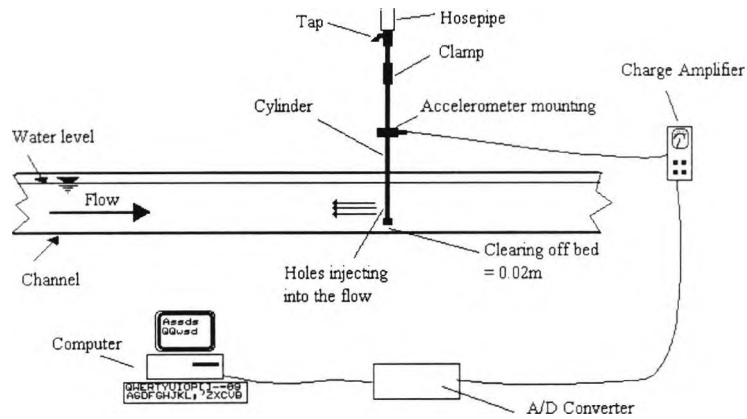


Figure 6.1: The experimental set-up.

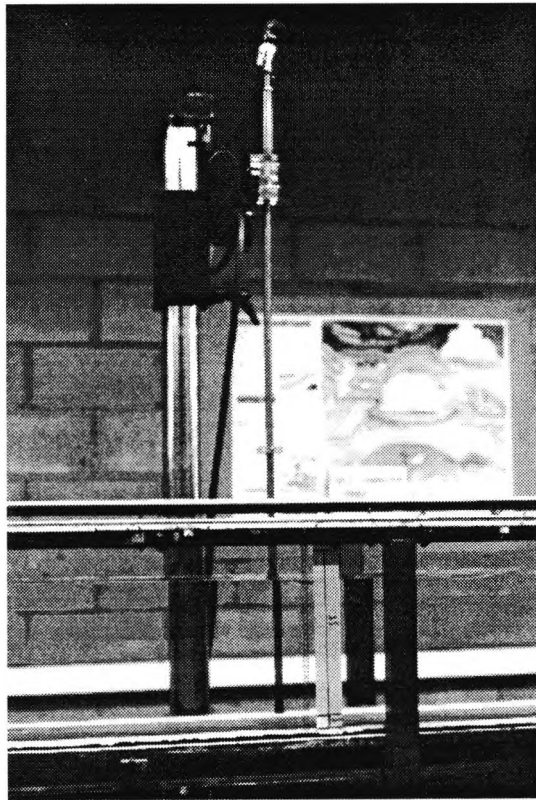


Figure 6.2: Picture of the laboratory and experimental set-up.

### 6.3 Data Reduction

A method to quantify the extent of reduction in the vortex-induced vibrations is needed. Comparisons between the root mean square (rms) of the voltage signal from the accelerometer before and after the injection provides a reliable measure of the relative reduction. This is quantified by a new parameter ( $V_r$ ) defined as:

$$V_r = \text{Change in rms voltage} = \frac{\text{rms after injection}}{\text{rms before injection}} \quad (6.3)$$

Obviously, any value of  $V_r$  above unity would mean an enhancement of the vibration; a value below unity would imply suppression of vortex-induced vibrations.

The objective was to find the smallest value  $V_r$  (i.e. the greatest suppression) for a large range of Reynolds numbers for a particular combination of  $G_1$  and  $G_2$ .

It was not deemed necessary to calibrate the accelerometers in order to obtain absolute values of the accelerations, since it is more important to assess the change in the strength of the vortex shedding associated with the fluid injection, rather than its absolute value. In addition, the equipment to calibrate the accelerometers was not readily available. Power spectra and Strouhal number analysis can still be carried out, as the frequency does not change with calibration.

The level of accuracy attainable with this data reduction method depends on the length of the sampling period and the sampling rate. This is especially the case when a clear power spectrum is required. These parameters were experimentally optimised at 15 seconds of sampling, with 15000 sampling points; i.e. data was collected at a sampling rate of 1000/s. Every data file contained seven seconds of pre-injection signal and seven seconds after injection, i.e. 7000 data points for each stage, with a one second interval in between to allow the effects of the injection to settle.

## 6.4 Results

### 6.4.1 Parametric Study

The parametric study experiments were split into four stages. They are explained in Table 6.1. The first stage was to determine the optimum number of holes. Experiments were thus carried out with the number of holes varied in the range 1-13. This corresponds to  $0.0006 \leq G_2 \leq 0.381$ ). All of the holes were at 10mm apart, with a diameter of 2mm. This gives  $G_1=0.167$ . The results for Stage 1 are shown in Figure 6.3 (a) and (b), for the in-line and transverse directions respectively. The results for 1 and 3 holes are not shown since these produced excessive enhancement of rms voltage. In some cases,  $V_r$  attained a value of 23. The results in Figure 6.3 show that suppression is obtained in the in-line direction, except for the Reynolds number range of 5000 to 6500, where  $V_r$  is dramatically enhanced. For the transverse direction, there is an increase of  $V_r$  up to Reynolds number of 3500, followed by suppression. The maximum suppression was achieved at  $Re=9300$ , with  $V_r=0.248$  for the in-line vibrations and  $V_r=0.267$  for transverse vibrations.

Stage 2 of the experiments involved experiments on a holes of 3mm diameter (i.e.  $G_1=0.25$ ). The distance between the holes was again kept at 10 mm again. The number of holes were set at 7 and 13. This gives  $G_2=0.197$  and 0.384. The results for a range of Reynolds numbers are shown in Figure 6.4 (a) and (b) for the in-line and the transverse directions. The change in  $V_r$  goes through several stages, depending on the Reynolds number. At low Reynolds numbers up to  $Re=4000$ , there is strong suppression in the in-line direction but enhancement in the transverse direction. At Reynolds numbers in the range 5000-7000,  $V_r$  in the in-line direction is enhanced, while transverse vibrations are suppressed. For Reynolds numbers of around 7000 both the in-line and the transverse  $V_r$  are reduced to about the same level ( $V_r \approx 0.3$ ). The vibrations are then seen to increase with further increase in Reynolds number.

Stage 3 of the experiments was based on Stage 2, but with an increase in hole diameters to 4mm (i.e.  $G_1=0.333$ ). The distance between the holes was kept at 10mm, again with 7 and 13 holes. This gives  $G_2=0.2$  and 0.388. The results for a range of Reynolds numbers are shown in Figure 6.5 (a) and (b) for in-line and transverse directions. The variation of  $V_r$  with Reynolds number is very similar to that seen for Stage 2, with the values of  $V_r$  being shifted upwards.

Stage	Diameter of holes (mm)	No. of holes	Distance between holes (mm)	$G_1$	$G_2$
1	2	1	-	0.167	0.0006
	2	3	10	0.167	0.069
	2	7	10	0.167	0.194
	2	13	10	0.167	0.381
2	3	7	10	0.25	0.197
	3	13	10	0.25	0.384
3	4	7	10	0.333	0.2
	4	13	10	0.333	0.388
4	3	13	20	0.25	0.759
	4	7	20	0.333	0.388

Table 6.1: Experiments performed.

The tests of Stage 4 were conducted in order to experiment further with the effects of the distance between the holes. The combinations of  $G_1$  and  $G_2$  that produced the best results for Stages 2 and 3 were chosen, and the distance between the holes increased to 20mm. Two cylinders were used, one with 3mm diameter holes (with 13 holes, and 20mm apart i.e.  $G_1=0.25$  and  $G_2=0.759$ ), and another with 4mm diameter holes (with 7 holes, and 20mm apart i.e.  $G_1=0.333$  and  $G_2=0.388$ ). The results for a range of Reynolds numbers are shown in Figure 6.6 (a) and (b) for the in-line and transverse directions. The results show the same pattern as for Stages 2 and 3.

A decision had to be made as to which geometry combinations gave the best suppression results. The 2mm diameter combinations were not satisfactory at all, as they enhanced  $V_r$  drastically in most cases. They were thus discarded. The remaining combinations were plotted on the same figure, in the in-line and transverse directions (see Figure 6.7 (a) and (b)). The lines on the graph are smoothed curves obtained by polynomial regression analysis of the third order. They show distinct behaviour for the in-line and transverse directions. The following combination was chosen as the one which maximises the effect over a wide range of Reynolds numbers:

Hole Diameter	Number of Holes	Distance Between Holes	$G_1$	$G_2$
3 mm	13	10 mm	0.250	0.384

Table 6.2: Optimum geometry for vortex suppression by forward injection.

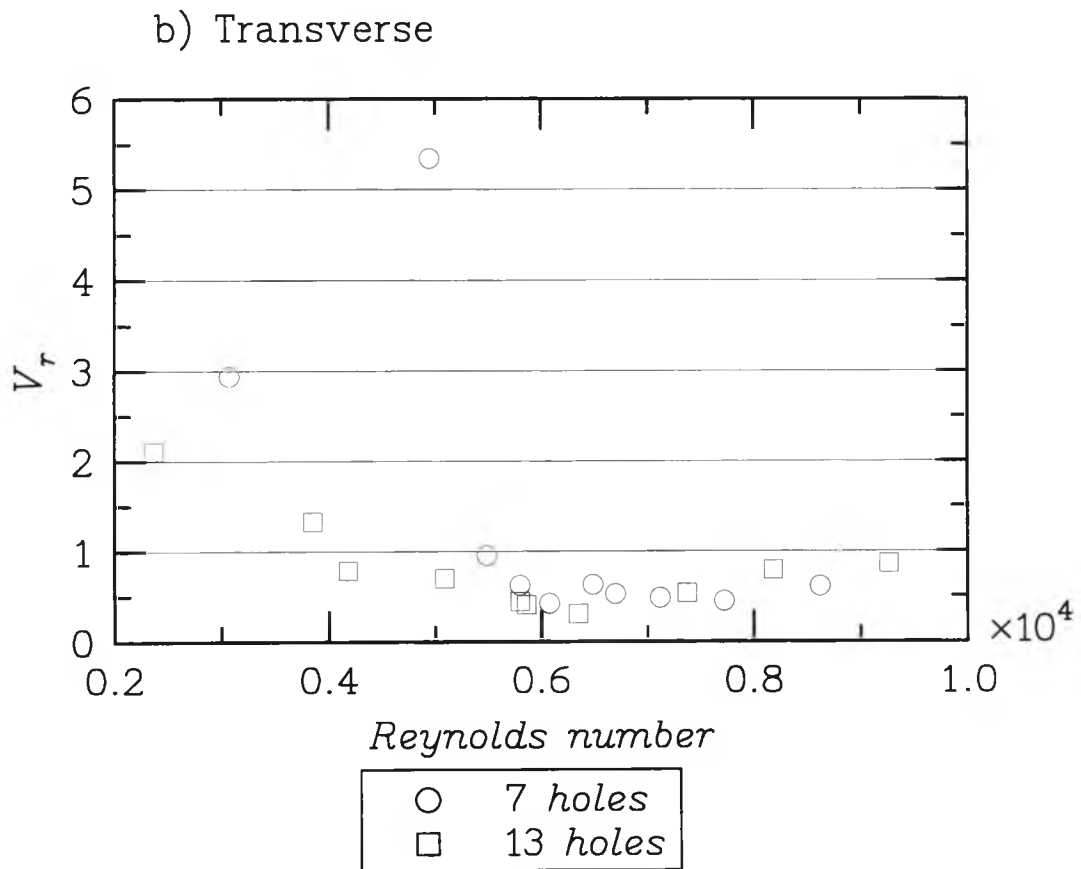
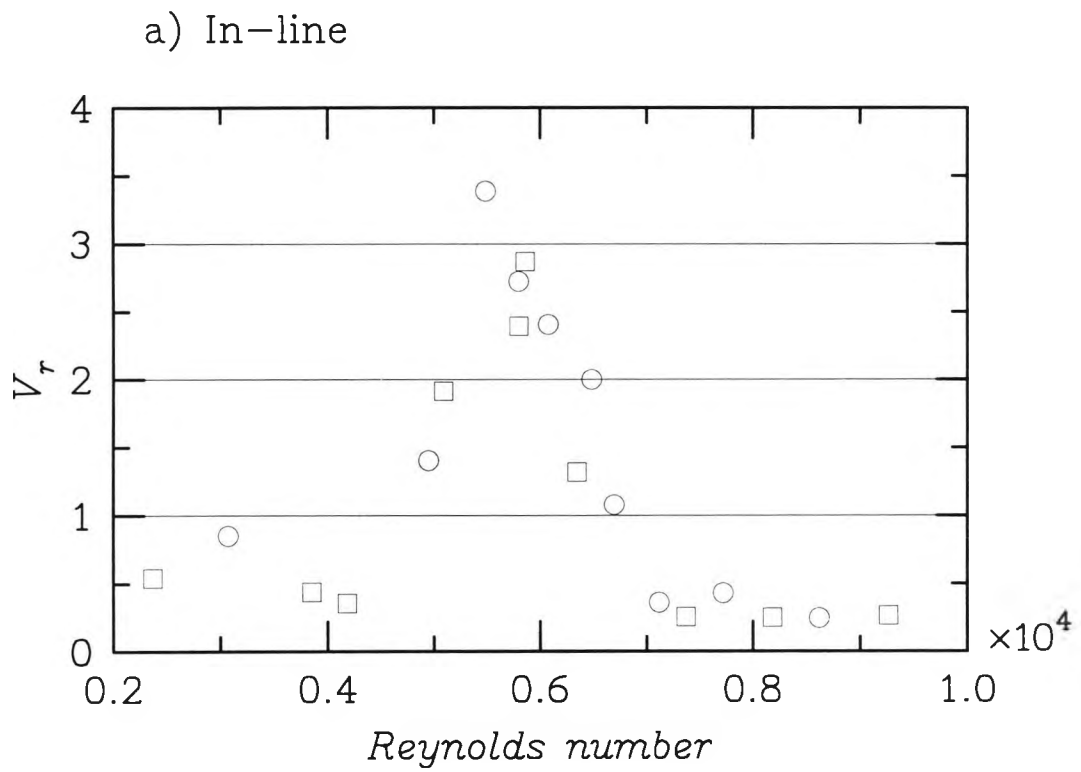


Figure 6.3: Stage I results for the variation of  $V_r$  with Reynolds number in the a) in-line and b) transverse directions.

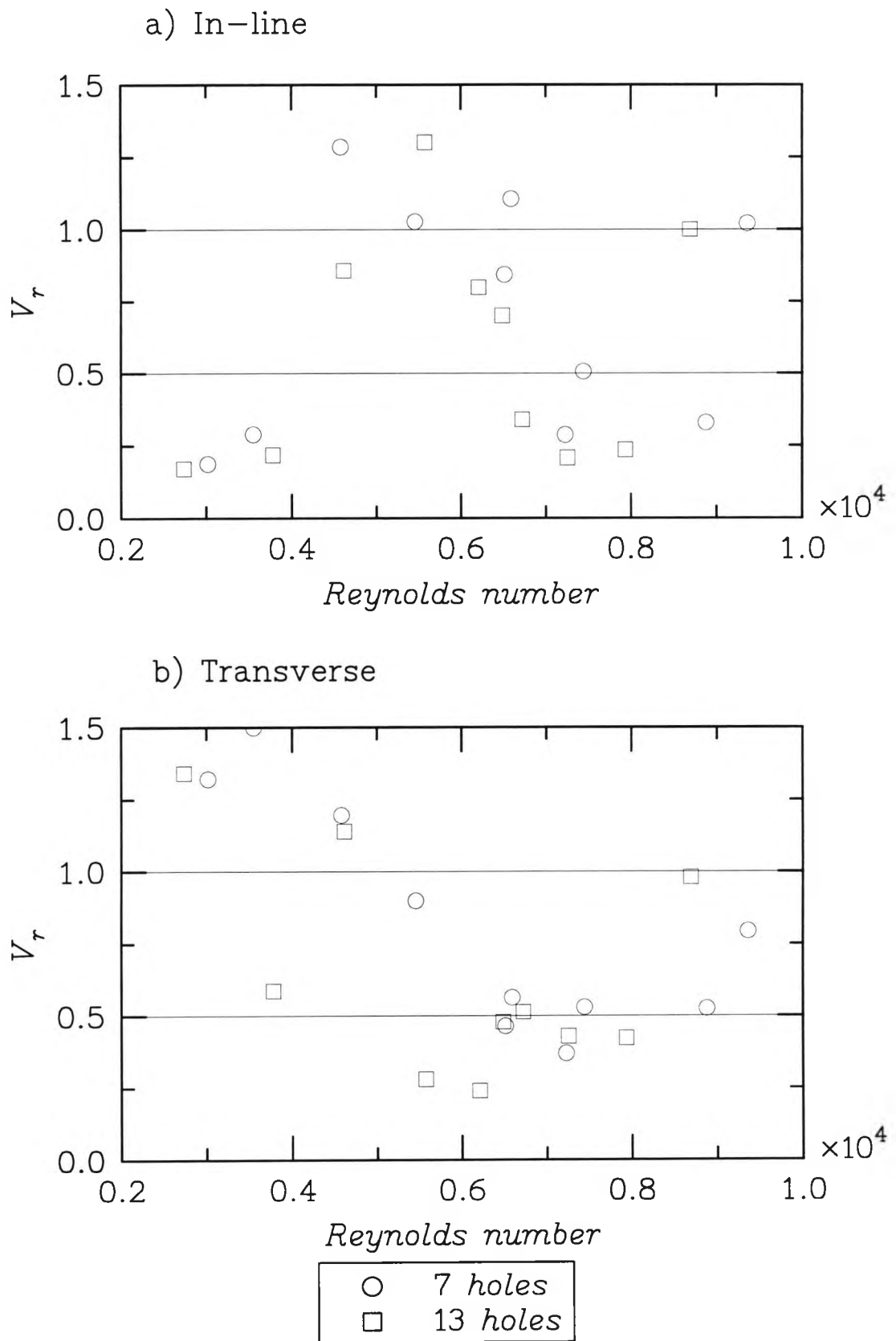


Figure 6.4: Stage 2 results for the variation of  $V_r$  with Reynolds number in the  
a) in-line and b) transverse directions.

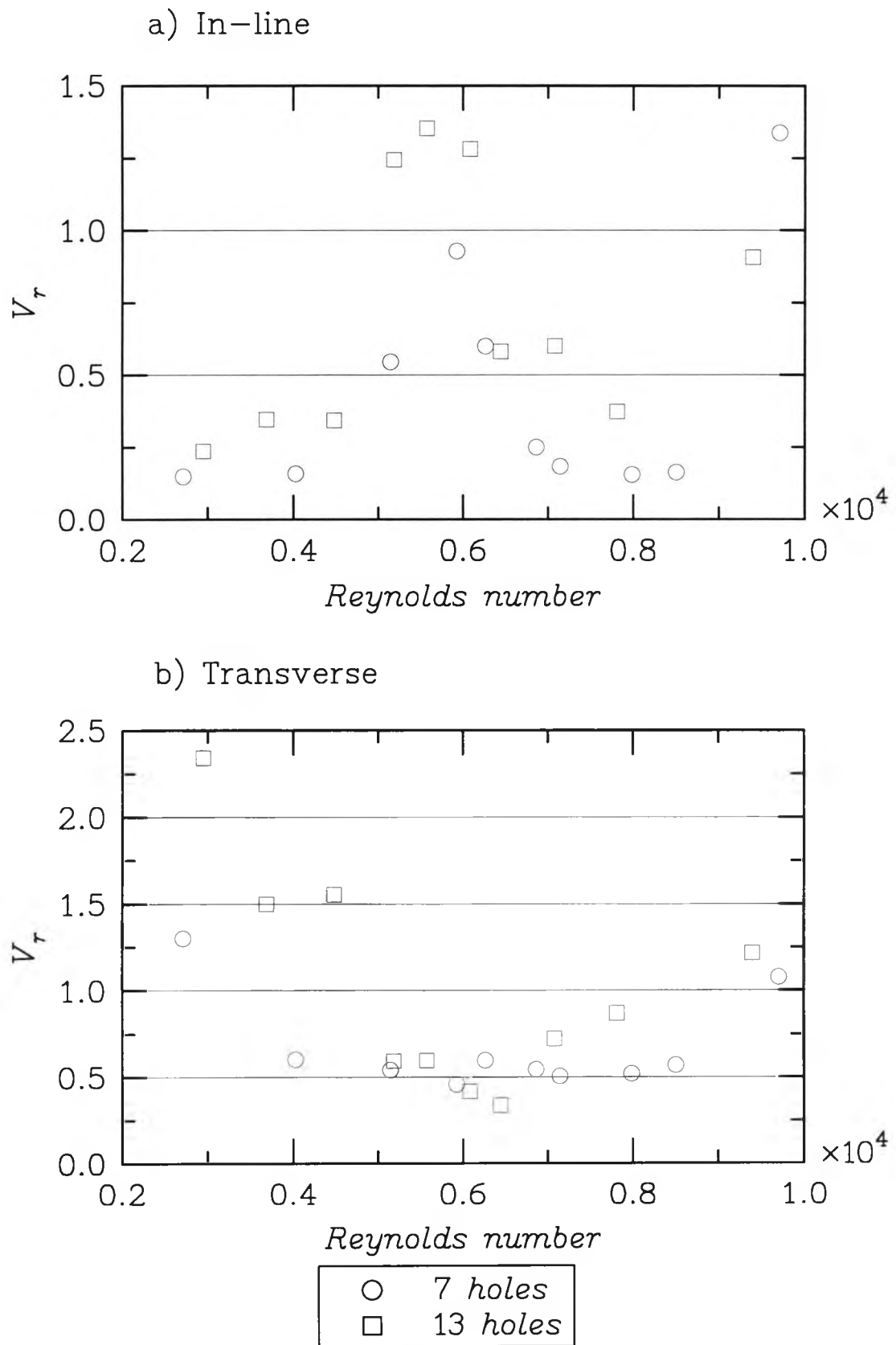


Figure 6.5: Stage 3 results for the variation of  $V_r$  with Reynolds number in the a) in-line and b) transverse directions.

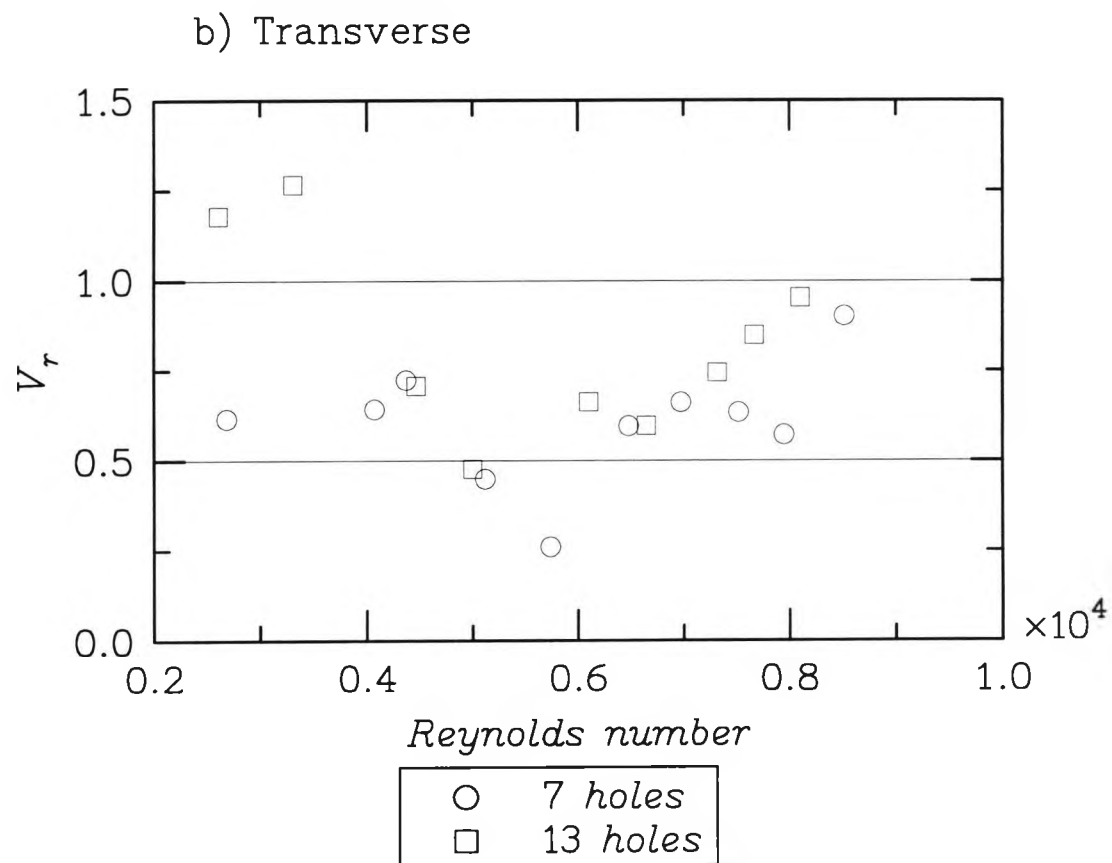
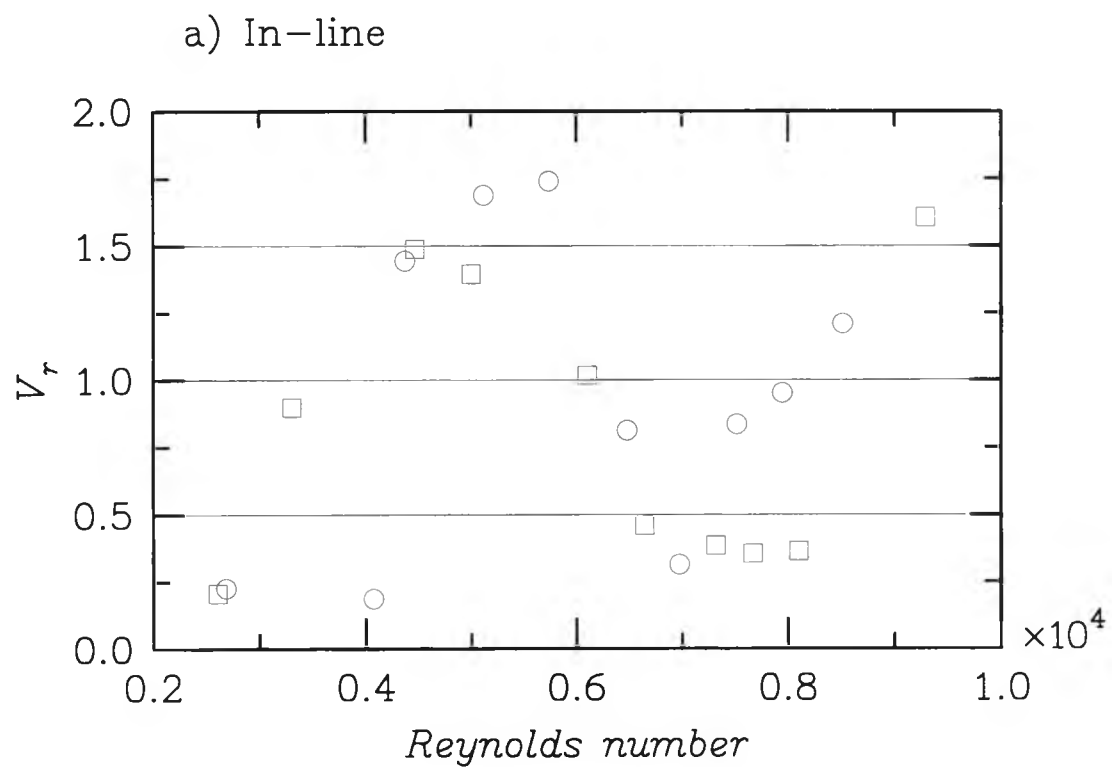
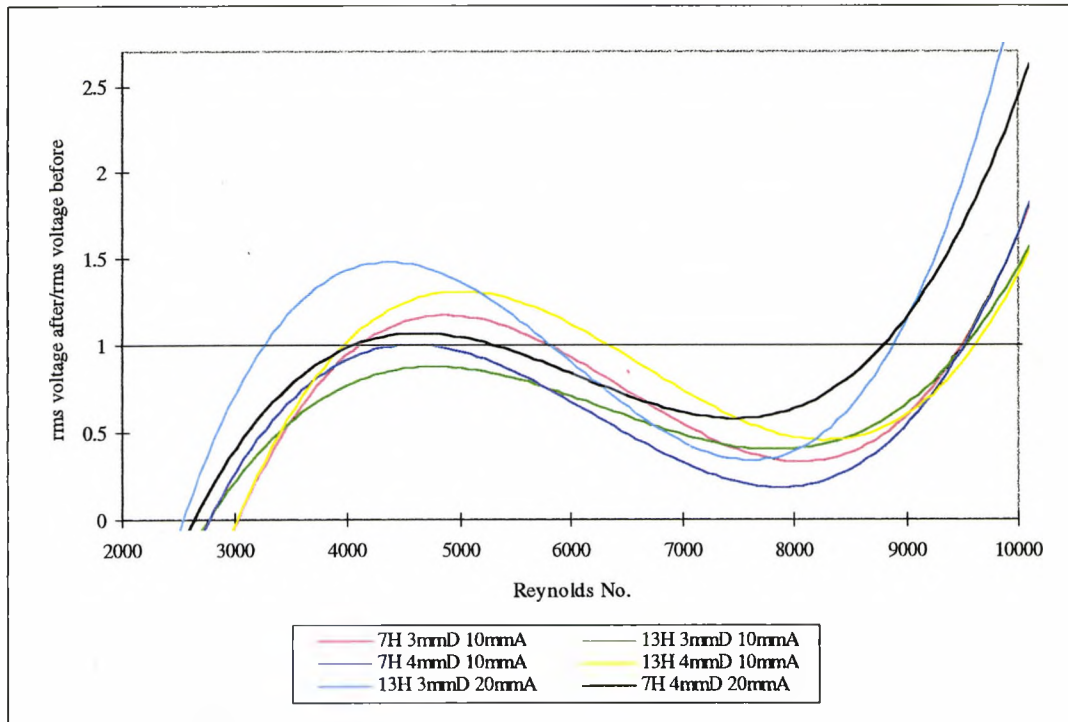


Figure 6.6: Stage 4 results for the variation of  $V_r$  with Reynolds number in the a) in-line and b) transverse directions.

a) In-line



b) Transverse

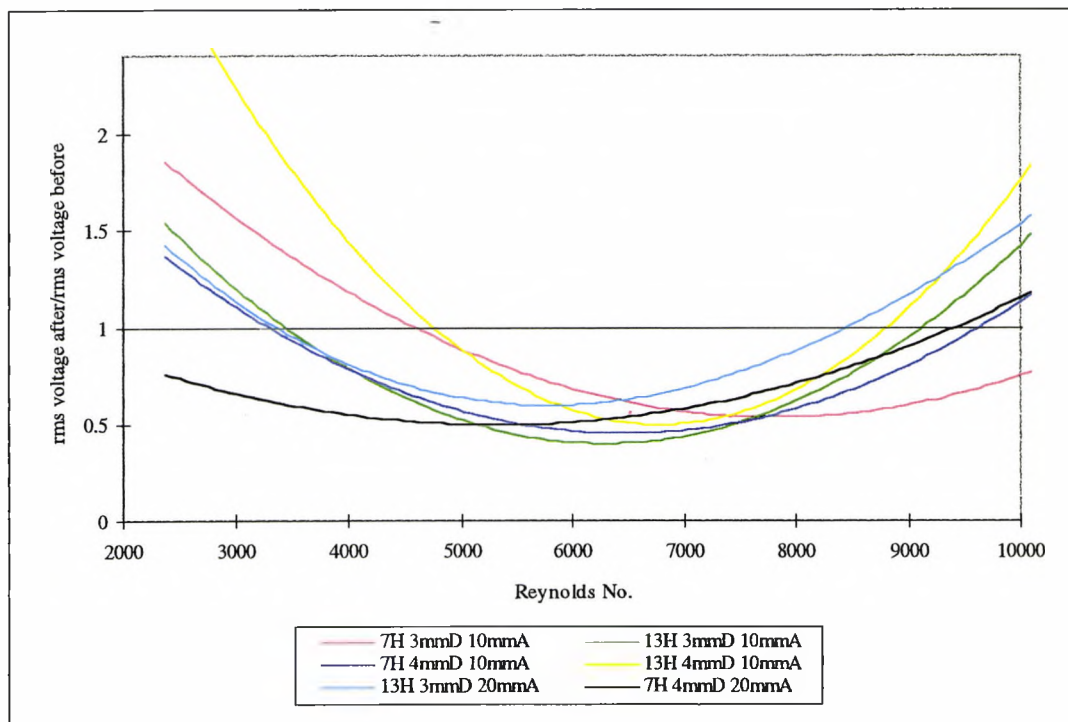


Figure 6.7: a) In-line b) transverse direction analysis of sensitivity of vortex shedding suppression to geometry.

## 6.4.2 Detailed Re analysis

Further analysis was carried out on the optimum geometry in order to quantify the behaviour of  $V_r$  with Reynolds number for the in-line and transverse direction vibrations.

Figure 6.8 shows the change in  $V_r$  with Reynolds numbers possible in the channel. The maximum value of Reynolds number attainable in the water channel was 9500. It is evident that up to  $Re \approx 3800$ , the in-line vibrations are suppressed but the transverse vibrations are enhanced. In the range,  $3800 < Re < 6000$ ,  $V_r$  increased for the in-line direction and reached its maximum, but it decreased for the transverse direction and reached its minimum. In the range  $6200 < Re < 8000$ , both the in-line and transverse vibrations are suppressed. Beyond  $Re \approx 8000$ , both the in-line and transverse vibrations are increased towards unity at around  $Re \approx 9500$ .

Figure 6.9 (a) and (b) show a trace of the accelerometer output for the in-line and transverse directions at  $Re=7517$ , before and after injection. Figure 6.10 shows the power spectra of the same traces. This is in the range of Reynolds numbers when both in-line and transverse vibrations are substantially suppressed. At this Reynolds number  $V_r=0.278$  for the in-line vibrations and  $V_r=0.349$  for the transverse vibrations.

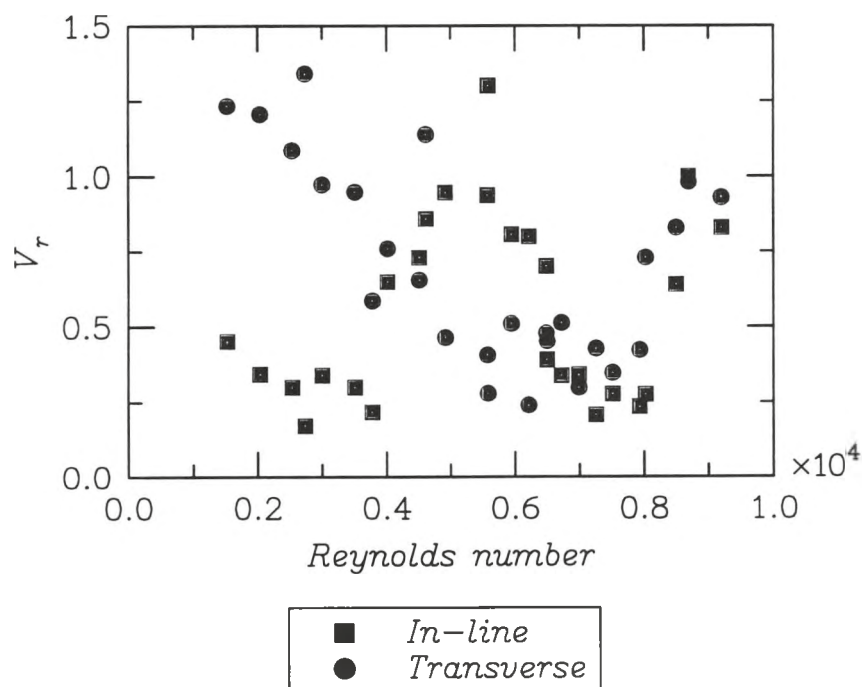
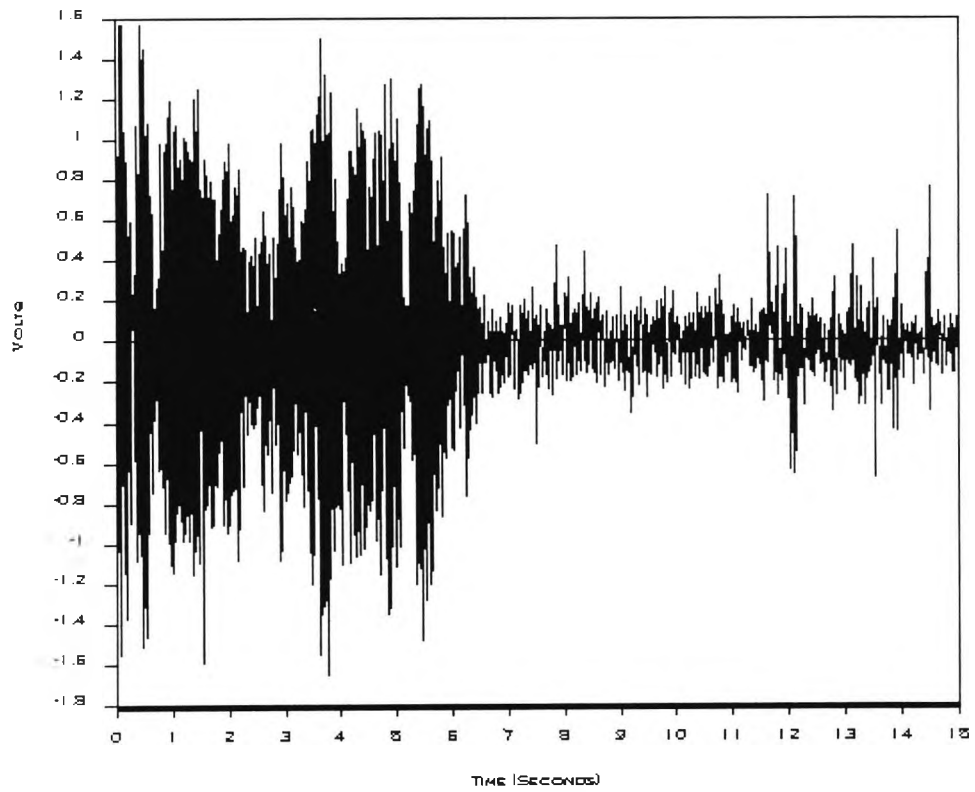


Figure 6.8: Detailed analysis of Reynolds number range for the geometry 13Holes, 3mm diameter, 10mm apart ( $G_1=0.250$ ,  $G_2=0.384$ ).

a) In-Line



b) Transverse

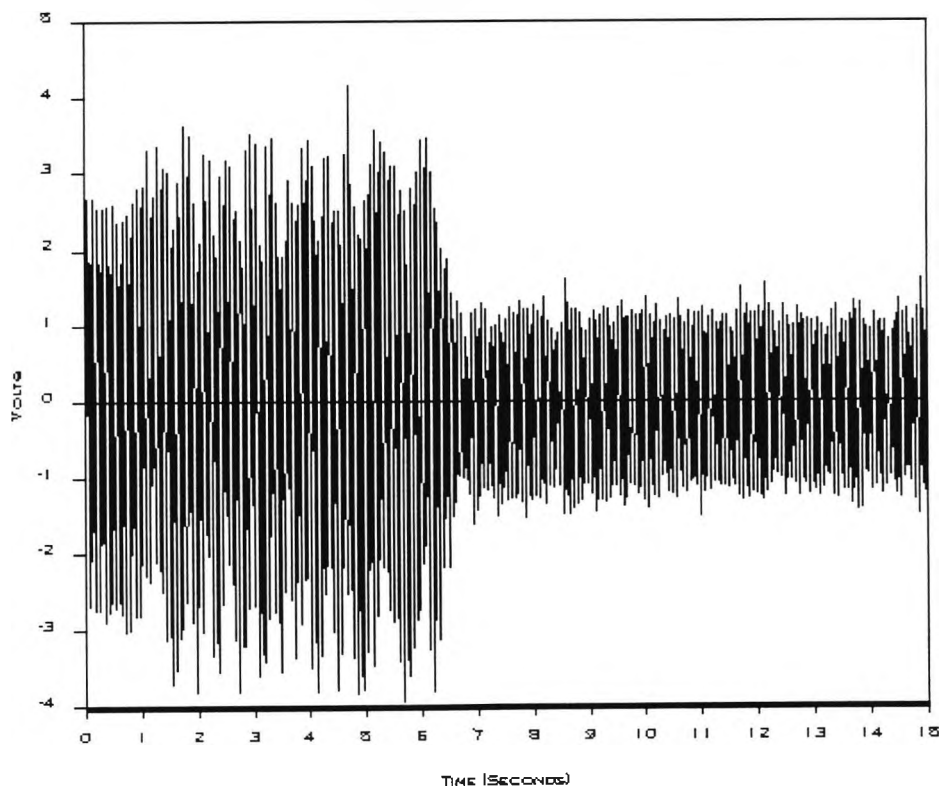
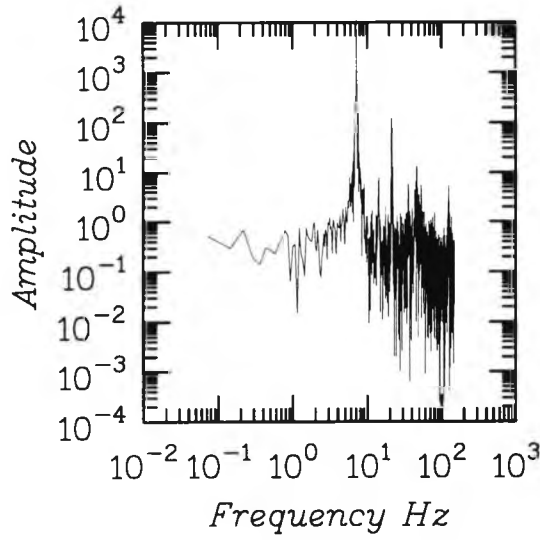
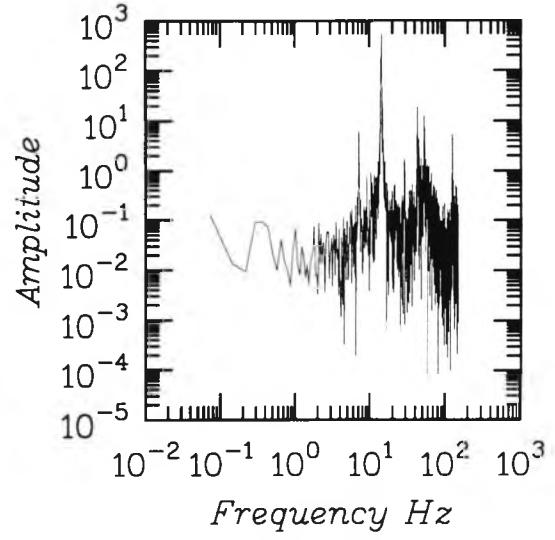


Figure 6.9: Trace of accelerometer output for a) In-line and b) transverse directions for geometry: 13 holes, 3mm diameter, 10mm apart at  $Re=7517$ .

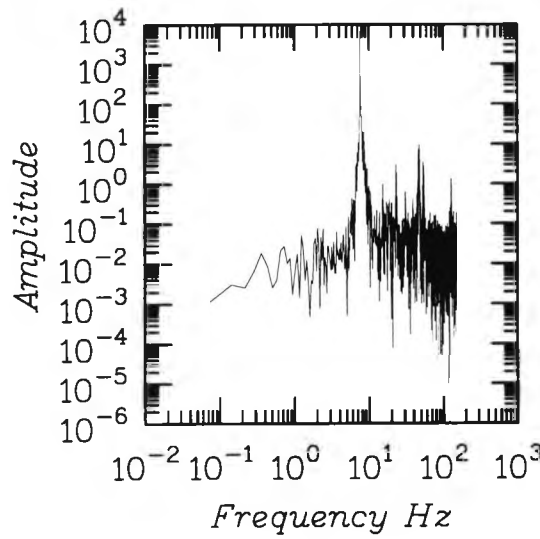
a) *In-Line Before*



b) *Transverse Before*



c) *In-Line After*



d) *Transverse After*

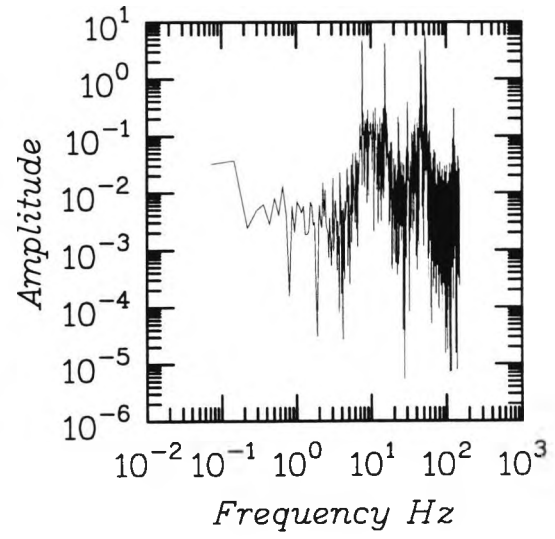


Figure 6.10: Power spectra for in-line and transverse direction signals, before and after injection for geometry: 13 holes, 3mm diameter, 10mm apart at  $Re=7517$ .

### 6.4.3 Strouhal Number Analysis

The vortex shedding frequency ( $f_s$ ) for the in-line and transverse vibrations is determined by analysing the signals from their respective accelerometers. This is done with a standard Fast Fourier Transform (FFT) routine. The frequency  $f_s$  is deemed to be the frequency corresponding to the greatest amplitude. The Strouhal number is quoted in terms of the dominant frequency in the transverse direction (i.e. in the lift direction).

Figure 6.10 (a) and (b) show the FFT results for the in-line and transverse signals before injection in for  $Re=7517$ . Figure 6.10 (c) and (d) show the FFT results for the same Reynolds number after injection. Note that this is the case where in-line vibrations were reduced to 0.278 of their original level, and transverse vibrations were reduced to 0.349 of their original level.

With no injection and for values of  $Re < 3000$ , no dominant shedding frequency can be discerned. The amplitude of vibrations is so low that high frequencies in the spectrum become dominant. For  $Re > 3000$ , the frequency of the in-line vibrations is double that for the transverse vibrations, as shown in Figure 6.11. This is the 'frequency doubling' phenomenon that has been mentioned earlier with respect to the predictions.

Figure 6.12 shows the Strouhal number variation for the range  $3000 < Re < 9500$ . The results are in good agreement with previous experimental results compiled by Lienhard (1966), which shows that Strouhal number decreases from 0.206 to 0.187 in the range  $3000 < Re < 10000$ .

There is no coherent vortex shedding frequency after injection. The FFT analysis show that the signals become chaotic with dominant frequencies either appearing in the high end of the spectrum or at around 7 Hz which is the natural frequency of the cylinder. One reason for the chaotic nature of the signal is that the vibrations caused by the flow of the injected fluid through the cylinder itself are not negligible. Tests in a stagnant channel with maximum injection from the cylinder showed a signal with rms value of 0.022 in the in-line and 0.037 in the transverse, with an in-line frequency of 7.617 Hz and transverse frequency of 29 Hz.

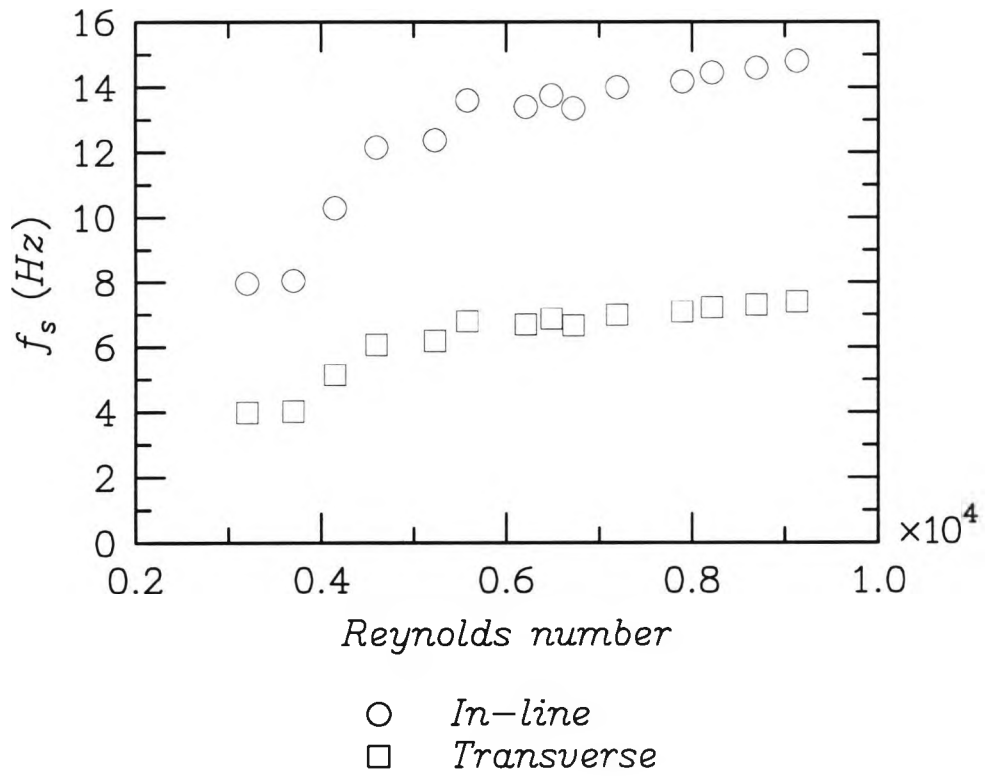


Figure 6.11: Vortex shedding frequency for the in-line and the transverse directions.

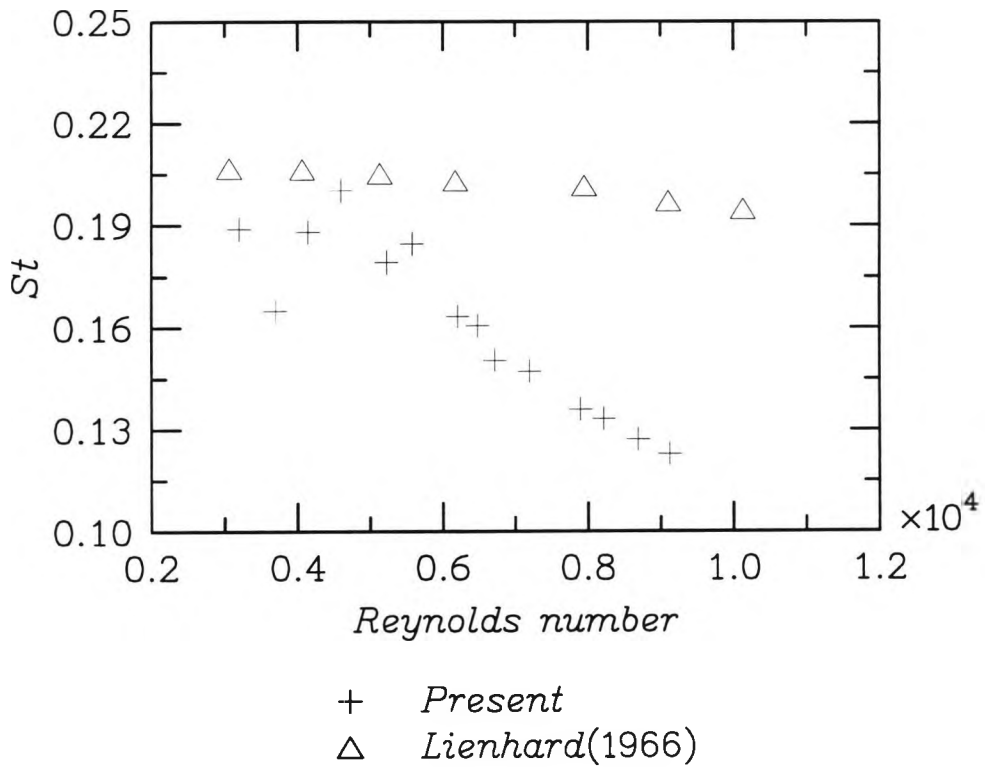
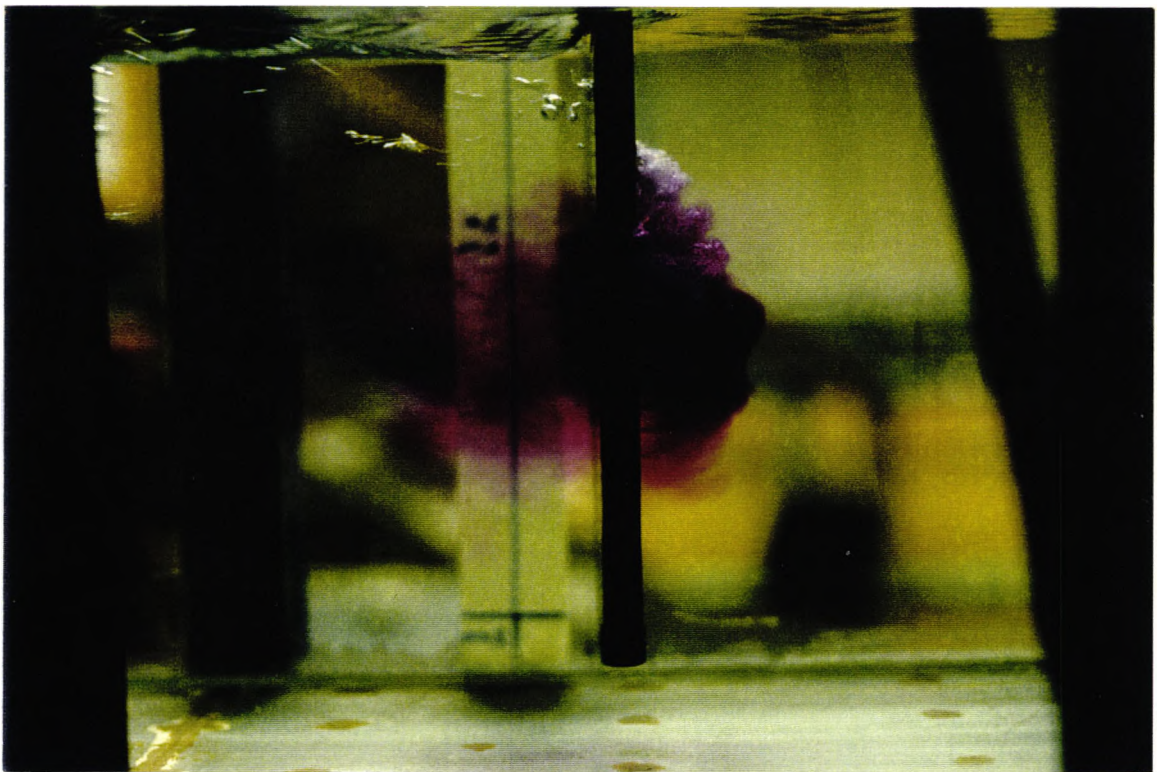


Figure 6.12: Relationship between Reynolds number and Strouhal number with no injection.

#### 6.4.4 Penetration Length

A small quantity of dye was introduced into the injected fluid in order to visualise the extent to which the injected fluid penetrates into the incoming flow. Figure 6.13 shows a still photograph of this test. It is clear that the injected fluid envelops the cylinder with a penetration length of around 1.5 to 2 times the cylinder diameter. Unfortunately, the dye diffuses very quickly after injection with the result that the measurements of the penetration length cannot be too accurate.



*Figure 6.13: Penetration length.*

### 6.4.5 Sensitivity To Yaw

The sensitivity of the injection method to yaw (i.e. inclination relative to the incident stream) was also investigated. The Reynolds number chosen for this test corresponds to that at which maximum suppression was detected (i.e.  $Re=7517$ ). The cylinder was turned on its axis by  $10^\circ$  intervals to  $60^\circ$  from its straight-ahead location. The tests were then repeated with the cylinder yawed in  $10^\circ$  intervals in the range  $180^\circ$ - $240^\circ$ . (see Figure 6.14). Figure 6.15 (a)-(d) show the effect of the yaw angle ( $\theta$ ) on the suppression process.

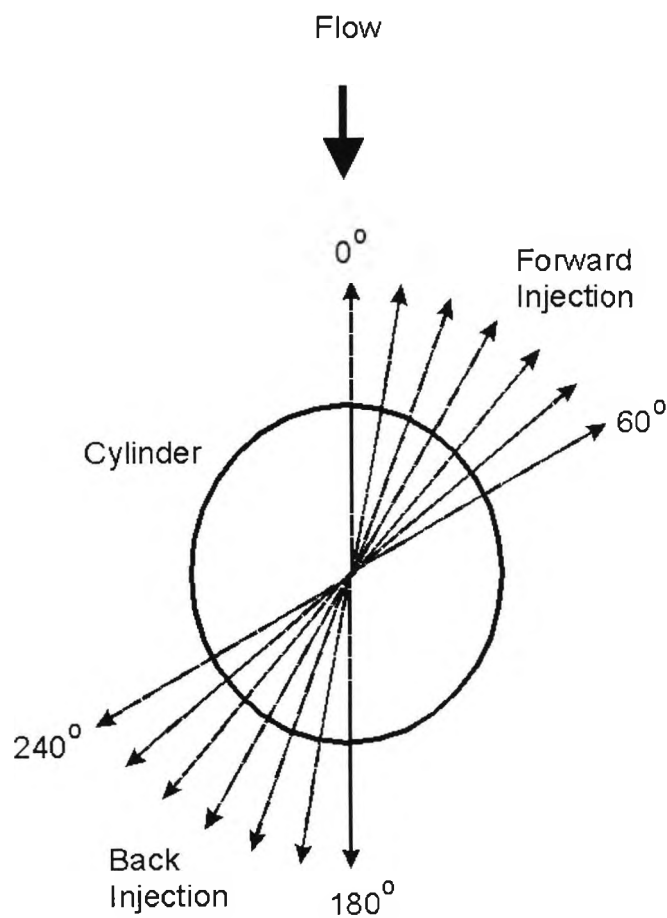


*Figure 6.14: Cylinder orientations in tests for sensitivity to yaw.*

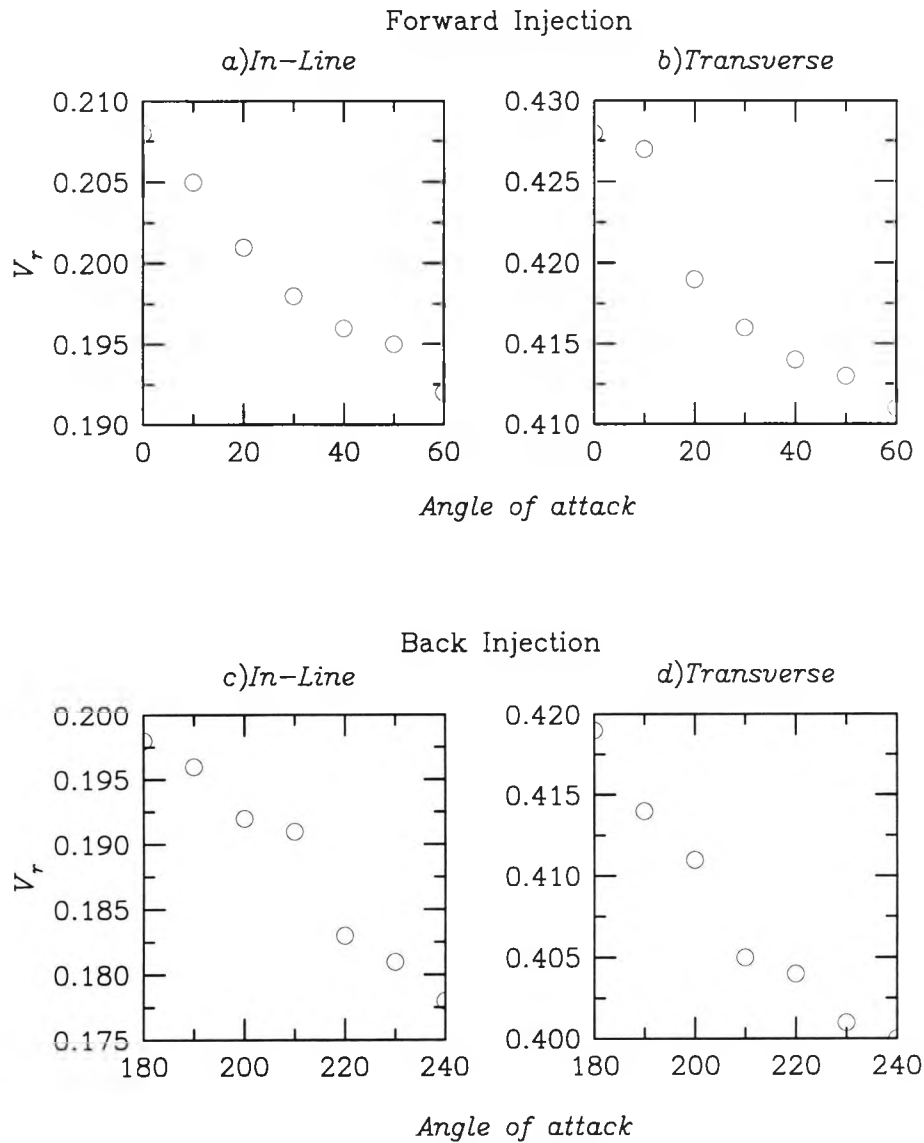


*Figure 6.15: Results for sensitivity to yaw.*

The results show that maximum suppression is obtained when the injection is placed at  $60^\circ$  and  $240^\circ$  to the incoming flow. Injection in the  $0^\circ$ - $60^\circ$  and in the  $180^\circ$ - $240^\circ$  ranges give almost similar results, although injection in the latter gives slightly better suppression. It was not possible to cover the area between  $60^\circ$  and  $90^\circ$  as the channel wall would interfere with the flow.

Back injection at  $180^\circ$  acts in a similar manner to a splitter plate. The suppression mechanism is of a completely different nature to that of forward injection.

## 6.5 Conclusions

The possibility of suppressing vortex shedding from a circular cylinder by forward injection was investigated in this chapter. As there are no previous data on this method, experimental test and data analysis methods were devised based on dimensionless numbers in order to reduce the number of experiments. Accelerometers connected to the cylinder measured accelerations in the in-line and transverse directions. The accelerometer voltage output was stored and analysed subsequently. The suppression was quantified in terms of the ratio of the root mean square value of accelerations before and after injection. The power spectra of the voltage signals were also analysed.

By conducting experiments with a variety of geometric parameters, the suppression was maximised over the range of Reynolds numbers between 1500 and 10000. The geometry giving the best suppression corresponded to a cylinder with 13 holes of 3 mm diameter, with a centre to centre distance of 10mm (i.e.  $G_1=0.250$  and  $G_2=0.384$ ). The maximum suppression achieved with this geometry was  $V_r \approx 0.3$  for both in-line and transverse directions.

The vibrations were enhanced at low Reynolds numbers ( $\approx 2000$ ) in the transverse and  $4000 < Re < 6000$  in the in-line direction. Both the in-line and transverse vibrations were suppressed in the range  $6000 < Re < 8000$ . For  $Re > 8000$   $V_r$  approached unity.

Before injection, the dominant frequencies in the in-line and transverse directions showed the classical 'frequency doubling' phenomenon associated with an organised vortex street. There were no dominant frequencies after injection.

The penetration length of the forward injection was approximated to around 1.5 to 2 times the cylinder diameter.

The sensitivity of this suppression technique to yaw was investigated. It was shown that even stronger suppression was possible when the injection holes were placed at  $60^\circ$  and  $240^\circ$  relative to the approach flow. It is also of note that injection at  $180^\circ$  showed the same level of suppression as forward injection (i.e. at  $0^\circ$ ).

# CHAPTER SEVEN: PREDICTION OF SUPPRESSION BY FORWARD INJECTION

## 7.1 Introductory Remarks

A number of techniques have been reported in the literature on the use of a 'secondary' flow in order to suppress the vortex shedding from a bluff body. These techniques include:

- 1) Base Bleed. Wood (1964, 1967) and Bearman (1967) employed base-bleed whereby the wake from a two-dimensional body with a blunt trailing edge was substantially modified by steady injection of fluid from the base of the body at low flow rates.
- 2) Blowing-Suction. This is a modified form of the base bleed technique. It involves the unsteady blowing of fluid and suction through very small, closely spaced holes along the base of the cylinder. This technique was introduced by Williams and Amato (1989). They showed that it is possible to suppress the near-wake Karman vortex formation and reduce the mean momentum deficit.
- 3) Forward Injection. This method was discussed in Chapter Six. No previous research exists on this topic.
- 4) Rear stagnation jet. This method involves the introduction at the rear of a cylinder of a jet with a velocity much greater than that of the incoming flow. Mo and Duke (1993) describe its application for a circular cylinder, while Koutmos et al.(1995) investigated this technique for a square cylinder. Their main finding was that rear stagnation jet forces a symmetrical wake flow pattern, thus eliminating the lift, while reducing the pressure on the cylinder surface. This method acts in a similar way to a splitter plate behind the cylinder. Present experiments (see Section 6.4.5) show that back injection does achieve suppression, but this phenomenon has not yet been investigated extensively.

It is not possible to numerically model the base bleed method, as the bleed fluid is injected through tiny holes. This would require very fine grids and, consequently, extensive computer resources. Blowing and suction is easier to model, but the

phenomenon is fully three-dimensional, and is thus outside the scope of this work. Attention is confined to the last two methods, i.e. forward injection and rear stagnation jet.

The possibility of the suppression of vortex shedding by forward injection from a circular cylinder was discussed in Chapter Six, where experimental evidence was presented. In this chapter, a numerical study of this phenomenon is presented and the possible reasons for its occurrence are discussed. Chapter Eight presents the results for the rear stagnation jet.

In order to compare the effectiveness of this method to the other suppression methods described earlier, it is proposed to simulate a laminar flow (i.e.  $Re=100$ ) and a fully turbulent flow (i.e.  $Re=6.5 \times 10^4$ ). In this way, it would be possible to compare the results with the two cylinders in tandem, and the control cylinder.

Certain modifications are necessary to the flow solver code in order to represent fluid injection. These modifications are described in Section 7.2. The grid considerations are discussed in Section 7.3. Laminar and turbulent flow results are presented in Section 7.4 and Section 7.5 respectively. The turbulence level of the injection jet is a major factor in the modelling of the injected fluid. The sensitivity of the results to this parameter is investigated in Section 7.6.

## **7.2 Computational Details**

Injection from the cylinder means that cells on the cylinder wall which were previously treated as a wall, now act as a secondary inlet into the domain. Therefore, the inlet and boundary conditions at the cylinder were adapted in order to enable the modelling of injection from the front and rear of the cylinder. Below is a summary of the main changes.

### **7.2.1 Boundary Conditions**

The initial field values of the variables  $U$ ,  $V$ ,  $k$ , and  $\epsilon$  are set within the flow solver. Injection is first introduced by prescribing a velocity ( $U_{hol}$ ) to the cells just inside the obstacle. If forward injection is to be modelled, then  $U_{hol}$  is assigned a negative value, since the injection is in the opposite direction to the incoming velocity ( $U_o$ ) (see Figure 7.1a). If a rear stagnation jet is to be modelled then the injection cells have

positive values of  $U_{hol}$  (see Figure 7.1b). Note that in both cases the V-component of the velocity is set to zero.

Injection introduces excess mass flow rate into the domain. To introduce the injection cells, an adjustment has to be made to the array storing cell face mass fluxes through the east face so that the ratio of outflow and inflow mass fluxes are balanced.

The coefficients  $A_E$  and  $A_W$  in Equation 2.26 contain contributions from the implicitly treated parts of convection and diffusion terms associated with the east and west neighbour of the cell just outside the cylinder. Therefore, to remove the boundary conditions for forward injection, the  $A_E$  coefficient of the cell outside the cylinder has to be associated with the injection velocity  $U_{hol}$  and added to the source terms  $S_\phi^C$  and  $S_\phi^P$  when the boundary conditions for the U velocity component and the k and  $\epsilon$  values are implemented. The same is done for  $A_W$  when a rear stagnation jet is modelled, considering that  $U_{hol}$  is positive.

Similarly, for the V-component of the velocity,  $A_E$  is recalculated and added to the  $S_\phi^C$  and  $S_\phi^P$  source terms. Since there is no V-component in the injection velocity, and  $A_E$  is calculated from  $-U_{hol}$ ,  $A_E$  will become negative. This will cause the V-component of the velocity in the cell west of the injection cell to be negative, and therefore wrong. Thus the modulus of  $A_E$  is taken and added to the source terms. Since for forward injection,  $U_{hol}$  is positive, there is no need to take the modulus of  $A_W$ , when considering the V-component of the velocity.

To account for the k and  $\epsilon$  boundary condition, their values are calculated at the cylinder wall cells with injection according to the  $U_{hol}$  velocity in those cells. The values of  $A_E$  (for forward injection) or  $A_W$  (for rear stagnation jet) are then calculated according to the k and  $\epsilon$  values at these cells, and added to the source terms.

## 7.2.2 Re-defining the Drag Term

The total drag on a body, often called the profile drag, is made up of two contributions, namely the pressure drag and the skin friction drag. The pressure drag is calculated from the forces due to the non-uniform pressure distribution on the body. The skin friction drag arises from the viscous forces at the surface.

When a secondary flow is introduced, by injection into the approach flow or into the wake, a force is applied on the injected fluid in the direction of the secondary flow. By applying Newton's third law, there is an equal reaction force on the cylinder in the opposite direction. The results presented in Chapters Seven and Eight take this added force into consideration by adding it to the profile drag. The reaction force ( $R_f$ ) is calculated thus:

$$\begin{aligned} R_f &= \dot{m}U_{\text{hol}} & (7.1) \\ R_f &= \rho A_{\text{inj}}(U_{\text{hol}})^2 \end{aligned}$$

where  $\dot{m}$  is the secondary mass flow rate and  $A_{\text{inj}}$  is the hole area.

In the case of forward injection,  $R_f$  is added to the drag force, as the reaction acts in the same direction as the profile drag. However, in the case of the rear stagnation jet,  $R_f$  is subtracted from the profile drag as the reaction acts in the opposite direction to the profile drag.

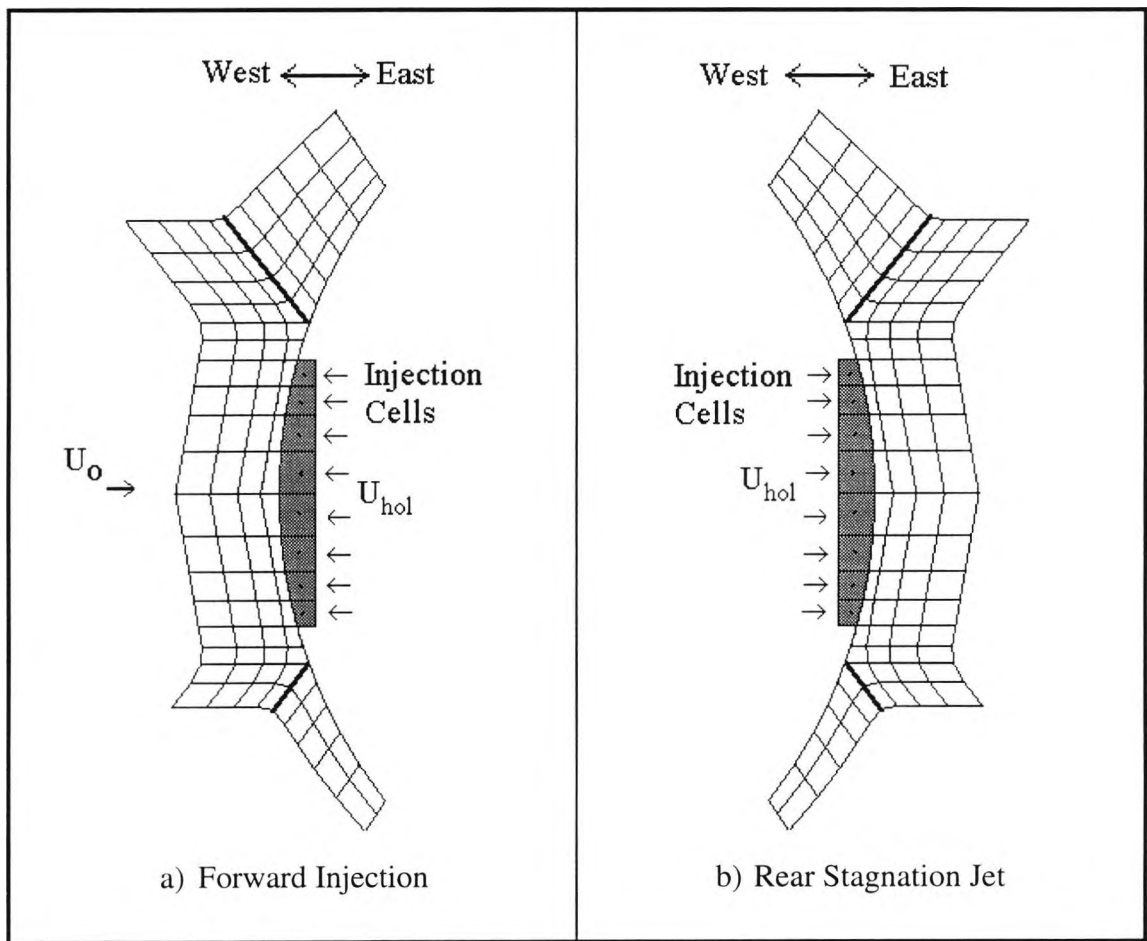


Figure 7.1: Injection cells on the a) west side of the cylinder for modelling forward injection and the b) east side of the cylinder modelling rear stagnation jet.

### 7.2.3 SIPSOL

Following the adaptations made to the code; further modifications had to be made to remove some anomalies in the results. When the program was run with increasing injection values, there was a certain bias towards either a non-zero lift coefficient, i.e. the lift cycle was not symmetric. This bias grew with increasing  $U_{hol}$ .

As described in Section 2.7 a system of  $M$  equations ( $M$  is the total number of control volumes) has to be solved for Equation 2.25. To do this, the Strongly Implicit Procedure of Stone (1968) (SIPSOL) is used. During the first inner iteration within this solver, the sum of absolute values of the initial residuals is stored in an array, which is used later to check the convergence of the outer iterations.

Figure 7.2(a) shows an example of how SIPSOL solves the set of equations for a simple grid. The inner iterations scan the field horizontally from the point  $i=1, j=1$  (S) of the grid sweeping to the East ( $i=16, j=1$ ). Then the pointer is set to the West again and incremented in the y-direction towards the North ( $i=1, j=2$ ), and scanning eastwards until all residuals are added up when F is reached ( $i=16, j=6$ ).

This method solves the south side of the obstacle first, thus possibly creating asymmetry in the solution. To remedy this problem, several methods were tried out, such as solving vertically, or from the east or the west. The method shown in Figure 7.2(b) was chosen as it produced the best results. This reduced the bias substantially, but asymmetry was still present in the flow with very large injection velocities.

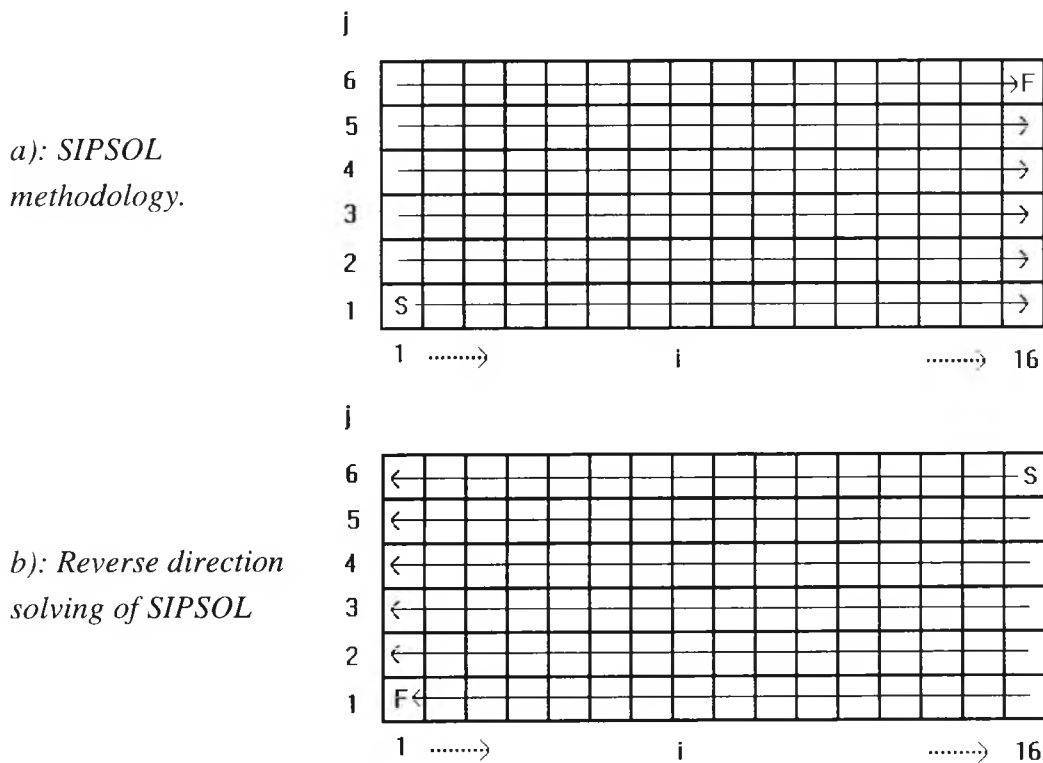
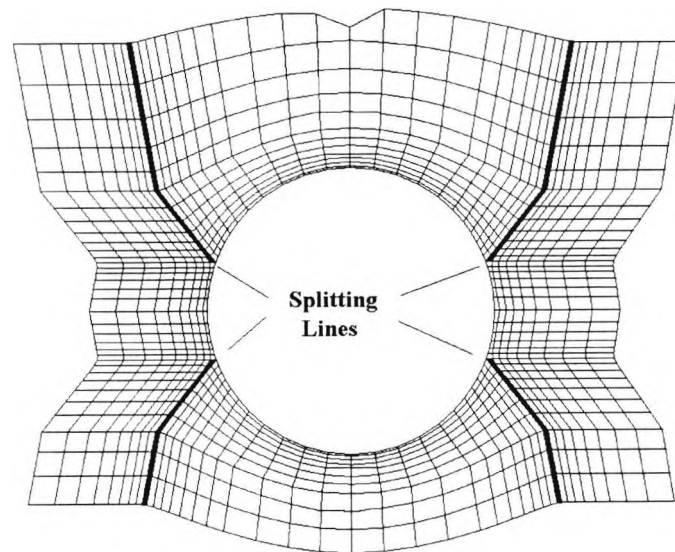


Figure 7.2: Solution to the asymmetry caused by SIPSOL.

### 7.3 Grid Generation

The greatest concern when creating grids for modelling injection is that there are enough grid nodes near the cylinder, so as to capture the correct behaviour of the injected fluid.

Asymmetry in the solutions can also arise if the injection cells coincide with the splitting lines (see Figure 7.3). The splitting lines cause a discontinuity in the solution domain, but are necessary to model curved obstacles. At first, the angle between the centroid of the cylinder and the splitting lines was set to  $8^\circ$ . By increasing this angle to  $18^\circ$ , it was possible to place the splitting lines outside the column of injection cells on the west side of the cylinder and virtually eliminate asymmetry in the flow. Asymmetry was still present at very high injection velocities, when the recirculation zone in front of the cylinder extended to the splitting lines.



*Figure 7.3: Close-up of the region around the cylinder, showing the splitting lines.*

## 7.4 Laminar Flow

The same grid (148x102) and start-up file for the circular cylinder at  $Re=100$  described in Section 3.4 (and used to model the control cylinder) was used here. Eight cells in the middle of the west wall of the cylinder were selected as the source of the secondary flow into the domain. The injection cells cover an area 0.185 the cylinder diameter. This is comparable to the experimental results shown in Chapter 6, when the ratio of  $G_1$  (ratio of hole diameter to cylinder diameter) was between 0.167 and 0.25.

Figure 7.4 shows the schematics of the forward injection, where  $U_o$  is the incoming velocity in the x-direction and  $U_{inj}$  is the injection velocity prescribed. In the flow solver,  $U_{inj}$  is represented by a negative value of  $U_{hol}$ . The parameter:

$$U_r = \frac{U_{inj}}{U_o} \quad (7.2)$$

is introduced and defined as the ratio of the injection velocity to the approach velocity.

Two parameters are introduced to measure the extent of suppression. These are the ratios of rms drag and lift after injection to before injection:

$$\tilde{C}_{D_r} = \frac{\tilde{C}_{D_{inj}}}{\tilde{C}_{D_{no\ injection}}} \quad (7.3)$$

and

$$\tilde{C}_{L_r} = \frac{\tilde{C}_{L_{inj}}}{\tilde{C}_{L_{no\ injection}}} \quad (7.4)$$

Table 7.1 shows the results for Reynolds number of 100 for values of  $U_r$  in the range 1.0-2.0. The simulations are started with a start-up flow field without forward injection. The non-dimensionalised time-step  $\Delta t^*$  was set to 0.054, which is the same as the single cylinder results of Chapter 3. As  $U_r$  was increased, a decrease in  $\Delta t^*$  became necessary, as the flow field around the cylinder became more complicated. The smallest time-step used at  $U_r=2.0$  was  $\Delta t^*=0.034$ . As before, the SMART scheme was used for the simulations.

The results in Table 7.1 compare mean drag, fluctuating drag, fluctuating lift and Strouhal number based on the lift cycle. Note that when  $U_r=0$ , there is no injection.

Runs below  $U_r=1.0$  were not analysed, as the injection velocity was not large enough to make an impact on the flow behaviour.

Figure 7.5 shows the behaviour of the main parameters,  $\bar{C}_D$ ,  $\tilde{C}_{D_r}$ ,  $\tilde{C}_{L_r}$ , and  $St$  with increasing  $U_r$ . These results clearly show that the flow experiences three distinct phases.

The first phase is for  $U_r=0.0$  to  $1.498$ . In this phase, mean drag is reduced from  $1.451$  at  $U_r=0$  to  $0.902$  at  $U_r=1.498$ . The fluctuating drag and lift coefficients are first enhanced slightly, up to  $1.160$  and  $1.099$  of their respective original values, but then reach a minimum at  $U_r=1.498$ . The Strouhal number remains essentially constant.

The second phase is for  $U_r=1.498$  to  $1.585$ . The mean drag is further reduced, but at a faster rate. It reaches its minimum value of  $0.719$ , which is half the original mean drag. There is a slight rise in fluctuating drag. Fluctuating lift is further reduced (at a faster rate) to  $0.43$  of its original value at  $U_r=1.552$ . The Strouhal number increases in this phase, but only slightly, to  $0.174$ .

The third phase is for  $U_r>1.585$ . In this phase, mean drag, and fluctuating drag and lift increase dramatically. The mean drag increases towards its original value, although not enough runs were made to establish the point where this happens. The fluctuating drag shoots up to  $10$  times its original value, while fluctuating lift achieves  $1.571$  times its original value. On the other hand, Strouhal number is decreased to very small values, indicating a large phase and small frequencies of vibration.

In order to determine the behaviour of the flow in these three phases, three injection velocity ratios are selected for further investigation. These lie within the three phases, and are at  $U_r=1.498$ ,  $1.552$ , and  $2.0$ .

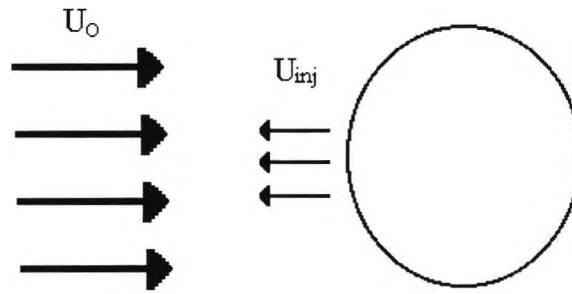


Figure 7.4: Schematics for forward injection.

RUN	$U_r$	$\bar{C}_D$	$\tilde{C}_D$	$\tilde{C}_{D_r}$	$\tilde{C}_L$	$\tilde{C}_{L_r}$	St
1	0.000	1.451	0.105	1.000	0.161	1.000	0.173
2	1.000	1.179	0.122	1.160	0.177	1.099	0.172
3	1.320	1.119	0.100	0.957	0.168	1.043	0.171
4	1.403	1.069	0.082	0.778	0.157	0.976	0.171
5	1.498	0.902	0.052	0.500	0.117	0.726	0.168
6	1.542	0.768	0.069	0.659	0.069	0.434	0.174
7	1.552	0.758	0.069	0.657	0.069	0.430	0.177
8	1.563	0.744	0.064	0.605	0.072	0.446	0.181
9	1.574	0.719	0.056	0.537	0.077	0.482	0.181
10	1.585	0.786	0.302	2.876	0.123	0.766	0.179
11	1.595	0.681	0.480	4.568	0.118	0.731	0.177
12	1.600	0.778	0.513	4.887	0.134	0.830	0.170
13	1.800	0.971	1.032	9.831	0.253	1.568	0.108
14	2.000	1.140	1.026	9.774	0.253	1.571	0.097

Table 7.1: Results for forward injection, for a circular cylinder at  $Re=100$ .

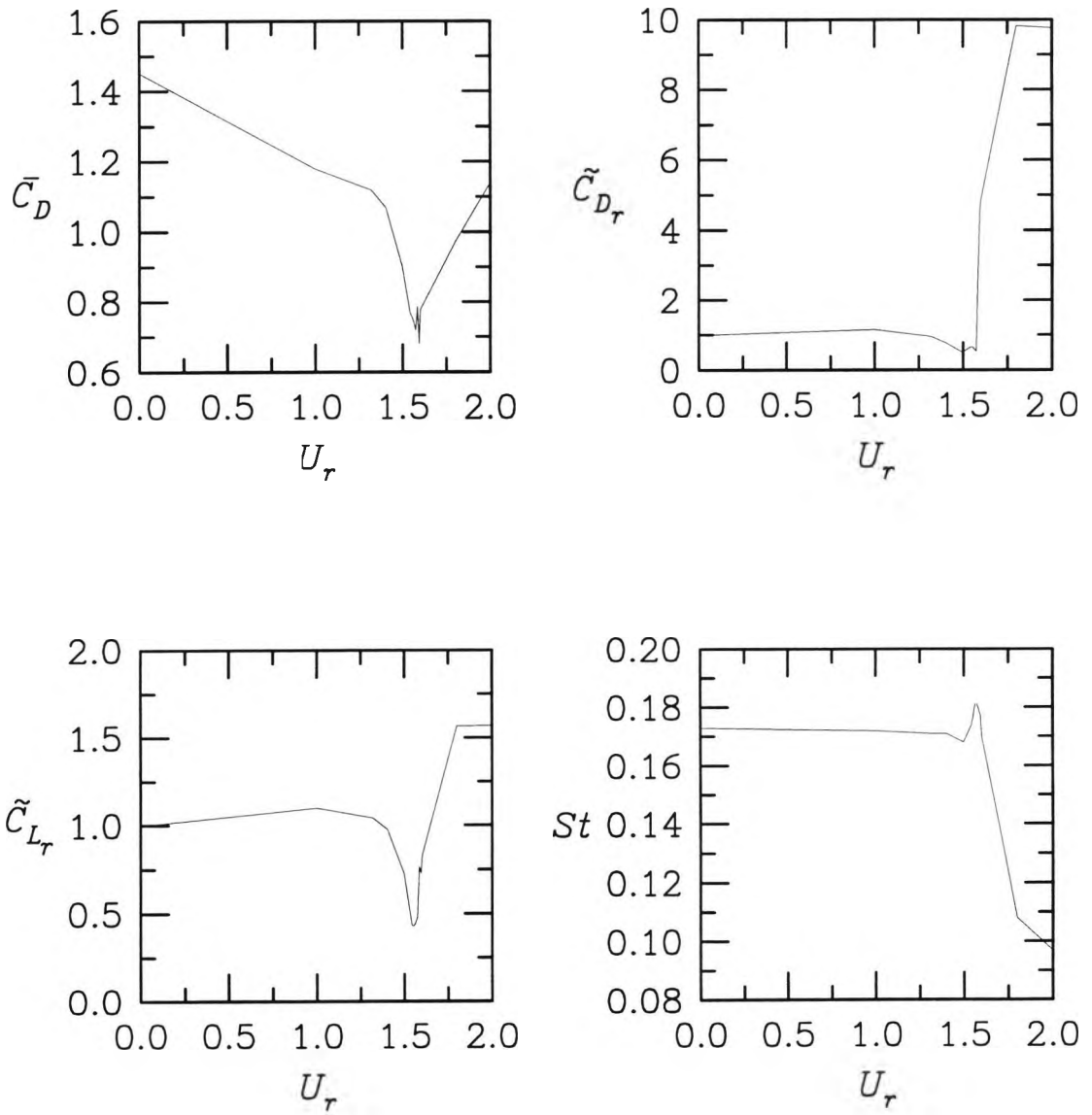


Figure 7.5: Behaviour of main parameters with  $U_r$  for laminar flow with forward injection.

Figure 7.7 to Figure 7.10 show the time histories for the drag and lift coefficients and their power spectra for the four injection ratios,  $U_r=0.$ , 1.498, 1.552, and 2.0. The patterns of the drag, lift and their spectra do not change much, except for  $U_r=2.0$ , where the periods of the drag and lift cycles are longer and the drag and lift coefficients obtain larger amplitudes. The mean drag is large at this point and is near its original value without injection.

Figure 7.11 to Figure 7.14 show the velocity vectors around the cylinder for all the values of injection ratio. The largest velocity vector is scaled to the highest injection ratio. These figures show that two recirculation zones are formed in front of the cylinder, on either side of the injection cells. This means that the stagnation point has been moved away from the cylinder, to a position upstream of it. At  $U_r=1.498$ , this position is at 0.6 cylinder diameters. It should be mentioned that the penetration length measured experimentally (in Section 6.4.4) was 1.5 to 2 cylinder diameters.

At the highest injection ratio investigated ( $U_r=2.0$ ), these recirculation zones become so large that they become unstable. With the lateral movement of the stagnation point, they are eventually shed from the front of the cylinder and contribute to a complex system of vortices behind the cylinder.

Figure 7.15 (a) to (d) show the streaklines around the cylinder for all the injection ratios investigated. The first three figures show that there is no change in the shape and dimensions of the vortex street behind the cylinder, although the fluctuating drag and lift forces are suppressed to around 0.5 of their original values. The Strouhal number however remains constant. Figure 7.15(d) shows the streaklines for  $U_r=2.0$ . The instability of the recirculation zones in front of the cylinder is evident in this figure.

Figure 7.16 and Figure 7.17 show a breakdown of the drag and lift coefficients around the cylinder for  $U_r=0.$  and  $U_r=1.498$ , when the fluctuating drag reaches its minimum value. The figures show five lift cycles for both cases. The cylinder surface is split into four quadrants with the drag and lift obtained for each one. These quadrants are labelled A to D. The sum of the drag and lift in all the quadrants equals the total drag and lift on the cylinder.

The drop in mean drag between the two figures is attributed to the two front quadrants (A and D). The stagnation point does not act directly on the cylinder surface anymore as it has moved upstream. The drag force in these quadrants are as a result of the reaction on the cylinder due to the injection force and the recirculation zones. However, the fluctuations in drag in the front two quadrants are increased. The overall decrease in fluctuations in drag is attributed to the back quadrants (B and C).

The lift cycle does not change significantly in the A and D quadrants while the fluctuations in the B and C quadrants are the main cause of the drop in the overall fluctuating lift.

Therefore, the main source of suppression in the mean drag is associated with changes occurring at the front of the cylinder where the two new recirculation zones are located. The suppression in fluctuating drag and lift is due to the weakening of vortex shedding behind the cylinder.

Figure 7.18 to Figure 7.21 show contours of vorticity around the cylinder with and without forward injection. Vorticity is the measure of rotation of fluid particles and is measured at any point in the fluid by:

$$\omega = \frac{\partial U}{\partial y} - \frac{\partial V}{\partial x} \quad (7.4)$$

This definition implies that positive vorticity represents the rate of rotation in a clockwise direction and negative vorticity represents rotation in an anti-clockwise direction. The contours have been scaled and colour coded to represent values of -1 to 1 for all the figures. Black represents no rotation. The contours were calculated at the same point of the lift cycle for all the figures, when the lift is zero.

Vorticity is generated where the flowing fluid meets a solid surface. The boundary layer on the cylinder is thus the source of the vorticity which is convected downstream in the wake. The way in which the vortical fluid leaves the surface is of great importance for it determines the flow over the back of the cylinder and thus the drag on the cylinder. Retarded by surface friction, the fluid of the boundary layer is ultimately unable to advance along the surface against the rising pressure over the back of the cylinder. Separation occurs. Beyond the separation point, the direction of the flow at the surface is reversed, so that the fluid moves towards the point from both directions. Between the separated vortical layer and the surface lies a

recirculating flow, which extends into a wider region behind the cylinder. This gives rise to vortex shedding.

The above description is evident in all the vorticity contour figures, where there is a concentration of vorticity at around  $90^\circ$ . This is the point of separation. This vorticity is convected downstream to form alternate vortices behind the cylinder.

There may be many factors involved in the suppression shown by the results.

With increasing injection, the recirculation zones in front of the cylinder extend into the incoming flow, and increase in vorticity. This induces a counter-flowing recirculation in front of the cylinder, which in turn may decrease the overall drag and lift on the cylinder. The reduction in fluctuating drag and lift can be attributed to the weakening of the vortices behind the cylinder as shown by the vorticity contours.

The most plausible explanation for the observed suppression is that the cylinder is streamlined by the presence of the vortices in front of the cylinder. This is shown in Figure 7.6 below, where the incoming flow encounters a tear-drop bluff body. With increasing injection velocity, this new body lengthens, until a point is reached when the vortices in front break up and are swept along the cylinder, creating a more complex flow pattern around the cylinder.

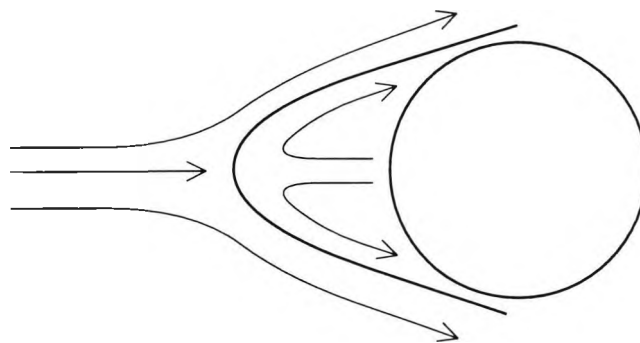


*Figure 7.6: Streamlining of bluff body by forward injection.*

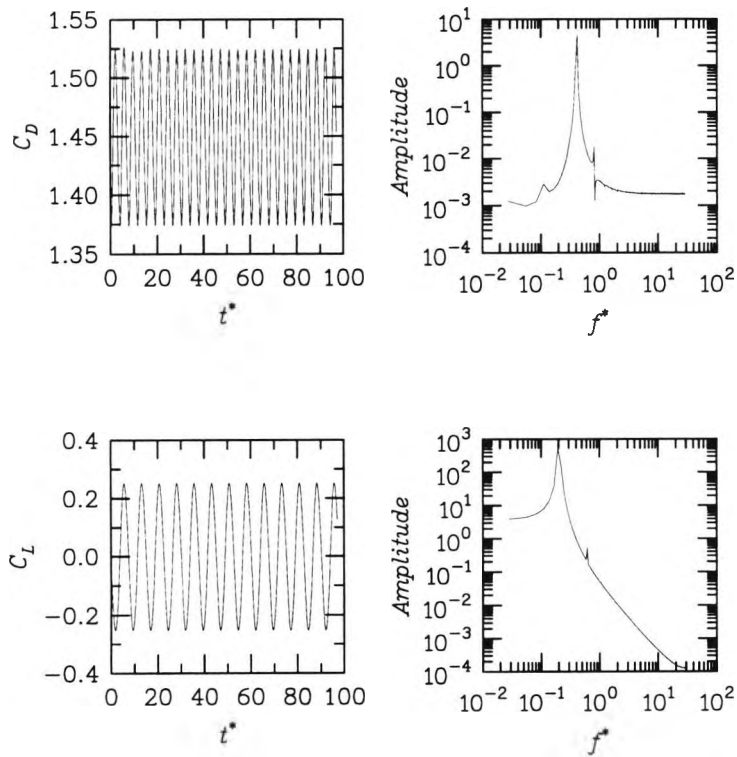


Figure 7.7: Drag and lift time histories with their power spectra for  $Re=100$ , with no forward injection.

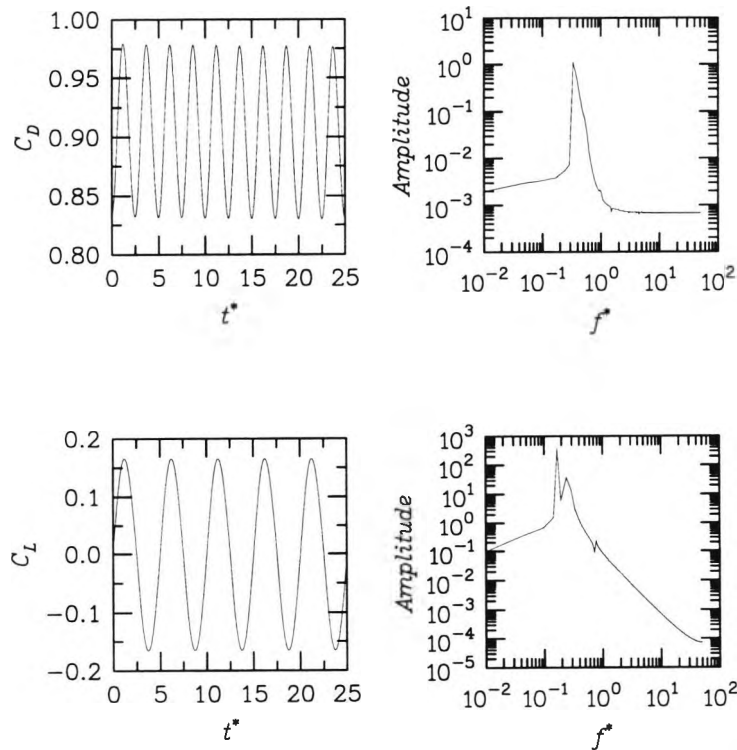


Figure 7.8: Drag and lift time histories with their power spectra for  $Re=100$ , with forward injection of  $U_r=1.498$ .

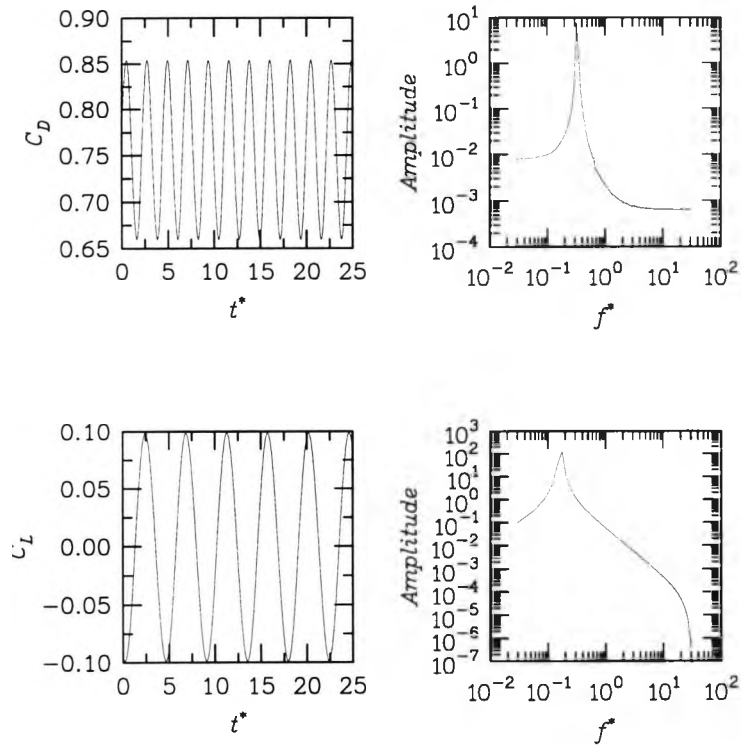


Figure 7.9: Drag and lift time histories with their power spectra for  $Re=100$ , with forward injection of  $U_r=1.552$ .

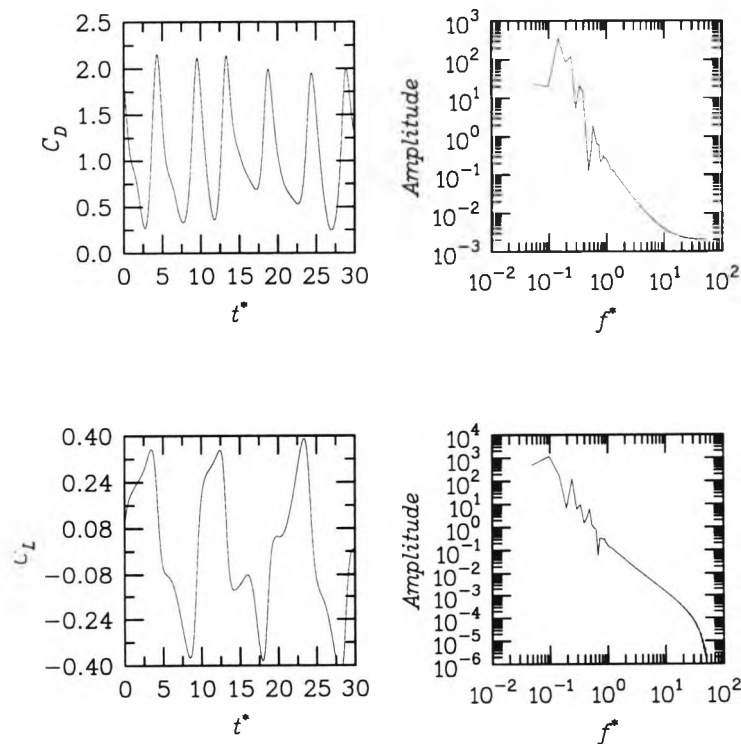
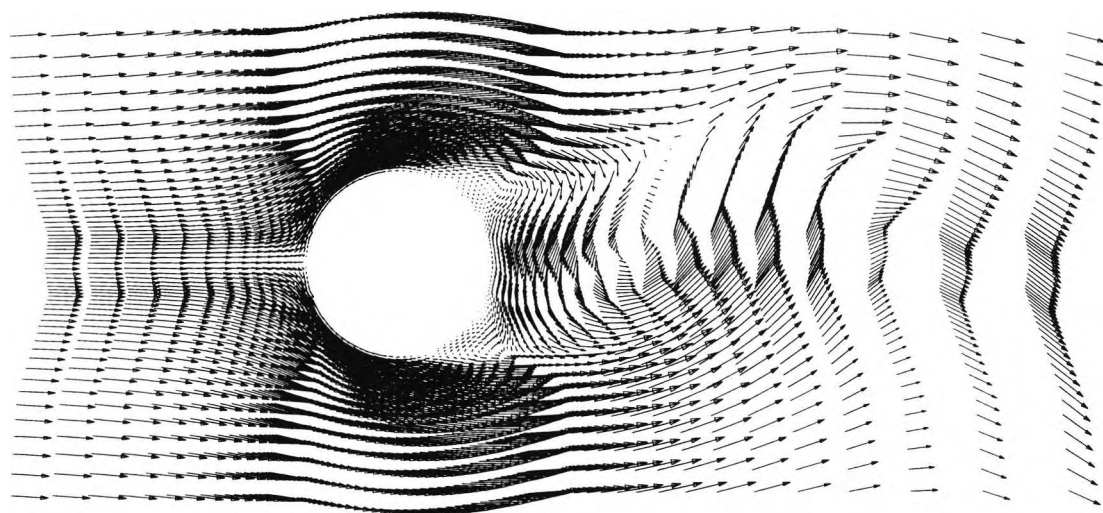
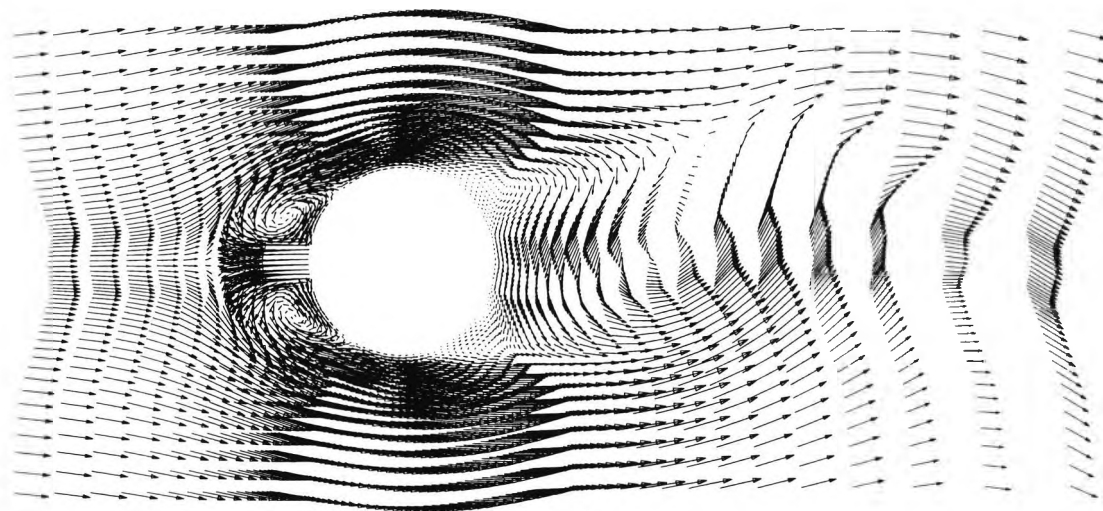


Figure 7.10: Drag and lift time histories with their power spectra for  $Re=100$ , with forward injection of  $U_r=2.0$ .



*Figure 7.11: Velocity vectors around a circular cylinder at  $Re=100$ , with no forward injection.*



*Figure 7.12: Velocity vectors around a circular cylinder at  $Re=100$ , with forward injection ratio of  $U_f=1.498$ .*

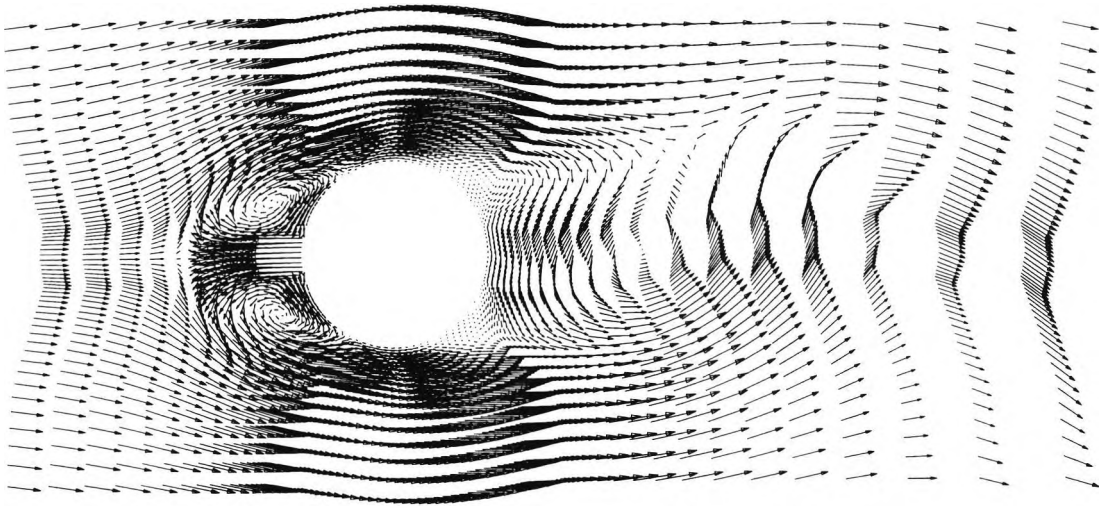


*Figure 7.13: Velocity vectors around a circular cylinder at  $Re=100$ , with forward injection ratio of  $U_r=1.552$ .*

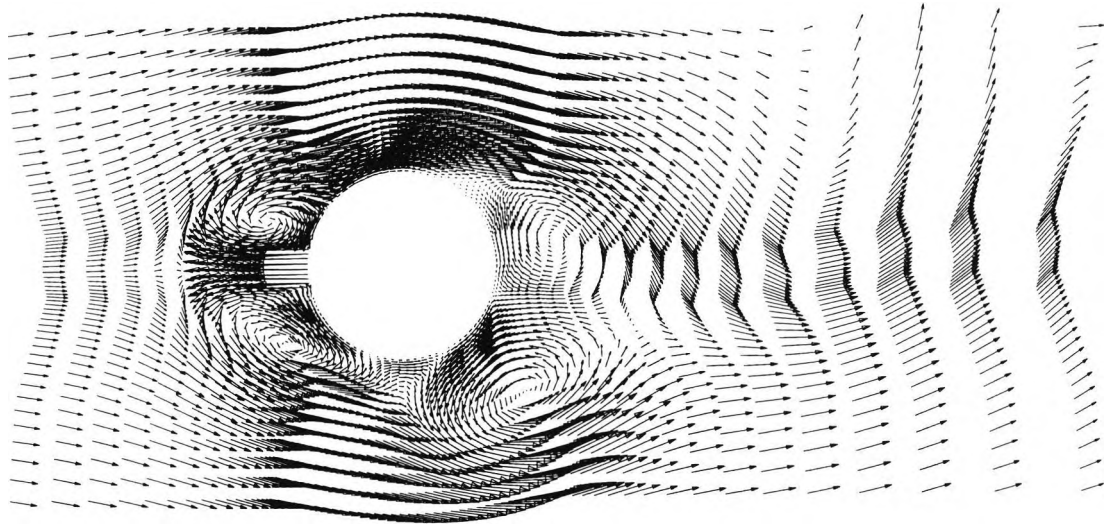


*Figure 7.14: Velocity vectors around a circular cylinder at  $Re=100$ , with forward injection ratio of  $U_r=2.0$ .*

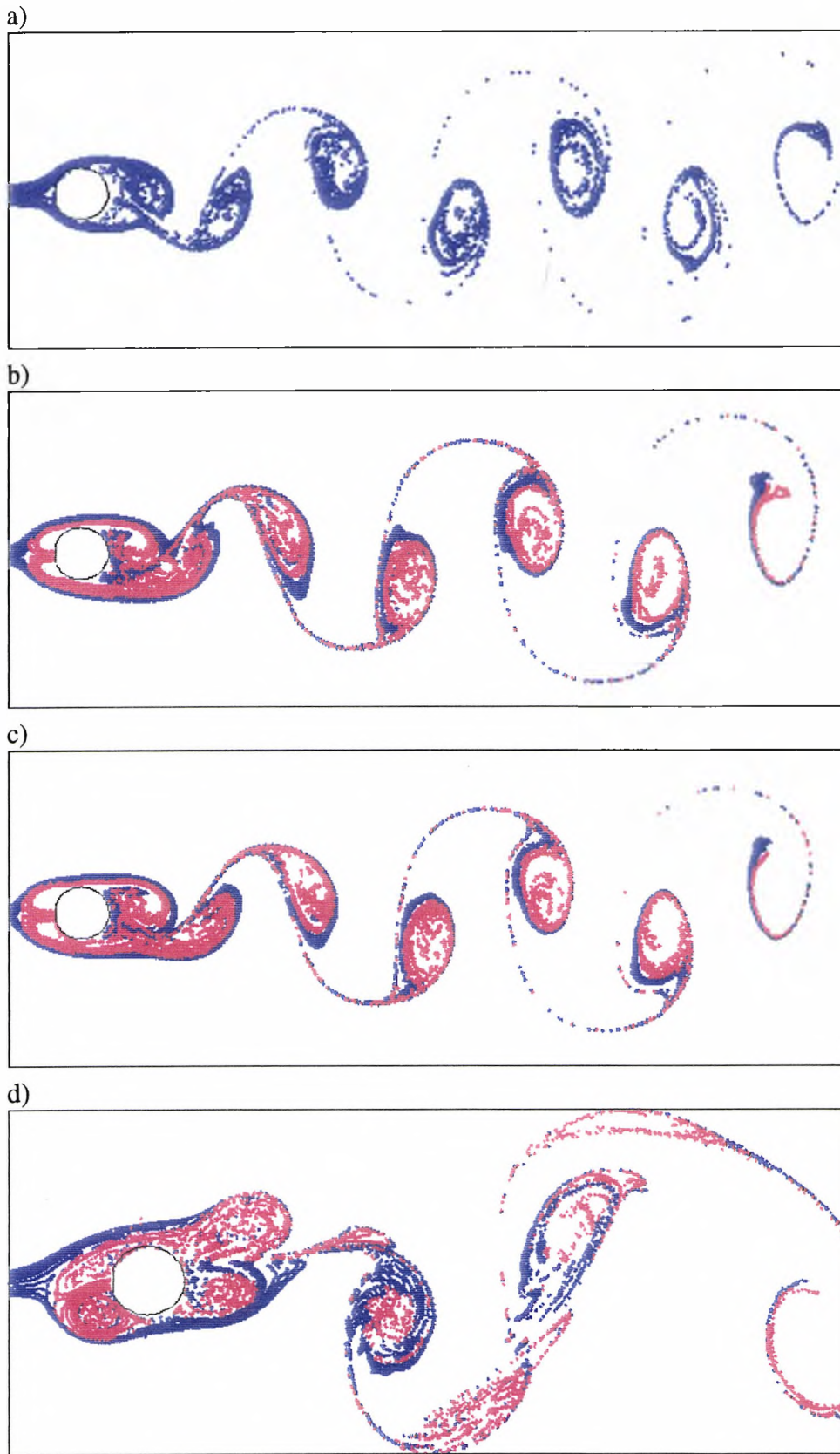


Figure 7.15: Streamlines for forward injection at  $Re=100$ , when a)  $U_t=0.$ , b)  $U_t=1.498$ , c)  $U_t=1.552$ , d)  $U_t=2.0$ .

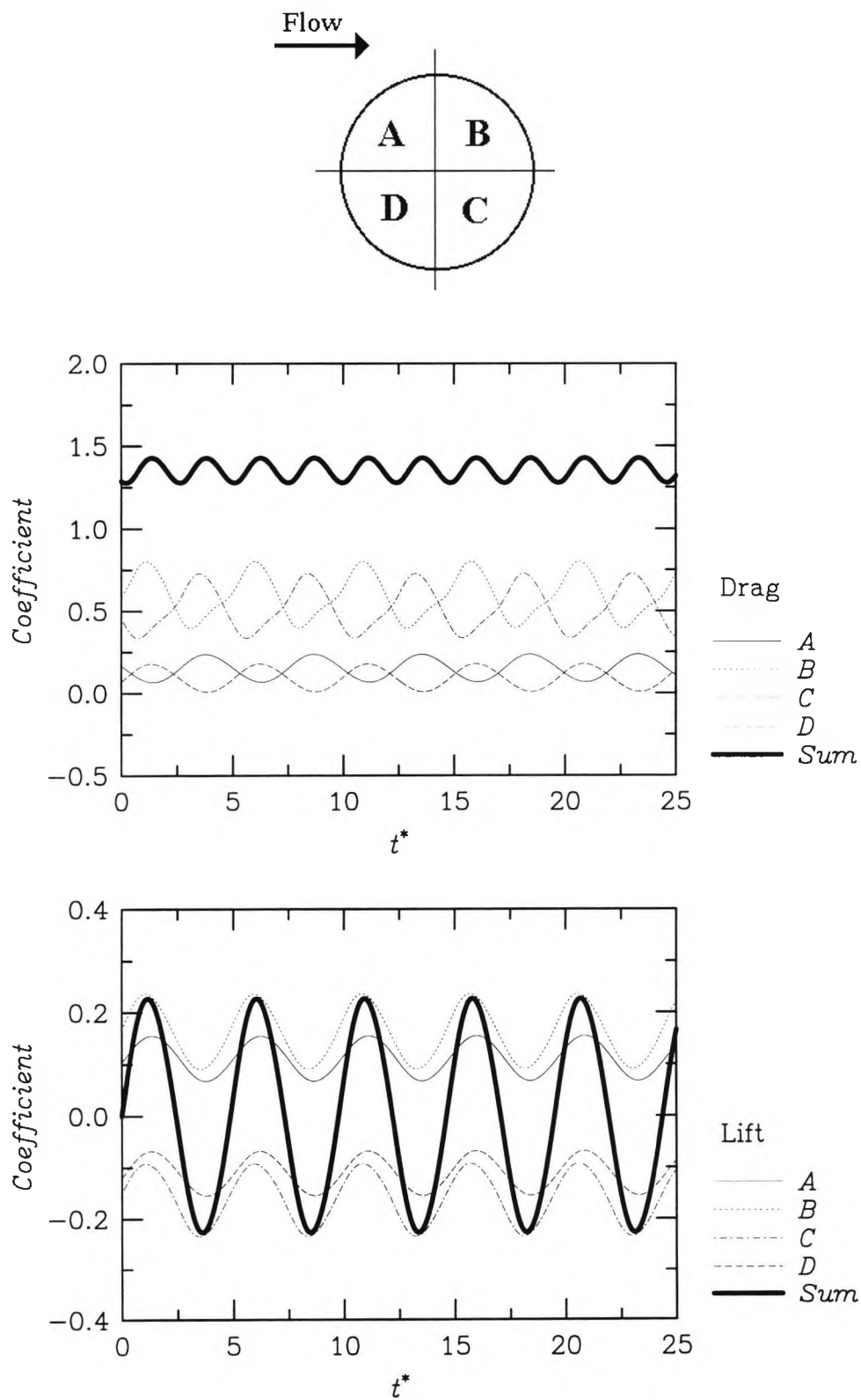


Figure 7.16: Breakdown of the drag and lift coefficient behaviour around a circular cylinder at  $Re=100$ , with no forward injection.

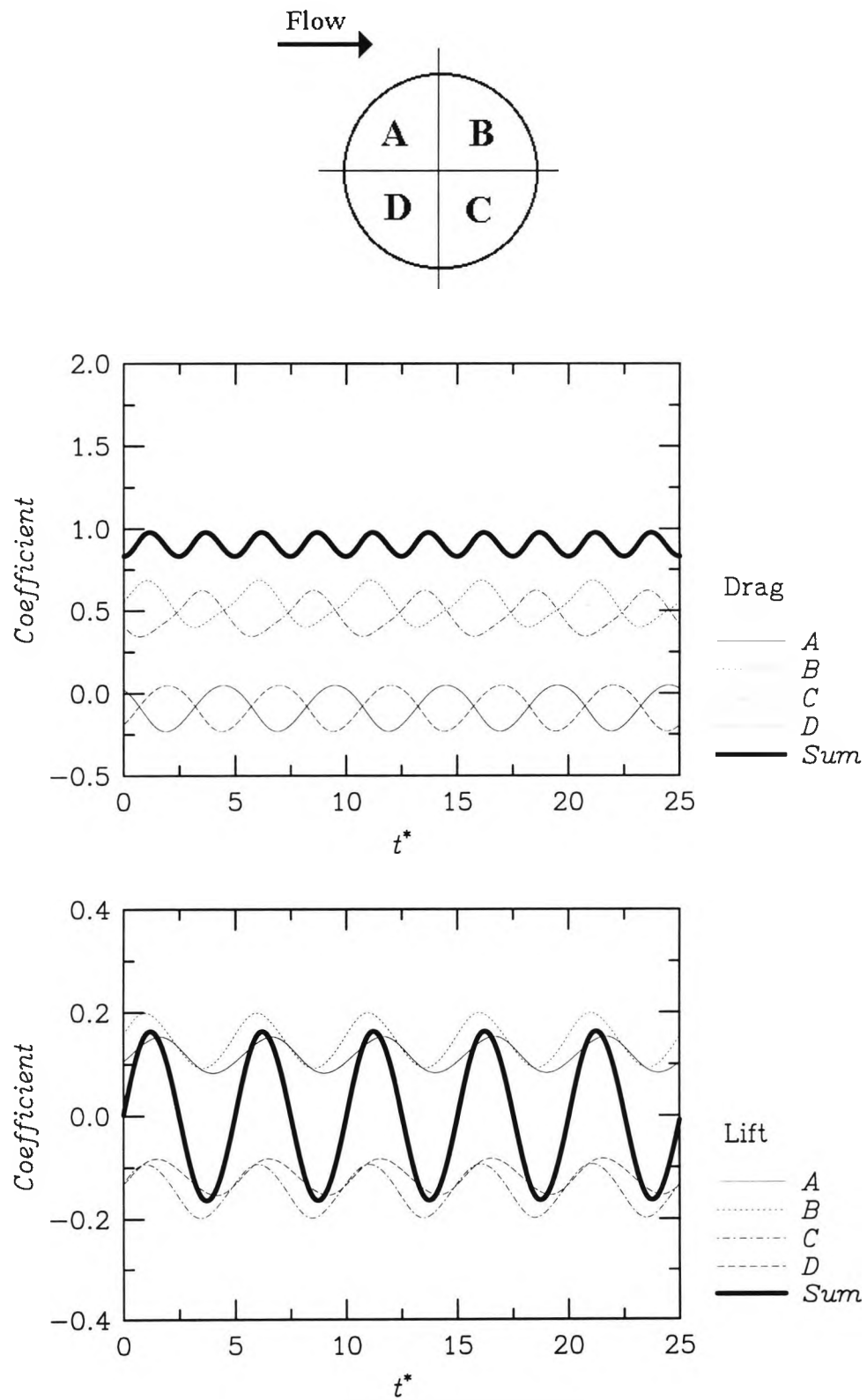


Figure 7.17: Breakdown of the drag and lift coefficient behaviour around a circular cylinder at  $Re=100$ , with forward injection ratio of  $U_r=1.498$ .

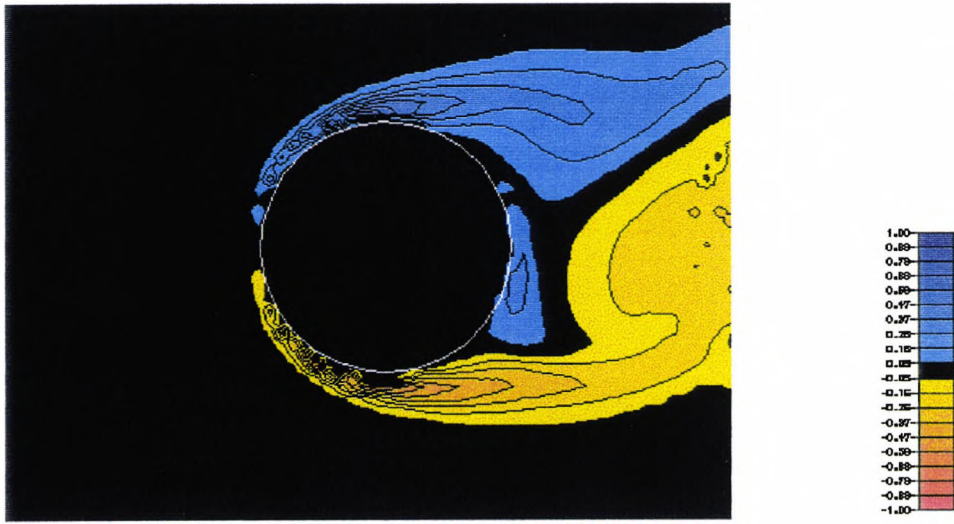


Figure 7.18: Vorticity contours around a cylinder at  $Re=100$ , without forward injection.

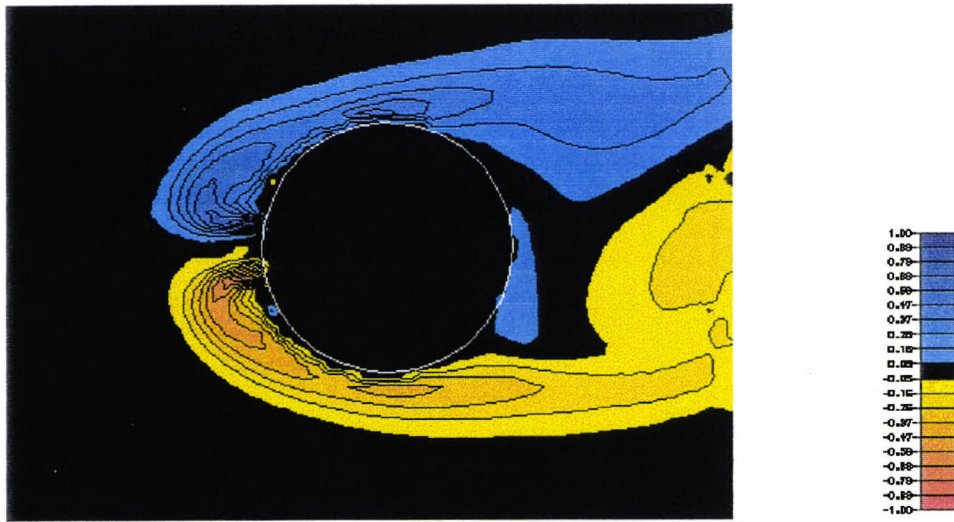


Figure 7.19: Vorticity contours around a circular cylinder at  $Re=100$ , with forward injection ratio of  $U_f=1.498$ .

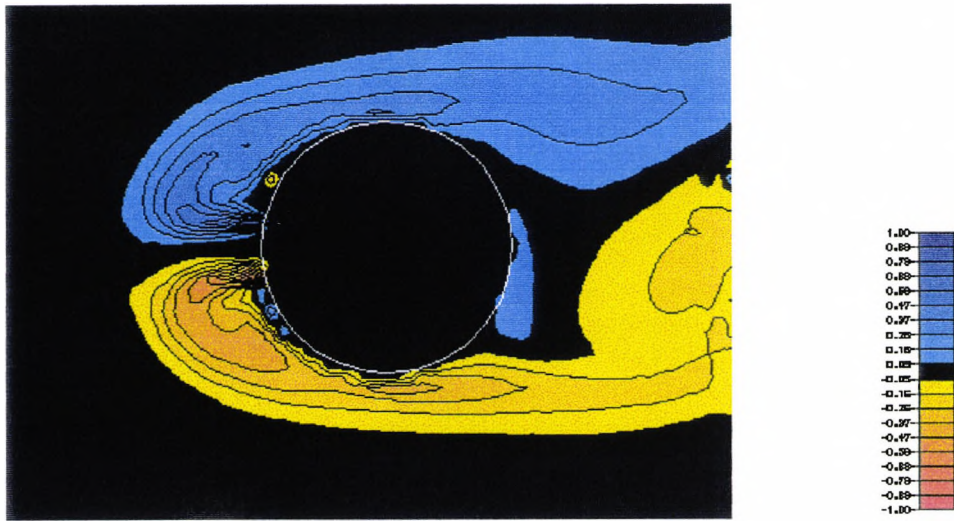


Figure 7.20: Vorticity contours around a circular cylinder at  $Re=100$ , with forward injection ratio of  $U_r=1.552$ .

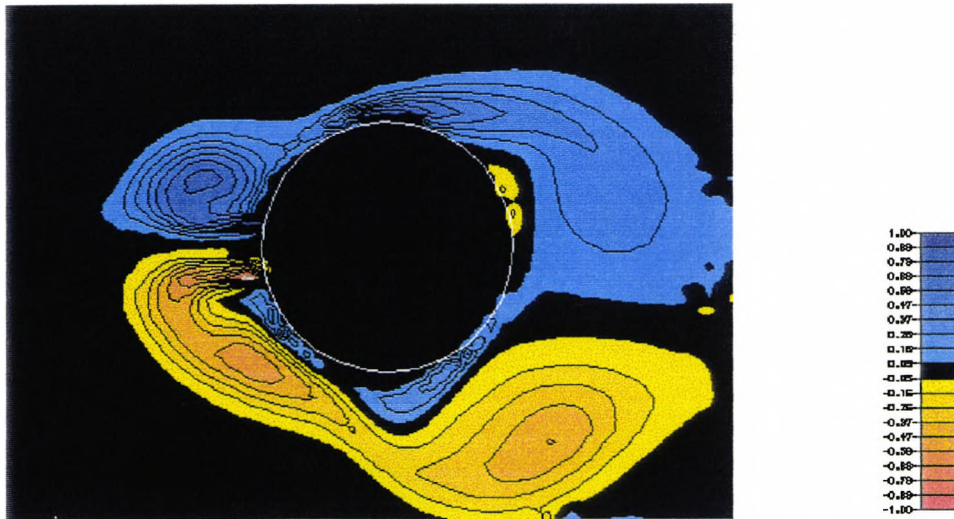


Figure 7.21: Vorticity contours around a circular cylinder at  $Re=100$ , with forward injection ratio of  $U_r=2.0$ .

## 7.5 Turbulent Flow

There are no previous experimental or numerical results for a circular cylinder in turbulent flow with forward injection. The present study is performed at Reynolds number of  $6.5 \times 10^4$ , in order to compare the results with those of the control cylinder and rear stagnation jet.

The same terminology and definitions are used as in the laminar flow case (see Section 7.4). The simulations were carried out with the  $195 \times 98$  grid used in earlier turbulent simulations for an isolated circular cylinder (see Section 3.7.2) and one with a control cylinder (see Section 5.6.1).

As in the laminar case, eight cells in the middle of the west wall of the cylinder were selected as the secondary inlet into the domain. The injection cells cover an area 0.185 times the cylinder diameter. This is comparable to the experimental results shown in Chapter 6, when the ratio of  $G_1$  (ratio of hole diameter to cylinder diameter) was between 0.167 and 0.25.

One of the major factors influencing turbulent flow calculations is the level of turbulence intensity prescribed at the inlet to the flow domain. The levels of  $k$  and  $\epsilon$  at the inlet are defined as follows:

$$k_{in} = \beta(T_u \cdot U_o)^2 \tag{7.5}$$
$$\epsilon_{in} = \frac{C_\mu k_{in}^2}{v_t}$$

Where:  $\beta = 1.5$

$T_u$  = Relative turbulence intensity at inlet = 3%

$U_o$  = Inlet velocity

$C_\mu = 0.09$

$v_t = 100v$

In the case of forward injection and rear stagnation jets, there are two inlets to the flow domain; one corresponding to the incoming flow, and one corresponding to the injected flow. The injected flow velocity is generally different from that at the main inlet. In some cases, it can be much larger. Therefore, the turbulence level should accordingly be altered.

Turbulence sensitivity tests were carried out for the forward injection case with a variety of values for  $(\beta)$  in Equation 7.5 to assess its effect on the main parameters. The tests were done for  $U_r=0.75$  and are shown in Table 7.2. They show that there is a breakdown of normal vortex shedding at excessively large values of this factor. High values of all the main parameters, except Strouhal number, along with an asymmetric, random signal rule out the use of factors above 100. At small values of  $\beta$ , the turbulence model is effectively switched off at the injection cells. A value of  $\beta=100.0$  was chosen to correct the turbulence level at the cylinder inlet. This value was used throughout the simulations for forward injection and rear stagnation jet.

The size of  $\Delta t^*$  is of major importance in the turbulent simulations of forward injection. With increasing injection ratios, the code failed to perform the inner iterations until  $\Delta t^*$  was decreased. The sensitivity of the solutions to the size of  $\Delta t^*$  is shown in Table 7.3. The results presented there are for  $Re=6.5 \times 10^4$  for a range of  $U_r$  values between 0.1 and 1.75. The Table lists the values of mean drag, fluctuating drag, fluctuating lift and Strouhal number based on the lift cycle. Note that when  $U_r=0$ , there is no jet present. The modified k- $\epsilon$  model with the SMART scheme was used throughout.

Figure 7.22 shows the behaviour of the main parameters,  $\bar{C}_D$ ,  $\tilde{C}_{D_r}$ ,  $\tilde{C}_{L_r}$ , and  $St$  with the injection velocity ratios.

The results show that the overall effects of injection on suppression of vortex shedding in turbulent flow are not to the same extent as in laminar flow. Mean drag and Strouhal number are decreased slightly, but fluctuating drag and lift are enhanced. The flow experiences two distinct phases.

The first phase is for  $0 < U_r < 0.75$ . The mean drag is reduced to 0.65 of its original value and Strouhal number is also decreased. The second phase commences from this point onwards, when all parameters increase at the same rate. The fluctuating drag and lift increase at the same rate throughout the simulations.

The phase when vortices are shed from the front of the cylinder, discussed earlier in the laminar flow simulations, is not reached here. This is because of the extensive computation times involved. The computation times increased dramatically once  $U_r$  increased beyond 0.75. A necessary drop in  $\Delta t^*$  caused the flow solver to take up to 24 hours to compute each cycle. It is expected that once  $U_r$  reaches a higher value, vortices would shed from the front of the cylinder as in the laminar case.

In order to study the behaviour of the flow, the velocity ratio of  $U_r=0.75$  was chosen for detailed presentation.

Figure 7.23 and Figure 7.24 show the time histories for the drag and lift coefficients and their power spectra for two injection ratios of  $U_r=0.$  and  $0.75.$  They show that mean drag was definitely reduced, while the fluctuating drag and lift were increased. The power spectra show a narrowing of the peak around the shedding frequency and an increase in amplitude of the higher frequencies.

Figure 7.25 and Figure 7.26 show velocity vectors around the cylinder at  $U_r=0.$  and  $0.75.$  Unlike the laminar flow results, the recirculation zones in front of the cylinder are not considerable in size. There are is no change to the vortices behind the cylinder.

Figure 7.27 and Figure 7.28 show the streaklines around the cylinder. Again, no apparent change is visible in the flow pattern behind the cylinder.

Figure 7.29 and Figure 7.30 show vorticity contours for the same velocity ratios. As in the laminar case, the contours are scaled between  $-1$  and  $1$  for both figures, with black representing no rotation. It is obvious that separation occurs further downstream in this turbulent case at around  $130^\circ.$  The effect of the injection on the vorticity contours is to weaken the strength of the vortices behind the cylinder, and create small vortices in front of the cylinder.

$\beta$	$\bar{C}_D$	$\tilde{C}_D$	$\tilde{C}_{D_r}$	$\tilde{C}_L$	$\tilde{C}_{L_r}$	St
0.5	0.848	0.278	2.000	1.446	1.453	0.269
1.5	0.841	0.264	1.893	1.439	1.447	0.267
10.0	0.836	0.250	1.744	1.425	1.432	0.264
100.0	0.797	0.232	1.667	1.282	1.288	0.265
1000.0	0.774	0.424	3.040	1.487	1.494	0.272
10000.0	0.762	0.741	5.326	2.458	2.471	0.275

Table 7.2: Turbulence sensitivity results for forward injection.

RUN	$U_r$	$\bar{C}_D$	$\tilde{C}_D$	$\tilde{C}_{D_r}$	$\tilde{C}_L$	$\tilde{C}_{L_r}$	St	$\Delta t^*$
1	0.000	1.025	0.139	1.000	0.995	1.000	0.292	0.001
2	0.100	0.913	0.146	1.051	1.060	1.065	0.290	0.001
3	0.250	0.873	0.150	1.077	1.074	1.079	0.285	0.001
4	0.500	0.822	0.175	1.256	1.193	1.199	0.277	0.001
5	0.750	0.797	0.232	1.667	1.282	1.288	0.265	0.0005
6	1.000	0.884	0.253	1.821	1.350	1.357	0.272	0.0005
7	1.250	0.929	0.292	2.103	1.391	1.398	0.276	0.0003
8	1.500	1.002	0.339	2.436	1.570	1.578	0.281	0.0002
9	1.750	1.153	0.374	2.692	1.809	1.818	0.287	0.0002

Table 7.3: Results for forward injection, for a circular cylinder at  $Re=6.5 \times 10^4$ .

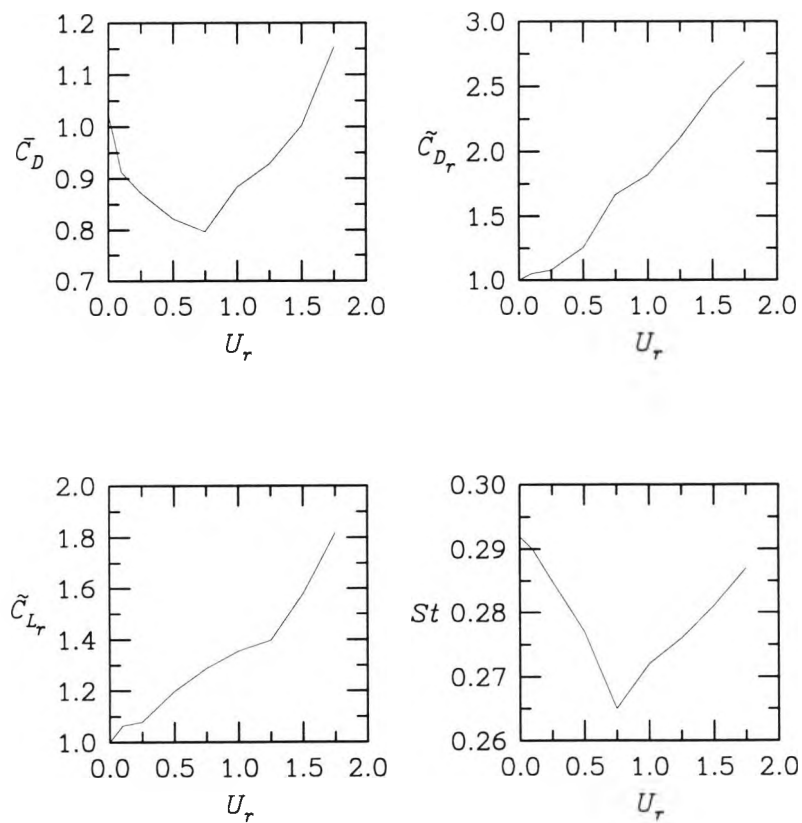


Figure 7.22: Behaviour of main parameters with  $U_r$  for turbulent flow with forward injection.

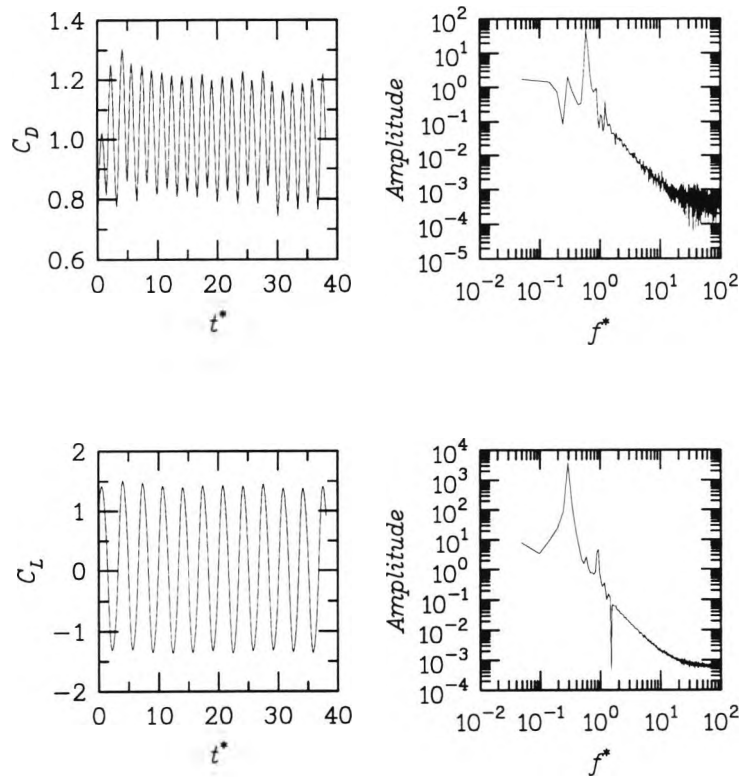


Figure 7.23: Drag and lift time histories with their power spectra for  $Re=6.5 \times 10^4$ , with no forward injection.

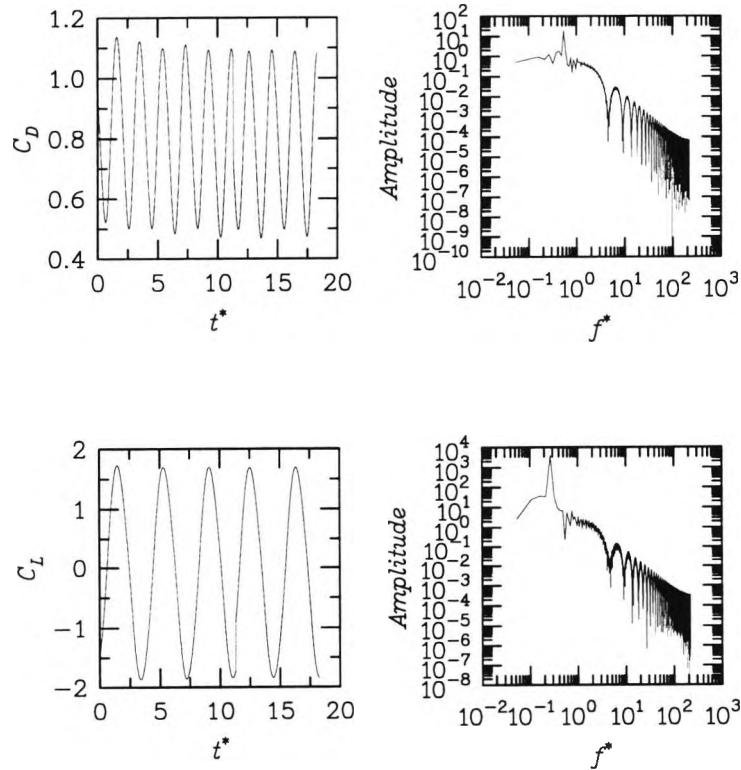


Figure 7.24: Drag and lift time histories with their power spectra for  $Re=6.5 \times 10^4$ , with forward injection at  $U_r=0.75$ .

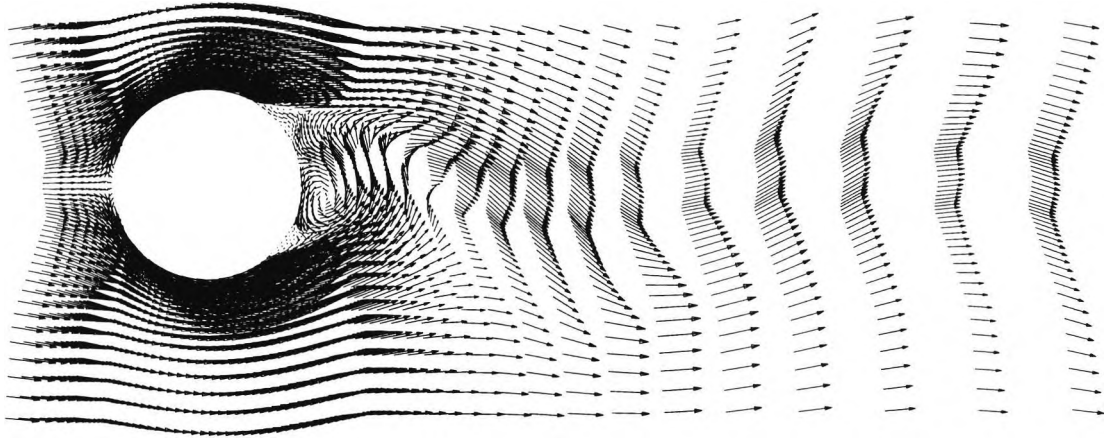


Figure 7.25: Velocity vectors around a circular cylinder at  $Re=6.5 \times 10^4$ , with no forward injection.

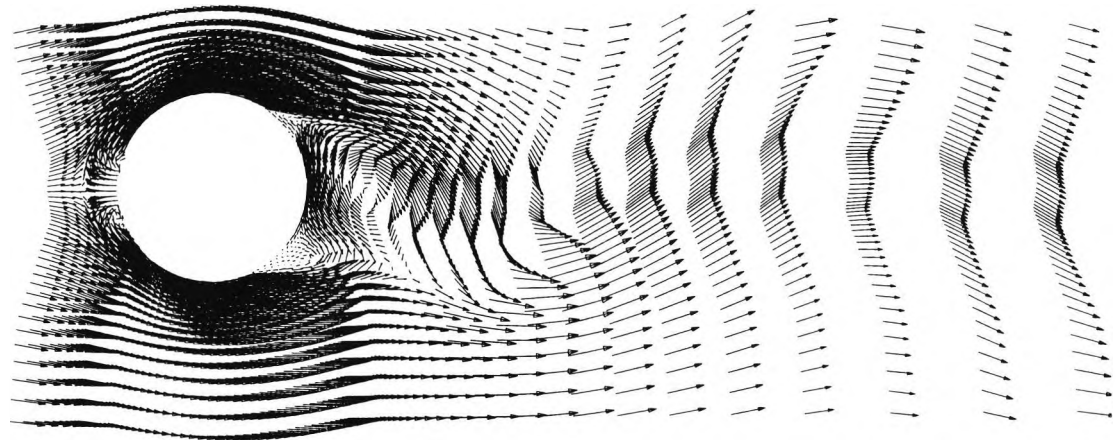


Figure 7.26: Velocity vectors around a circular cylinder at  $Re=6.5 \times 10^4$ , with forward injection at  $U_r=0.75$ .

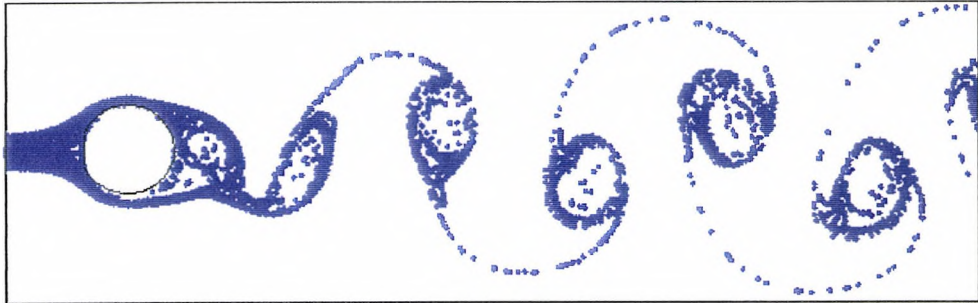


Figure 7.27: Streaklines around a circular cylinder at  $Re=6.5 \times 10^4$ , with no forward injection.

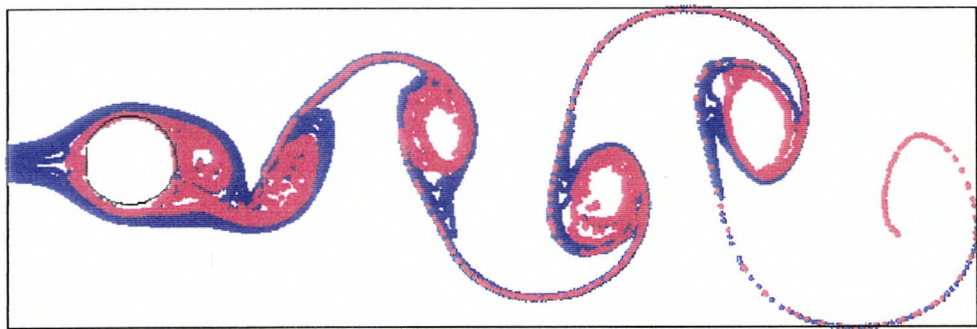


Figure 7.28: Streaklines around a circular cylinder at  $Re=6.5 \times 10^4$ , with forward injection at  $U_r=0.75$ .

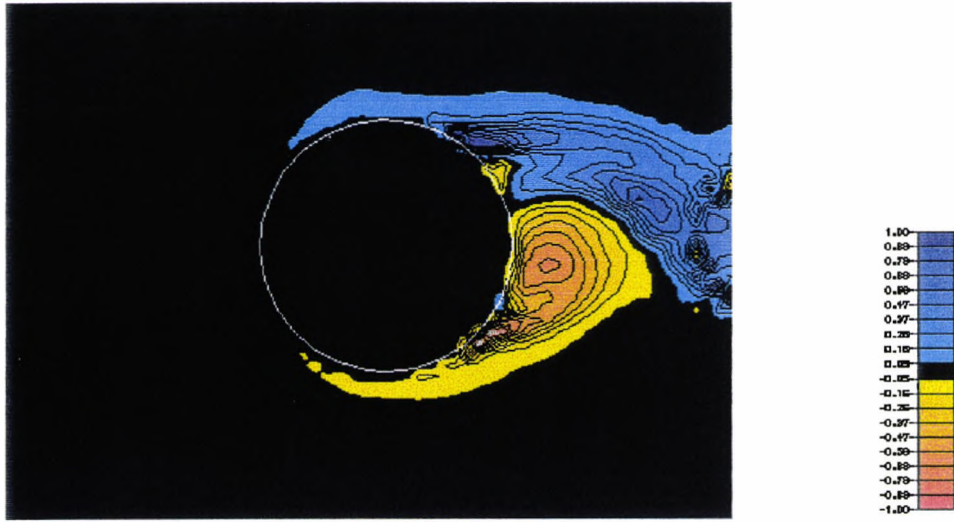


Figure 7.29: Vorticity around a circular cylinder at  $Re=6.5 \times 10^4$ , with no forward injection.

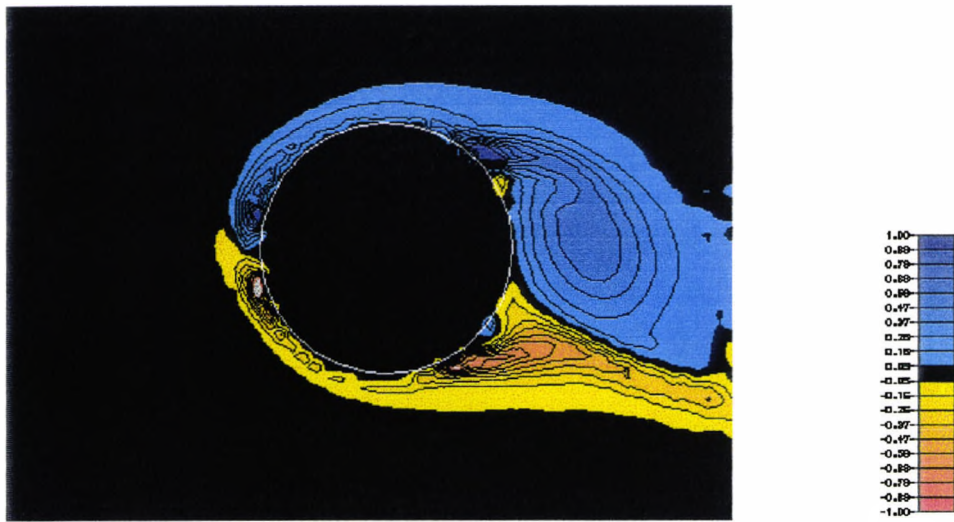


Figure 7.30: Vorticity contours around a circular cylinder at  $Re=6.5 \times 10^4$ , with forward injection at  $U_r=0.75$ .

## 7.6 Conclusions

Laminar and turbulent simulations were performed to determine whether it is possible to predict the suppression of vortex shedding by forward injection. The simulations were done with the same hole geometry that gave optimum suppression in the experiments. Unfortunately, it was not possible to carry out simulations in 3D due to lack of computer resources. It was found that suppression was obtained when the flow was modelled at  $Re=100$ . It was further found that the flow experiences three distinct phases with increasing injection velocity. Optimum results were achieved for  $1.498 < U_r < 1.585$ , where the mean drag, and the fluctuating drag and lift were all suppressed to around 50% of their original values. This ratio is not as good as the maximum suppression of 30% achievable in the experiments. This comparison is not necessarily exact, as the simulations are two-dimensional.

The simulations also showed that the vortex street behind the cylinder is not altered when forward injection is introduced. The reason for suppression was deduced from the vorticity contours. These showed that two vortices were formed in front of the cylinder. The effect was to counteract the vortices formed behind the cylinder. The strength of the vortices behind the cylinder was also weakened, which contributed to overall suppression. The streamlining of the cylinder may be a major cause for the suppression.

When the injection velocity was increased further, the two vortices in front of the cylinder became unstable. They broke up and shed from the front of the cylinder. This introduces excessive forces on the cylinder, signified by a dramatic rise in mean drag and fluctuating drag and lift coefficients. In the experiments, optimum suppression was achieved with a penetration length of 1.5 to 2 cylinder diameters, while the simulations showed a length of 0.6. This may be because the simulations predict the break up of the front vortices prematurely.

The turbulent results showed that mean drag can be reduced, but the fluctuating drag and lift coefficients remained large. This may be due to the lack of accuracy on the part of the flow solver, and the fact that the simulations were not carried out in three-dimensions. With increasing velocity ratios, the simulations had to be carried out at a fraction of the original  $\Delta t^*$ . This greatly increased the computation times.

# CHAPTER EIGHT: PREDICTION OF SUPPRESSION BY A REAR STAGNATION JET

## 8.1 Introductory Remarks

The possibility of the suppression of vortex shedding by the introduction of a rear stagnation jet was introduced in Chapter Seven. In this chapter, a numerical study of this phenomenon is presented and the possible reasons for its occurrence are discussed.

The rear stagnation jet involves the introduction at the rear of a cylinder of a jet with a velocity much greater than that of the incoming flow. Duke and Mo (1993) describe its application for a circular cylinder, while Koutmos et al. (1995) investigated this technique for a square cylinder. The main finding from both studies was that the rear stagnation jet forces a symmetrical wake flow pattern, thus eliminating the lift force. This method acts in a similar way to a splitter plate placed behind the cylinder. Present experiments (see Section 6.4.5) show that back injection does achieve suppression.

The code modification and grid generation details for the numerical simulation of forward injection were presented in Chapter Seven. The procedures are identical to forward injection, the only difference being that the injection is on the east side of the obstacle.

Results obtained for a circular cylinder in laminar flow are presented in Section 8.2. The results for both square and circular cylinder in turbulent flows, are presented in Section 8.3.

## 8.2 Laminar Flow

Experimental evidence for the effects of a rear stagnation jet on the flow around a circular cylinder was reported by Duke et al. (1992) for Reynolds numbers in the range  $600 < Re < 2500$ . With a jet velocity to incoming flow velocity ratio of 25, the wake behind the cylinder was observed to remain fully attached. Mo and Duke (1993) conducted a numerical study on this phenomenon for  $Re=200$ . Their results showed that the wake became symmetric with a velocity ratio as low as 1. The size of the

symmetric recirculation regions became smaller as the velocity ratio increased. When the flow became symmetric, the lift force was eliminated.

The experiments and numerical simulations carried out by Duke et al. (1992) and Mo and Duke (1993) are rather incomplete. It was therefore decided to conduct numerical simulations for a circular cylinder at Reynolds number of 200 for a range of jet velocity ratios.

By using the 148x102 grid in Figure 3.3(a) there is a fine enough grid arrangement behind the cylinder. This grid provided adequate results in modelling a circular cylinder in laminar flow (see Section 3.5.1). Two cells in the middle of the east wall of the cylinder were selected as the secondary inlet. The jet cells cover an area 0.029 times the cylinder diameter. This is comparable to the experimental studies of Duke et al. (1992), where the jet cells covered an area 0.027 times the cylinder diameter. Figure 8.1 shows the schematics of the rear stagnation jet. A  $\Delta t^*$  value of 0.048 was used throughout the calculations.

In Figure 8.1,  $U_o$  is the incoming velocity in the x-direction and  $U_{sj}$  is the prescribed jet velocity. The 'strength' of the rear stagnation jet is quantified by the parameter  $U_r$ , defined as:

$$U_r = \frac{U_{sj}}{U_o} \quad (8.1)$$

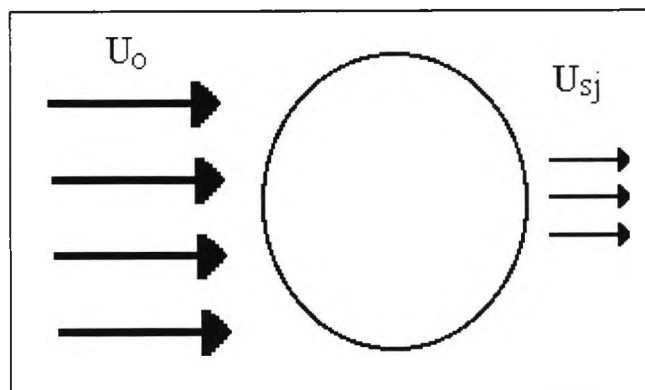


Figure 8.1: Schematics for the rear stagnation jet.

Two further parameters are introduced to quantify the extent of suppression. These are the ratios of rms drag and lift after the introduction of the jet to their values with , i.e.:

$$\tilde{C}_{D_r} = \frac{\tilde{C}_{D_{sj}}}{\tilde{C}_{D_{no\ jet}}} \quad (8.2)$$

and

$$\tilde{C}_{L_r} = \frac{\tilde{C}_{L_{sj}}}{\tilde{C}_{L_{no\ jet}}} \quad (8.3)$$

Table 8.1 shows the results for Reynolds number of 200 for values of  $U_r$  in the range 0.642-10.0. The Table lists the values of the mean drag, the fluctuating drag, the fluctuating lift and Strouhal number based on the lift cycle. Note that when  $U_r=0$ , there is no jet present.

Figure 8.2 shows the variation of,  $\bar{C}_D$ ,  $\tilde{C}_{D_r}$ ,  $\tilde{C}_{L_r}$ , and St with  $U_r$ . The mean drag becomes zero at around  $U_r=4.9$ , suggesting that the reaction and profile drag forces are equal. With increasing jet velocity, the mean drag becomes negative suggesting that the net force on the cylinder is now 'thrust'. At higher jet velocities, the thrust on the cylinder increases beyond the drag for a cylinder without a jet. Also shown are the results of Mo and Duke (1993) for the mean drag. Their results were obtained using a grid of 61x61 with  $\Delta t^*=0.05$ . With the means of velocity vectors and pressure distributions, they showed that the flow field becomes symmetric. Figure 8.2 shows that they predicted the mean drag to increase with increasing jet velocity. A similar trend is obtained in this work when the reaction force is excluded from the computation of the drag term.

From Figure 8.2, it can be seen that the fluctuating drag and lift are almost completely suppressed, although the rms drag does increase at higher jet velocities. The flow does generally become more unstable as the jet ratio becomes larger. This is shown by the increase in rms drag and lift after  $U_r \geq 8.565$ . Mean lift is not affected. The Strouhal number values increase rapidly with jet ratios after an initial value of zero at  $U_r=0.642$ .

RUN	$U_r$	$\bar{C}_D$	$\tilde{C}_D$	$\tilde{C}_{D_r}$	$\tilde{C}_L$	$\tilde{C}_{L_r}$	St
1	0.000	1.353	$5.32 \times 10^{-2}$	1.000	0.190	1.000	0.195
2	0.642	1.118	$1.36 \times 10^{-3}$	0.256	0.072	0.378	0.0 *
3	3.000	0.680	$1.34 \times 10^{-3}$	0.025	$7.98 \times 10^{-3}$	0.042	0.641
4	4.282	0.285	$2.11 \times 10^{-3}$	0.040	$3.04 \times 10^{-3}$	0.016	1.157
5	8.565	-2.520	$3.09 \times 10^{-2}$	0.581	$4.94 \times 10^{-3}$	0.026	4.281
6	10.00	-4.637	$1.75 \times 10^{-2}$	0.329	$7.22 \times 10^{-3}$	0.038	6.648

Table 8.1: Results for rear stagnation jet behind a circular cylinder at  $Re=200$ .

\* The Strouhal number was too low to be measured

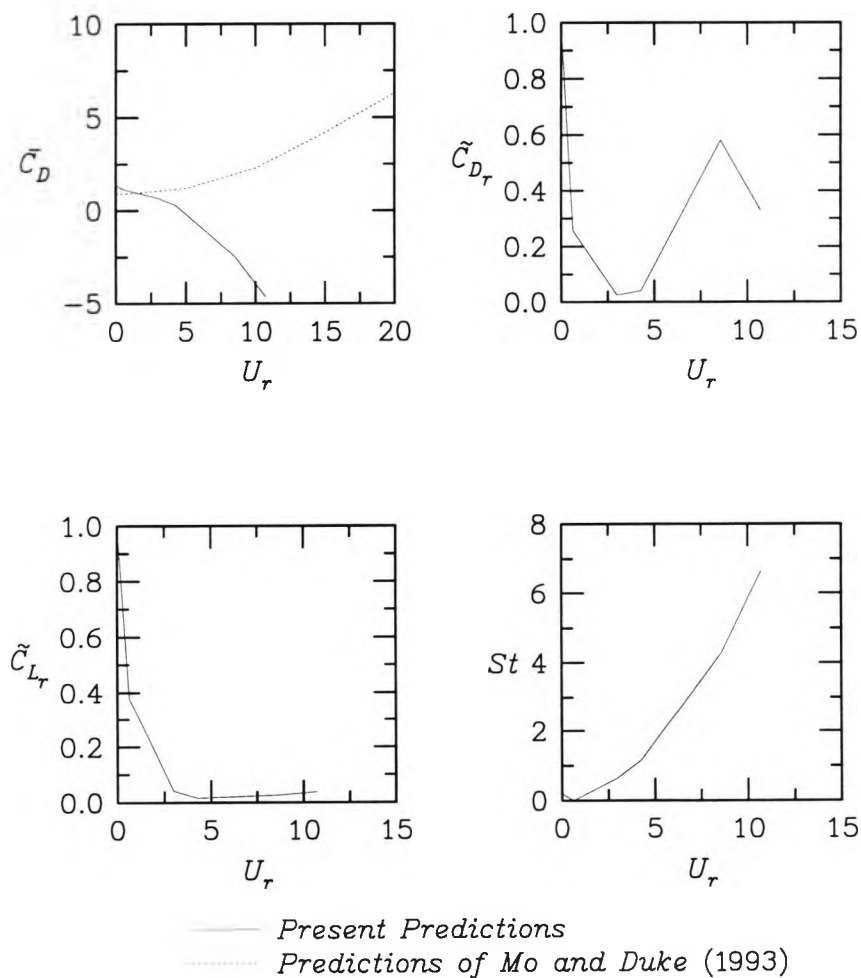


Figure 8.2: Behaviour of drag and lift coefficients with  $U_r$ .

The two values of  $U_r=3.0$  and  $10.0$  were chosen for more detailed investigations. The strongest suppression with the least energy input into the system was obtained at  $U_r=3.0$ . At  $U_r=10.0$ , the mean drag on the cylinder became too large and the fluctuating forces increased.

Figure 8.3 and Figure 8.4 show the time histories of the fluctuating drag and lift coefficients before and after the introduction of the rear stagnation jet. A clear reduction in the intensity of the oscillations is visible from the figures. In addition, the rise in the fluctuations is shown in Figure 8.4 at  $U_r=10.0$ . This is more pronounced in the drag than in the lift coefficient.

Figure 8.5 and Figure 8.6 show velocity vectors around the cylinder at the two velocity ratios. The largest velocity vector is scaled to the largest jet velocity. It is interesting to see that at  $U_r=3.0$ , although there was a larger suppression of the fluctuating drag and lift coefficients, vortices are being shed from the cylinder. At  $U_r=10.0$  there were no vortices at all. This is more evident from the streaklines presented in Figure 8.7 and Figure 8.8. There seems to be some sort of small scale shedding at the smaller velocity ratio. These vortices are further away from the cylinder than their counterparts when there is no jet present. At the larger velocity ratio, there was no shedding at all, but the flow developed a trailing tail, oscillating approximately at eight cylinder lengths downstream of the cylinder.

The behaviour of the rear stagnation jet is very similar to that of a splitter plate placed behind the cylinder. Kwon & Choi (1996) investigated, numerically, the control of laminar vortex shedding behind a circular cylinder using splitter plates. They found that the vortex street disappeared when the length of the splitter plate was larger than a critical length. This length was proportional to the Reynolds number. The Strouhal number however, decreased rapidly with increased plate length until the length of the splitter plate was approximately equal to the diameter of the cylinder. They attributed this decrease to the plate's direct interference with the vortex street. The vortices generated interact with each other further downstream. Accordingly, the interaction period became larger and the Strouhal number decreased rapidly. A similar explanation was given by Apelt et al. (1973). The Strouhal number increased as the length of the splitter plate was increased beyond the cylinder diameter. A smaller secondary vortex was shed from the tip of the plate, but with a higher vorticity level. The interaction of the primary and secondary vortices caused an increase in Strouhal number.

The present simulations show very similar trends, with the Strouhal number decreasing to a minimal value, and then increasing rapidly (See Figure 8.2). Generally, it is shown that the effects of the rear stagnation jet are analogous to that of a splitter plate, except that the mean drag increases rapidly at higher velocity ratios. This means that a critical velocity ratio (around  $U_r=4.9$ ) exists when mean drag is zero and the fluctuating forces are suppressed.

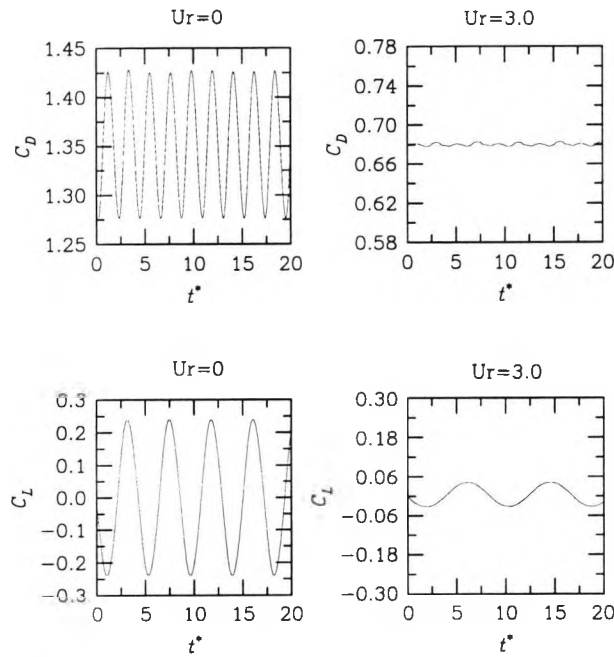


Figure 8.3: Time histories of drag & lift before and after rear stagnation jet ( $U_r=3$ )

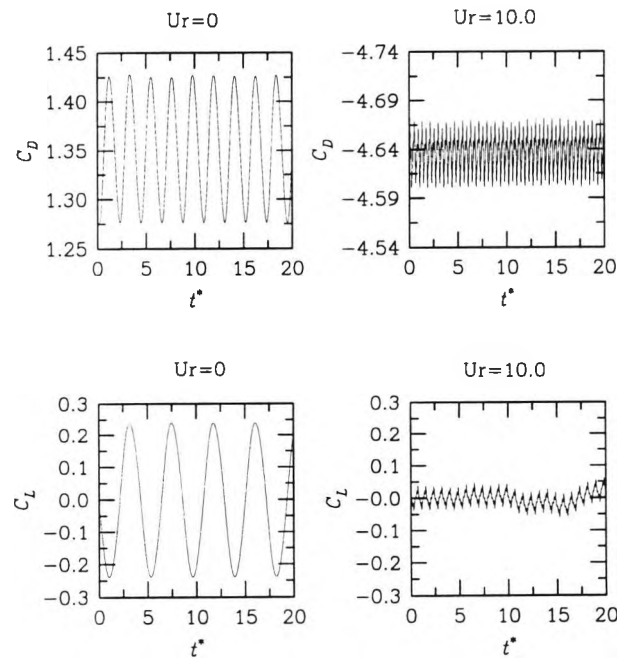


Figure 8.4: Time histories of drag & lift before and after rear stagnation jet ( $U_r=10$ )

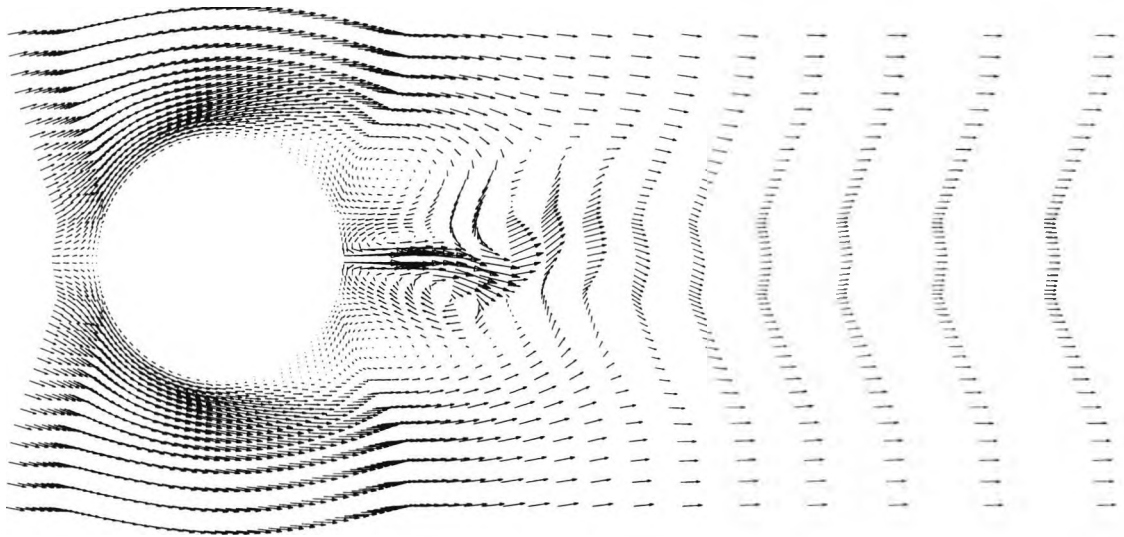


Figure 8.5: Velocity vectors behind cylinder at rear stagnation jet of  $U_r=3$ .

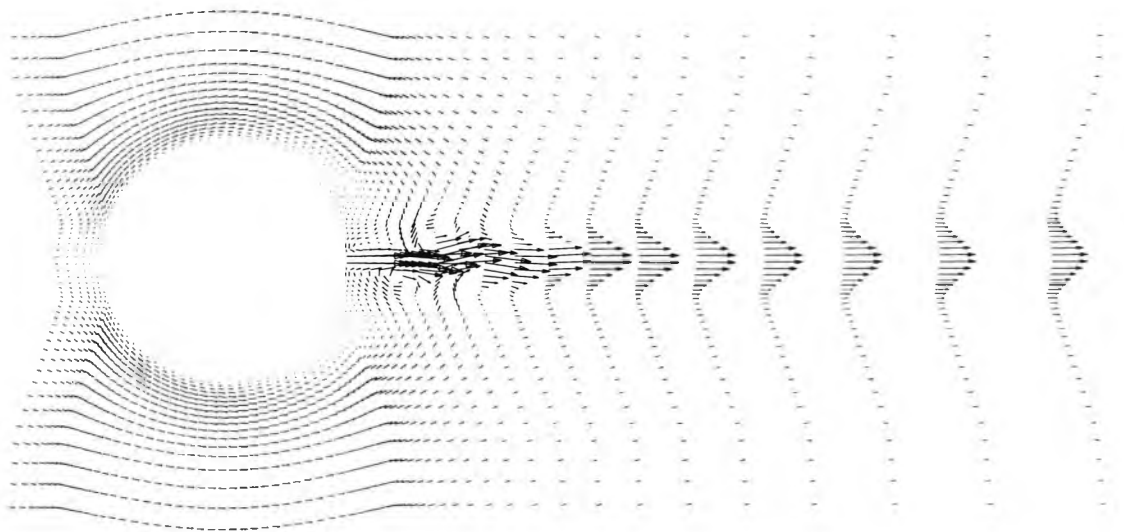


Figure 8.6: Velocity vectors behind cylinder at rear stagnation jet of  $U_r=10$ .

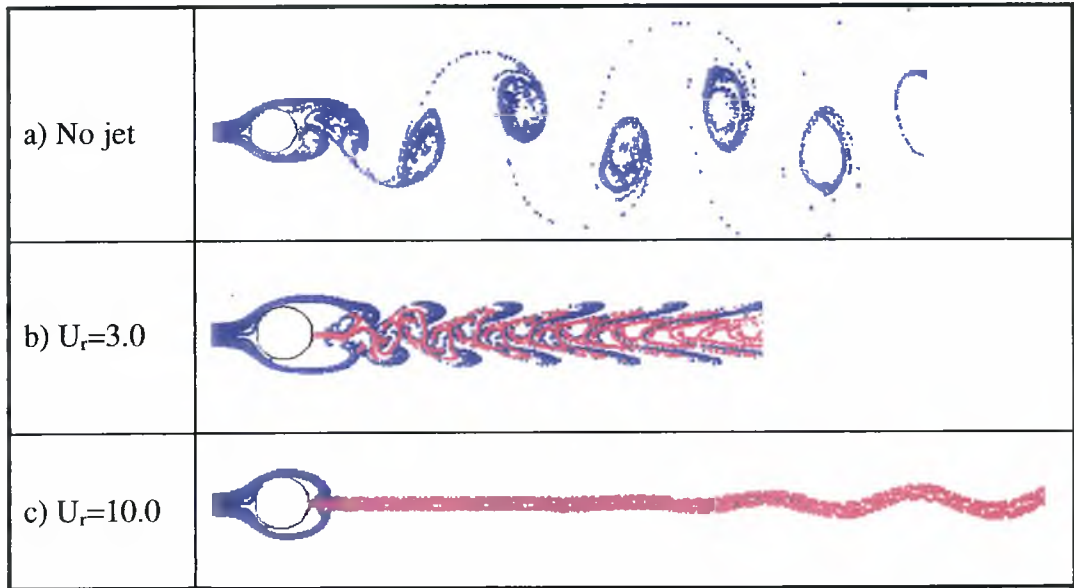


Figure 8.7: Streaklines for rear stagnation jet.

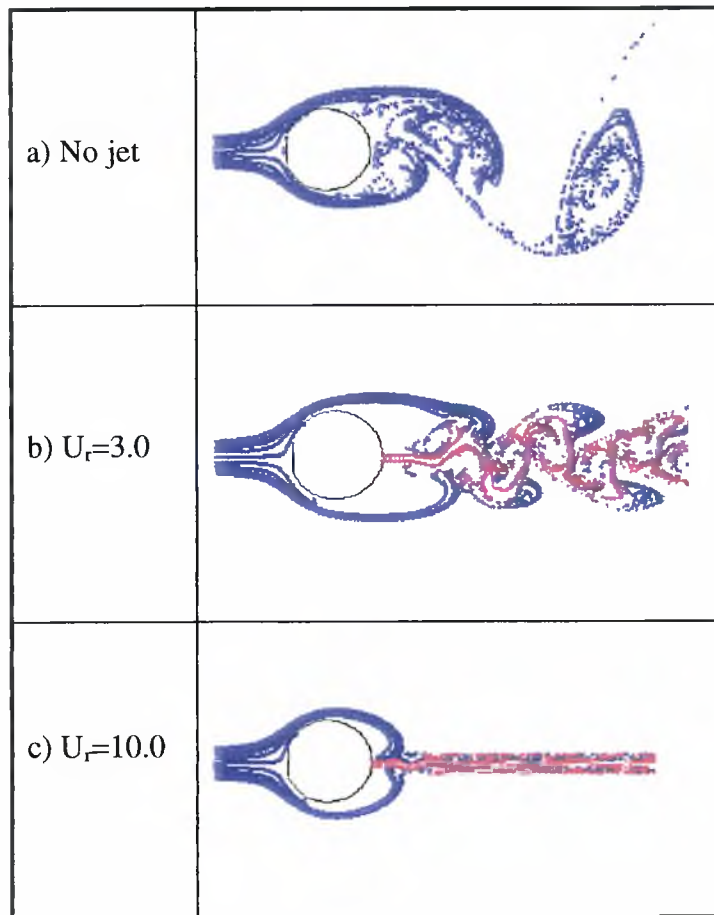


Figure 8.8: Zoom in on streaklines for rear stagnation jet.

## 8.3 Turbulent Flow

Predictions are obtained for both square and circular cylinders in the turbulent regime with a rear stagnation jet.

### 8.3.1 Square Cylinder

Koutmos et al. (1995) conducted experimental and numerical studies into the effects of a rear stagnation jet on square cylinders in turbulent flow. They considered the Reynolds numbers range of 8520-14285, with jet ratios up to  $U_r=2.38$ . Their power spectra of the U-component velocity showed that, at low jet ratios, the dominant frequency was very close to the cylinder shedding frequency without a jet. As the jet ratio increased, the jet interference with the vortex street amplified, and a broadening of the energy peak around the dominant frequency was observed. This continued until the shedding process was completely suppressed when the jet eventually reached  $U_r=1.6$ .

Koutmos et al. (1995) used two numerical methods in their investigations. The LES methodology gave good results for a square cylinder with no injection, but when it was applied to the injection case, it revealed excessive mesh density requirements for an accurate resolution of the jet. The second method they used was based on the k- $\epsilon$  model with the evaluation of the eddy-viscosity performed by the Smagorinsky model from the LES formalism. This hybrid model proved successful in reproducing the measured trends. Both the splitting effect of the jet leading to a quasi-periodic interruption and the eventual interruption of the shedding process were captured by the hybrid k- $\epsilon$  method.

The 136x118 grid described in Section 3.5.2, which was also used to model a square cylinder with a control cylinder, was used here. The modified k- $\epsilon$  model, using the SMART scheme, with  $\Delta t^*=2.4 \times 10^{-3}$  were used throughout. The Reynolds number was fixed at 14285. Four cells in the middle of the east side of the cylinder were chosen to introduce the jet. This covers an area 0.120 times the cylinder height, which is comparable to the jet area used by Koutmos et al. (1995) which amounted to 0.125 times the cylinder height.

The experimental and numerical results of various authors for a single square cylinder in turbulent flow at Reynolds numbers of  $14285 < Re < 22000$  are shown in Table 8.2. The present predictions are clearly in good agreement with the data. In contrast,

the predictions of Koutmos et al. (1995) using both the LES and hybrid k- $\epsilon$ , show slight overestimation in the mean drag and Strouhal number. Koutmos et al. (1995) used a grid of 201x175 nodes for the hybrid k- $\epsilon$  model and a 3-D grid of 95x89x20 nodes for the LES model.

Table 8.3 shows the results obtained at  $Re=14285$  for values of  $U_r$  in the range 0.1-3.0. The Table lists the values of the mean drag, fluctuating drag, fluctuating lift and Strouhal number based on the lift cycle. Note that when  $U_r=0$ , there is no jet present.

Figure 8.9 shows the behaviour of the main parameters,  $\bar{C}_D$ ,  $\tilde{C}_{D_r}$ ,  $\tilde{C}_{L_r}$ , and  $St$  with increasing jet velocity ratios. The trends are similar to those of the laminar simulations with a circular cylinder. Vortex shedding was comprehensively suppressed with the introduction of the jet. The fluctuating drag and lift were almost completely non-existent. Again, with increasing jet velocity, the mean drag eventually becomes negative. The Strouhal number attained minimal values at  $U_r \geq 1.0$ .

Two values of  $U_r$  were chosen for more detailed investigations. These were for  $U_r=0.1$ , which was the smallest velocity ratio, and  $U_r=1.0$ , which gave the largest suppression in terms of the fluctuating drag and lift and Strouhal number.

Figure 8.10 to Figure 8.12 show the time histories for the drag and lift coefficients and their power spectra when  $U_r=0.0, 0.1$ , and  $1.0$  respectively.

Even at the low  $U_r$  value of 0.1, there is clearly quite significant suppression of the drag and lift coefficients relative to the same  $U_r$  in the laminar case. What is interesting here was the appearance of excessive noise at the higher frequencies in the power spectra. Otherwise, the time histories were very similar to the case without a jet, with signs of frequency doubling. Streaklines for  $U_r=0.1$  are shown in Figure 8.13(b). There is a slight widening of the vortex street, and spacing out of the vortices. The jet fluid, highlighted by the light coloured streaklines, was not strong enough to forge a straight path through the vortices, but mixed as it left the outlet from the cylinder. The suppression is caused by this mixing zone. It creates a buffer behind the cylinder and causes the vortices to be shed further away from it.

The time histories of the drag and lift coefficients for  $U_r=1.0$ , shown in Figure 8.12, present an even more dramatic suppression of the vortex shedding. There was no vortex shedding at all, with no fluctuations in the drag and lift. Figure 8.13(c) shows the streaklines at this jet velocity. Unlike the laminar circular cylinder case, when there

were slight fluctuations at high jet velocities, there are no snake-like effects downstream of the cylinder. There was no mixing of the fluids, with the jet fluid forging a straight path through the wake. All the parameters were at their lowest (almost non-existent) values at this jet ratio. The flow behaved as if there was a splitter plate placed behind the cylinder. There was no opportunity for it to develop secondary shedding at the tip, as it was too far downstream.

Higher velocity ratios gave a further decrease in the mean drag, as seen case of the circular cylinder in laminar flow.

Koutmos et al. (1995) found that the jet ratio at which suppression was most effective was  $U_j=1.6$  which is comparable to the present findings. Otherwise their results did not show any indication of the impact of the jet on the drag, and lift coefficients.

	Re	Grid	$\Delta t$	$\bar{C}_D$	$\tilde{C}_D$	$\tilde{C}_L$	St
Experimental Koutmos et al (1995)	14285	-	-	-	-	-	0.176
Experimental Lee (1975)	20000	-	-	2.050	0.180	1.320	0.126
LES Koutmos et al (1995)	14285	95x89x20	$1 \times 10^{-5}$	2.367	-	-	0.177
Hybrid k- $\epsilon$ Koutmos et al (1995)	14285	157x121	$2 \times 10^{-5}$	2.370	-	-	0.178
k- $\epsilon$ Launder & Kato (1993)	22000	104x70	-	2.050	-	0.917	0.145
Modified k- $\epsilon$ Present	14285	136x118	$2.4 \times 10^{-3}$ *	2.080	0.128	1.200	0.138
Modified k- $\epsilon$ Present	20000	136x118	$2.3 \times 10^{-3}$ *	2.104	0.291	1.321	0.132

Table 8.2: Experimental and numerical results for  $Re=14285\sim 22000$ .

\* Denotes that the time-steps were non-dimensionalised

Run	$U_r$	$\bar{C}_D$	$\tilde{C}_D$	$\tilde{C}_{D_r}$	$\tilde{C}_L$	$\tilde{C}_{L_r}$	St
1	0.00	2.080	0.128	1.000	1.200	1.000	0.138
2	0.10	1.145	$5.79 \times 10^{-3}$	0.045	0.035	$2.91 \times 10^{-2}$	0.141
3	0.25	1.005	$7.13 \times 10^{-3}$	0.056	0.030	$2.50 \times 10^{-2}$	0.138
4	0.50	0.862	$8.10 \times 10^{-3}$	0.063	$2.65 \times 10^{-3}$	$2.21 \times 10^{-3}$	0.126
5	0.75	0.500	$1.13 \times 10^{-3}$	0.009	$1.65 \times 10^{-3}$	$1.38 \times 10^{-3}$	0.054
6	1.00	0.122	$1.00 \times 10^{-3}$	0.008	$9.76 \times 10^{-5}$	$8.13 \times 10^{-5}$	0.000
7	1.50	-1.134	$6.43 \times 10^{-3}$	0.050	$7.65 \times 10^{-5}$	$6.38 \times 10^{-5}$	0.001
8	2.00	-2.432	$3.32 \times 10^{-3}$	0.026	$1.34 \times 10^{-4}$	$1.12 \times 10^{-4}$	0.002
9	3.00	-7.656	$6.52 \times 10^{-3}$	0.051	$1.63 \times 10^{-3}$	$1.36 \times 10^{-3}$	0.002

Table 8.3: Results for rear stagnation jet behind a square cylinder at  $Re=14285$ .

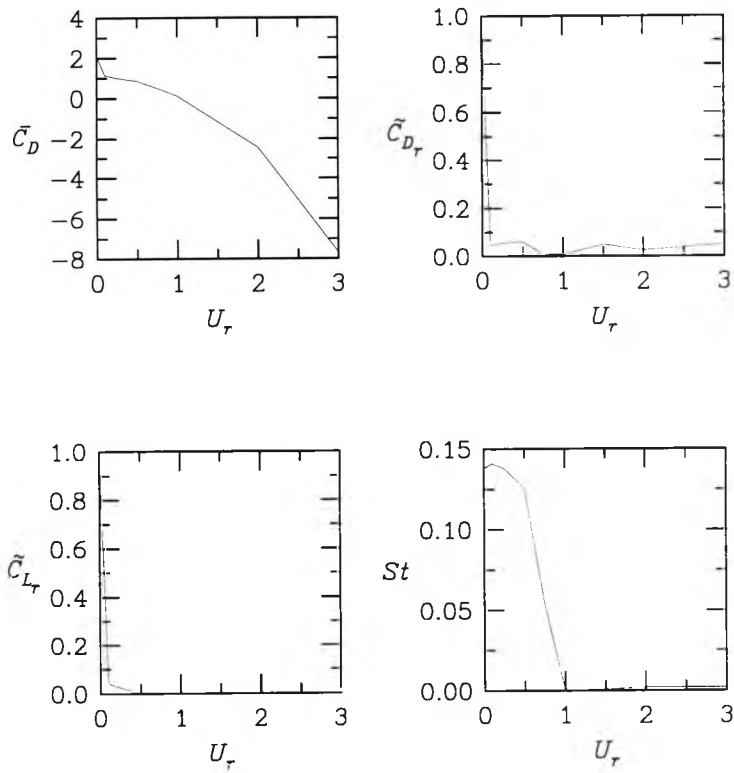


Figure 8.9: Behaviour of drag, lift, and Strouhal number with  $U_r$ .

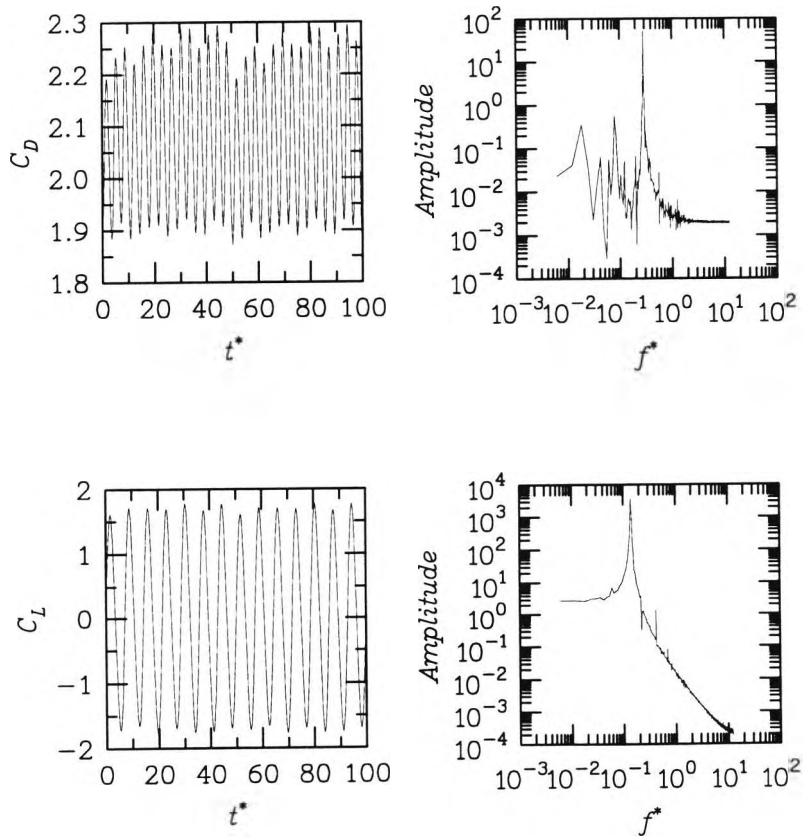


Figure 8.10: Time histories of drag and lift coefficients for a square cylinder at  $Re=14285$ ; showing also the power spectra.

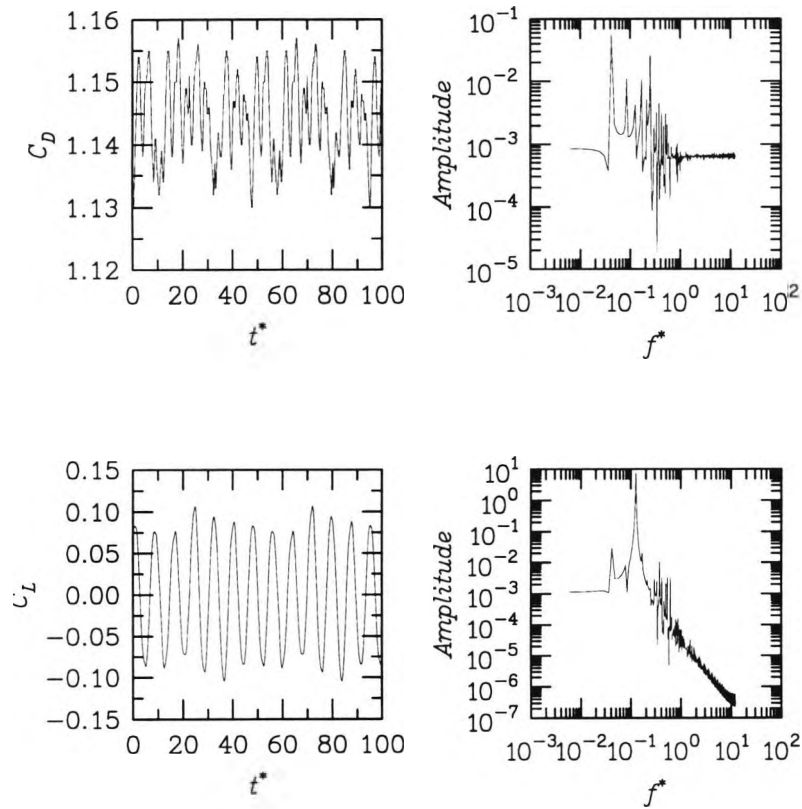


Figure 8.11: Time histories of drag and lift coefficients for a square cylinder at  $Re=14285$  with a rear stagnation jet of  $U_r=0.1$ ; showing also the power spectra.

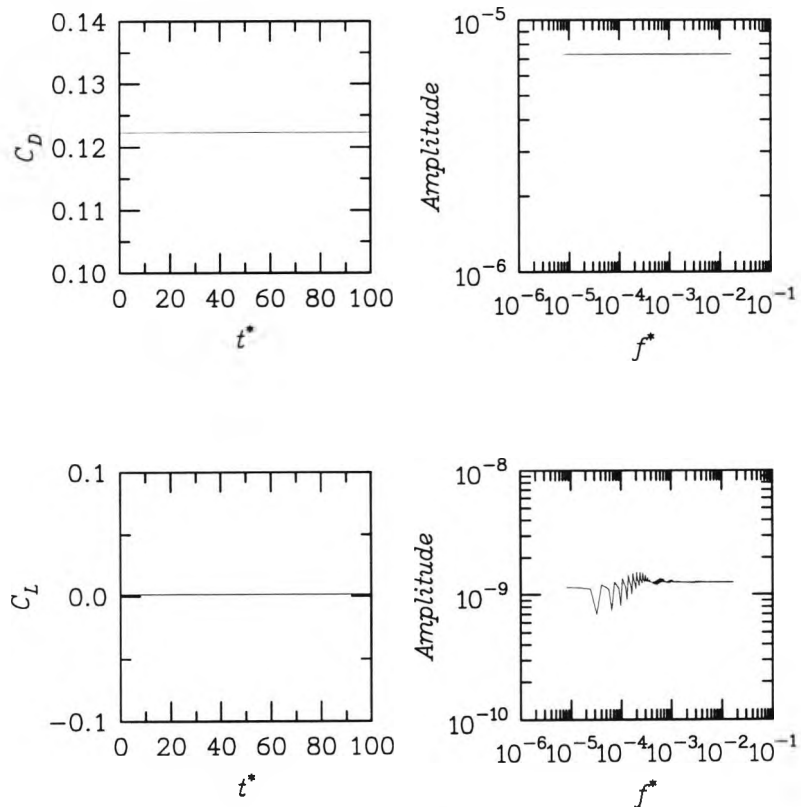
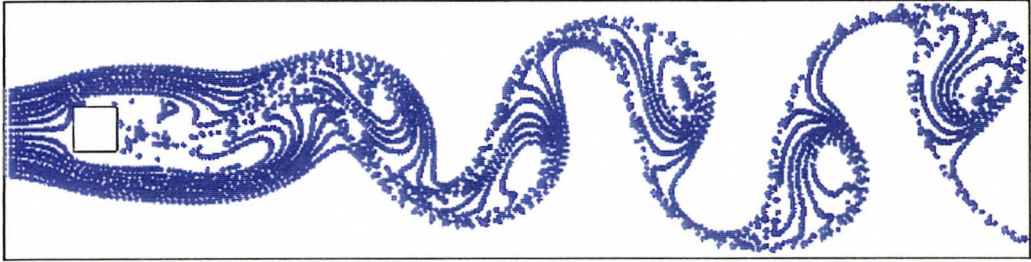
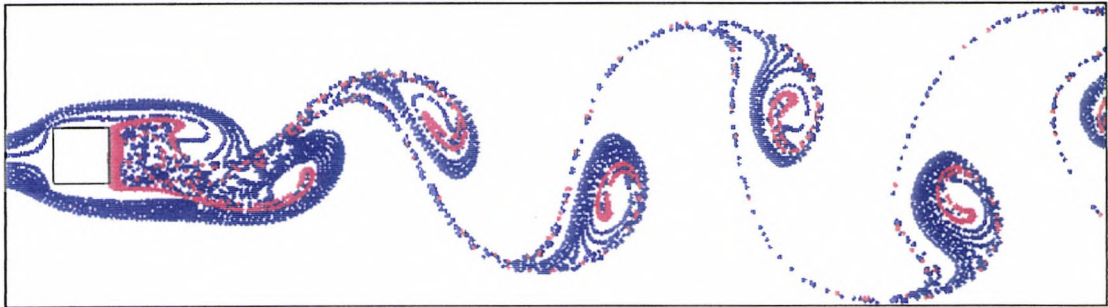


Figure 8.12: Time histories of drag and lift coefficients for a square cylinder at  $Re=14285$  with a rear stagnation jet of  $U_r=1.0$ ; showing also the power spectra.

a)  $U_r=0.0$



b)  $U_r=0.1$



c)  $U_r=1.00$

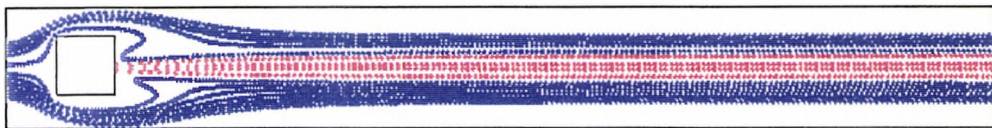


Figure 8.13: Streaklines for a square cylinder at  $Re=14285$  without and with rear stagnation jet at jet velocities of a)  $U_r=0.0$ , b)  $U_r=0.1$  and c)  $U_r=1.00$ .

### 8.3.2 Circular Cylinder

There are no previous experimental or numerical results for a circular cylinder in turbulent flow with a rear stagnation jet. Therefore, the present study is performed at a Reynolds number of  $6.5 \times 10^4$  in order to compare the results with those obtained for forward injection.

A grid of  $195 \times 98$  nodes was used, with two cells in the middle of the east side of the obstacle designated as the secondary inlets. The jet cells covered an area 0.031 times the cylinder diameter, which is comparable to the laminar flow tests of Duke et al. (1992), where a ratio of 0.027 was used. A  $\Delta t^*$  value of 0.001 was used throughout the simulations.

Table 8.4 shows the results obtained for  $Re=6.5 \times 10^4$  for values of  $U_r$  in the range 0.1-7.0. The Table lists the values of the mean drag, the fluctuating drag, the fluctuating lift and Strouhal number based on the lift cycle. Note that when  $U_r=0$ , there is no jet present.

Figure 8.14 shows the behaviour of the main parameters,  $\overline{C_D}$ ,  $\tilde{C}_{D_r}$ ,  $\tilde{C}_{L_r}$ , and  $St$  with jet velocity ratios. The trends are comparable to those of the laminar simulations with a circular cylinder and the turbulent simulations with the square cylinder and show clearly that the flow experiences three distinct phases.

The first phase is for  $0.1 < U_r < 0.5$ , when the mean drag was reduced at a constant rate. The fluctuating drag was reduced to its minimum of 0.504 its original value. The fluctuating lift and Strouhal number were also decreased at a constant rate.

The second phase is for  $0.5 < U_r < 3.0$ , where all the main parameters remained almost constant.

The third phase is for  $U_r > 3.0$ , when the mean drag turns into thrust. The fluctuating drag increased and stayed constant at higher jet ratios. The fluctuating lift decreased rapidly. Also, the Strouhal number increased rapidly.

RUN	$U_r$	$\bar{C}_D$	$\tilde{C}_D$	$\tilde{C}_{D_r}$	$\tilde{C}_L$	$\tilde{C}_{L_r}$	St
1	0.00	1.025	0.139	1.000	0.995	1.000	0.292
2	0.10	0.829	0.120	0.863	0.811	0.815	0.299
3	0.25	0.697	0.110	0.791	0.614	0.617	0.291
4	0.50	0.549	0.070	0.504	0.393	0.395	0.275
5	0.75	0.524	0.075	0.540	0.379	0.381	0.206
6	1.00	0.520	0.090	0.647	0.351	0.353	0.150
7	1.50	0.515	0.090	0.647	0.351	0.353	0.121
8	3.00	0.439	0.092	0.662	0.348	0.350	0.110
9	5.00	-0.072	0.106	0.763	0.186	0.187	11.523
10	7.00	-0.911	0.103	0.741	0.038	0.038	18.103

Table 8.4: Results for rear stagnation jet behind a circular cylinder at  $Re=6.5 \times 10^4$ .

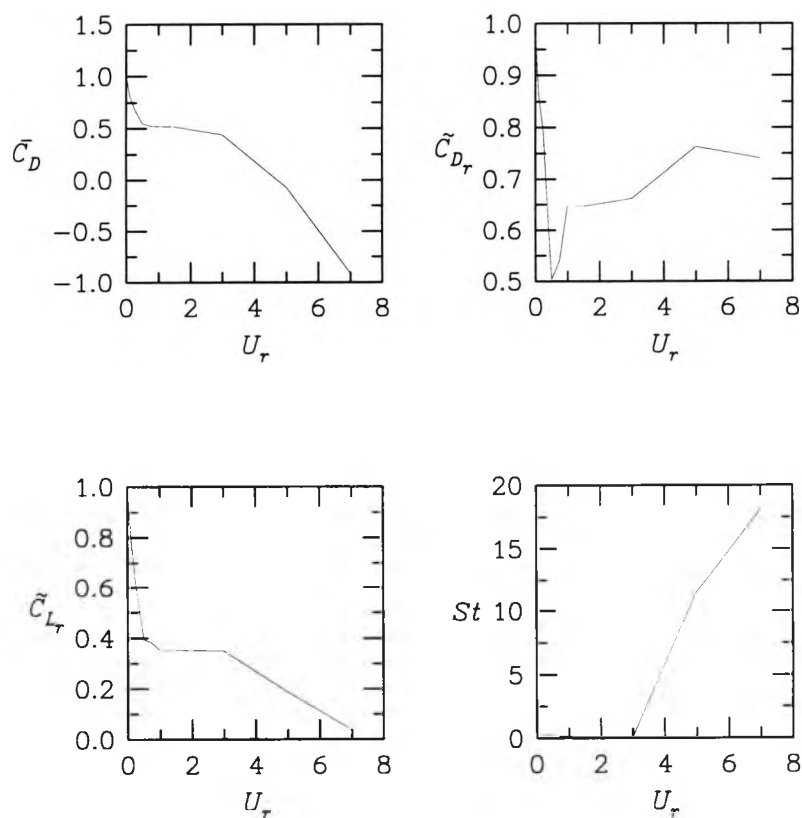


Figure 8.14: Behaviour of drag, lift, and Strouhal number with  $U_r$ .

In order to determine the behaviour of the flow in these three phases, three jet ratios were selected for further investigation. These lie within the three phases being at  $U_j=0.5$ , 1.5, and 5.0.

Figure 8.15 shows the time histories for the drag and lift coefficients and their power spectra when there is no rear stagnation jet (i.e. when  $U_j=0$ ).

Figure 8.16 shows the same parameters when  $U_j=0.5$ , which is in the first phase. The lift and drag coefficients do not vary smoothly with time, and many frequencies were visible in the power spectra. An organised vortex street does exist, as can be seen from the velocity vectors in Figure 8.20 and the streaklines in Figure 8.23(b). The velocity vectors show the rear stagnation jet being deflected by the uppermost vortex. As this deflection oscillated with the shedding of the vortices, there was strong mixing which can be seen in the streaklines.

Figure 8.17 shows the time histories and power spectra for  $U_j=1.5$ . This is in the second phase, when there is no change in the main parameters with increasing jet velocity. The time histories of the coefficients are even more chaotic. The velocity vectors (Figure 8.21) and streaklines (Figure 8.23(c)) show a longer jet penetration length; though it was still being deflected by the separated flow. Vortices were attached to the jet and subsequently shed from its tip. This, together with the swaying action of the jet, resulted in the unstable nature of the flow. There was less mixing of the two fluids.

Figure 8.18 shows the time histories and power spectra for  $U_j=5.0$ . This is in the third phase, when the mean drag is very small and negative. The time histories of the drag and lift coefficients are much more chaotic, with high frequencies visible in both the drag and lift spectra. The velocity vectors (Figure 8.22) and streaklines (Figure 8.23(d)) show that the jet was so powerful that it was not being deflected by the separated flow. The jet appeared to act as a solid extension of the cylinder, rather like a splitter plate. Vortices were shed from the tip of the jet. There was less mixing.

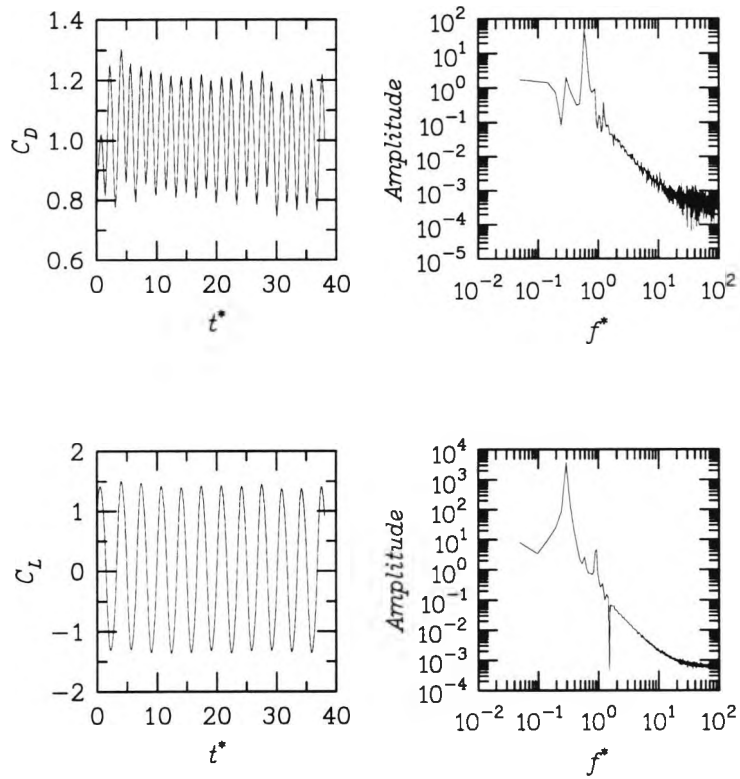


Figure 8.15: Drag and lift time histories and power spectra for the case with no rear stagnation jet at  $Re=6.5 \times 10^4$ .

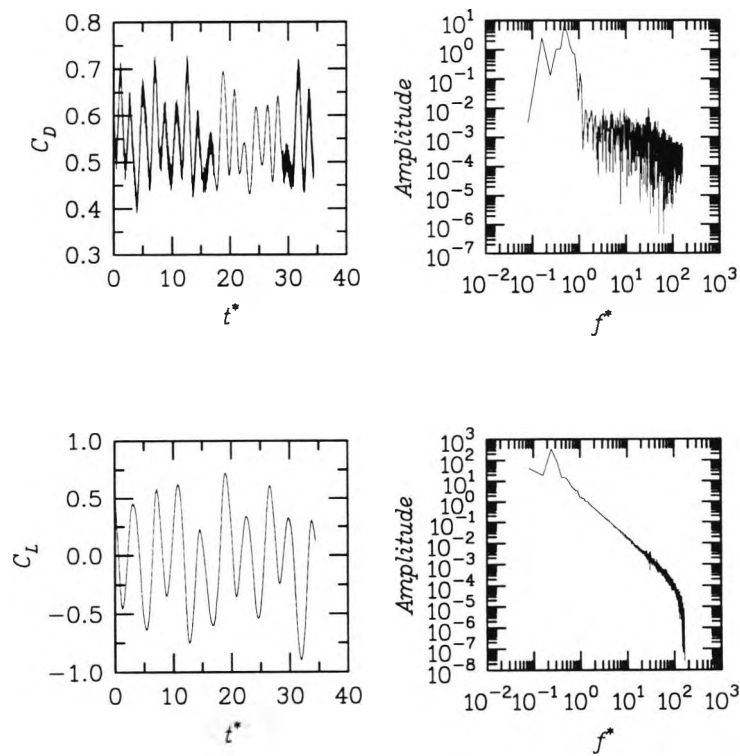


Figure 8.16: Drag and lift time histories and power spectra for the case with rear stagnation jet of  $U_r=0.5$  at  $Re=6.5 \times 10^4$ .

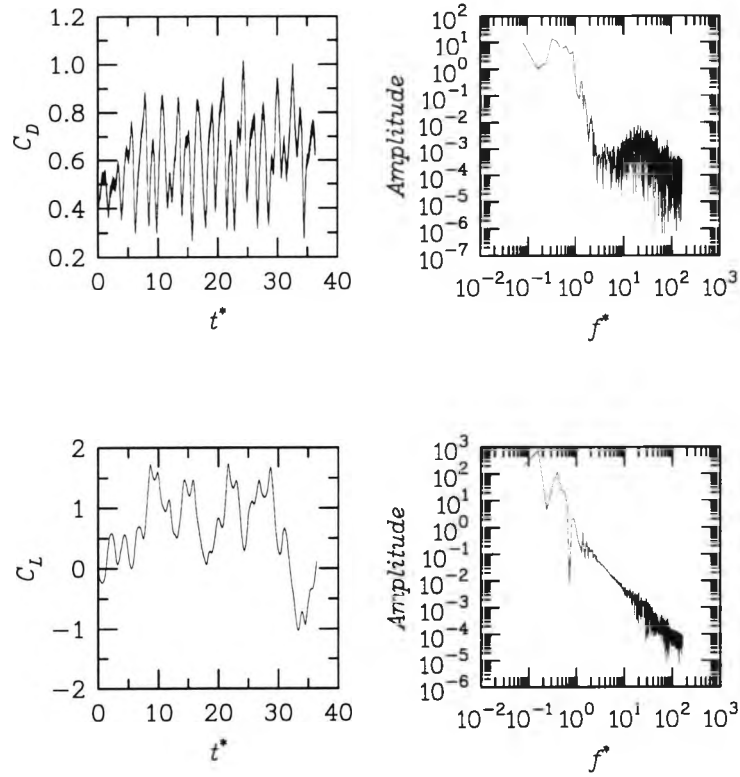


Figure 8.17: Drag and lift time histories and power spectra for the case with rear stagnation jet of  $U_r=1.5$  at  $Re=6.5 \times 10^4$ .

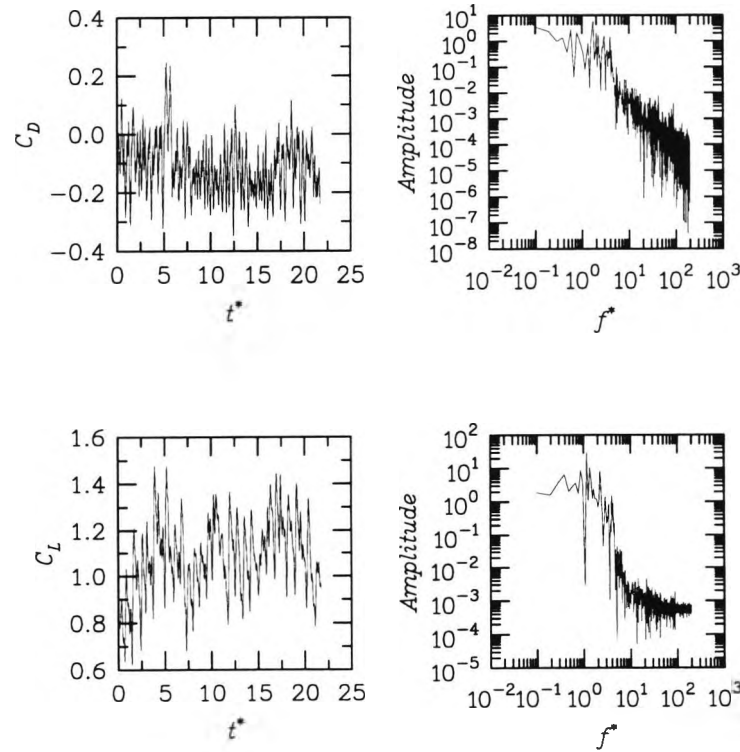


Figure 8.18: Drag and lift time histories and power spectra for the case with rear stagnation jet of  $U_r=5.0$  at  $Re=6.5 \times 10^4$ .

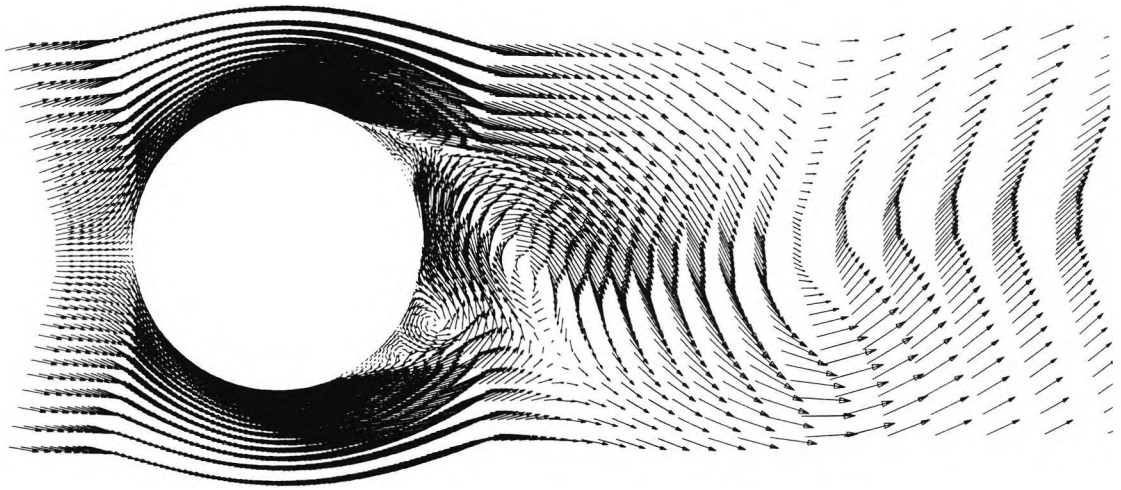


Figure 8.19: Velocity vectors around a circular cylinder at  $Re=6.5 \times 10^4$ .

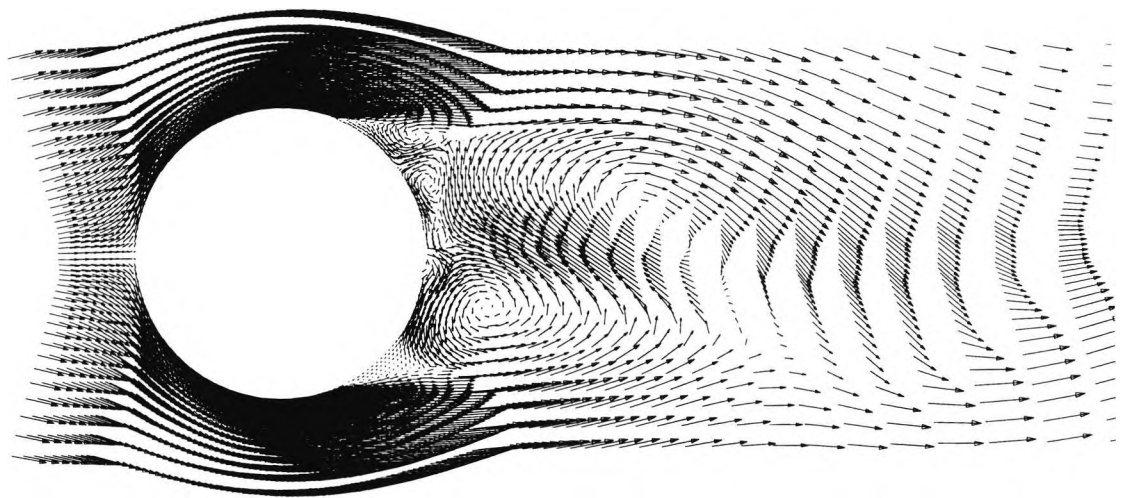


Figure 8.20: Velocity vectors around a circular cylinder at  $Re=6.5 \times 10^4$ , with rear stagnation jet of  $U_r=0.5$ .

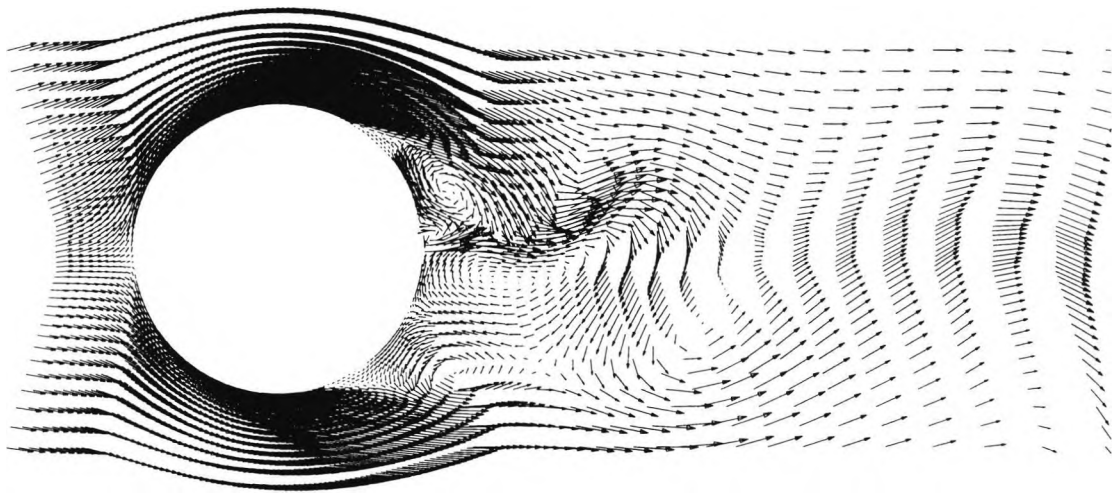


Figure 8.21: Velocity vectors around a circular cylinder at  $Re=6.5 \times 10^4$ , with rear stagnation jet of  $U_r=1.5$ .

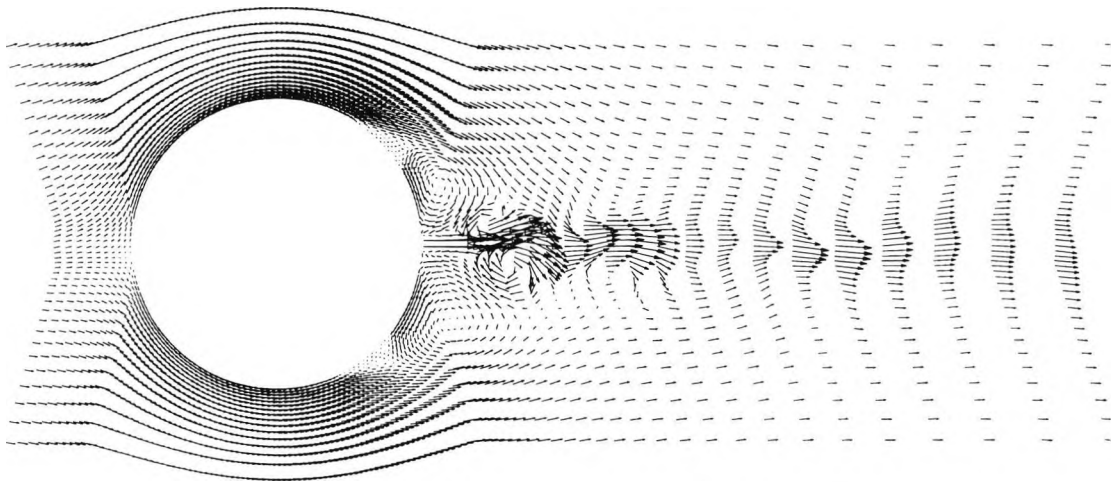


Figure 8.22: Velocity vectors around a circular cylinder at  $Re=6.5 \times 10^4$ , with rear stagnation jet of  $U_r=5.0$ .

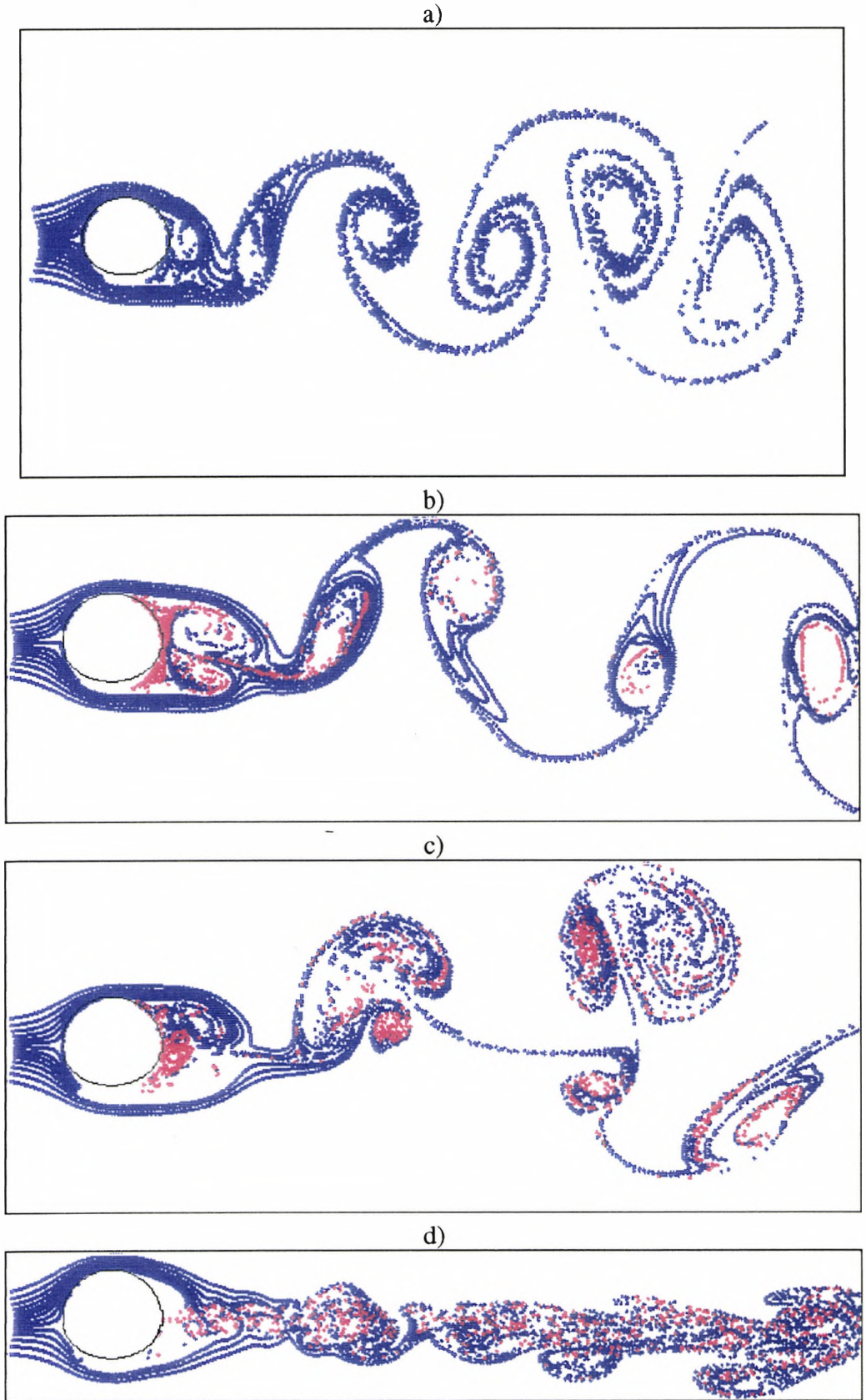


Figure 8.23: Streaklines for a circular cylinder at  $Re=6.5 \times 10^4$  without and with rear stagnation jet at jet velocities of a)  $U_r=0.$ , b)  $U_r=0.5$ , c)  $U_r=1.5$ , and d) 5.0.

## 8.4 Conclusions

The mechanism of suppression of vortex shedding by means of a rear stagnation jet is quite simple. The jet forms a solid barrier behind the cylinder restricting the formation of vortices. This works in exactly the same way as a splitter plate, which is a traditional means of suppressing vortex shedding. There are however differences between the two methods.

At low jet velocities, a great deal of mixing between the jet fluid and the incoming flow takes place. This has the effect of infringing on the vortex formation process and thus suppressing it.

At slightly higher jet velocities, the mixing is reduced, but the jet is seen to sway from side to side. There is added separation and vortex formation at the tip of the jet. This created a complex flow structure behind the cylinder, which in turn induced chaotic oscillations of the cylinder with higher frequencies. The secondary vortex formation at the tip of the jet is also a feature of the splitter plate.

The rear stagnation jet produces a reaction force in the opposite direction to the drag. At higher jet velocities, the mean drag was reduced until the net force on the cylinder became negative and the cylinder eventually experienced a thrust force acting on it. In this instance, there was less mixing, as the jet was so strong that the separated flow had very little effect on it.

The fluctuations in the drag and lift coefficients can be suppressed down to 2.5% of their original values for a circular cylinder in laminar flow. The suppression for the square cylinder in turbulent flow was even stronger, with the drag and lift fluctuations being suppressed down to 0.8% and 0.008% of their respective original values. The suppression is not as strong for the circular cylinder in turbulent flow, where the fluctuations of the drag and lift coefficients were around 50% and 11% their original values. These figures show higher reduction in the fluctuating coefficients than the forward injection, which showed a suppression of 30% in the experiments and 50% for the numerical results.

## CONCLUSIONS AND FURTHER WORK

The main objective of the present work was to investigate, experimentally and numerically, vortex shedding from cylinders submerged in laminar and turbulent flows and various means for its control.

The numerical model used is based on the finite-volume method for the discretisation of the transport equations governing laminar and turbulent flows.

In all the flows considered without the use of control, the time histories of both  $C_D$  and  $C_L$  were predicted to be fairly smooth and the frequency of  $C_D$  was predicted to be twice that of  $C_L$ , as expected. Streaklines were computed and found to present a view of the flow field which is in accord with published flow visualisations.

Grid and time-step dependence checks were carried out. It was shown that laminar flow calculations are independent of grid effects. Finer grids were used at high Reynolds numbers to capture the details of the ensuing turbulent flow. The results showed the insensitivity of the solutions to the time-step size, as long as the value of the latter was smaller than that required by the non-dimensionalised time step criteria.

Predictions were obtained using the Upwind, Linear Upwind and SMART schemes for a circular and square cylinder without control. The results showed that the third order bounded SMART scheme provides the most accurate results for a given grid.

The k- $\epsilon$  turbulence model was used when simulating Reynolds numbers higher than 1400. The Younis (1987) and Przulj & Younis (1993) modification, which accounts for the effects of periodicity on the turbulence spectrum was further tested and proved to be adequate for the present flows.

At higher values, above  $Re=20000$ , the present method underestimates the values of mean drag and overestimates the Strouhal number. The present method also failed to capture the drag crisis and the supercritical regime. The transcritical regime was investigated. It was found that the mean drag was underestimated and the fluctuating lift and Strouhal number overestimated with respect to the experimental data. The predicted mean drag remains constant at  $Re=5 \times 10^7$ , while the fluctuating lift and Strouhal number fall significantly.

The flow field that develops around two circular cylinders in tandem was investigated numerically in laminar and turbulent flow regimes. The wide range of well established flow phenomena observed experimentally were reproduced.

In the laminar flow calculations, the experimentally observed 'vortex suppression' regime at small spacings and the 'vortex formation' regime at large spacings were obtained in the predictions. A wide range of spacings was investigated in the turbulent flow regime, for which no previous numerical results exist. The critical spacing, when the two cylinders stop behaving as one, was predicted to lie in the range  $2.5 < P/D < 4$ . The key regimes, dependent on the cylinder spacing were found. It was observed that the mean drag of the downstream cylinder can become negative at small spacings in the vortex suppression regime.

Three methods of vortex suppression were selected for detailed study. The first one was the use of control cylinders. A small control cylinder was placed near the main cylinder to reduce or eliminate oscillations caused by vortex shedding on the main cylinder. The present results for square and circular cylinders with control cylinders placed at different points in laminar and turbulent flows were compared with previous experimental and numerical results where available.

The vortex shedding from circular and square cylinders in laminar flows was suppressed most effectively when the control cylinder was placed above and behind the main cylinder (at  $x/D=1$  and  $y/D=1$ ). The fluctuating drag and lift coefficients were reduced to around 1% their original values. The vortex street was shown to disappear for these predictions.

The vortex shedding from a circular cylinder in turbulent flow was suppressed most effectively when the control cylinder controlled the boundary layer along the surface of the cylinder or when the separated shear layer was controlled. The fluctuating drag and lift coefficients were reduced to 25% and 9% of their original values.

The vortex shedding from a square cylinder in turbulent flow was most effectively suppressed when the control cylinder was placed along the outer boundary of the separated shear layer. The fluctuating drag and lift coefficients were reduced to 50% and 36% of their original values

The second method of suppression was a novel one and consisted of the injection of fluid into the approach flow. As there are no previous data on this method, experimental test and data analysis methods were devised in order to reduce the number of experiments. By conducting experiments with a variety of geometric parameters, the suppression was maximised over a range of Reynolds numbers.

The geometry giving the best suppression corresponded to a cylinder with 13 holes of 3 mm diameter, with a centre to centre distance of 10mm. The maximum suppression achieved with this geometry was 30% for both in-line and transverse vibrations. There were no dominant frequencies after injection. The penetration length of the forward injection was approximated to around 1.5 to 2 times the cylinder diameter. It was shown that even stronger suppression was possible when the injection holes were placed at  $60^\circ$  and  $240^\circ$  relative to the approach flow.

Forward injection was investigated numerically for a circular cylinder in laminar and turbulent flows. It was found that suppression was obtained for laminar flow. The streaklines did not show any sign of change in the vortex street. Fluctuating drag and lift were suppressed to 50% their original values. A breakdown of the drag and lift coefficients around the cylinder and vorticity contours showed that suppression is caused by two vortices formed in front of the cylinder, which in turn weaken the vortices shed behind the cylinder. The streamlining of the cylinder is suspected to be the major contributor to the suppression.

The third method of suppression was the rear stagnation jet, which acts in a similar way to a splitter plate placed behind the cylinder. The fluctuations in the drag and lift coefficients can be suppressed down to 2.5% of their original values for a circular cylinder in laminar flow. The suppression for the square cylinder in turbulent flow was even stronger, with the drag and lift fluctuations being suppressed down to 0.8% and 0.008% of their respective original values. The suppression is not as strong for the circular cylinder in turbulent flow, where the fluctuations of the drag and lift coefficients were around 50% and 11% their original values. At high jet velocities, the mean drag was reduced until the net force on the cylinder became negative. In this instance, there was less mixing, as the jet was so strong that the separated flow had very little effect on it.

The work here is a step forward towards a better understanding of the mechanisms involved in vortex shedding and its control. Overall, it was shown that CFD can be reliably used to assess the qualitative nature of the vortex shedding and its control. In terms of quantitative results, some inaccuracies still exist, but it should be remembered that accurate experimental measurements are also difficult to obtain for these flows.

Further numerical work could be carried out with three-dimensional grids to obtain more accurate results, especially in the case of forward injection. Furthermore, more accurate results could be obtained, if improvements were made to the prediction of the laminar-turbulent transition on the surface of the cylinder.

Further experimental work could be carried out on the forward injection method, to obtain more detailed analysis of the flow field around the cylinder and important parameters, such as the drag and lift coefficients.

## REFERENCES

- Appelt, C.J., West, G.S. and Szewczyk, A.A. (1973) "The Effects of Wake Splitter Plates on The Flow Past a Circular Cylinder in The Range  $10^4 < Re < 5 \times 10^5$ ", *Journal Of Fluid Mechanics*, No. 61, pp 187-198.
- Basara, B. and Younis, B.A. (1992) "Progress in The Prediction of Turbulent Wind Loading on Buildings", *Journal Of Wind Engineering and Industrial Aerodynamics*, Vol. 44, pp 2863-2874.
- Basara, B. and Younis, B.A. (1993) "Prediction of Two- and Three-Dimensional Separated Flows with a Non-Linear k- $\epsilon$  Model", *Proceedings IUTAM Symposium On Bluff-Body Wakes, Dynamics and Instabilities*, Göttingen, Germany, Springer-Verlag.
- Basara, B. and Younis, B.A. (1995) "Assessment of The SSG Pressure-Strain Model in 2-Dimensional Turbulent Separated Flows" *Applied Scientific Research*, Vol. 55, No. 1, pp 39-61.
- Basu, R.I. (1985) "Aerodynamic Forces on Structures of Circular Cross Section. Part I.", *Journal Of Wind Engineering and Industrial Aerodynamics*, Vol. 21, pp 273-294.
- Bearman, P.W. (1967) "The Effect of Base Bleed On The Flow Behind a Two Dimensional Model of a Blunt Trailing-Edge", *Aeronautical Quarterly*, Vol. 18, pp 207-244.
- Bearman, P.W. (1984) "Vortex Shedding From Oscillating Bluff Bodies", *Annual Review Of Fluid Mechanics*, pp 195-222.
- Bearman, P.W. and Obasaju, E.D. (1982) "An Experimental Study of Pressure Fluctuations On Fixed and Oscillating Square-Section Cylinders", *Journal Of Fluid Mechanics*, Vol. 119, pp 297-321.
- Bearman, P.W. and Trueman, D.M. (1972) "An Investigation of Flow Around Rectangular Cylinders", *Aeronautical Quarterly*, Vol. 23, pp 229-237.
- Behr, M., Liou, J., Shih, R., Tezduyar, T.E. (1991) "Vorticity Streamfunction Formulation of Unsteady Incompressible-Flow Past a Cylinder", "Sensitivity of The Computed Flow Field To The Location of The Outflow Boundary", *International Journal For Numerical Methods In Fluids*, Vol. 12, No. 4, pp 323-342.

Berger, E. and Schumm, M. (1988) "Untersuchungen der Instabilitaetsmechanismen im Nachlauf von Zylindern", Contract Report No. Be 343/18-1, Technical University of Berlin, Germany.

Biermann, D. and Herrstein, W.H. Jr (1933) "The Interference Between Struts in Various Combinations", National Advisory Committee For Aeronautics, Tech Report 468, pp 515-524.

Blevins, R.D. (1990) "Flow Induced Vibrations", Van Nostrand Reinhold, New York.

Bloor, M. S. (1964) "The Transition to Turbulence in The Wake of a Circular Cylinder", Journal Of Fluid Mechanics No. 19, pp 290.

Bosch, G. and Rodi, W. (1996) "Simulation of Vortex Shedding Past a Square Cylinder Near a Wall", International Journal Of Heat And Fluid Flow, Vol. 17, No. 3, pp 267-275.

Boussinesq, J. (1887) "Theorie de l'ecoulement tourbillant", Mem. Pre. Par. div Sav. 23, Paris.

Braza, M., Chassaing, P., Minh H.H. (1986) "Numerical Study and Physical Analysis of The Pressure and Velocity Fields in The Near Wake of a Circular-Cylinder", Journal Of Fluid Mechanics, Vol.165, No. Apr, pp 79-130.

Cantwell, B. and Coles, D. (1983) "An Experimental Study of Entrainment and Transport in The Turbulent Near-Wake of a Circular Cylinder", Journal of Fluid Mechanics, Vol. 136, pp 321-374.

Celik, I., Patel, V.C., Landweber, L. (1985) "Calculation of The Mean Flow Past Circular Cylinders by Viscous Inviscid Interaction", Journal Of Fluid Mechanics, Vol. 107, pp 218-223.

Chen, S.S. (1987) "Flow-Induced Vibration of Circular Cylindrical Structures", Hemisphere Publishing Corporation.

Chorin, A.J. (1967) "A Numerical Method for Solving Incompressible Viscous Flow Problems", Journal Of Computer Physics, Vol. 2, pp 12-26.

Couder, Y. and Basdevant, C. (1986) "Experimental and Numerical Studies of Vortex-Couples in Two-Dimensional Flow", Journal Of Fluid Mechanics, Vol. 173, pp 225-251.

Davis, R.W. and Moore, E.F. (1982) "A Numerical Study of Vortex Shedding from Rectangles", Journal Of Fluid Mechanics, Vol. 116, No. Mar, pp 475-506.

Demiridzic, I. and Peric, M. (1988) "Space Conservation Law in Finite Volume Calculations of Fluid Flow", *International Journal Numerical Methods In Fluids*, Vol. 8, pp 1037-1050.

Deng, G.B., Piquet, J., Queutey, P., Visonneau, M. (1994) "Incompressible-Flow Calculations With a Consistent Physical Interpolation Finite-Volume Approach" *Computers And Fluids*, 1994, Vol. 23, No. 8, pp 1029-1047.

Douglas, J.F., Gasiorek, J.M. and Swaffield J.A. (1985) "Fluid Mechanics", Second edition, Longman Scientific & Technical.

Duke, M.R., Shrader, B. and Mo, J.D. (1992) "Effect of a Rear Stagnation Jet on The Wake Behind a Cylinder", *AIAA Journal*, Vol. 31, No. 9, pp 1727-1729.

Durao, D.F.G., Heitor, M.V., Pereira, J.C.F. (1988) "Measurements of Turbulent and Periodic Flows Around A Square Cross-Section Cylinder", *Experiments In Fluids*, Vol. 6, No.5, pp 298-304.

van Dyke, M. (1982) "An Album of Fluid Motion", The Parabolic Press.

Engleman, M. and Jamnia, M.A. (1990) "Transient Flow Past a Circular Cylinder: A Benchmark Solution", *International Journal Of Numerical Methods In Fluids*, Vol. 11, pp 985-1000.

Every, M.J., King, R. and Weaver, D.S. (1982) "Vortex Excited Vibrations of Cylinders and Cables and Their Suppression", *Ocean Engineering*, Vol. 9, pp 135-157.

Fage, A. and Warsap, J.H. (1929) "The Effects of Turbulence and Surface Roughness on Drag of A Circular Cylinder", *British Aerodynamics Research Council*, Reported Memo. 1283.

Fage, A. and Johansen, F.C. (1927) "On The Flow of Air Behind Inclined Flat Plate of Infinite Span", *ARC R.&M.*, No. 1143.

Farell, C. (1981) "Flow Around Fixed Circular Cylinders: Fluctuating Loads", *Proceedings Of ASCE, EM3*, Paper No. 16330, pp 565-588.

Franke, R. and Rodi, W. (1991) "Calculation of Vortex Shedding Past a Square Cylinder with Various Turbulent Models", *Proceedings 8th Symposium On Turbulent Shear Flows*, Technical University Of Munich, Germany.

Franke, R., Rodi, W. and Schonung, B. (1990) "Numerical Calculation of Laminar Vortex-Shedding Flow Past Cylinders", *Journal Of Wind Engineering And Industrial Aerodynamics*, Vol. 35, No. 1-3, pp 237-257.

Gaskell, P.H and Lau, A.K.C (1988) "Curvature Compensated Convective Transport: SMART, A New Boundness Preserving Transport Algorithm", *International Journal Of Numerical Methods In Fluids*, Vol. 8, pp 617-641.

Gresho, P.M., Chan, S.T., Lee, R.L., Upson, C.D.(1984), "A Modified Finite-Element Method for Solving The Time-Dependent, Incompressible Navier-Stokes Equations" *International Journal For Numerical Methods In Fluids*, Vol.4, No.7, pp 619-640.

Griffin, O.M. (1982) "Vortex Streets and Patterns", *Mechanical Engineering*, March 1982, pp 56-61.

Griffin, O.M. and Ramberg, S.E. (1974) "The Vortex-Street Wakes of Vibrating Cylinders", *Journal Of Fluid Mechanics*, Vol. 66, pp 553-576.

Griffin, O.M. and Ramberg, S.E. (1976) "Vortex Shedding From a Cylinder Vibrating In-Line With an Incident Uniform Flow", *Journal Of Fluid Mechanics*, Vol. 75, pp 257-271.

Grimminger, G. (1945) "The Effect of Rigid Guide Vanes on The Vibration and Drag of a Towed Circular Cylinder", *David Taylor Basin, Washington*, Rep 504.

Hafen, B.E. and Meggit, D.J. (1971) "Cable Strumming Suppression", *Civil Engineering Laboratory, Naval Construction Battalion Centre, Port Hueneme, Calif.*, Report TN-1499, DN787011.

Hanko, Z.G. (1967) "Vortex Induced Vibration at Low-Head Wires", *Proceedings Of ASCE, Journal Of Hydraulics Division*, Vol. 93, pp 255-270.

Hori, E. (1959) "Experiments On Flow Around A Pair of Parallel Circular Cylinders", *Proceedings 9<sup>th</sup> Japan National Congress for Applied Mechanics*, Tokyo, pp 231-234.

Igarashi, T. (1978) "Flow Characteristics Around a Circular Cylinder With A Slit", *Bull. JSME*, Vol. 21, pp 656-664.

Igarashi, T. (1981) "Characteristics of Flow around Two Circular Cylinders Arranged In Tandem", *Bull. JSME*, Vol. 24, No. 188, pp 323-331.

Igarashi, T. and Tsutsui, T. (1989) "Flow Control Around a Circular Cylinder by a New Method", *Transactions of JSME*, Vol. 55, No.511, pp 701-713.

Jendrzejczyk, J.A. and Chen, S.S. (1985) "Fluid Forces on Two Circular Cylinders in Crossflow", Argonne National Lab., ANL-85-35.

Jendrzejczyk, J.A. and Chen, SS (1986) "Fluid Forces Acting on Circular Cylinders in Liquid Cross-Flow in Flow Induced Vibrations", ASME PVP, Vol. 104, pp 1-13.

Jing, L., Jiong, S. and Roux, B. (1992) "Numerical Study of an Oscillating Cylinder in Uniform Flow and in The Wake of an Upstream Cylinder", Journal Of Fluid Mechanics, Vol. 237, pp 457-478.

Kato, M. and Launder, B.E. (1993) "The Modelling of Turbulent Flow Around Stationary and Vibrating Square Cylinders", Proceedings 9<sup>th</sup> Symposium on Turbulent Shear Flows, Kyoto, Japan.

Kelkar, K.M., Patankar S.V. (1992) "Numerical Prediction of Vortex Shedding Behind a Square Cylinder" International Journal For Numerical Methods In Fluids, Vol. 14, No. 3, pp 327-341.

Koutmos, P., Mavridis, C. and Papailiou, D. (1995) "A Study of Unsteady Wake Flows Past Two-Dimensional Square Cylinder With and Without Planar Jet Injection Into The Vortex Formation Region", Applied Scientific Research, Vol. 55, No. 3, pp 187-210.

Kovasznyay, L.S.G. (1949) "Hot-Wire Investigation of the Wake Behind Cylinders at Low Reynolds Numbers", Proceedings Royal Society of London A, Vol. 198, pp 174-190.

Kwon, K. and Choi, H. (1996) "Control of Laminar Vortex Shedding Behind a Circular Cylinder Using Splitter Plates", Physics Of Fluids, Vol. 8, No. 2, pp 479-486.

Launder, B.E. and Spalding, D.B. (1974) "The Numerical Computations of Turbulent Flows", Computer Methods In Applied Mechanics And Engineering., Vol. 3, pp 269-289.

Lee, B.E. (1975) "The Effect of Turbulence on The Surface Pressure Field of a Square Prism", Journal Of Fluid Mechanics, Vol. 69, pp 263-282.

Li, J., Chambarel, A., Donneaud, M. and Martin, R. (1991) "Numerical Study of Laminar Flow Past One and Two Cylinders", Computers And Fluids, Vol. 19, No.2, pp 155-170.

Lienhard, J.H. (1966) "Synopsis of Lift, Drag and Vortex Frequency Data for Rigid Circular Cylinders", Bull. 300, College of Engineering, Research Division, Washington State University, Pullman , WA.

- Lin, S.Y. and Wu, T.M. (1994) "Flow Control Simulations Around a Circular Cylinder By a Finite Volume Scheme", Numerical Heat Transfer, Part A, Vol. 26, pp 301-319.
- Lyn, D.A. (1989) "Phase-Averaged Turbulence Measurements In The Separated Shear Layer Region of Flow Around A Square Cylinder", Proceedings 23<sup>rd</sup> Cong. International Ass. Hydraulic Research, Ottawa, Canada, A85-A92.
- Mo, J.D. and Duke, R. (1993) "Numerical Investigation of Cylinder Wake Flow With a Rear Stagnation Jet", AIAA Journal, Vol. 32, No. 5, pp 1095-1098.
- Oka, S., Kostic, Z.G. and Sikmanovic, S (1972) "Investigation of The Heat Transfer Processes in Tube Banks in Cross Flow", International Seminar on Recent Developments In Heat Exchangers, Trogir, Yugoslavia.
- Okajima, A. (1982) "Strouhal Numbers of Rectangular Cylinders", Journal Of Fluid Mechanics , Vol. 123, pp 379-398.
- Ongoren, A. and Rockwell, D. (1988) "Flow Structure from an Oscillating Cylinder. Part I: Mechanisms of Phase Shift and Recovery of the Near-Wake", Journal Of Fluid Mechanics, Vol. 191, pp 197-223.
- Patankar, S.V. (1980) "Heat Transfer And Fluid Flow", McGraw Hill Book Company.
- Patankar, S.V. and Spalding, D.B. (1972) "A Calculation Procedure for Heat, Mass and Momentum Transfer In Three-Dimensional Parabolic Flows", International Journal of Heat Mass Transfer, Vol. 15, pp 1787.
- Peric, M. (1985) "A Finite Volume Method for The Prediction of Three-Dimensional Fluid Flow In Complex Ducts", PhD. Thesis, University of London.
- Prandtl, L., (1914) Göttinger Nachrichten, pp 177-190.
- Price, P. (1956) "Suppression of the Fluid-Induced Vibration of Circular Cylinders", Proceedings ASCE, Journal of Engineering Mechanics Division, Vol. 82, pp 1030.
- Przulj, V. and Younis, B.A. (1993) "Some Aspects of The Prediction of Turbulent Vortex Shedding From Bluff Bodies", Forum On Unsteady Separated Flows, ASME Fluids Engineering Conference.
- Razavi, A.K. (1992) "Suppression of Vortex Shedding Instabilities by Injection Into the Free Stream", Final Year Project at City University, London, (unpublished).

Ren, G. and Blachen, J.G. (1993) "Finite Element Simulation of The Development of Vortex Shedding From A Pair of Circular Cylinders", Proceedings of the 3<sup>rd</sup> International Offshore and Polar Engineering Conference, Vol. 3, pp 384-391.

Reynolds, O. (1883) "An Experimental Investigation of The Circumstances Which Determine Whether The Motion of Water Shall Be Direct Or Sinuous, and of The Law of Resistance In Parallel Channels", Phil. Trans. Roy. Soc., Vol. 174, pp 935-982.

Rhie, C.M., Chow, W.L. (1983) "Numerical Study of The Turbulent-Flow Past an Airfoil With Trailing Edge Separation", AIAA Journal, Vol.21, No.11, pp 1525-1532.

Rockwell, D. (1990) "Active Control of Globally-Unstable Separated Flows", ASME International Symposium on Nonsteady Fluid Dynamics, Vol. 92, pp 379-94.

Rogers, A.C. (1983) "An Assessment of Vortex Suppression Devices for Production Risers and Towed Deep Ocean Pipe Strings", paper 4594, 15th Annual offshore Technology Conference, Houston, Texas.

Roshko, A. (1961) "Experiments on The Flow Past a Circular Cylinder at Very High Reynolds Numbers", Journal Of Fluid Mechanics, Vol. 78, pp 561-576.

Sakamoto, H. and Haniu, H. (1994) "Optimum Suppression of Fluid Forces Acting on a Cylinder", Journal Of Fluids Engineering, June, Vol. 116, pp 221-227.

Sakamoto, H., Tan, K. and Haniu, H. (1991) "An Optimum Suppression of Fluid Forces By Controlling a Shear Layer Separated From a Square Prism", Journal Of Fluids Engineering, June, Vol. 113, pp183-189.

Sarpkaya, T. and Ihrig, C.J. (1986) "Impulsively Started Steady Flow about Rectangular Prisms Experiments and Discrete Vortex Analysis", Journal Of Fluids Engineering", Transactions Of The ASME, Vol. 108, No. 1, pp 47-54.

Sasaki, K. and Kiya, M. (1984), "" Transaction Of JSME, Vol. 50, No. 456, pp 1842-1846.

Scruton, C. and Walshe, D.E.J. (1957) "A Means for Avoiding Wind-Excited Oscillations of Structures with Circular or Nearly Circular Cross Section", National Physics Laboratory (U.K.), Aero. Rep. 335.

Schewe, G. (1983) "On The Force Fluctuations Acting on a Circular-Cylinder in Cross-Flow from Subcritical up to Transcritical Reynolds-Numbers", Journal Of Fluid Mechanics, Vol. 133, No. Aug., pp 265-285.

- Shin, Y.S. and Wambsganss, M.W. (1977) "Flow-Induced Vibration In LMFBR Steam Generators: A State-Of-The-Art Review", Nucl. Eng. Des., Vol. 40, pp 235-284.
- Song, C.C.S. and Yuan, M. (1990) "Simulation of Vortex Shedding Flow about a Circular Cylinder at High Reynolds Numbers", Journal Of Fluid Engineering, Vol. 112, pp 155-163.
- Speziale, C.G. (1987) "On Nonlinear k-l and k- $\epsilon$  Models of Turbulence", Journal Of Fluid Mechanics, Vol. 178, pp 459-475.
- Stansby, P. and Slaouti, A. (1991) "Flow Around Multiple Cylinders by The Random Vortex Method", Proceedings 1<sup>st</sup> International Offshore and Polar Engineering Conf., Vol. 3, pp 228-235.
- Stephens, A.B., Bell, J.B., Solomon, J.M. and Hackerman, L.B. (1984) "A Finite-Difference Galerkin Formulation for The Incompressible Navier Stokes Equations", Journal of Computational Physics, Vol. 53, pp 152-172.
- Stone H.J. (1968), "Iterative Solution of Approximations of Multi-Dimensional Partial Differential Equations", S.I.A.M. Journal Of Numerical Analysis, Vol. 5, pp 530-558.
- Strykowski, P.J. and Sreenivasan, K.R. (1985) "The Control of Vortex Shedding Behind Circular Cylinders at Low Reynolds Numbers", Proceedings Of The Fifth Symposium On Turbulent Shear Flows, Cornell University, Ithaca.
- Strykowski, P.J. and Sreenivasan, K.R. (1990) "On The Formation and Suppression of Vortex Shedding at Low Reynolds Numbers", Journal Of Fluid Mechanics, Vol. 218, pp 71-107.
- Sun, J., Li, J. and Roux, B. (1993) "Flow Regimes and Frequency Selection of a Cylinder Oscillating in an Upstream Cylinder Wake", International Journal For Numerical Methods In Fluids, Vol. 16, pp 915-929.
- Tennekes, H. and Lumley, J.L. (1972) "A First Course in Turbulence", MIT Press.
- Thomas, D.G. and Kraus, K.A. (1964) "Interaction of Vortex Streets", Journal Of Applied Physics, Vol. 35, No.12, pp 3458-3459.
- Tokumar, P.T. and Dimotakis, P.E. (1989) "Rotary Oscillation Control of a Cylinder Wake", AIAA paper No. 819-1023, AIAA Second Shear Flow Control Conference, March 13-16, Temp, AZ.

- Walshe, D.E. and Wootton, L.R. (1970) "Preventing Wind-Induced Oscillations of Structures of Circular Section", Proceedings Inst. Civil Eng., Vol. 47, pp 1-24.
- West, G.S. and Apelt, C.J. (1993) "Measurements of Fluctuating Pressures and Forces on a Circular Cylinder in The Reynolds Number Range  $10^4$  To  $2.5 \times 10^5$ ", Journal Of Fluids And Structures, Vol. 7, No. 3, pp 227-244.
- Wieselberger, C. (1923) "Versuche über den Luftwiderstand Gerundeter und Kantiger Körper", Ergebnisse Aerodyn. Versuchsanstalt Göttingen (ed. L. Prandtl), pp 23.
- Williams, C.R. and Amato, C. (1989) "Unsteady Pulsing of Cylinder Wakes", In Frontiers In Experimental Fluid Mechanics (ed. M. Gad-el-Hak). Lecture Notes in Engineering 46, pp 337-364.
- Williamson, C. and Roshko, A. (1988) "Vortex Formation in The Wake of an Oscillating Cylinder", Journal Of Fluids And Structures, Vol. 2, pp 355-381.
- Wong, H.Y., Kokkalis, A. (1982) "A Comparative Study of Three Aerodynamic Devices for Suppressing Vortex Induced Oscillation", Journal Of Wind Engineering And Industrial Aerodynamics Vol. 10, pp 21-29.
- Wood, C.J. (1964) "The Effect of Base Bleed on a Periodic Wake", Journal Of Royal Aeronautic Society, Vol. 68, pp 477-482.
- Wood, C.J. (1967) "Visualisation of an Incompressible Wake With Base Bleed", Journal Of Fluid Mechanics, Vol. 29, pp 259-272.
- Woodgate, L. and Maybrey, J.F.M. (1959) "Further Experiments on the Use of Helical Strakes for Avoiding Wind Excited Oscillations of Structures of Circular or Nearly Circular Section", National Physics Laboratory (U.K.), Aero. Rep. 381.
- Wootton, L.R. and Yates, D. (1970) "Further Experiments on Drag Perforated Shrouds", National Physics Laboratory (U.K.), Aero Rep. 1321.
- Younis, B. A. (1987) "On Modelling The Vortex Shedding from Bluff Bodies in Laminar and Turbulent Streams", Proc. 7<sup>th</sup> Int. Conference on Offshore Mechanics & Arctic Eng., Houston, Texas, Feb 7-12, pp 223-228
- Younis, B.A. and Razavi, A.K. (1996) "On A Novel Method for The Control of Vortex Shedding From A Cylinder", Third International Colloquium on Bluff Body Aerodynamics & Applications, Virginia Polytechnic, USA.

Zdravkovich, M.M. (1981) "Review and Classification of Various Aerodynamic and Hydrodynamic Means of Suppressing Vortex Shedding", Journal Of Wind Engineering And Industrial Aerodynamics, Vol. 7, pp 145-189.

Zdravkovich, M.M. (1977) "Review of Flow Interference Between Two Circular Cylinders in Various Arrangements", Journal Of Fluids Engineering, Vol. 99, pp 618-633.

Zdravkovich, M.M. (1985) "Flow Induced Oscillations of Two Interfering Circular Cylinders", Journal Of Sound And Vibration , Vol. 101, No.4, pp 511-521.